10-15-2021 2:00 PM

Crack Self-Healing in Alkali-Activated Materials: From Mechanisms to Strategies for Enhancing the Healing Efficiency

Lei Zhang, *The University of Western Ontario*

Supervisor: Nehdi, Moncef L., *The University of Western Ontario*

A thesis submitted in partial fulfillment of the requirements for the Doctor of Philosophy degree in Civil and Environmental Engineering

ABSTRACT

The increasing concern for decarbonizing concrete manufacturing is calling for sustainable construction materials since portland cement production contributes about 8% of global anthropogenic carbon dioxide emissions. Alkali-activated materials (AAMs) have emerged as promising alternative binders to curb carbon dioxide emissions from portland cement production and allow more sustainable construction. In addition, AAMs have desirable mechanical properties and high resistance to acidic and sulphate attacks.

Like conventional concrete, AAMs are quasi-brittle materials with low tensile strength, demonstrating susceptibility to cracking. Cracking-initiated deteriorations such as reinforcing steel corrosion, sulphate attack, and freeze-thaw damage, pose severe threats to the service life of concrete structures. Yet, sustainability is not readily achievable even if structures were made of environmentally friendly AAMs. Increasing awareness of sustainability has promoted the development of crack self-healing technologies. While crack self-healing in cement-based materials has been a topic of extensive research, very few studies have so far investigated the self-healing of AAMs. Therefore, there is need to explore self-healing approaches for improving the crack self-healing capability of AAMs.

This dissertation is centered on exploring the possibilities of enhancing the self-healing efficiency in fibre-reinforced alkali-activated slag-based composites via using calcium hydroxide powder, crystalline additives, expansive minerals, and biomineralization. The self-healing effect was evaluated using a portfolio of techniques, including optical microscopy, compressive and tensile tests, sorptivity tests, mercury intrusion porosimetry (MIP), inductively coupled plasma optical emission spectroscopy (ICP-OES), and X-ray microcomputed tomography (μCT). Crack self-healing products were characterized using scanning electron microscopy with energy dispersive X-ray (SEM-EDS) analysis and Raman spectroscopy. Ultimately, a chemistry-informed machine learning model was proposed to estimate the compressive strength of AAMs, therefore guiding the design of AAMs that meet the requirements for construction. The results demonstrate that all healing strategies explored herein improved the crack closure ratio significantly. In addition, the mechanical properties, watertightness, and pore structure were enhanced. SEM-EDS revealed that the main self-

healing product was calcium carbonate. The computational intelligence model developed permits accurate prediction of the mechanical strength of AMMs and the effects of influential mixture design parameters. The findings of this study should bridge the knowledge gaps in crack self-healing of AAMs, thereby removing the hindrances that impede broader implementation of AAMs in construction applications.

Keywords

Alkali-activated materials; crack; self-healing; fibre; self-healing strategies; assessment of healing efficiency; mechanical properties; transport properties; self-healing products; machine learning model.

SUMMARY FOR LAY AUDIENCE

Except for water, concrete is the most widely used material in this world. It plays a vital role in developing urbanization and modernization. However, as the primary ingredient of concrete, portland cement requires fossil fuels and causes substantial greenhouse gas emissions during its production, thereby accelerating climate change. The increasing concern for a sustainable world is calling for green construction materials. Alkali-activated materials (AAMs), the products of reactions between industrial by-products or wastes and alkaline solutions, can be a green alternative to cement, with less environmental impacts. AAMs showed desirable performances comparable to that of their concrete counterparts.

Both AAMs and concrete are susceptible to cracking due to their brittle nature, which may threaten the lifespan of structures. The problem with cracks in a structure is that they provide preferential ways for the ingress of water, oxygen and chloride ions to steel rebars, thereby causing costly corrosion, and potentially compromising the safety of structures. To make AAMs more durable in response to cracking, the self-healing techniques inspired by nature, where organs can heal wounds automatically, were adopted in this study.

This dissertation aims to explore the self-healing improvement of AAMs using various additives and limestone-forming bacteria. The self-healing performance was investigated using multiple techniques. The results demonstrate that all the self-healing approaches improved the crack sealing significantly. It was also confirmed that the main self-healing product that healed surface cracks was limestone. The findings in this study help enhance the understanding of self-healing in AAMs, paving the way for developing sustainable green construction materials.

CO-AUTHORSHIP STATEMENT

This thesis has been prepared following the regulation of the integrated-article format stipulated by the Faculty of Graduate Studies at Western University. All the work stated in this thesis, including experimental testing, data analysis, and writing draft manuscripts for publication, was carried out by the candidate under the supervision and guidance of Dr. Moncef L. Nehdi. Any other co-authors assisted in modelling, conducting the experimental program and/or revision of the initial draft of the manuscript. The following publications have been either accepted or submitted to peer-reviewer technical journals and international conferences:

1) **L.V. Zhang**, A.R. Suleiman, and M. L. Nehdi, "Self-healing in fiber-reinforced alkali-activated slag composites incorporating different additives," *Construction and Building Materials*, 262 (2020): 120059. **Published**
2) **Lei V. Zhang**, Ahmed R. Suleiman, and Moncef L. Nehdi, "Crack self-Healing in NaOH-activated slag-based composites incorporating calcium hydroxide," *Journal of Materials in Civil Engineering*, 33(4):04021012. **Published**
3) **Lei V. Zhang**, Moncef L. Nehdi, Ahmed R. Suleiman, Malihe M. Allaf, Afshin Marani, and Murat Tuyan, "Crack Self-healing in Bio-Green Concrete," *Composites Part B: Engineering.* **Ready to Re-submit Revised Manuscript**
4) **Lei V. Zhang**, Ahmed R. Suleiman, Malihe M. Allaf, Afshin Marani, and Moncef L. Nehdi, "Crack self-healing in alkali-activated slag composites incorporating immobilized bacteria," *Construction and Building Materials.* **Submitted**
5) **Lei V. Zhang**, Afshin Marani, and Moncef L. Nehdi, "Chemistry-informed Machine Learning Prediction of Compressive Strength for Alkali-Activated Materials", *Journal of Cleaner Production*. **Submitted**
6) **Lei V. Zhang**, Murat Tuyan, Moncef L. Nehdi, Ahmed R. Suleiman, Afshin Marani, and Amir Ali Shahmansouri, "Self-healing in cementitious materials: A review of recent advances in methodologies, and evaluation techniques," *Construction and Building Materials*. **Prepare to submit before defense**
7) **L.V. Zhang**, A.R. Suleiman, A. Marani, and M.L. Nehdi, "Effect of various temperatures and relative humidities on crack self-healing in fiber-reinforced mortars

incorporating crystalline additives," *CSCE 2021 Annual Conference*, Niagara Falls, Canada. **In press**

8) **L.V. Zhang**, A.R. Suleiman, A. Marani, and M.L. Nehdi, "Comparative study on self-healing behavior of alkali-activated composites and cement-based materials," *CSCE 2021 Annual Conference*, Niagara Falls, Canada. **In press**

DEDICATION

This thesis is dedicated to:

My Grandmother Farihah Ma in heaven (Allah bless her soul)

My Mother Tianyue Zhu

My Father Desheng Zhang

My Mother-in-law Yuan Ren

My Beloved Wife Vanchy

My Beloved Daughter Elena

ACKNOWLEDGMENTS

How time flies. Sometimes it is hard to realize that I will farewell to my student life. I have enjoyed every moment at Western in the past four years, whether strolling on campus, feeding Canada geese, or even making concrete samples in labs. I do cherish all ineffable memories here, and even time cannot dissipate them.

My deep gratitude, thanks, and sincere appreciation go to my advisor Dr. Moncef L. Nehdi, for his guidance, support, encouragement, and patience throughout my research while providing me with the flexibility to work in my way. I am immensely grateful for studying under your precious guidance in the past four years.

The research work reported in this thesis was sponsored by China Scholarship Council (CSC) and Western University. I would like to express my appreciation for these institutes.

I am very thankful to Dr. Aiham Adawi and all the Department of Civil and Environmental Engineering staff members at Western University for their help and support during my study at Western.

I would like to thank Dr. Malihe Mehdizadeh Allaf for her valuable contribution to my research regarding *S. pasteurii* culture. My colleagues, Dr. Ahmed Ramadan Suleiman and Afshin Marani, gave me immense help with my research. The help from the other two colleagues, Abdullah Ramadan and Abdul-Aziz Younis, regarding my teaching assistant work is appreciated. Without them, I will be struggling with my TA duties. The support all my colleagues have shown throughout encouraged me when the finish line seemed far away.

From the depths of my heart, I would like to thank my parents for their continuous support. They did not get much education; however, they still believe education is the best self-empowerment. I never forget the moment in my childhood when my mother brought me a space science book with a gorgeous hardcover for $30 without any hesitation. She was a porter for carrying propane cylinders. This amount of money means that she had to take 80 lbs of a propane cylinder to the fifth floor of a building without elevators 40 times. She is the definition of a hero in my mind that never changes. I would like to thank my wife, mother-in-law, and lovely six-month-old daughter Elena for their accompany and endless

encouragement while working on my thesis. They have made many sacrifices throughout this doctoral journey. Without their love, tremendous support, and encouragement, it would never be possible to accomplish my academic goals.

TABLE OF CONTENTS

LIST OF TABLES

LIST OF FIGURES

Chapter 1

1 INTRODUCTION

1.1 RESEARCH BACKGROUND

Except for water, concrete is the world's most widely used material and has been a backbone of urbanization, industrialization and modernization (Alyousef *et al.*, 2020; Li *et al.*, 2018; Yıldırım *et al.*, 2015; Wang *et al.*, 2019). It was estimated that concrete consumption is approaching 30 billion tonnes per year (Monteiro *et al.*, 2017). An essential ingredient of concrete, ordinary portland cement (OPC) has been the most extensively used binder in civil infrastructure. The global cement production has grown consistently at an annual rate of about 9% over the past decades and is estimated to reach 6.1 billion metric tons in 2050 (Ranjbar *et al.*, 2020; Amran *et al.*, 2019). Nevertheless, the high production of OPC is now facing the challenge of massive carbon dioxide (CO_2) emissions, mainly due to the thermal decomposition of limestone, the primary raw material in cement manufacturing (Provis and Bernal, 2014). It has been reported that cement manufacturing contributes about 8% of the global anthropogenic CO_2 emissions (Miller *et al*., 2016). Increasing levels of CO_2 into the atmosphere cause accelerated climate change. Annual greenhouse gas emissions in 2019 hit a record high with a sharp increase in OPC production globally, raising concerns about the associated environmental impacts. In addition, OPC production consumes a large amount of energy, and existing data shows that 4 GJ of energy provided by coal or other fossil fuels is required to produce one tonne OPC (Gartner, 2004). Therefore, pursuing an eco-friendly alternative to OPC is of utmost importance to mitigate environmental pollution, save energy, avert the threat of climate change, and attain sustainability goals.

Alkali-activated materials (AAMs), clinker-free binders derived from the reaction products between solids in powder form containing aluminosilicate resources and aqueous alkaline activators, provide a sustainable way for lowing the CO_2 footprint of concrete through clinker-free cement production and utilization of wastes (Singh and Middendorf, 2020). The solid precursors containing aluminosilicates can be beneficiated industrial by-products (e.g., fly ash from coal combustion or metallurgical slag from iron production) or thermally treated clays (e.g., metakaolin). Apart from saving large amounts of CO_2 compared to ordinary cement production, AAMs also have demonstrated unconventionally superior performance regarding their high strength after proper curing, high-temperature resistance, acid resistance, and superior immobilization of heavy metal ions (Ding *et al*., 2016).

It is well known that concrete is susceptible to cracking due to various sources due to its inherent brittleness and fracture in tension (Li *et al*., 2018). The occurrence of cracks threatens the durability and integrity of reinforced concrete structures since cracks provide an open gateway for hostile media such as oxygen, sulphates, and chloride ions to ingress into the cementitious matrix. If cracks are not repaired properly within the stipulated time, the steel reinforcement may corrode, endangering the durability and service life of reinforced concrete structures (Priya *et al*., 2019).

Similarly, AAMs also are quasi-brittle materials and vulnerable to cracks (Krizan and Zivanovic, 2002). Numerous studies have revealed that the risk of early-age cracking caused by drying shrinkage in AAMs was considerably higher than that for OPC-materials (Atiş *et al*., 2009; Song *et al*., 2016). This would impose restrictions on wide construction applications of AAMs. *In-situ* crack repair can be challenging due to inaccessibility. In addition, conventional repair methods are typically onerous, laborious, and time-consuming, thus causing enormous financial burdens (Yıldırım *et al*., 2015). For instance, In the UK, repair and maintenance costs occupy more than 45% of the annual expenditure on construction. The increasing concern regarding the resilience of AAM infrastructure is calling for novel approaches that can heal cracks automatically without human intervention.

Inspired by nature, where biological systems possess the ability to recover from physical damage, tremendous research efforts have been devoted to crack self-healing, from macromolecular compounds (Ma *et al*., 2019) to electronic materials (Markvicka *et al*., 2018) and metals (Ferguson *et al*., 2014). The self-healing phenomenon was also observed in cementitious materials, which can be adopted to self-heal cracks. Usually, self-healing in OPC-based materials can be divided into autogenous healing and autonomous healing (Wu *et al*. 2012). Autogenous healing can be defined as an inherent ability to seal cracks automatically without any human intervention. The autogenous healing occurs primarily due to the formation of $CaCO_3$ and carbonation of dissolved $Ca(OH)_2$, sealing cracks by impurities from water or debris particles caused by crack spalling. Other mechanisms include prolonged hydration of unreacted cement or other cementitious materials and swelling of hydrated cementitious products (C-S-H) (Reinhardt *et al*., 2013). In comparison, autonomous healing can be achieved by introducing three main substances: mineral admixtures, mineral-forming bacteria, and encapsulated healing agents. A variety of novel approaches have been explored to achieve self-healing structures, which can significantly impact sustainability and economics (Li and Herbert, 2012). In contrast, very few studies have reported that AAMs were capable to self-heal cracks (Shen *et al*., 2008; Nicolas *et al*., 2014). The self-healing behaviour in AAMs may be due to unreacted particles resulting in a prolonged geopolymerization (Tang *et al*., 2019). The concern for the sustainability of AAMs structures calls for developing new self-healing green construction materials.

1.2 RESEARCH NEEDS AND MOTIVATION

Despite the remarkable progress achieved in self-healing in OPC-based materials, systematic research on the self-healing of AAMs is still lacking. Therefore, there is a need to discover self-healing behaviour in AAMs. Exploring the ability to endow AAMs with crack self-healing ability has paramount importance as AAMs will be implemented in more and more construction applications. This dissertation attempts to employ several autonomous self-healing techniques in alkali-activated slag-based materials to enhance self-healing efficiency. The effect of the environment in AAMs matrix on the efficiency

of the autonomous healing methods is still questionable, indicating an excellent opportunity to explore.

Despite the remarkable progress achieved in self-healing of OPC-based materials, systematic research on the self-healing of AAMs is still lacking. Therefore, there is need to investigate the self-healing behaviour of AAMs. Exploring the ability to endow AAMs with crack self-healing ability has paramount importance since AAMs are being implemented in increasing construction applications with diverse environmental exposures. This dissertation attempts to employ several autonomous self-healing techniques in alkali-activated slag-based materials to enhance their self-healing efficiency. The effect of the exposure environment of the AAMs matrix on the efficiency of the autonomous healing methods is still questionable, indicating an excellent opportunity for research discovery.

1.3 OBJECTIVES OF THIS RESEARCH

To address the research needs and motivation mentioned above, this dissertation aims to improve the current limited knowledge on crack self-healing behaviour in AAMs and autonomous self-healing mechanisms. The specific objectives of this research are detailed below:

- Conducting a systematic and critical overview of the state-of-the-art on self-healing approaches and assessment techniques for cementitious materials.
- Exploring the effect of $Ca(OH)_2$ on the self-healing performance of alkali-activated slag composites.
- Experimentally investigating the self-healing efficiency of alkali-activated slag composites incorporating crystalline additives and expansive minerals such as bentonite.
- Investigating the crack self-healing effectiveness of alkali-activated slag composites incorporating mineral-forming bacteria (*S. pasteurii*).
- Evaluating the crack healing efficiency in terms of surface crack closure ratio and regained transport properties.

- Examining the influence of the self-healing behaviour using the aforementioned techniques (e.g. bacteria) on the hydration kinetics and mechanical properties.
- Visualizing the crack healing and characterizing the self-healing compounds using a portfolio of testing techniques, such as X-ray computed tomography, SEM-EDS, and Raman spectroscopy.
- Developing a machine learning model to estimate the compressive strength of AAMs based on mixture proportions, chemical compositions of precursors, and activators.

1.4 STRUCTURE OF THE THESIS

This dissertation has been prepared according to the integrated-article format predefined by the Faculty of Graduate Studies at Western University, London, Ontario, Canada. It compromises 8 chapters covering the scope of this study: Crack self-healing in alkali-activated materials: From mechanisms to strategies for enhancing the healing efficiency. Several parts of this thesis have been published, accepted, or submitted in peer-reviewed journals.

This chapter, **Chapter 1,** outlines the research background, research motivation, objectives, and thesis structure.

Chapter 2 presents a state-of-the-art review on the self-healing mechanisms of cementitious materials, self-healing strategies, and assessment methods to evaluate the self-healing effectiveness. It also discusses contemporary challenges that have arisen in implementing self-healing into construction materials.

Chapter 3 experimentally explores the crack self-healing capability of alkali-activated slag composites incorporating calcium hydroxide. The surface crack healing ratio was linked with the concentration of calcium ions measured by inductively coupled plasma optical emission spectroscopy. The pore structure was investigated by mercury intrusion porosimetry. Furthermore, the self-healing compounds formed within cracks were characterized by scanning electron microscopy coupled with energy-dispersive X-ray spectroscopy (SEM-EDS). X-ray microcomputed tomography (μCT) provided a detailed visualization of self-healing as a function of crack depth via 3D reconstruction analysis.

In **Chapter 4**, the effect of crystalline additives and bentonite on the crack self-healing capability of alkali-activated slag composites was investigated. Apart from the evaluation techniques used in the previous chapter, the effect of the minerals on mechanical properties (e.g., compressive strength and tensile strength) was explored.

Chapter 5 investigates the potential of *S. pasteurii* bacteria to impart crack self-healing in alkali-activated slag-based composites. Porous expanded glass granules made from recycled glass were used as bacterial and nutrient carriers. The effect of environmental exposures on self-healing effectiveness was also discussed.

Chapter 6, based on chapter 5, investigates the effect of different calcium sources (e.g. calcium lactate and calcium chloride) on the reaction kinetics, mechanical properties, capillary water absorption, and final self-healing compounds.

Chapter 7 proposes a chemistry-informed machine learning model to estimate the compressive strength of AAMs based on their mixture proportions and the chemical compositions of their precursors and activators.

Chapter 8 summarizes the conclusions of this study along with recommendations for future research.

1.5 REFERENCES

Alyousef, R. A. M., Alabduljabbar, H. A. M., and El-Zeadani, M. (2020). Clean production and properties of geopolymer concrete; A review.

Amran, Y. M., Alyousef, R., Alabduljabbar, H., and El-Zeadani, M. (2019). Clean production and properties of geopolymer concrete: A review. *Journal of Cleaner Production*, 119679.

Atiş, C. D., Bilim, C., Çelik, Ö., and Karahan, O. (2009). Influence of activator on the strength and drying shrinkage of alkali-activated slag mortar. *Construction and Building Materials, 23*(1), 548-555.

Ding, Y., Dai, J.-G., and Shi, C.-J. (2016). Mechanical properties of alkali-activated concrete: A state-of-the-art review. *Construction and Building Materials, 127*, 68-79.

Ferguson, J., Schultz, B. F., and Rohatgi, P. K. (2014). Self-healing metals and metal matrix composites. *Jom, 66*(6), 866-871.

Gartner, E. (2004). Industrially interesting approaches to "low-CO2" cements. *Cement and Concrete Research, 34*(9), 1489-1498.

Krizan, D., and Zivanovic, B. (2002). Effects of dosage and modulus of water glass on early hydration of alkali–slag cements. *Cement and Concrete Research, 32*(8), 1181-1188.

Li, V. C., and Herbert, E. (2012). Robust self-healing concrete for sustainable infrastructure. *Journal of Advanced Concrete Technology, 10*(6), 207-218.

Li, W., Dong, B., Yang, Z., Xu, J., Chen, Q., Li, H., Xing, F., and Jiang, Z. (2018). Recent advances in intrinsic self-healing cementitious materials. *Advanced Materials, 30*(17), 1705679.

Ma, X., Shi, C., Huang, X., Liu, Y., and Wei, Y. (2019). Effect of natural melanin nanoparticles on a self-healing cross-linked polyurethane. *Polymer Journal, 51*(6), 547.

Markvicka, E. J., Bartlett, M. D., Huang, X., and Majidi, C. (2018). An autonomously electrically self-healing liquid metal–elastomer composite for robust soft-matter robotics and electronics. *Nature materials, 17*(7), 618-624.

Miller, S. A., Horvath, A., and Monteiro, P. J. (2016). Readily implementable techniques can cut annual CO2 emissions from the production of concrete by over 20%. *Environmental Research Letters, 11*(7), 074029.

Monteiro, P. J., Miller, S. A., and Horvath, A. (2017). Towards sustainable concrete. *Nature materials, 16*(7), 698-699.

Priya, T. S., Ramesh, N., Agarwal, A., Bhusnur, S., and Chaudhary, K. (2019). Strength and durability characteristics of concrete made by micronized biomass silica and Bacteria-Bacillus sphaericus. *Construction and Building Materials, 226*, 827-838.

Provis, J. L., and Bernal, S. A. (2014). Geopolymers and related alkali-activated materials. *Annual Review of Materials Research, 44*, 299-327.

Ranjbar, N., and Zhang, M. (2020). Fiber-reinforced geopolymer composites: A review. *Cement and Concrete Composites, 107*, 103498.

Reinhardt, H., Jonkers, H., Van Tittelboom, K., Snoeck, D., De Belie, N., De Muynck, W., Verstraete, W., Wang, J., and Mechtcherine, V. (2013). Recovery against environmental action *Self-Healing Phenomena in Cement-Based Materials* (pp. 65-117): Springer.

San Nicolas, R., Bernal, S. A., de Gutiérrez, R. M., van Deventer, J. S., and Provis, J. L. (2014). Distinctive microstructural features of aged sodium silicate-activated slag concretes. *Cement and Concrete Research, 65*, 41-51.

Shen, W., Zhou, M., Xiao, L., Ma, W., and Cai, Z. (2008). Morphology difference between the alkali activated cement and portland cement paste on multi-scale. *Journal of Wuhan University of Technology-Mater. Sci. Ed., 23*(6), 923-926.

Singh, N., and Middendorf, B. (2020). Geopolymers as an alternative to Portland cement: An overview. *Construction and Building Materials, 237*, 117455.

Song, C., Choi, Y. C., and Choi, S. (2016). Effect of internal curing by superabsorbent polymers–internal relative humidity and autogenous shrinkage of alkali-activated slag mortars. *Construction and Building Materials, 123*, 198-206.

Tang, Z., Li, W., Hu, Y., Zhou, J. L., and Tam, V. W. (2019). Review on designs and properties of multifunctional alkali-activated materials (AAMs). *Construction and Building Materials, 200*, 474-489.

Wang, X., Zhang, J., Han, R., Han, N., and Xing, F. (2019). Evaluation of damage and repair rate of self-healing microcapsule-based cementitious materials using electrochemical impedance spectroscopy. *Journal of Cleaner Production, 235*, 966-976.

Wu, M., Johannesson, B., and Geiker, M. (2012). A review: Self-healing in cementitious materials and engineered cementitious composite as a self-healing material. *Construction and Building Materials, 28*(1), 571-583.

Yıldırım, G., Keskin, Ö. K., Keskin, S. B., Şahmaran, M., and Lachemi, M. (2015). A review of intrinsic self-healing capability of engineered cementitious composites: Recovery of transport and mechanical properties. *Construction and Building Materials, 101*, 10-21.

Chapter 2

2 LITERATURE REVIEW

This chapter presents an overview of mechanisms of autogenous self-healing and autonomous self-healing in cementitious materials, followed by stimulated autogenous healing and autonomous healing methods employed to enhance the self-healing efficiency. In addition, comprehensive evaluations of self-healing effectiveness are reviewed.

2.1 SELF-HEALING MECHANISMS IN CEMENTITIOUS MATERIALS

Self-healing in cementitious materials is usually categorized into autogenous healing and autonomous healing based on whether this self-healing is originated from a host (i.e., cementitious matrix) or is triggered by a guest (i.e., extrinsic materials are embedded in the cementitious matrix) (Li *et al*., 2018).

2.1.1 Autogenous healing

In cement-based materials, autogenous crack healing is an inherent capability occurring in the presence of moisture (Qiu *et al*., 2019). This phenomenon is associated with the physical properties and/or chemical compositions of the matrix. Based on existing research, autogenous healing can be primarily attributed to further hydration of residual cement in an initial stage (Huang *et al.*, 2016; Qiu *et al.*, 2019) and carbonation of dissolved calcium hydroxide at later ages (Cuenca and Ferrara, 2017; Wang *et al.*, 2019; Yıldırım *et al.*, 2018). Apart from the aforementioned mechanisms, swelling of hydrated cementitious materials and debris settlement partially contribute to autogenous crack healing (Sangadji, 2017) (see **Figure 2-1**).

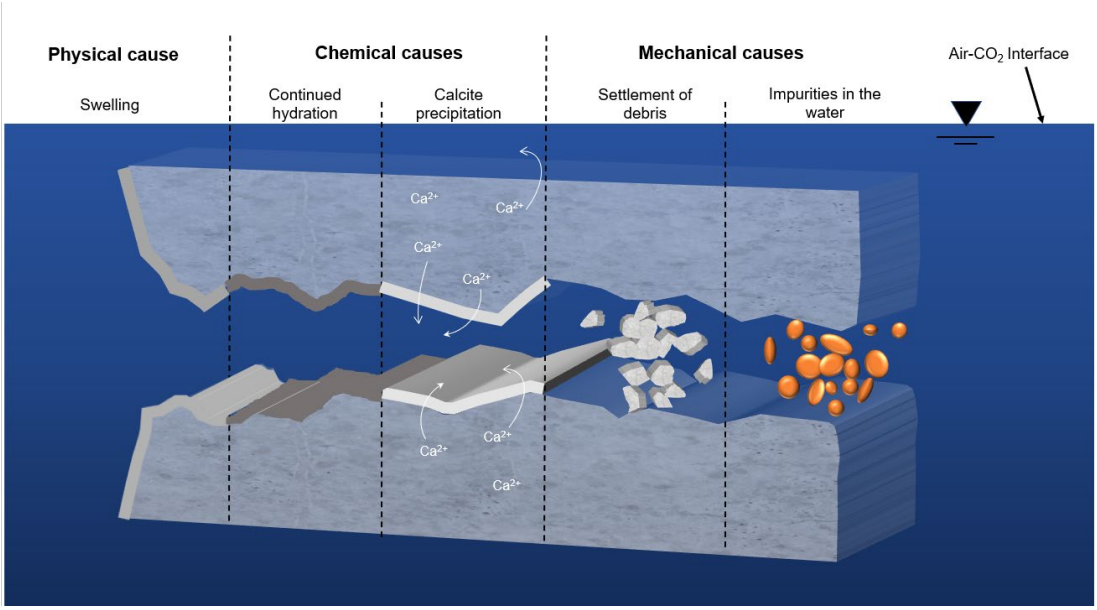

Figure 2-1: Main mechanisms facilitating autogenous self-healing in cementitious materials. Reproduced from (De Rooij *et al*., 2013).

The further hydration of residual cement is a common phenomenon occurring in young concrete. During the period of cement hydration, the reaction slows down probably because a layer of reaction product (C-S-H) forms, thereby preventing the further reaction by hindering anhydrous particles from being accessible to water. However, the rehydration of unreacted cement particles can be triggered upon contacting water in the presence of cracks (Neville, 1995). Therefore, additional hydration products fill the cracks. Reactions related to cement rehydration are depicted in **Figure 2-1**.

The crystallization of calcium carbonate is the primary mechanism contributing to self-healing in mature cement-based materials (Palin *et al.*, 2016; Pang *et al.*, 2016). When the cement-based material is exposed to water, the Ca^{2+} ions from $Ca(OH)_2$ leach out of the cementitious matrix. CO_2 from the atmosphere dissolves in water and converts to H_2CO_3. However, H_2CO_3 quickly decomposes into HCO_3^- and CO_3^{2-} owing to its instability. Calcium carbonate is then formed by the reaction between CO_3^{2-} or HCO_3^- and Ca^{2+} ions. The precipitation of calcium carbonate can be described by **Eqs. 6-1 to 6-3**. It was inferred that a higher pH value promotes the precipitation of calcium carbonate

according to **Eq. 6-1** because higher pH shifts the H_2CO_3 equilibrium, converting to the formation of CO_3^{2-} (Sisomphon *et al.*, 2012; Wang *et al.*, 2014b; Zhang *et al.*, 2017b).

$$2OH^- + H_2CO_3 \leftrightarrow CO_3^{2-} + 2H_2O \quad \text{Eq. 6-1}$$

$$Ca^{2+} + CO_3^{2-} \rightarrow CaCO_3 \ (pH_{water} > 8) \quad \text{Eq. 6-2}$$

$$Ca^{2+} + HCO_3^- \rightarrow CaCO_3 + H^+ \ (7.5 < pH_{water} < 8) \quad \text{Eq. 6-3}$$

It is worth noting that the concentrations of CO_3^{2-} and HCO_3^- decrease as the crack depth increases (Sisomphon *et al.*, 2012). Therefore, most calcium carbonate precipitates near the surface of cracks (Suleiman *et al.*, 2019).

In AAMs, autogenous healing could be responsible for further geopolymerization of unreacted compounds or carbonation (Glukhovskij *et al.*, 1983; Nguyễn *et al.*, 2018; Zhang *et al.*, 2020).

The capability of autogenous healing to seal cracks is only effective in small width cracks (Aldea *et al.*, 2000; Reinhardt and Jooss, 2003). Several studies have revealed that the maximum healable crack width by autogenous healing ranges from 150-300 μm (Suleiman and Nehdi, 2018b). To improve autogenous healing, numerous approaches have been proposed. These methods include introducing fibre reinforcements (Askarinejad and Rahbar, 2017; Choi *et al.*, 2016; Feng *et al.*, 2019; Qiu *et al.*, 2019), a supply of water for further hydration by employing superabsorbent polymers (SAP) (Gruyaert *et al.*, 2016a; Hong and Choi, 2017; Lefever *et al.*, 2020; Snoeck *et al.*, 2016), or lightweight aggregates (LWA) (Alghamri *et al.*, 2016; Dembovska *et al.*, 2019; Tziviloglou *et al.*, 2016; Wang *et al.*, 2018) and extending the curing time by developing polymer modified concrete (PMC) (Hu *et al.*, 2017; Korkmaz and Al-Durzi, 2016; Mazzoni *et al.*, 2017).

2.1.2 Autonomous healing

Numerous studies have been devoted to the development of approaches that can attain crack autonomic healing in cementitious materials. There are three typical approaches used to achieve autonomous healing in cement-based materials according to different

healing mechanisms: (1) mineral admixtures (Alghamri *et al*., 2018; Jiang *et al.*, 2019; Qureshi *et al.*, 2019; Wang *et al.*, 2018; Yuan *et al.*, 2019); (2) capsulated self-healing agents (Hia *et al.*, 2018; Hu *et al.*, 2018; Kosarli *et al.*, 2019); and (3) microbially induced calcite precipitation (MICCP) (Ansari *et al.*, 2020; Seifan *et al.*, 2018b; Tan *et al.*, 2019; Tziviloglou *et al.*, 2016).

Many studies have reported that the maximum healable crack width through autonomous healing is much larger than that for autogenous healing. Erşan *et al.* (2016), for instance, found that the highest crack width healed by the microbial self-healing strategy was 480 ± 16 μm in 56 days. Similarly, Du *et al*. (2019) developed novel microcapsules with toluene-di-isocyanate (TDI) used as the core and paraffin used as the shell material for crack self-healing of concrete. The results showed that the mortar with a crack width of 400 μm was self-healed by the microcapsules in 6h.

2.2 SELF-HEALING STRATEGIES

2.2.1 Stimulated autogenous healing approaches

According to earlier discussion in **Section 2.1.1**, effectively enhanced autogenous healing can be achieved by controlling the crack width physically, supplying extra water resulting in rehydration and crystallization, and/or triggering pozzolanic reactions. In this case, some of the recent works are summarized below.

2.2.1.1 Synthetic fibres

To control the crack width and therefore promote crack autogenous healing, engineered cementitious composite (ECC), a class of high-performance strain-hardening cement-based composite (SHCC), was first developed by Li *et al*. who continued to improve it over the past decades (Liu *et al*., 2017; Yang *et al*., 2005; Yang *et al*., 2011). ECC has a strain capacity within the range of 3–7% under uniaxial tension, which is hundreds of times that of conventional cement-based materials (Li, 2003). Essentially, when ECC is overstretched or bent, multiple microcracks, typically below 60 μm occur, rather than a few wide cracks in the case of ordinary cement-based materials (Huang *et al*., 2016; Li *et al*., 2001; Liu *et al*., 2017; Sahmaran *et al*., 2013; Wu *et al*., 2020; Yang *et al*., 2007).

This microcracking behaviour leads to superior autogenous healing since narrower cracks are more likely to be healed than wider cracks (Liu *et al*., 2019; Qiu *et al*., 2016; Suleiman and Nehdi, 2018).

Synthetic fibres usually include polypropylene (PP), polyethylene (PE) and polyvinyl alcohol (PVA) fibres. The highest self-healing efficiency can be achieved by incorporating PVA fibres as confirmed by previous studies (Cuenca and Ferrara, 2017; Homma *et al*., 2009; Nishiwaki *et al*., 2012). This can be attributed to the hydroxyl group within the PVA fibre molecules having the highest polarity strength to attract calcium ions and promote nucleation sites for calcium carbonate growth (Choi *et al*., 2016; Feng *et al*., 2019; Wang *et al*., 2019).

2.2.1.2 Superabsorbent polymer (SAP)

SAPs are synthetic 3D cross-linked hydrogels with a high capacity to absorb water through hydrogen bonding with water molecules (Chindasiriphan *et al*., 2020; Mechtcherine *et al*., 2018; Saini *et al*., 2018; Xiao *et al*., 2017). SAPs can swell substantially up to 1000g/g, as depicted in **Figure 2-2 (a)**. Apart from SAP implementation in multiple application domains (e.g., sanitary, agriculture sector, and biomedical purposes) (Caló and Khutoryanskiy, 2015; Kim *et al*., 2015; Silva *et al*., 2015), the use of SAPs in cementitious materials has recently been gaining increasing attention (Cunha *et al*., 2019; Kang *et al*., 2018a, b; Mechtcherine *et al*., 2018). SAPs are usually introduced to cementitious systems to change the rheology (Ma *et al*., 2019), increase the freeze-thaw resistance (Hong *et al*., 2018; Kim *et al*., 2019; Mechtcherine *et al*., 2017; Wong, 2018; Yang *et al*., 2018), and mitigate autogenous shrinkage (Kang *et al*., 2018b; Liu *et al*., 2019; Yang *et al*., 2020; Yang *et al*., 2019). Moreover, incorporating SAPs as crack self-healing promoters has attracted much attention (Mignon *et al*., 2017).

The self-healing mechanisms in cementitious materials attained by incorporating SAPs can be categorized into a physical blocking effect and triggering of further hydration or precipitation of calcium carbonate, as schematically illustrated in **Figure 2-2(b)** (Snoeck *et al*., 2020; Van Tittelboom and De Belie, 2013). For autogenous healing, liquid water in

the surrounding environment is essential to trigger self-healing via further cement hydration or calcium carbonation. However, SAPs can initiate self-healing by absorbing humid air, making crack self-healing less dependent on surrounding liquid water (Lee *et al*., 2016).

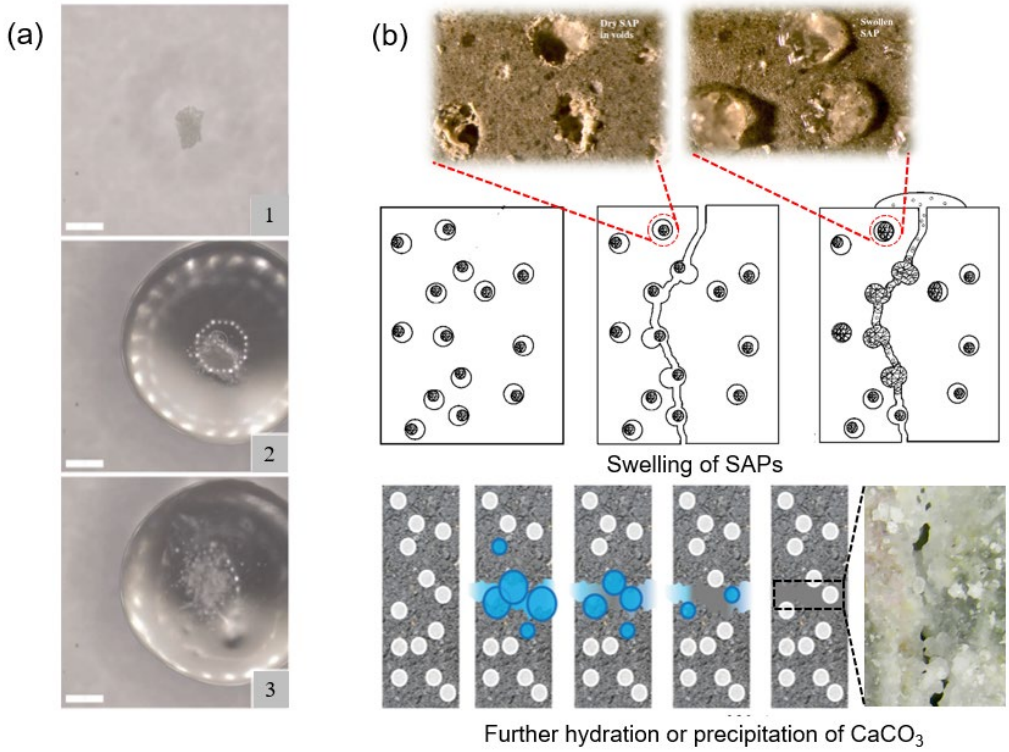

Figure 2-2: Characteristics of SAP: (a) visualization of the SAP particle after absorbing water (Snoeck *et al*., 2014); (b) schematic illustration of SAP particles facilitating autogenous healing via physical blocking and triggering further hydration or carbonation. Reproduced from (Lee *et al*., 2010, 2016; Snoeck *et al*., 2020).

It is worth noting that the swelling of SAP particles is sensitive to the pH value and concentration of ionic species. For instance, a pH-dependent swelling and Ca^{2+} ions sensitiveness test of SAPs was fundamentally studied by Migon *et al*. (2015), which showed that SAPs exhibited the largest fluid uptake capability at pH = 7 at low concentration of calcium chloride. However, a noticeable drop was observed when increasing the pH above 7 and the calcium chloride concentration (Wang *et al*., 2019).

Since SAPs are incorporated into the concrete batch, they show a much lower fluid uptake capability than in plain water. This is because cement paste has high alkalinity (pH of 12.5-13) with high ionic concentrations, including Ca^{2+}, Na^{+}, and SO_4^{2-} (Ferrara *et al*., 2018; Lee *et al*., 2016; Mechtcherine *et al*., 2018). SAP particles shrink gradually after discharging the absorbed water due to cement hydration, creating many macropores (Gwon *et al*., 2019; Mechtcherine *et al*., 2018; Mignon *et al*., 2019; Yao *et al*., 2012). Cracks caused by varying deterioration mechanisms propagate through these macropores. When concrete is exposed to external wetting and moisture, the dormant SAPs will be reactivated by water ingress and can swell again. SAPs will swell more substantially if the fluid coming inside of cracks has lower ionic concentration, thereby expanding beyond macropores and filling into cracks. Another mechanism can be explained by the role of SAPs as water reservoirs, especially when concrete is subjected to low relative humidity or cyclic water, triggering continuous hydration and precipitation of calcium carbonate for self-healing (Lee *et al*., 2010). Snoek *et al*. incorporated 1% of SAPs by weight of cement into a cementitious composite. At 90% relative humidity, SAPs stimulated further hydration; however, no healing was observed in the reference samples (Snoeck *et al*., 2020).

2.2.1.3 Supplementary cementitious materials (SCM)

Considerable studies have demonstrated that incorporating SCMs, such as blast furnace slag, fly ash, and silica fume, significantly improved the properties of cementitious materials. Moreover, the blending of SCMs in concrete dramatically reduced calcium dioxide emissions due since they do not require clinkering procedures in cement kilns, thus contributing to sustainability of concrete construction (Juenger and Siddique, 2015; Lothenbach *et al*., 2011; Sharma and Khan, 2017; Siddique and Cachim, 2018).

Apart from the aforementioned benefits of SCMs, they can improve the self-healing potential of cementitious materials owing to their latent pozzolanic reactions and ongoing hydration. Qiu *et al*. (2016) systematically investigated the influence of blast furnace slag on the autogenous healing of ECCs. They reported that the autogenous healing efficiency was improved by incorporating slag as demonstrated by crack width reduction and resonant frequency recovery. Similarly, according to Chindasiriphan *et al*. (2020), the

midterm self-healing capability of concrete can be improved by the synergistic effect of fly ash and SAP.

Pozzolanic reactions are a long-term process involving aluminosilicates and calcium hydroxide in water, to form a cementitious matrix. Sufficient calcium hydroxide and a higher pH above 12 are needed to initiate or trigger the pozzolanic reactions (Van Tittelboom *et al*., 2012b). Cement could not be replaced with fly ash or slag at a large percentage since calcium hydroxide produced from cement hydration may be insufficient to support the pozzolanic reactions (Huang *et al*., 2014a). Effects of the slag content were investigated by Qiu *et al*. (2016) using resonant frequency and microstructure analysis, which showed that up to 30% of slag could achieve best self-healing capability. The obtained results are consistent with observations from the study by Li *et al*. (2020).

2.2.1.4 Polymer-modified concrete (PMC)

Polymer-modified concrete (PMC), also named polymer-cement concrete (PCC), is a type of concrete using water-dispersed polymers to partially substitute for cement (Taha, 2018). Coalescence of the polymer initiates during cement hydration, thereby creating a co-matrix of organic polymer and hydrated cement particles (Schlangen, 2005). A classification of organic polymer admixtures for PMC is shown in **Figure 2-3**.

An interpenetrating network in PMC achieved by polymer and cement co-binder exhibits much higher flexural and tensile strength and long-term durability than ordinary cement-based concrete (Ferdous *et al*., 2020; Priniotakis *et al*., 2018). The changed phase of polymers in PMCs owing to external stimuli could also allow the repair of damaged concrete. For instance, Childers *et al*. (2017) developed a novel polymer-cement composite containing epoxies for geothermal wellbore applications, which demonstrated superior self-healing ability by sealing cracks widths of 0.3−0.5 mm.

The self-healing efficiency in PMC is affected by various factors, including temperature, alkalinity, type of cement, chemical contents in PMC, etc. (Muhammad *et al*., 2016; Taha, 2018). For example, Yuan *et al*. (2017) used ethylene-vinyl acetate (EVA) copolymer in hydraulic fracturing wells. Their experimental results show that the EVA-modified

cement yielded considerable self-healing efficiency when increasing the temperature below 110°C. Similarly, one type of epoxy can be hardened in the presence of calcium hydroxide, resulting in a cross-linked structure (Huseien *et al*., 2015; Łukowski and Adamczewski, 2013; Sam *et al*., 2015). There is an excess of unhardened epoxy resin wrapped in hardened epoxy. When cracks caused by various deteriorations penetrate through the unhardened epoxy resin, the epoxy flows and fills the microcracks. Then the cracks are tightened as the resin contacts calcium hydroxide (De Belie *et al*., 2018).

Recently, a novel deployment of shape memory polymer (SMP) for triggering self-healing in concrete was proposed (Teall *et al*., 2018). The SMP tendons cast in concrete could alter their physical shapes in response to external stimuli, closing cracks via compressive stress (Hazelwood *et al*., 2014; Teall, 2016). For the first time, a large-scale application of an SMP-based system for self-healing concrete was designed and tested by Davies *et al*. in the United Kingdom. They used polyethylene terephthalate (PET) strips placed in a concrete panel to induce compressive stress, reducing the crack width and enhancing self-healing. The results showed that the panel with PET strips exhibited significant crack closure and recovery of structural stiffness (Davies *et al*., 2018).

Figure 2-3: Classification of polymeric admixtures for PMC. Reproduced from (Ohama, 1997).

2.2.1.5 Shape-memory-alloy (SMA)

Shape-memory-alloys (SMA) are metallic alloys that can recover plastic deformation triggered by external stimuli such as heat, and thus generate thermal-induced forces (Li *et al.*, 2016). This behaviour is achieved by transformable changes in the crystalline structure due to temperature and the shape memory effect. The reversible phase changes include the transition from a more-ordered austenite phase to a less-ordered martensite phase (Young and Hirst, 2012). SMAs are widely used in many applications such as automotive, spacecraft, robotics, biomedical, etc.

SMAs exploited as smart materials have become a research hotspot owing to their substantial potential for repairing and retrofitting structural elements, seismic-resistant design, and reinforcement in civil applications. In particular, SMAs applied to self-repair concrete cracks is a relatively novel application that has been receiving considerable attention. The self-healing mechanism of SMA in concrete refers to SMA wires embedded in concrete exhibiting heat-responsive recovery because of their shape-memory effect, thereby closing cracks (Bonilla *et al*., 2018; Wang*et al*., 2019; Zhang *et al*., 2020). When cracks occur in SMA-reinforced concrete, SMA wires or bars are stretched by plastic strain and then bridge cracks. The wires or bars apply compressive stress to the concrete matrix by shrinking back to their pre-deformed shape if heated above the shape transformation temperature, thereby clamping cracks (Misra, 2013).

SMAs have various composite systems, including iron-based and copper-based alloys, such as Fe-Pd, Fe-Mn, Fe-Mn-Si, Cu-Zn, Cu-Zn-Al Cu-Zn-Al-Mn-Zr, and Cu-Al-Be (Alam *et al*., 2007). Although iron-based and copper-based SMAs are low-priced and commercially available, their poor thermo-mechanic performance and instability hinder their widespread use. In contrast, NiTi-based SMAs are much preferable for a majority of concrete applications. Extensive research on NiTi-based SMAs applied to repair cracks of concrete structures has been undertaken. Some previous experimental results about the self-healing efficiency using NiTi-based SMAs with various transformation temperature ranges are summarized in **Table 2-1**.

Table 2-1: Crack healing after applying NiTi-based SMAs

Type	Shape	Diameter	Number	Crack healing ratio	Reference
$Ni_{49.2}$-$Ti_{50.8}$	Straight	2 mm	4	83.7% (w_0=3.98 mm)	Li *et al*., 2006
$Ni_{50.5}$-$Ti_{49.5}$	Straight	1 mm	5	61.4% (w_0=0.57 mm)	Choi *et al*., 2014
$Ni_{50.5}$-$Ti_{49.5}$	Dog-bone	1 mm	5	34.7% (w_0=0.46 mm)	
Ni_{57}-Ti_{43}	Straight	0.67 mm	2	73.2% (w_0=0.56 mm)	Lee *et al*., 2018
Ni_{57}-Ti_{43}	Straight	0.67 mm	3	92.4% (w_0=0.53 mm)	
Ni_{57}-Ti_{43}	Straight	0.67 mm	4	100% (w_0=0.57 mm)	
Ni_{57}-Ti_{43}	Dog-bone	0.67 mm	2	44.9% (w_0=0.49 mm)	
Ni_{57}-Ti_{43}	Dog-bone	0.67 mm	3	47.2% (w_0=0.53 mm)	
Ni_{57}-Ti_{43}	Dog-bone	0.67 mm	4	62.5% (w_0=0.56 mm)	
Ni_{45}-Ti_{43}-Nb_{12}	Straight	0.67 mm	2	43.4% (w_0=0.53 mm)	
Ni_{45}-Ti_{43}-Nb_{12}	Straight	0.67 mm	3	46.2% (w_0=0.54 mm)	
Ni_{45}-Ti_{43}-Nb_{12}	Straight	0.67 mm	4	76.8% (w_0=0.56 mm)	
$Ni_{50.8}$-$Ti_{49.2}$	Straight	2 mm	5	85.7% (w_0=6.3 mm)	Kuang and Ou, 2008
$Ni_{50.8}$-$Ti_{49.2}$	Straight	2 mm	5	100% (w_0=1 mm)	
-	Straight	0.5 mm	-	36.1% (w_0=3.1 mm)	Sun *et al*., 2013

2.2.2 Autonomous healing methods

As mentioned in **Section 2.1.2**, autonomous healing can be artificially triggered by embedding mineral admixtures, chemical or biological self-healing agents into the cementitious matrix. These agents are usually directly incorporated into concrete mixtures; however, some are impregnated in porous materials such as expanded perlite (EP), encapsulated using a vascular network, or macro/microcapsules to improve the self-healing efficiency.

2.2.2.1 Mineral admixtures

To date, the autonomous healing by mineral admixtures can be further categorized into three main groups: crystalline admixtures, geomaterials, and expansive additives, as shown in **Table 2-2**.

Table 2-2: Different admixtures facilitating self-healing via different reactions

Category	Materials	Mechanism	References
Crystalline admixtures	Sodium silicate	$Na_2SiO_3 + Ca(OH)_2 \rightarrow x(CaO \cdot SiO_2) \cdot H_2O + Na_2O$	
	Na_2CO_3, $NaHCO_3$	$R_2CO_3 + Ca(OH)_2 \rightarrow CaCO_3 + 2\ ROH$	Azarsa *et al*., 2019; Beglarigale *et al*., 2018; Cuenca *et al*., 2018; Roig-Flores *et al*., 2016; Wang *et al*., 2018
	Li_2CO_3		
	Colloidal silica	$SiO_2 + Ca(OH)_2 \rightarrow x(CaO \cdot SiO_2) \cdot H_2O$	
	Ethyl silicates	$Si(OC_2H_5)_4 + 4H_2O \rightarrow Si(OH)_4 + 4C_2H_5OH$ $Si(OH)_4 + Ca(OH)_2 \rightarrow x(CaO \cdot SiO_2) \cdot H_2O$	
	Synthetic crystalline additive (CA)	$3CaO\text{-}SiO_2 + M_xR_x + H_2O \rightarrow Ca_xSi_xO_xR\text{-}(H_2O)_x + M_xCaR_x\text{-}(H_2O)_x$	
Swelling admixtures	Calcium Sulphoaluminate (CSA)	React with water or compounds in ordinary Portland cement to form expansive products, such as ettringite, magnesium hydrate, magnesium carbonate to block the cracks	Buller *et al*., 2019; Kishi, 2007; Sánchez *et al*., 2006
	Anhydrite ($CaSO_4$)		
	Free lime (CaO)		
	Bentonite		
	MgO		

Various mineral admixtures, including geomaterials, expansive agents, and chemical agents, were employed by Ahn and Kishi (2010) to investigate their enhancement of the crack self-healing in concrete. Results showed that the crack width decreased significantly within 28 days due to a combination of swelling effect, expansion effect, and re-crystallization. In a similar study, Sherir *et al.* (2017) confirmed that incorporating MgO-type expansive agents achieved sealing of micro-cracks of engineering cementitious composites (ECC) and higher flexural strength recovery than their counterparts without MgO.

Crystalline additives (CAs), as a type of permeability-reducing admixture containing reactive silica and crystalline catalysts with hydrophilic nature, have been widely employed in watertight concrete structures such as dams and piers (Azarsa *et al*., 2019). The active components of CAs react with compounds from cement in the presence of water, which forms water-insoluble precipitates that block pores and seal cracks. The component reacting with CAs is tricalcium silicate (C_3S) (see **Eq. 2-4**), yet some researchers stated that $Ca(OH)_2$ is the reactive component (Roig-Flores *et al*., 2016; Sisomphon *et al*., 2012).

$$3CaO - SiO_2 + M_xR_X + H_2O \rightarrow Ca_xSi_xO_xR - (H_2O)_x + M_xCaR_x - (H_2O)_x \quad \text{Eq. 2-4}$$

Recent developments of CAs in the self-healing of cementitious materials have attracted much attention. Sisomphon *et al.* (2012) investigated the self-healing potential of mortars incorporating CA and reported favourable crack-sealing ability. Crack widths of up to 370 μm were completely healed in the mortars containing 4% (by weight of cement) CA. The results, however, indicated the best self-healing efficiency was attained when 1.5 wt.% CA or 10 wt.% calcium sulfoaluminate based expansive additive (CSA) was added to the mixture, thereby completely sealing crack widths of up to 400 μm. In addition, the analyses showed that high calcium concentrations owing to the incorporation of CA and higher pH value favoured the precipitation of self-healing products.

Roig-Flores *et al.* (2015) also studied the effect of CA on the self-healing of concrete under various environmental exposures. In their study, the concrete containing CA exposed to water immersion achieved the highest self-healing efficiency, fully healed cracks that had initial width of up to 0.25 mm. Later, self-healing properties and durability characteristics of concrete incorporating CA were fundamentally studied by Azarsa *et al.* (2019) using a portfolio of tests including a rapid chloride permeability (RCP), self-healing test, surface/bulk electrical resistivity tests, compressive strength test, and salt ponding test. The obtained results showed that concrete incorporating CA exhibited much more significant reduction in the water permeability coefficient and higher rate of self-healing ratio in comparison with reference specimens. Recently, Li *et al.* (2020) investigated the synergetic effect of SAP and CA on macrocracks (width larger

than 0.5 mm). The influential factors, such as the initial crack width, water curing time, and SAP/CA dosage, were also studied. They found that the CA containing citric acid was the most suitable type for achieving crack self-healing, and the combination of SAP and CA with an optimum dosage was suggested for enhancing self-healing.

2.2.2.2 Encapsulation of self-healing agents

Encapsulation of self-healing agents in cementitious materials was inspired by research of White *et al.* (2001), who proposed a concept of microencapsulated-based self-healing mechanism. The self-healing is accomplished when damage-induced cracks rupture the microcapsules, the releasing encapsulated healing agents into the gaps via capillary suction. Polymerization is then triggered when the healing agents react with embedded catalytic chemicals within the matrix, thereby bridging cracks. Encapsulation has been considered a promising self-healing system since this process is promptly activated when cracks generate, allowing a site-specific crack repair.

Encapsulation-based self-healing in cementitious materials can be broadly classified into microencapsulation, macro-encapsulation, and vascular self-healing system differed by sequestering the healing functionality when triggered by cracking (De Belie *et al*., 2018; White *et al*., 2011). Numerous factors affecting the design of the self-healing encapsulation system should be considered, such as crack patterns (Van Tittelboom *et al*., 2011, 2012a, and 2015), encapsulation materials (Xue *et al*., 2019), the composition of self-healing agents (Jackson *et al*., 2011), as well as the curing conditions (Jin *et al*., 2014; Yuan *et al*., 2013). In this section, the state-of-the-art progress for encapsulated self-healing pathways is summarized.

a. Microcapsule (< 1mm) embedment

Microencapsulation is a promising technique for providing autonomic self-healing by sequestering self-healing minerals or agents in micron-sized inert shells, which isolate and prevent core materials from harsh external environments (Benita, 2005; Ghosh, 2006). In this mechanism, microcapsules are directly implanted into the cementitious matrix, and self-healing is only triggered by releasing core materials when microcapsules rupture owing to cracking-based damage. Numerous investigations have been conducted

to test the efficiency of microcapsule-based autonomic healing in cementitious materials (Dong *et al*., 2015; Kanellopoulos *et al*., 2017; Yang *et al*., 2011). To date, a great variety of novel synthesis approaches, shell compositions, properties, and core materials have been extensively researched, as summarized in **Table 2-3**.

b. Macro-encapsulation

While the feasibility of microencapsulation in self-healing cementitious materials has been proven either in lab-scale or in field applications (Paine *et al*., 2019a), a possible concern is that the microcapsules embedded in the concrete matrix could not seal large cracks due to the limited amount of released self-healing agents. Therefore, geometry parameters of macro-encapsulation have been considered.

As a possible alternative to micro-capsules, macro-capsules applied in crack self-healing of cementitious materials have been extensively investigated. Dry (1993 and 1994) conducted one of the earliest studies on macro-encapsulation with hollow fibres and tubes containing a more significant self-healing agent than microcapsules, thereby offering multiple quality self-healing. Mono- and multicomponent methyl methacrylate were used as core material for healing. The agents with high viscosity can easily flow into cracks when the fibres and tubes were ruptured. Subsequently, a passive smart-healing engineered cementitious composite (PSS-ECC) was developed by Li *et al*. (1998). In their study, hollow glass fibres (100 mm in length, 0.8 mm interior diameter, and 1 mm exterior diameter) carrying 50 μl air-curing superglue (ethyl cyanoacrylate) were embedded in the ECC matrix. The self-healing effect was validated via regained stiffness capacity tests.

More recently, dry expansive minerals (MgO, bentonite, and quicklime) encapsulated in concentric glass macrocapsules for self-healing were proposed by Qureshi *et al*. (2016). The encapsulation system has two thin-walled capsules, where the core capsule carried water, and the outer capsule contained the minerals. The results showed that the specimens exposed to water submersion yielded the best healing capacity, with around 95% crack sealing and about 25% strength recovery in 28 days. However, undesired alkali-silica reactions may occur when using glass tubes or capsules. In addition, glass

tubes or capsules cannot resist the mixing process of concrete, thereby causing ruptures before cracking. Ceramic and polymeric capsules carrying self-healing agents, therefore, were developed as alternatives to their glass counterparts. For example, Tittelboom *et al*. (2011) developed tubular ceramic capsules filled with healing agents and embedded the capsules in the mortar matrix. The results showed that more than half of the original strength and stiffness could be restored in pre-cracked mortars. Three types of lab-scale polymeric capsules, namely, Poly(lactic acid) (PLA), Polystyrene (PS), and Poly(methyl methacrylate/n-butyl methacrylate) (P(MMA/n-BMA)), were made by Hilloulin *et al*. (2015) to increase the survival ratio of the capsules during the mixing of concrete. **Table 2-4** lists more detailed research findings on different types of macro-capsules triggering self-healing.

Table 2-3: A summary of microcapsules embedded in cementitious materials

Synthesis methods	Shell material	Core material	Diameter (μm)	Shell thickness (μm)	Dosage (% of cement)	Maximum healed width (μm)	Self-healing performance	References
Emulsion & polymerization	UF	$Ca(NO_3)_2$	70	0.81	0.5-1.25	N/A	N/A	Al-Ansari *et al*., 2017
Sol-gel	Silica	Epoxy	N/A	N/A	5	N/A	Sorptivity coefficient ↓	Calvo *et al*., 2017
ROMP	UF	DCPD and SS	80-600	0.23-0.7	0.5; 1.0; 2.5; 5.0	N/A	N/A	Gilford III *et al*., 2014
Complex coacervation	Gum Arabic/ gelatine	SS emulsion in oil (1:1)	290–700	N/A	0.8; 1.6; 2.3; 3.1; 4.6; 5; 6	170	Crack mouth healing (20–77%↑); Crack depth (↓); Capillary absorption (54%↓)	Kanellopoulos *et al*., 2016; Paine *et al*., 2019b
N/A	Hydrogel	Bacterial spores	N/A	N/A	2; 5	507	water permeability (68%↓)	Wang *et al*., 2014a
Poly-condensation	Melamine	Bacterial spores	N/A	N/A	1; 2; 3; 4; 5	970	Maximum 80 mm^2 of healed area;	Wang *et al*., 2014b
Extrusion/ Photopolymer-ization	Modified alginate	Bacterial spores	20-100	N/A	0.5; 1	N/A	N/A	Wang *et al*., 2015

Table 2-3: Continued

Synthesis methods	Shell material	Core material	Diameter (μm)	Shell thickness (μm)	Dosage (% of cement)	Maximum healed width (μm)	Self-healing performance	References
Emulsion/ dispersion	Gelatine	Epoxy, tung oil, and $Ca(OH)_2$	50	N/A	5	N/A	N/A	Cailleux and Pollet, 2009
Double emulsions	Acrylate	PVA, colloidal silica; HDDA; IBOA; BisGMA	88; 110	2-7	N/A	N/A	Interfacial bonding↑;	Souza and Al-Tabbaa, 2018
Chemical triggering, emulsion, and extrusion	EC	MFP	400-1200	145-183	0; 3; 5	N/A	N/A	Dong *et al*., 2015

Note: UF: urea-formaldehyde; ROMP: ring-opening metathesis polymerization; DCPD: dicyclopentadiene SS: sodium silicate; PVA: poly(vinyl alcohol); HDDA: 1,6-hexanediol diacrylate; IBOA: isobornyl acrylate; BisGMA: bisphenol A glycerolate dimethacrylate; EC: ethylene cellulose; MFP: monofluorophosphate.

Table 2-4: Different macro-capsule materials for self-healing cementitious materials

Literatures	External diameter (mm)	Shell thickness (mm)	Length (mm)	Shell materials	Capsule shapes	Healing agents	Maximum healed crack width	Other test results
Hilloulin *et al.*, 2015	1.9-7.2	0.4-1.7	50; 100	Poly(lactic acid); Polystyrene; Poly(methyl methacrylate/ n-butyl methacrylate)	Cylinder	—	—	—
Lv *et al.*, 2020	8	1	20	cellulose and gelatine coated with waterproofing mortar	Cylinder	Epoxy acrylate- based UV adhesive	—	21.3 % self-healing efficiency; maximum contributed to about 83.33% reduction of the water permeability.
Li *et al.*, 1998	1	0.1	100	Glass	Cylinder	Ethyl cyanoacrylate	—	—
Qureshi *et al.,* 2016	11.4	0.45	50	Glass	Cylinder	MgO, CaO, and bentonite	400 μm	Optimum healing efficiency with around 95% crack sealing and 25% strength recovery in 28 days.
Araújo *et al.*, 2018	10	0.7	50	Glass and Poly(methyl methacrylate) (PMMA)	Cylinder	water-repellent agent	—	—
Feiteira *et al.*, 2016 and 2017	3.35	0.18	50	Glass	Cylinder	Polyurethane-based products	—	A maximum stiffness regain of 35% was achieved

Table 2-4: Continued

Literatures	External diameter (mm)	Shell thickness (mm)	Length (mm)	Shell materials	Capsule shapes	Healing agents	Maximum healed crack width	Other test results
Gruyaert *et al.*, 2016b	2.3-3	0.3	50	Polymer, ceramic, and glass	Cylinder	Polyurethane	—	The water absorption was reduced by 41%
Tsangouri *et al.*, 2019a	3; 5	0.175; 0.5	75	Glass	Tubular	Polyurethane -based adhesive	—	Fracture toughness increased up to 35%
Šavija *et al.* 2017	6.14-8.4	0.26-1.19	50	Poly(methyl methacrylate) (PMMA); Polylactic acid	Cylinder	Polyethylene glycol monomethyl ether (PEG)	—	—
Wu *et al.* 2020	2	—	—	Geopolymers	Spherical	Bacterial spore powder	550 μm	The permeability declined by about two orders of magnitude
Tittelboom *et al.*, 2011	2.20; 3.35; 3.86	0.1; 0.17; 0.26	15; 18.4; 41.3	Glass and ceramic	Cylinder	Polyurethane	—	The water permeability reduced by a factor 10^2 to 10^4
Joseph *et al*., 2010	—	—	100	Glass	Cylinder	Cyanoacrylat -e	—	—
Maes *et al*., 2014	3.35	0.175	50	Glass	Cylinder	Polyurethane	—	Higher possibility than spherical ones for encountering cracks

c. Vascular self-healing system

Vascular-based self-healing in concrete was inspired by vascular network systems in nature, such as the mammal cardiovascular system that allows blood to circulate and transport oxygen, hormones, nutrients, etc., and plant vascular tissue system that transfers fluid and nutrients internally, via xylem and phloem. Similarly, liquid healing agents in the vascular system can be delivered to damaged zones via the network, thereby sealing cracks. In addition, liquid healing agents can be continuously supplied externally. Compared to either micro-encapsulation or macro-encapsulation, the vascular self-healing system can heal much wider cracks since there is technically no limit on the amount of healing agents filling cracks.

The vascular healing system can be classified into 1D, 2D, and 3D vessel channel networks based on the layout. The simplest form is 1D channels with both ends accessible from the concrete surface (Mihashi *et al*., 2000). 1D channel is usually applied when a one-component healing agent is used (Van Tittelboom and De Belie, 2013). More complicated 2 and 3D vessel networks were created to realize complex transport paths for healing agents delivered to the cracked sites via multi-flow junction nodes (Davies *et al*., 2015). Healing agents flow to cracked zones under the action of gravity, capillary force, and pressure difference (Gardner *et al*., 2014; Joseph *et al*., 2010) when brittle vessels rupture due to concrete cracking.

Extensive research on the efficacy and reliability of vascular-based self-healing systems in concrete has been undertaken. In 1994, the vascular concept in concrete was firstly proposed by Dry (1994), who used thin hollow glass fibres containing methyl methacrylate embedded within concrete for healing cracks. The results showed that both permeability and flexural toughness were significantly improved without losing strength. Joseph *et al*. (2010) conducted a series of experiments on crack self-healing in reinforced mortar beams embedded with adhesive-filled glass tubes as a 1D vascular channel. Results showed that both primary and secondary healing occurred during the two loading cycles. In addition, low-viscosity cyanoacrylate was proven to be one of the most promising healing agents in this healing system. Huang *et al*. (2014b) investigated self-

healing in cementitious composites deploying saturated calcium hydroxide solution as the healing agent supplied by capsules and vascular networks. They found that the vascular method was superior to the capsulation approach because the vascular healing system provided a constant supply of healing agents. To address a full range of complex physical damage in cementitious infrastructure systems, EPSRC funded the Materials for Life (M4L) project led by Cardiff University, the University of Cambridge, University of Bath, and the University of Bradford, which developed the first UK full-scale field trials on self-healing concrete using a combination of healing techniques in 2015. As one of the techniques, a 2D vascular network with mineral healing agents was adopted in concrete wall panels on-site (Al-Tabbaa *et al*., 2018; Davies *et al*., 2016; Davies *et al*., 2018; Teall *et al*., 2016). More recently, Li *et al*. (2020) designed and fabricated novel biomimetic 1D, 2D, and 3D vascular systems in prismatic cementitious specimens through 3D printing. The results showed that the 3D vascular-cement system achieved the best crack healing. The recovery of mechanical properties via self-healing was 34% in specimens embedded with 3D vascular networks compared to 20% for the 1D and 2D specimens.

2.2.2.3 Microbially Calcium Carbonate Precipitation (MICCP)

MICCP is a biochemical process by which microorganisms produce calcium carbonate via diverse metabolic pathways. This phenomenon is ubiquitous in nature, and can be found in soils, freshwater, marine sediments, etc. (Castro-Alonso *et al*., 2019). MICCP has been introduced as a promising and effective self-healing method addressing cracking issues in concrete while showing its eco-friendly potential (De Belie *et al*., 2018). There are many types of microorganisms applied in the self-healing of concrete structures. **Figure 2-4** depicts the statistical percentage of cement-based materials incorporating bacteria over the last decade. In recent years, considerable interest has been directed toward the bacterial genus Bacillus (over 80% of total bacteria) considering its high resistance to unfavourable conditions.

Different species of bacteria may facilitate the precipitation of calcium carbonate via varied metabolic pathways. Therefore, four main carbonatogenesity mechanisms including nitrogen cycle, sulphur cycle, photosynthesis, and aerobic respiration (Lee and

Park, 2018; Li *et al*., 2018) have been proposed. The four pathways for self-healing of cement-based materials reported in previous references are summarized in **Table 2-5**.

The nitrogen cycle can be defined as a biogeochemical cycle in which nitrogen is transformed into various chemical forms via bacterial activities, thereby facilitating calcium carbonate precipitation. This cycle consists of two pathways, including ureolysis and denitrification.

An enzyme urease governs the urea hydrolysis within ureolytic bacteria such as *S. pasteurii*, *B. sphaericus*, etc., including a series of reactions, shown in **Eqs. 2-5** to **2-9**. Urea hydrolyzed intracellularly by urease results in the production of carbamate and ammonia, followed by being spontaneously hydrolyzed to form additional ammonia and carbonic acid. Furthermore, ammonia reacts with water and is then converted to hydroxide ions. Finally, the concentration of carbonate increases, inducing an increase in the supersaturation level, thus triggering calcium carbonate precipitation around the *S. pasteurii* cell wall when the soluble calcium ions are sufficient in the surrounding environment (**Eqs. 2-10** and **2-11**).

Table 2-5: Four main pathways of bio-inspired crack self-healing of concrete

Category	Strains	Nutrient for carbonation	Concentration (cells/mL)	Immobilized methods	Maximum healed crack width	References
Nitrogen cycle	*S. pasteurii*	Urea	10^9	calcium sulphoaluminate cement and silica fume; direct mix	417 μm;	Ruan *et al*., 2019; Xu and Wang, 2018
	B. subtilis	Carbo-hydrates and salts; $CaCl_2$	10^5	Direct mix; Recycled brick coarse aggregate	400 μm; 920 μm	Nguyen *et al*., 2019; Saleem *et al*., 2021
	B. sphaericus	Urea, organic carbon; $Ca(NO_3)_2.4H_2O$; $CaCl_2$; Calcium formate	10^9	Microcapsule; silica gels; polyurethane; Diatomaceo-us earth; iron oxide nanoparticles; hydrogels	970 μm; 170 μm; 700 μm; 450 μm	Da Silva *et al*., 2015; Erşan *et al*., 2015; Seifan *et al*., 2018a; Wang *et al*., 2012; Wang *et al*., 2014; Wang *et al*., 2014b; Wang *et al*., 2012
	B. licheniformis	Urea, $CaCl_2$	-	Iron oxide nanoparticles	-	Seifan *et al*., 2018a
	B. cereus CS1	Urea	9.6×10^8	Coating bio-capsules	550 μm	Wu *et al*., 2020
	B. megaterium	Urea, Calcium lactate	10^3, 10^5, 10^7	Direct mix	-	Andalib *et al*., 2016

Table 2-5: Continued-1

Category	Strains	Nutrient for carbonation	Concentration (cells/mL)	Immobilized methods	Maximum healed crack width	References
	D. nitroreducens	$Ca(NO_3)_2$, calcium formate	-	Expanded clay; Diatomaceo-us earth	370 ± 20 μm	Erşan *et al*., 2015; Erşan *et al*., 2016
	Pseudomonas aeruginosa	$Ca(NO_3)_2$, calcium formate	-	Expanded clay	480 ± 16 μm	Erşan *et al*., 2016
	Bacillus sp. CT-5	Urea, $CaCl_2$	5×10^6, 5×10^7, and 5×10^8	Direct mix	460 μm	Achal *et al*., 2013
Sulphur cycle	*D. desulfuricans*	Organic matter and sulfate	10^8–10^9	-	-	Braissant *et al*., 2007
	D. vulgaris	Organic matter and sulfate	-	-	-	Baumgartner *et al*., 2006
Photosynth esis	Cyanobacteria	CO_2, H_2O	-	-	-	Lee and Park, 2018
Aerobic respiration	*B. alcalophilus*	Calcium lactate, glucose	2.16×10^9	Direct mix	400-500 μm	Su *et al*., 2020
	S. pasteurii	Calcium lactate	10^6	Zeolite;	-	Bhaskar *et al*., 2017
	S. ureae	Calcium lactate	10^6	Zeolite	-	Bhaskar *et al*., 2017

Table 2-5: Continued-2

Category	Strains	Nutrient for carbonation	Concentration (cells/mL)	Immobilize-d methods	Maximum healed crack width	References
Aerobic respiration	*B. cohnii*	Calcium acetate; calcium lactate; calcium glutamate	10^8; 1.2×10^7; 10^7; 3.6×10^9	Direct mix; lightweight aggregates; expanded perlite with geopolymer coating	<1 mm; 400 µm; 790 µm	Jonkers *et al*., 2010; Sierra-Beltran *et al*., 2014; Xu and Yao, 2014; Zhang *et al*., 2017a)
	B. pseudofirmus	Calcium acetate and calcium lactate	6×10^8; 7.4×10^9, 1.85×10^{10}, 3.7×10^{10}, 5.55×10^{10}, 7.4×10^{10}, 1.5×10^9	Direct mix; expanded perlite; lightweight aggregates	<1 mm	Alazhari *et al*., 2018; Balam *et al*., 2017; Jonkers *et al*., 2010
	B. alkalinitrilicus	Calcium lactate	1.7×10^5	Expanded clay	460 µm	Wiktor and Jonkers, 2011
	B. subtilis	Calcium lactate	3×10^8; 1.9×10^7;	lightweight aggregates; recyled coarse aggregates	820 µm; 1150 µm	Khaliq and Ehsan, 2016; Khushnood *et al*., 2020
	Lysinibacillus sphaericus	Calcium lactate	7×10^7	Direct mix	-	Chaerun *et al*., 2020

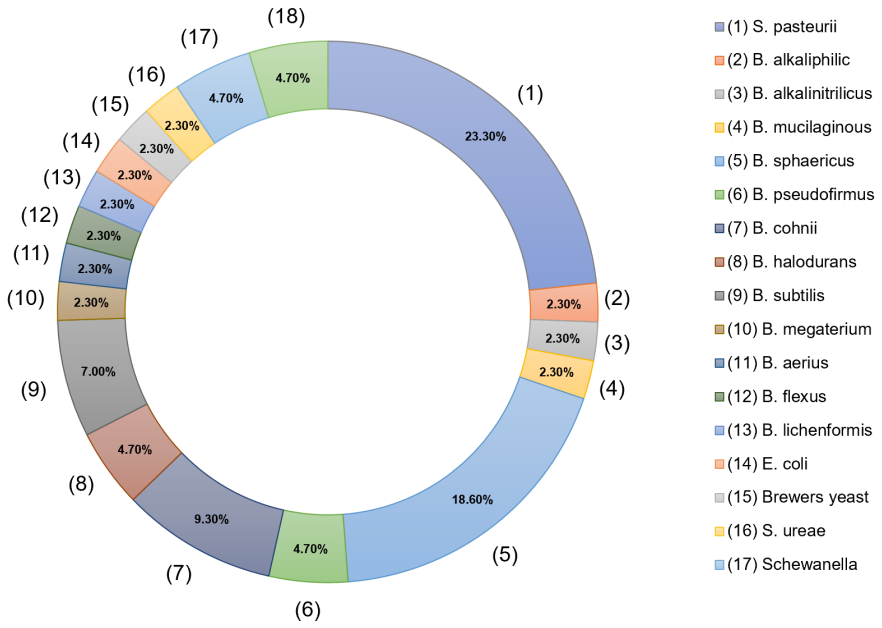

Figure 2-4: Statistics of bacterial applications in cementitious materials (Nguyen *et al.*, 2019).

$$CO(NH_2)_2 + H_2O \xrightarrow{\text{Urease}} NH_2COOH + NH_3 \quad \text{Eq. 2-5}$$

$$NH_2COOH + H_2O \rightarrow H_2CO_3 + NH_3 \quad \text{Eq. 2-6}$$

$$H_2CO_3 \leftrightarrow HCO_3^- + H^+ \quad \text{Eq. 2-7}$$

$$2NH_3 + 2H_2O \leftrightarrow 2NH_4^+ + 2OH^- \quad \text{Eq. 2-8}$$

$$HCO_3^- + H^+ + 2NH_4^+ + 2OH^- \leftrightarrow CO_3^{2-} + 2NH_4^+ + 2H_2O \quad \text{Eq. 2-9}$$

$$Ca^{2+} + Cell \rightarrow Cell - Ca^{2+} \quad \text{Eq. 2-10}$$

$$Cell - Ca^{2+} + CO_3^{2-} \rightarrow Cell - CaCO_3 \quad \text{Eq. 2-11}$$

Denitrifying bacteria such as genus *Pseudomonas*, *Thiobacillus*, *Castellaniella*, *Denitrobacillus*, *Alcaligenes*, *Micrococcus*, *Diaphorobacter*, etc., are the second species that induce $CaCO_3$ precipitation via nitrate reduction under anaerobic conditions (Seifan *et al.*, 2016). Denitrifiers can use nitrate (NO_3^-) as an alternative electron acceptor rather

than O_2 under oxygen-limited conditions. The products of this reaction are CO_3^{2-} and HCO_3^- ions, which are crucial for the precipitation of $CaCO_3$ when sufficient calcium ions appear (**Eqs. 2-12** to **2-16**).

$$2HCOO^- + 2NO_3^- + 2H^+ \rightarrow 2CO_2 + 2H_2O + 2NO_2^- \quad \text{Eq. 2-12}$$

$$HCOO^- + 2NO_2^- + 3H^+ \rightarrow CO_2 + 2NO + 2H_2O \quad \text{Eq. 2-13}$$

$$HCOO^- + 2NO + H^+ \rightarrow CO_2 + 2N_2O + 2H_2O \quad \text{Eq. 2-14}$$

$$HCOO^- + 2N_2O + H^+ \rightarrow CO_2 + N_2 + 2H_2O \quad \text{Eq. 2-15}$$

$$Ca^{2+} + CO_2 + H_2O \rightarrow CaCO_3 + 2H^+ \quad \text{Eq. 2-16}$$

The sulphur cycle is primarily driven by sulphate dissimilatory reduction via sulphate-reducing bacteria. During this process, calcium sulphate ($CaSO_4$) is converted to calcium sulphide (CaS) through biochemical oxidation, as shown in **Eqs. 2-17** to **2-20**. $CaCO_3$ is produced when the intermediate ($Ca(OH)_2$) reacts with CO_2 (Ehrlich *et al*., 2002).

$$CaSO_4 + 2(CH_2O) \rightarrow CaS + 2CO_2 + 2H_2O \quad \text{Eq. 2-17}$$

$$CaS + 2H_2O \rightarrow Ca(OH)_2 + H_2S \quad \text{Eq. 2-18}$$

$$CO_2 + H_2O \rightarrow H_2CO_3 \quad \text{Eq. 2-19}$$

$$Ca(OH)_2 + H_2CO_3 \rightarrow CaCO_3 + 2H_2O \quad \text{Eq. 2-20}$$

Photosynthesis is also an autotrophic process producing $CaCO_3$ in the presence of calcium ions. Two main groups of bacteria perform photosynthesis, namely, oxygenic and anoxygenic photosynthetic bacteria. Oxygenic and anoxygenic photosynthesizing bacteria use different electron donors to generate methane. As shown in **Eqs. 2-21** and **2-22**, oxygenic photosynthesis requires water as the electron donor; however, hydrogen sulphide (H_2S) is the electron donor in the anoxygenic photosynthesis process (Okafor, 2011). The decarbonization via the abovementioned two photosynthesis processes shifts the equilibrium to the right (see **Eq. 2-23**), converting to the formation of carbonates, thereby facilitating $CaCO_3$ precipitation (Hammes and Verstraete, 2002).

$$CO_2 + H_2O \rightarrow \text{ Oxygenic Photosynthesis } (CH_2O) + O_2 \quad \text{Eq. 2-21}$$

$$CO_2 + 2H_2S + H_2O \rightarrow \text{ Anoxygenic Photosynthesis } (CH_2O) + 2S + 2H_2O \quad \text{Eq. 2-22}$$

$$2HCO_3^- \leftrightarrow CO_2 + CO_3^{2-} + H_2O \quad \text{Eq. 2-23}$$

Aerobic respiration is a type of heterotrophic pathway in which microorganisms such as *Bacillus*, *Arthrobacter*, and *Rhodococcus* species convert organic compounds (lactate, acetate, oxalate, glyoxylate, citrate, succinate, and malate) into $CaCO_3$ precipitation, CO_2 and H_2O under alkaline conditions as shown in the following reaction (**Eq. 2-24**) for the metabolic oxidation of calcium lactate ($CaC_6H_{10}O_6$) (De Belie and Wang, 2016; Seifan *et al*., 2016).

$$CaC_6H_{10}O_6 + 6O_2 \rightarrow CaCO_3 + 5CO_2 + 5H_2O \quad \text{Eq. 2-24}$$

2.3 ASSESSMENTS OF SELF-HEALING EFFICENCY

There has been plenty of test methods to evaluate the efficiency of self-healing cementitious composites. These methods can be generally classified as visualization and characterization, regained resistivity, transport properties, and regained mechanical performances determined either by destructive or non-destructive test methods. A schematic representation of test methods evaluating self-healing efficiency is depicted in **Figure 2-5**.

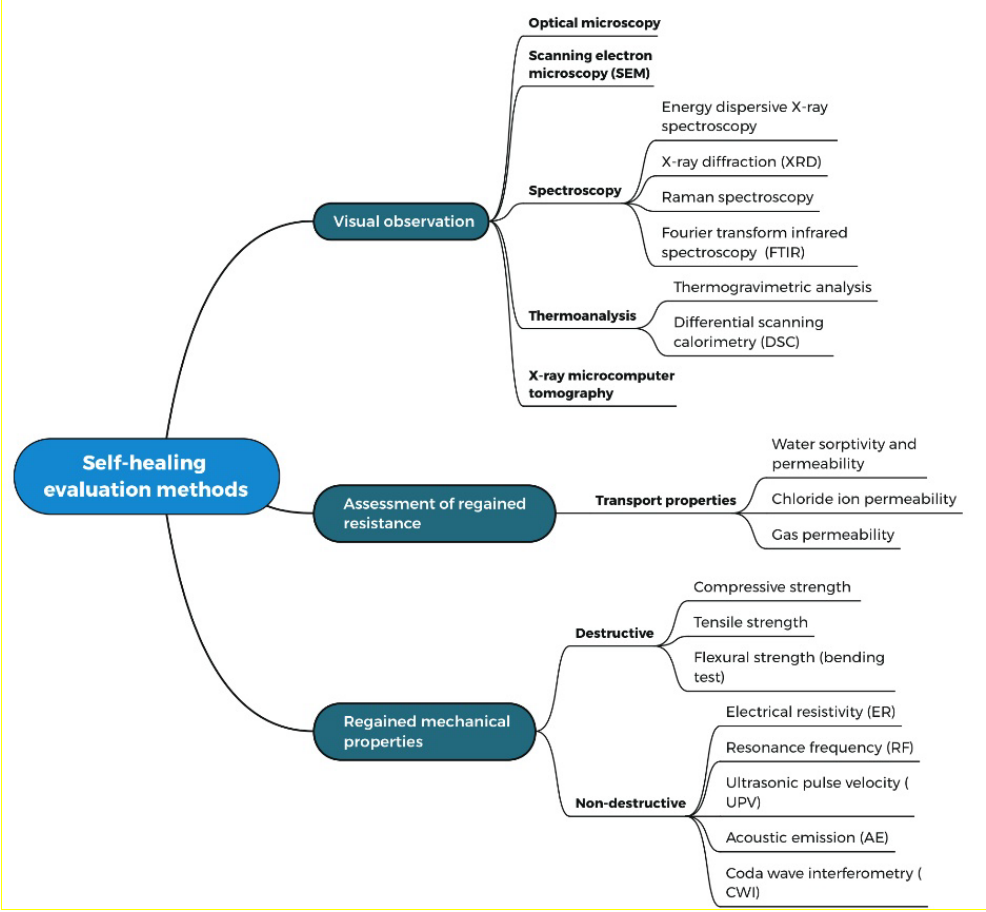

Figure 2-5: Schematic representation of test methods evaluating self-healing efficiency.

2.3.1 Visualization and characterization

This class of self-healing evaluation approaches includes various qualitative and quantitative techniques to characterize self-healing products, monitor the surface crack self-healing process, and visualize the internal self-healing. These methods give remarkable results about the crack-healing efficiency of cementitious materials. As shown in **Figure 2-5**, the assessment methods could be classified into microcomputed optical microscopy, scanning electron microscopy (SEM), spectroscopy, X-ray microcomputed tomography (X-ray μCT), thermogravimetric analysis, etc.

2.3.1.1 Optical microscopy and SEM

Optical microscopy is one of the most widely used visual observation methods to determine self-healing efficiency. In examinations using optical microscopy, only surface cracks are investigated due to the structure of optical microscopes. In several studies, cracking regions of cement-based materials were examined using a stereomicroscope designed for low magnification observation (Kanellopoulos *et al*., 2016; Zheng and Qian, 2020; Zheng *et al*., 2020). Optical microscopy has been frequently employed by researchers investigating the self-healing efficiency through comparing the surface crack width before and after healing, showing a visual comparison (Gwon *et al*., 2019; Kanellopoulos *et al*., 2016; Park and Choi, 2018; Zhang *et al*., 2020; Zhang *et al*., 2020; Zheng and Qian, 2020; Zheng *et al*., 2020). Stuckrath *et al.* (2014) of processed crack self-healing images from optical microscopy with Matlab scripts. All cracks are detected using pixel intensity classifiers and morphological operations, and the healing can be calculated through two processed images upon cracking and after healing along the cracks.

In a similar study, Rajasegar and Kumaar (2021) explored the synergistic effect of expansive minerals, nano-silica, and rice husk ash on surface crack self-healing. During the crack width investigation, the crack area before and after the healing was binarized, followed by removing noise and adding threshold limits. Finally, the area of cracks was calculated based on pixel count in cracks. The Image-J software was used by Qureshi *et al.* (2018) to measure the cracking area change. Some concepts for defining self-healing capability were proposed, such as crack closure index (Suleiman and Nehdi, 2018; Suleiman *et al*., 2019) and crack sealing ratio (Zhang *et al*., 2020).

To investigate the morphology and crystallographic structure of self-healing products within cracks, SEM analysis was extensively carried out. SEM scans the sample's surface with a focused electron beam, producing images containing surface topography information. Numerous studies have examined either autogenous healing or autonomic healing with SEM. For example, Suleiman *et al.* (2019) investigated crack self-healing in cement-based materials incorporating different minerals (metakaolin, bentonite, and calcium carbonate micro-filler) under various environmental exposures. It was shown

that rhombohedron-shaped crystals precipitated within the cracks, indicating the existence of calcium carbonate. In another study, Wiktor and Jonkers (2011) conducted comprehensive research on quantifying the crack self-healing potential of a novel two-component bio-concrete. The SEM results exhibited two primary morphologies: lamellar rhombohedra-shaped clusters and needle-like crystals.

2.3.1.2 Spectroscopy

Spectroscopic techniques refer to a fundamental tool that investigates the composition, physical and electronic structure of molecules and atoms by recording the spectrum of a beam of transmitted light through the testing specimen (Tang *et al*., 2015). This analysis gives detailed information about the self-healing products by exploring the position, intensities, and peaks of the spectrum. The major spectroscopy applied in characterizing self-healing products includes X-ray spectroscopy (usually coupled with SEM), Raman spectroscopy, Fourier transform infrared spectroscopy (FTIR), and X-ray diffraction (XRD).

The chemical compositions of self-healing products can be identified by energy-dispersive X-ray spectroscopy (EDS) analysis to complement the morphology information provided by SEM. In many studies on crack self-healing, SEM coupled with EDS analysis was carried out to characterize the self-healing compounds of concrete incorporating expansive agents (Qureshi *et al*., 2016; Sherir *et al*., 2016; Sisomphon *et al*., 2013), SAP (Chindasiriphan *et al*., 2020; Wang *et al*., 2019), minerals (Kanellopoulos *et al*., 2015), crystalline additives (Cuenca *et al*., 2018; Park and Choi, 2018 and 2020), and mineral-forming bacteria (Alazhari *et al*., 2018; Balam *et al*., 2017; Kua *et al*., 2019; Luo and Qian, 2016; Pungrasmi *et al*., 2019). These studies stated that the main elements of the self-healing products within cracks were Ca, C and O, indicating that calcium carbonate was the dominant product of the self-healing compounds.

XRD is one such characterization tool commonly employed to identify the atomic and molecular structure of crystalline materials by measuring the angles and intensities of these diffracted beams. This method provides information on the lengths and types of bonds, crystallinity, structural parameters, etc. (Kohli and Mittal). XRD was extensively

used in many studies on crack self-healing in cement-based materials as a powerful non-destructive tool. For example, Liu *et al.* (2019) used XRD to identify the self-healing compounds in cement paste under wet-dry cycles in seawater. The XRD patterns of the self-healing products precipitating within cracks under the condition of seawater immersion demonstrated the formation of brucite, portlandite, aragonite, and calcite. However, halite, an evaporative deposit of NaCl, was observed in addition to the abovementioned compounds of the specimens exposed to wet-dry cycles of seawater. In the study of Xue *et al.* (2019), the peaks between 5° 2θ and 30° 2θ indicated that calcite was the major self-healing product. Similarly, Zhang *et al.* (2017a) used XRD to determine the chemical composition of the mineral precipitate formed within the crack of expanded perlite immobilized bacteria-based concrete. The XRD analysis confirmed that the mineral precipitating within the cracks were calcite crystals.

FTIR analysis is a technique employed to obtain an infrared spectrum of absorption or emission of a matter with any state (Thomas and Maria, 2016). The spectrum was interpreted by the raw data (interferogram) via Fourier transform. Either organic or inorganic matter can be identified via FTIR within the infrared absorption frequency range 4000 and 400 cm^{-1}, which complement the XRD analysis when testing the specimen containing organic molecules. Recently, a growing body of literature has analyzed crack self-healing products in cement-based materials via FTIR. For instance, Reddy *et al.* (2020) examined the self-healing ability of fibre-reinforced concrete incorporating crystalline admixture and silica fume exposed to different exposure conditions. It was found that two discrete peaks formed at 1320 and 840 cm^{-1}, corresponding to the C-O bonds. This suggests that the main self-healing products were portlandite and calcium carbonate. In a similar study, Xue *et al.* (2021) investigated the self-healing capability of pre-cracked cementitious composites containing a crystalline admixture and MgO expansive agent under a chloride laden environment. The FTIR spectra obtained from the specimens revealed that the signals were linked with the vibration of Si-O bonds, C-O bonds, confirming the existence of calcite, aragonite, and calcium hydrated crystals.

Raman spectroscopy is a vibrational spectroscopic technique that provides detailed molecular fingerprints (e.g., vibration modes of molecules, rotational state), thereby enabling it to probe the chemical composition of materials (Mason, 1999). This method can sometimes be considered as the complementary approach to FTIR. Raman spectroscopy was used in numerous studies to investigate the chemical composition of self-healing products. For instance, Hu *et al.* (2018) examined the effect of triethanolamine (TEA) on the mechanism of the self-healing behaviour of sulphur-resistant oil well cement paste. It was found that the spectra of C-S-H dominated at 658 cm^{-1}, 990 cm^{-1}, and 1074 cm^{-1}, respectively. In another study, Raman spectroscopy was employed to characterize the polymorphic calcium carbonate formed in the presence of mineral-forming bacteria. Sharma *et al.* (2017) investigated the potential of alkaliphilic *Bacillus* species in microcrack remediation in concrete. The Raman spectra revealed that the calcium carbonate forming within the crack was a mixture of calcite and aragonite.

2.3.1.3 X-ray μCT

X-ray μCT is an imaging technique that enables visualization of the interior features of solid objects. Hundreds of thousands of image slices taken from different angles with a rotating X-ray tube can then be reconstructed into 3-D geometries ad properties (Kalender, 2006). X-ray μCT was innovatively applied to monitor the self-healing process of cracked cementitious materials in many studies. For example, Snoeck *et al.* (2016) investigated the extent of autogenous healing of cementitious materials incorporating SAPs. With the help of X-ray μCT, it was found that calcium carbonate formed only near the crack mouth with a maximum depth of 1mm. In a similar study, Zhang *et al.* (2020) investigated the self-healing mechanism with additives in slag-based binders activated by alkalis. X-ray μCT analysis providing detailed information of self-healing as a function of crack depth showed that most self-healing products precipitated in the region near the crack surface. In some other studies, the crack profile was segmented via 3D segmentation software after X-ray μCT, and the volume of the self-healing product was then quantitatively calculated by subtracting the crack volume upon cracking and after self-healing (Fan and Li, 2014; Fang *et al*., 2018; Suleiman *et al*.,

2019). Therefore, the self-healing efficiency can be evaluated based on the crack volume change.

2.3.1.4 Thermoanalysis

Thermoanalysis refers to the technique measuring the change of materials' properties with temperature. Thermogravimetric analysis (TGA) is one of the most commonly used analyses in characterizing self-healing products as complementary tools in addition to spectroscopic techniques. The chemical compositions of the self-healing compounds can be interpreted via typical temperature vs. mass (or mass percentage) plots (Ramalingam and Ramakrishna, 2017). In most cases, TGA coupled with DSC was employed in determining the chemical composition of self-healing products (Stuckrath *et al*., 2014; Wang *et al*., 2014a). Compared to spectroscopic techniques, fewer researchers used TGA-DSC. Wang *et al.* (2012) immobilized *B. sphaericus* solution into silica gel and polyurethane for developing self-healing concrete. The TGA results proved the existence of calcium carbonate precipitate via the metabolic pathway of the bacteria. In a similar study, calcium carbonate was confirmed as the self-healing product in oxide and bentonite particle immobilized *B. subtilis*-based concrete via TGA analysis (Shaheen *et al*., 2019).

2.3.2 Assessment of transport properties

The transport properties of concrete refer to the process where fluids and ions move through the cementitious matrix. Comparison of the transport properties of a pre-cracked concrete specimen after healing with a reference sample can be a good indicator determining the self-healing efficiency (Song *et al*., 2011). Thus, the common evaluation methods in assessing transport properties include water and gas permeability, sorptivity, and chloride diffusion. In the following section, the abovementioned four evaluation methods are discussed.

2.3.2.1 Water and gas permeability

Water and gas permeability measures the tightness of concrete against the penetration of water and gas. These tests are two of the most well-known approaches for evaluating the self-healing efficiency of concrete (Akhavan and Rajabipour, 2017; C-204-11, 1995). The permeability coefficient is a quantitative measure of the rate at which water or gas can penetrate a membrane. Therefore, the permeability coefficient was used as an indication of measuring the regained water and gas tightness after self-healing processes.

Jiang *et al.* (2015) investigated the effects of various mineral additives and environmental exposure (i.e., expansive agents, swelling minerals, crystalline additive, and silica-based materials) on the self-healing performance of cementitious materials. Water permeability was measured using a set-up with a constant water head. It was observed that the permeability dropped significantly in the first 10d after being subjected to water. This test was also employed successfully by Homma *et al.* (2009) and Roig-Flores *et al.* (2015). In another study conducted by Zheng *et al.* (2020), the recovery rate of water permeability over time was determined in bio-concrete containing low alkali sulpho-aluminate cement as the carrier to protect the microbial spores. As a result of examining the relationship between the healing time up to 28d and the permeability recovery rate, it was found that with the increase of the healing time, the recovery rate of the permeability coefficient also increased exponentially, especially when using microbial group agents. In abiotic and spore groups, the recovery rate remained much lower compared to that for the microbial group. This may be explained by more precipitates forming within the crack of the specimens from the microbial group. Cuenca *et al.* (2021) studied the self-healing capacity of ultra-high-performance concrete (UHPC) reinforced by alumina nano-fibres. The permeability coefficient difference between cracking and after self-healing process was expressed as a permeability index in the study. The results showed a linear relationship (R = 0.7) between crack sealing and permeability index. However, it was found that as the crack width increased, the index of permeability decreased gradually. The recovery of permeability of the specimens immersed in geothermal water for one month at a crack width of about 50 μm was found to be 100%.

Compared to the water permeability test, fewer studies on self-healing evaluations used gas permeability tests. Yildirim *et al.* (2015) investigated the effect of cracking and self-healing behaviour on the gas permeability of Engineered Cementitious Composites (ECC). Gas permeability tests using both O_2 and N_2 were performed as per RILEM (TC, 1999). Hagen-Poiseuille equation was used to determine the apparent gas permeability coefficient (K). It was shown that more than 90% of the reduction in gas permeability coefficient was due to the self-healing products forming within the crack, thereby preventing the penetration of the gases. Other studies investigating the effect of expansive minerals on the autogenous healing capacity of OPC paste were carried out by Qureshi *et al.* (2018 and 2019). The liquid methanol gas-based permeability tests showed that the gas permeability coefficient of the control cracked samples was approximately seven times higher than that of the sound specimens; however, the cracked samples with combined minerals substitution showed significant improvement with a gas permeability coefficient nearly doubled compared to that of the control uncracked specimens. In addition, the gas permeability coefficient increased when extending the cracking age. In another study conducted by Kanellopoulos *et al.* (2015), three different liquid self-healing agents (i.e., tetraethyl orthosilicate, colloidal silica, and sodium silicate) and one powdered mineral (MgO) encapsulated in soda glass were used as self-healing materials in cement-based materials. The gas permeability coefficient of the samples using self-healing agents was lower than that of the cracked control samples, with a reduction rate from 18% to 69%. The best improvement was found in the specimens containing colloidal silica. As for the MICCP-based autonomic healing, few studies have addressed the effect of bacteria on concrete gas permeability, which is highly related to durability. Nguyen *et al.* (2019) employed a gas permeability measurement system to evaluate the porosity of concrete incorporating *B. subtilis* as a healing adjuvant. The addition of bacterial solution with nutrients improved the tightness of the concrete against gas penetration. In addition, an increase in the curing time resulted in a drop of gas permeability. The same trend was also observed for porosity results.

2.3.2.2 Sorptivity

Sorptivity of concrete refers to the transport of liquids in concrete driven by capillary forces (Hewlett and Liska, 2019). It reflects the pore structure and capillary pore network that affect the transmission rate of fluid through concrete (Kalyoncu, 1997; Sabir *et al*., 1998). The crack healing efficiency can be assessed by measuring the sorptivity for pre-cracked concrete upon cracking and after healing (De Rooij *et al*., 2013).

To this aim, many studies have examined this subject as an indication of crack self-healing capability. For example, Sherir *et al.* (2018) investigated the effect of MgO addition on the sorptivity property of ECC under different (water, natural, and autoclave) curing conditions. It was concluded that the sorptivity of the cracked MgO-based ECC exposed to water curing for a long time was lower than specimens subjected to water submersion for a short time. However, in ECC exposed to the same curing condition, the sorptivity rate of the uncracked specimens was lower than that of the cracked ones. Suleiman and Nehdi (2018) investigated the effect of environmental exposure on autogenous self-healing of cracked cementitious materials. Pre-cracked samples with different crack widths were exposed to different environments (cyclic temperature and relative humidity, water submersion). Capillary water absorption results revealed that the sorptivity coefficient significantly increased after crack creation. In addition, specimens with smaller cracks exhibited lower sorptivity coefficient. It was also found that pre-cracked specimens exposed to water submersion attained much higher water absorption recovery than samples subjected to cyclic temperature and relative humidity. In another study conducted by Zhu *et al.* (2020), the autogenous self-healing behaviour in ECC was investigated, and the sorptivity coefficient upon cracking and after wet-dry cycles in different pre-loaded tensile strains was determined. It was found that a preloading strain below 1.5% led to a desirable sorptivity recovery, which indicates a great extent of self-healing. Other researchers also examined the sorptivity in pre-cracked concrete containing microencapsulated healing agents (Mao *et al*., 2020) and minerals (Kanellopoulos *et al*., 2015).

2.3.2.3 Chloride ion diffusion

Chloride ion diffusion in concrete is another parameter that evaluates concrete's resistance to chloride migration. Like other techniques determining the concrete transport properties, chloride diffusion tests were performed to evaluate the level of regained resistance against the ingress of chloride ions as an indication of self-healing efficiency (Tang *et al*., 2015).

Few studies have addressed the natural change in chloride ion diffusion resulting from cracking and self-healing, considering the long exposure time (Van Belleghem *et al*., 2017). According to Akhavan and Rajabipour (2013), the chloride ion diffusion coefficient was largely dependent on the crack volume and tortuosity. While little research has been conducted on natural chloride diffusion in concrete, the rapid chloride-ion permeability tests (RCPT) as per ASTM C1202 and AASHTO T277 "Standard method of test for rapid determination of the chloride permeability of concrete" have been widely employed to determine the chloride ion transmission, thereby evaluating the self-healing capability of cracked concrete. RCPT usually takes a few hours, which is much more timesaving than natural chloride ion exposure, which takes months or even years. Nguyen *et al.* (2019) investigated the crack self-healing effectiveness of fly ash concrete with *S. subtilis* spores using RCPT. All specimens after environmental exposure were placed in a vacuum container filled with 112g/L NaCl solution and 12g/L NaOH solution on each side. The migration of chloride ions was conducted for 24 h through creating a potential difference between the two sides. The crack self-healing can therefore be evaluated by the Cl^- diffusion coefficient. The RCPT results showed that the specimens incorporating *S. subtilis* adjuvant with nutrients exhibited a significant drop in chloride ions diffusion. In a similar study on microbial concrete (Zheng *et al*., 2020), the performance of different agents such as abiotic, spores and microbial groups was examined for RCPT. After a healing period of 28-d, the repair ratio of chloride-ion permeability was determined as 60% upon self-healing with the microbial group. In spores and abiotic groups, the recovery rate remained approximately 15% and 5%, respectively, at the end of 28-d.

2.3.3 Evaluation of regained mechanical properties

Mechanical properties are the main characteristics being appraised when evaluating the quality of concrete. The restoration of continuity of concrete via self-healing of cracks may result in a recovery of mechanical properties. Therefore, it is of interest to investigate the regained mechanical properties as an indication of self-healing efficiency. For this reason, the studies on regained mechanical properties in self-healing concrete are examined in this section. The tests carried out on the self-healing concrete can be divided into two main types, namely, destructive tests and non-destructive tests.

2.3.3.1 Destructive tests

2.3.3.1.1 Compression test

The uniaxial compressive strength, reflecting the integrity of concrete, is among the most essential properties of concrete. Therefore, compression tests have been widely employed to evaluate crack self-healing effectiveness.

Reddy and Ravitheja (2019) investigated the self-healing capability of concrete incorporating CA under various curing conditions using compression tests. It was stated that the rate of regained compressive strength reached 100% under the condition of water immersion. When exposed to air exposure under laboratory conditions, this rate dropped to 80%. This result can be attributed to self-healing products filling the cracks when water existed. The recovery rate of compressive strength reached 70% in samples containing expansive minerals including MgO, bentonite and quick lime (Qureshi *et al*., 2019). In another study by Kanellopoulos *et al.* (2015), according to the results of the loading test on samples obtained with different glass encapsulated chemical compounds (tetraethyl orthosilicate, MgO, colloidal silica, and sodium silicate), it was observed that specimens incorporating MgO had the lowest load recovery (5%); however, the samples incorporating sodium silicate attained the highest load recovery (18%). In another study, a type of modified polymer was used as a self-healing agent. The recovery rate of compressive strength in the polymer-modified concrete specimens reached almost 90% (Du *et al*., 2020). When the compressive strength of bacteria-based self-healing concrete samples before and after cracks was examined, it was found that the recovery ratio of the

compressive strength varied between 60% and 90% (Khushnood *et al*., 2020; Sun *et al*., 2020). A low recovery ratio of compressive strength was reported by Huang *et al.* (2020), who found that the environmentally friendly fibre-reinforced concrete containing 5% crumb rubber exhibited compressive strength regain ranging from 2.28% to 3.277%.

2.3.3.1.2 Tensile test

Although tensile tests may not provide detailed information due to significant instability following the post-cracking response (Ferrara *et al*., 2018), they still have been frequently employed by many researchers to evaluate self-healing efficiency via measuring the first-cracking strength (Deng and Liao, 2018; Liu *et al*., 2017), tensile stiffness (Hung and Su, 2016; Liu *et al*., 2017), and regained tensile strength (Gilabert *et al*., 2017; Zhang *et al*., 2013). Since conventional concrete is weaker in tensile strength, fibre reinforced ECCs capable of sustaining more considerable strain were often used for tensile tests to determine crack healing efficiency. Regained tensile stress through autogenous healing of ECCs under different exposure conditions (water, $Ca(OH)_2$, and Na_2SO_4) were evaluated by Guan *et al.* (2020). They reported that the tensile strain recovery rate of the samples was over 80% under all exposure conditions. Su *et al.* (2020) examined the self-healing efficiency of zeolite in ECC mixtures. Although there was a slight decrease in the tensile strength recovery ratio as the zeolite replacement ratio increased to 15%, it was determined that the recovery ratio remained above 70% for all zeolite replacement levels. In two studies conducted by Hung *et al.* (2017 and 2018), the tensile behaviour for different humidity conditions (water, high humidity, moderate humidity, and dry) of ECC and strain-hardening cementitious composites (SHCC) was examined. Tensile stiffness retention was determined in the samples subjected to different pre-strains (0.5% and 1%) in ECCs. While this factor increased to 50% in water conditions, it decreased to 15% in moderate humidity conditions. Tensile strength retention factors were also determined in fly ash- and slag-based SHCCs. The slag ratio positively affected the retention factor for all humidity conditions, and the lowest value among all samples was 70%. Apart from the direct tensile tests, the splitting tensile test also has been widely used for assessing durability-recovery healing in cylindrical specimens. For example, Reddy and Ravitheja (2019) determined the splitting tensile strength recovery rate of crystalline admixture-

based samples exposed to different environmental conditions. It has been determined that there was a higher recovery rate for samples immersed in water (80%) compared to samples under air exposure in laboratory conditions (50%).

2.3.3.1.3 Flexural test (bending test)

The flexural test measures the concrete tensile strength indirectly. It evaluates the capability of a concrete beam to withstand failure in bending. Three- and four-point bending tests are the most popular methods used. Several researchers carried out flexural tests to investigate autogenous and autonomic healing through SCMs (Van Tittelboom *et al*., 2012a), MICCP (Wang *et al*., 2015), CA (Ferrara *et al*., 2014), etc. The self-healing effectiveness is usually evaluated with the stiffness and strength recovery.

Cuenca *et al.* (2021) carried out 4-point bending tests to examine the effects of alumina nano-fibres on the mechanical performance of UHPC and the effectiveness in improving the resistance of the composite to aggressive conditions. The recovery index of flexural strength and stiffness in the specimens exposed to geothermal water for up to 6 months was observed to be higher than 90%. In a similar study on autogenous healing in UHPC undertaken by Granger *et al.* (2007), a 3-point bending test was employed. In another research on self-healing composites without incorporating fibres undertaken by Mao *et al.* (2020), the recovery percentage of the flexural strength was determined in specimens containing sodium silicate microencapsulated oil well cement. It was stated that with the microcapsule content increasing from 2.5% to 7.5%, the recovery percentage rose from 10% to 25%. Ferrara *et al.* (2014) proposed the index of load recovery (ILR) and index of damage recovery (IDR) as two indirect evaluation indices of crack autogenous healing. Results showed that a crack sealing ratio of over 70–80% was necessary to recover stiffness and load-bearing capacity. In addition, the recovery of mechanical properties appeared to proceed behind the surface crack healing.

2.3.3.2 Non-destructive tests

Non-destructive testing (NDT) in concrete is a broad group of techniques that examine the properties of concrete specimens indirectly without causing damage. NDT techniques have been gradually employed as an effective tool to evaluate the self-healing efficiency since the continuity and other properties change during the self-healing process. Compared to destructive methods, NDT methods have numerous advantages (Feiteira *et al*., 2017; Hilloulin *et al*., 2016): a) standard error can be minimized when using an identical specimen for NDT methods all through the self-healing process; b) reliability can be increased since each specimen can be tested several times via NDT; c) NDT approaches are more suitable to be used directly on-site without interruptions on the structure during evaluations, thereby allowing continuous monitoring (Wang *et al*., 2019). NDT methods, including electrical resistivity (ER), resonant frequency (RF), ultrasonic pulse velocity (UPV), acoustic emission (AE), and coda wave interferometry (CWI), were commonly employed by many researchers for investigating the effectiveness of the varied self-healing technologies.

2.3.3.2.1 Electrical resistivity (ER)

ER, sometimes called electrical conductivity (EC) inversely, is a fundamental property of a material based on the flow of electrical current. In terms of concrete, this property is an indicator of the pore solution conductivity of the concrete and, accordingly, its pore structure (Sengul, 2014). However, there are few studies on the regained ER of self-healing concrete. Vijay and Murmu (2019) examined the effect of calcium lactate on compressive strength and self-healing effectiveness in microbial concrete. The ER results showed that cracking decreased the ER value. In addition, the resistivity of healed concrete was also higher than that for cracked concrete. This can be explained by the cracks filled with calcium carbonate as the self-healing product, thereby increasing the ER value. In a similar study, Tayebani *et al.* (2019) conducted an experimental investigation on the self-healing behaviour of normal and lightweight aggregate concrete (LWAC) incorporating *S. pasteurii* spores. Approximately 20% and 10% increase in ER was observed in LWAC and normal concrete, respectively. It is worth noting that the moisture content for all testing specimens should be kept constant to ensure accurate

results since ions in the pore solutions transfer the electrical current through the cementitious matrix (Chen *et al*., 2014; Yoo *et al*., 2017).

2.3.3.2.2 Resonant frequency (RF)

RF refers to the frequency where the object vibrates at the highest amplitude. The RF of cementitious materials is greatly influenced by continuity. The formation of cracks in the concrete matrix impedes resonance transmission. Therefore, the RF test can be a promising technique to monitor the extent and rate of crack self-healing.

Herbert and Li (2013) surveyed the self-healing extent and rate of ECC materials exposed to natural environments for one year using RF. It was found that all ECC specimens exhibited 95%-105% RF recovery after one-year of environmental exposure. In another study, RF testing was performed on MgO and fly ash-based ECC samples activated by carbonation curing (Zhang *et al*., 2020). Results revealed that the RF recovery rate was close to 100% in all specimens with different mixture proportions and exposed to various curing and pre-loading conditions. In another study undertaken by Su *et al.* (2020), the effect of zeolite as an internal curing compound on the self-healing efficiency of ECC samples was examined. The RF results showed that the ECC specimens with 15% zeolite exposed to 7 wet/dry cycles exhibited the best recovery ratio. Similarly, Hung *et al.* (2017) investigated the effect of various humidity conditions on the self-healing capacity of ECC specimens. They stated that the RF retention factor was almost 1 when using water curing. However, the retention factor dropped to 0.7 in the samples exposed to moderate humidity. Their subsequent study determined the RF retention factor in strain-hardening cementitious composites containing slag and type-F fly ash under different humidity conditions (Hung *et al*., 2018). It was observed that there was no significant change in the RF retention factor when changing the curing condition. The retention factor was found to be above 0.7 and 0.55, respectively, in all samples subjected to 0.5% and 1% pre-strain.

2.3.3.2.3 Ultrasonic pulse velocity (UPV)

UPV of concrete is a non-destructive and *in-situ* test to examine the homogeneity, quality, and flaws by measuring the velocity of the ultrasonic waves transmitting through concrete specimens (Pacheco-Torgal *et al*., 2018). An increase in the transmission time reflects defects and cracks since ultrasonic waves propagate more slowly in the liquid or gas phase than in the concrete itself. Following the ASTM C597-16 (ASTM, 2009) and EN 12504-4 standards (EN, 2004), UPV has been widely employed to investigate the crack self-healing efficiency via different healing methods, including CAs (Ferrara *et al*., 2014, 2017), MICCP (Van Tittelboom *et al*., 2010; Williams *et al*., 2016; Xu and Yao, 2014), and encapsulated healing solutions (Aghamri and Al-Tabbaa, 2016; Mostavi *et al*., 2015).

Suleiman and Nehdi (2021) used a non-destructive shear wave velocity technique to evaluate the effect of autogenous crack self-healing on mechanical strength recovery of cement mortar under various environmental exposure. Their results showed that autogenous crack self-healing in cement-based materials had a negligible influence on their ability to achieve mechanical strength recovery. On the other hand, latent cementitious hydration and pozzolanic reactions were the main cause for cement-based materials to gain mechanical strength recovery.

Tomczak *et al.* (2020) investigated the efficiency of self-healing in cement composites containing F-type fly ash. It was reported that the ultrasonic self-healing ratio was between 35% and 55% for samples with different mixture proportions after 150 days of curing. In addition, the UPV self-healing efficiency in the specimens increased slightly with the addition of fly ash. In the study conducted by Su *et al.* (2020) mentioned above in the resonance frequency test section, the UPV test was also performed on ECC samples made with different zeolite ratios. The experimental results revealed a close relationship between the UPV test and the resonance frequency test. Considering the effect of the zeolite ratio, similar trends were obtained in both test methods. Another experimental study was carried out by Tsangouri *et al.* (2019b) to investigate the healing feasibility of the vascular system of macro-tube containing healing agents into a real-scale concrete slab. A portfolio of advanced monitoring techniques including the UPV

test was employed. Based on the test results, it was concluded that crack self-healing via vascular network was evident, indicating the precipitation of the healing agent. In some studies, the UPV data was computed and processed as healing indications to be correlated with recovery of mechanical properties (Ferrara *et al*., 2017, 2014), water permeability, and visual observation of crack healing ratio (Van Tittelboom *et al*., 2010), which proved a good agreement.

2.3.3.2.4 Acoustic emission (AE)

The AE technique is a passive NDT method that monitors the transient elastic waves generated due to the release of energy from fracture or cracking within a solid material (Wang *et al*., 2014). The mechanical energy resulting from transient elastic waves is converted into electrical signals via an AE transducer. The AE technique has been widely used in monitoring the cracking and healing process of cementitious materials. When cracking appears in the cementitious matrix, the energy generated creates stress waves that are then collected by sensors. Therefore, the self-healing effectiveness can be evaluated by comparing the signal counts upon cracking and after healing (Li *et al*., 2017; Van Tittelboom *et al*., 2016). In contrast to other NDT methods, the AE technique is usually combined with mechanical tests to verify AE events (Wang *et al*., 2014). Li *et al.* (2017) used AE *in-situ* to investigate the efficacy of poly-urea-formaldehyde (PUF) microcapsules enclosing epoxy resins for crack self-healing. Matrix cracking and debonding of the interface as two representative AE signals were used for calibration. The AE results indicated that 4% microcapsules and 60% of maximum load resulted in the most common AE hits, representing the activation of the self-healing mechanism. Similarly, self-healing efficiency via polyurethane (PU) and SAPs was compared in laboratory specimens using the AE method. The self-healing mechanism activated by the breakage of glass capsules containing PU was captured by AE analysis.

2.3.3.2.5 Coda wave interferometry

Coda wave interferometry (CWI) is an ultrasound technique for detecting damage in scattering media. Coda waves are super sensitive to small cracks because elastic waves are scattered along the pathways within heterogeneous media caused by the cracking, and

the waves repeatedly travel through the cracking (Wang *et al*., 2019). If there is no change in the cementitious matrix over time, coda waves are highly repeatable. Liu *et al.* (2016) conducted a CWI test to investigate the feasibility of MICCP for crack self-healing. In addition, the self-healing behaviour of internal microcracks was monitored via the CWI technique. It was found that the relative wave velocity change in pre-cracked bacterial mortars was more significant than that of pre-cracked neat specimens. This indicates that the cracks in the bacterial mortars were filled with more calcium carbonate deposits via bacterial metabolism when the required nutrients were added. The CWI results were in line with the data obtained from compressive tests. A similar study with CWI application was conducted by Hilloulin *et al.* (2016), who observed that the CWI results were sensitive in the initial stage of autogenous healing, suggesting continued cement hydration contributing to self-healing.

2.4 CONCLUSIONS

Cracking-induced deteriorations in cement-based materials are inevitable processes during any stage of civil infrastructure service life, causing detrimental effects on durability and resilience. In addition, the cracking-related degradations result in enormous maintenance and repair costs. This problem can be addressed either by stimulated autogenous healing or autonomous healing strategies to self-heal small cracks. Crack self-healing helps extending the lifetime of infrastructures, enhancing the resilience and durability of concrete structures, and alleviating burdens on government budgets and resources. This chapter provides a comprehensive overview of a variety of experimental techniques and methods that have been employed to characterize self-healing mechanisms and evaluate the effectiveness of crack self-healing in cementitious materials. In addition, the correlation between different parameters (e.g., crack healing ratio and recovery of transport/mechanical properties) has also been highlighted.

While tremendous efforts have been devoted to enhancing the self-healing efficiency in traditional cement-based materials, there are only very few studies that have explored the self-healing in AAMs in the open literature. The research gap mentioned in this chapter will be addressed in the subsequent chapters. A deeper insight into the self-healing

behaviour of AAMs using different self-healing approaches will be gained in this thesis. The potential of self-healing in AAMs will be determined in the following chapters.

2.5 REFERENCES

Achal, V., Mukerjee, A., and Reddy, M. S. (2013). Biogenic treatment improves the durability and remediates the cracks of concrete structures. *Construction and Building Materials, 48*, 1-5.

Achal, V., and Mukherjee, A. (2015). A review of microbial precipitation for sustainable construction. *Construction and Building Materials, 93*, 1224-1235.

Aghamri, R., and Al-Tabbaa, A. (2016). *Impregnation of lightweight aggregates with sodium silicate for self-healing concrete.* Paper presented at the Proceedings of the 11th fib International PhD Symposium in Civil Engineering, FIB 2016.

Ahn, T.-H., and Kishi, T. (2010). Crack self-healing behavior of cementitious composites incorporating various mineral admixtures. *Journal of Advanced Concrete Technology, 8*(2), 171-186.

Akhavan, A., and Rajabipour, F. (2013). Evaluating ion diffusivity of cracked cement paste using electrical impedance spectroscopy. *Materials and Structures, 46*(5), 697-708.

Akhavan, A., and Rajabipour, F. (2017). Quantifying permeability, electrical conductivity, and diffusion coefficient of rough parallel plates simulating cracks in concrete. *Journal of materials in civil engineering, 29*(9), 04017119.

Al-Ansari, M., Abu-Taqa, A. G., Hassan, M. M., Senouci, A., and Milla, J. (2017). Performance of modified self-healing concrete with calcium nitrate microencapsulation. *Construction and Building Materials, 149*, 525-534.

Al-Tabbaa, A., Lark, B., Paine, K., Jefferson, T., Litina, C., Gardner, D., and Embley, T. (2018). Biomimetic cementitious construction materials for next-generation infrastructure. *Proceedings of the Institution of Civil Engineers-Smart Infrastructure and Construction, 171*(2), 67-76.

Alam, M., Youssef, M., and Nehdi, M. (2007). Utilizing shape memory alloys to enhance the performance and safety of civil infrastructure: a review. *Canadian Journal of Civil Engineering, 34*(9), 1075-1086.

Alazhari, M., Sharma, T., Heath, A., Cooper, R., and Paine, K. (2018). Application of expanded perlite encapsulated bacteria and growth media for self-healing concrete. *Construction and Building Materials, 160*, 610-619.

Aldea, C.-M., Song, W.-J., Popovics, J. S., and Shah, S. P. (2000). Extent of healing of cracked normal strength concrete. *Journal of materials in civil engineering, 12*(1), 92-96.

Alghamri, R., Kanellopoulos, A., and Al-Tabbaa, A. (2016). Impregnation and encapsulation of lightweight aggregates for self-healing concrete. *Construction and Building Materials, 124*, 910-921.

Alghamri, R., Kanellopoulos, A., Litina, C., and Al-Tabbaa, A. (2018). Preparation and polymeric encapsulation of powder mineral pellets for self-healing cement based materials. *Construction and Building Materials, 186*, 247-262.

Andalib, R., Abd Majid, M. Z., Hussin, M. W., Ponraj, M., Keyvanfar, A., Mirza, J., and Lee, H.-S. (2016). Optimum concentration of Bacillus megaterium for strengthening structural concrete. *Construction and Building Materials, 118*, 180-193.

Ansari, A., Siddiqui, V. U., Khan, I., Akram, M. K., Siddiqi, W. A., Khan, A., and Asiri, A. M. (2020). Effect of self-healing on zeolite-immobilized bacterial cementitious mortar composites *Self-Healing Composite Materials* (pp. 239-257): Elsevier.

Araújo, M., Chatrabhuti, S., Gurdebeke, S., Alderete, N., Van Tittelboom, K., Raquez, J.-M., Cnudde, V., Van Vlierberghe, S., De Belie, N., and Gruyaert, E. (2018). Poly (methyl methacrylate) capsules as an alternative to the ‘‘proof-of-concept’’glass capsules used in self-healing concrete. *Cement and Concrete Composites, 89*, 260-271.

Askarinejad, S., and Rahbar, N. (2017). Effects of Cement–Polymer Interface Properties on Mechanical Response of Fiber-Reinforced Cement Composites. *Journal of Nanomechanics and Micromechanics, 7*(2), 04017002.

Astm, C. (2009). 597, Standard test method for pulse velocity through concrete. *ASTM International, West Conshohocken, PA*.

ASTM, C. (2012). Standard test method for electrical indication of concrete’s ability to resist chloride ion penetration. *Annual Book of ASTM Standards, 4*(7).

Azarsa, P., Gupta, R., and Biparva, A. (2019). Assessment of self-healing and durability parameters of concretes incorporating crystalline admixtures and Portland Limestone Cement. *Cement and Concrete Composites, 99*, 17-31.

Balam, N. H., Mostofinejad, D., and Eftekhar, M. (2017). Effects of bacterial remediation on compressive strength, water absorption, and chloride permeability of lightweight aggregate concrete. *Construction and Building Materials, 145*, 107-116.

Baumgartner, L. K., Reid, R. P., Dupraz, C., Decho, A. W., Buckley, D., Spear, J.R., Przekop, K.M. and Visscher, P.T. (2006). Sulfate reducing bacteria in microbial

mats: changing paradigms, new discoveries. *Sedimentary Geology, 185*(3-4), 131-145.

Beglarigale, A., Seki, Y., Demir, N. Y., and Yazıcı, H. (2018). Sodium silicate/polyurethane microcapsules used for self-healing in cementitious materials: Monomer optimization, characterization, and fracture behavior. *Construction and Building Materials, 162*, 57-64.

Benita, S. (2005). *Microencapsulation: methods and industrial applications*: Crc Press.

Bhaskar, S., Hossain, K. M. A., Lachemi, M., Wolfaardt, G., and Kroukamp, M. O. (2017). Effect of self-healing on strength and durability of zeolite-immobilized bacterial cementitious mortar composites. *Cement and Concrete Composites, 82*, 23-33.

Bonilla, L., Hassan, M. M., Noorvand, H., Rupnow, T., and Okeil, A. (2018). Dual self-healing mechanisms with microcapsules and shape memory alloys in reinforced concrete. *Journal of materials in civil engineering, 30*(2), 04017277.

Braissant, O., Decho, A. W., Dupraz, C., Glunk, C., Przekop, K. M., and Visscher, P. T. (2007). Exopolymeric substances of sulfate-reducing bacteria: interactions with calcium at alkaline pH and implication for formation of carbonate minerals. *Geobiology, 5*(4), 401-411.

Buller, A. S., Lee, K.-M., and Jang, S. Y. (2019). Using the steady-state chloride migration test to evaluate the self-healing capacity of cracked mortars containing crystalline, expansive, and swelling admixtures. *Materials, 12*(11), 1865.

C-204-11, A. (1995). Standard test methods for fineness of hydraulic cement by air permeability apparatus. *West Conshohocken.*

Cailleux, E., and Pollet, V. (2009). *Investigations on the development of self-healing properties in protective coatings for concrete and repair mortars.* Paper presented at the Proceedings of the 2nd International Conference on Self-Healing Materials, Chicago, IL, USA.

Caló, E., and Khutoryanskiy, V. V. (2015). Biomedical applications of hydrogels: A review of patents and commercial products. *European Polymer Journal, 65*, 252-267.

Calvo, J. G., Pérez, G., Carballosa, P., Erkizia, E., Gaitero, J., and Guerrero, A. (2017). Development of ultra-high performance concretes with self-healing micro/nano-additions. *Construction and Building Materials, 138*, 306-315.

Castro-Alonso, M. J., Montañez-Hernandez, L. E., Sanchez-Muñoz, M. A., Macias Franco, M. R., Narayanasamy, R., and Balagurusamy, N. (2019). Microbially Induced Calcium Carbonate Precipitation (MICP) and Its Potential in

Bioconcrete: Microbiological and Molecular Concepts. *Frontiers in Materials, 6*. doi: 10.3389/fmats.2019.00126

Chaerun, S. K., Syarif, R., and Wattimena, R. K. (2020). Bacteria incorporated with calcium lactate pentahydrate to improve the mortar properties and self-healing occurrence. *Sci Rep, 10*(1), 1-9.

Chen, C.-T., Chang, J.-J., and Yeih, W.-c. (2014). The effects of specimen parameters on the resistivity of concrete. *Construction and Building Materials, 71*, 35-43.

Childers, M. I., Nguyen, M.-T., Rod, K. A., Koech, P. K., Um, W., Chun, J., Glezakou, V.A., Linn, D., Roosendaal, T.J., Wietsma, T.W. and Huerta, N.J. (2017). Polymer-cement composites with self-healing ability for geothermal and fossil energy applications. *Chemistry of Materials, 29*(11), 4708-4718.

Chindasiriphan, P., Yokota, H., and Pimpakan, P. (2020). Effect of fly ash and superabsorbent polymer on concrete self-healing ability. *Construction and Building Materials, 233*, 116975.

Choi, E., Kim, D. J., Chung, Y.-S., Kim, H. S., and Jung, C. (2014). Crack-closing of cement mortar beams using NiTi cold-drawn SMA short fibers. *Smart Materials and Structures, 24*(1), 015018.

Choi, H., Inoue, M., Kwon, S., Choi, H., and Lim, M. (2016). Effective crack control of concrete by self-healing of cementitious composites using synthetic fiber. *Materials, 9*(4), 248.

Cuenca, E., D'Ambrosio, L., Lizunov, D., Tretjakov, A., Volobujeva, O., and Ferrara, L. (2021). Mechanical properties and self-healing capacity of Ultra High Performance Fibre Reinforced Concrete with alumina nano-fibres: Tailoring Ultra High Durability Concrete for aggressive exposure scenarios. *Cement and Concrete Composites, 118*, 103956.

Cuenca, E., and Ferrara, L. (2017). Self-healing capacity of fiber reinforced cementitious composites. State of the art and perspectives. *KSCE Journal of Civil Engineering, 21*(7), 2777-2789.

Cuenca, E., Tejedor, A., and Ferrara, L. (2018). A methodology to assess crack-sealing effectiveness of crystalline admixtures under repeated cracking-healing cycles. *Construction and Building Materials, 179*, 619-632.

Cunha, T. A., Agostinho, L. B., and Silva, E. F. (2019). *Application of Nano-silica Particles to Improve the Mechanical Properties of High Performance Concrete Containing Superabsorbent Polymers.* Paper presented at the International Conference on Application of Superabsorbent Polymers and Other New Admixtures Towards Smart Concrete.

Da Silva, F. B., De Belie, N., Boon, N., and Verstraete, W. (2015). Production of non-axenic ureolytic spores for self-healing concrete applications. *Construction and Building Materials, 93*, 1034-1041.

Davies, R., Pilegis, M., Kanellopoulos, A., Sharma, T., Teall, O., Gardner, D., Jefferson, A. and Lark, R. (2016). Multi-scale cementitious self-healing systems and their application in concrete structures.

Davies, R., Teall, O., Pilegis, M., Kanellopoulos, A., Sharma, T., Jefferson, A., Gardner, D., Al-Tabbaa, A., Paine, K. and Lark, R. (2018). Large scale application of self-healing concrete: Design, construction, and testing. *Frontiers in Materials, 5*, 51.

Davies, R. E., Jefferson, A., Lark, R., and Gardner, D. (2015). A novel 2D vascular network in cementitious materials.

De Belie, N., Gruyaert, E., Al-Tabbaa, A., Antonaci, P., Baera, C., Bajare, D., Darquennes, A., Davies, R., Ferrara, L., Jefferson, T. and Litina, C. (2018). A review of self-healing concrete for damage management of structures. *Advanced materials interfaces, 5*(17), 1800074.

De Belie, N., and Wang, J. (2016). Bacteria-based repair and self-healing of concrete. *Journal of Sustainable Cement-Based Materials, 5*(1-2), 35-56.

De Rooij, M., Van Tittelboom, K., De Belie, N., and Schlangen, E. (2013). *Self-healing phenomena in cement-Based materials: state-of-the-art report of RILEM technical committee 221-SHC: self-Healing phenomena in cement-Based materials* (Vol. 11): Springer.

Dembovska, L., Bajare, D., Korjakins, A., Toma, D., and Jakubovica, E. (2019). *Preliminary research for long lasting self-healing effect of bacteria-based concrete with lightweight aggregates.* Paper presented at the IOP Conference Series: Materials Science and Engineering.

Deng, H., and Liao, G. (2018). Assessment of influence of self-healing behavior on water permeability and mechanical performance of ECC incorporating superabsorbent polymer (SAP) particles. *Construction and Building Materials, 170*, 455-465.

Dong, B., Wang, Y., Fang, G., Han, N., Xing, F., and Lu, Y. (2015). Smart releasing behavior of a chemical self-healing microcapsule in the stimulated concrete pore solution. *Cement and Concrete Composites, 56*, 46-50.

Dry, C. (1993). Passive smart materials for sensing and actuation. *Journal of Intelligent Material Systems and Structures, 4*(3), 420-425.

Dry, C. (1994). Matrix cracking repair and filling using active and passive modes for smart timed release of chemicals from fibers into cement matrices. *Smart Materials and Structures, 3*(2), 118.

Du, W., Yu, J., Gu, Y., Li, Y., Han, X., and Liu, Q. (2019). Preparation and application of microcapsules containing toluene-di-isocyanate for self-healing of concrete. *Construction and Building Materials, 202*, 762-769.

Du, W., Yu, J., He, B., He, Y., He, P., Li, Y., and Liu, Q. (2020). Preparation and characterization of nano-SiO2/paraffin/PE wax composite shell microcapsules containing TDI for self-healing of cementitious materials. *Construction and Building Materials, 231*, 117060.

Ehrlich, H. L., Newman, D. K., and Kappler, A. (2002). *Geomicrobiology*: M. Dekker.

EN, T. (2004). 12504-4. Testing concrete–Part 4: determination of ultrasonic pulse velocity. *British Standards Institution*, 18.

Erşan, Y. Ç., Da Silva, F. B., Boon, N., Verstraete, W., and De Belie, N. (2015). Screening of bacteria and concrete compatible protection materials. *Construction and Building Materials, 88*, 196-203.

Erşan, Y. Ç., Hernandez-Sanabria, E., Boon, N., and De Belie, N. (2016). Enhanced crack closure performance of microbial mortar through nitrate reduction. *Cement and Concrete Composites, 70*, 159-170.

Fan, S., and Li, M. (2014). X-ray computed microtomography of three-dimensional microcracks and self-healing in engineered cementitious composites. *Smart Materials and Structures, 24*(1), 015021.

Fang, G., Liu, Y., Qin, S., Ding, W., Zhang, J., Hong, S., Xing, F. and Dong, B. (2018). Visualized tracing of crack self-healing features in cement/microcapsule system with X-ray microcomputed tomography. *Construction and Building Materials, 179*, 336-347.

Feiteira, J. (2017). Self-Healing concrete–Encapsulated polymer precursors as healing agents for active cracks. *Ghent University*.

Feiteira, J., Gruyaert, E., and De Belie, N. (2016). Self-healing of moving cracks in concrete by means of encapsulated polymer precursors. *Construction and Building Materials, 102*, 671-678.

Feiteira, J., Tsangouri, E., Gruyaert, E., Lors, C., Louis, G., and De Belie, N. (2017). Monitoring crack movement in polymer-based self-healing concrete through digital image correlation, acoustic emission analysis and SEM in-situ loading. *Materials and Design, 115*, 238-246.

Feng, J., Su, Y., and Qian, C. (2019). Coupled effect of PP fiber, PVA fiber and bacteria on self-healing efficiency of early-age cracks in concrete. *Construction and Building Materials, 228*, 116810.

Ferdous, W., Manalo, A., Wong, H. S., Abousnina, R., AlAjarmeh, O. S., Zhuge, Y., and Schubel, P. (2020). Optimal design for epoxy polymer concrete based on mechanical properties and durability aspects. *Construction and Building Materials, 232*, 117229.

Ferrara, L., Ferreira, S., Krelani, V., da Cunha, N., Moreira, T., Silva, F. D. A., and Toledo Filho, R. (2017). Self-healing capacity of hybrid sisal-steel fiber reinforced cementitious composites and comparison with steel only HPFRCCs. *Submitted to Construction and Building Materials*.

Ferrara, L., Krelani, V., and Carsana, M. (2014). A "fracture testing" based approach to assess crack healing of concrete with and without crystalline admixtures. *Construction and Building Materials, 68*, 535-551.

Ferrara, L., Krelani, V., Moretti, F., Flores, M. R., and Ros, P. S. (2017). Effects of autogenous healing on the recovery of mechanical performance of High Performance Fibre Reinforced Cementitious Composites (HPFRCCs): Part 1. *Cement and Concrete Composites, 83*, 76-100.

Ferrara, L., Van Mullem, T., Alonso, M. C., Antonaci, P., Borg, R. P., Cuenca, E., Jefferson, A., Ng, P.L., Peled, A., Roig-Flores, M. and Sanchez, M. (2018). Experimental characterization of the self-healing capacity of cement based materials and its effects on the material performance: a state of the art report by COST Action SARCOS WG2. *Construction and Building Materials, 167*, 115-142.

Gardner, D., Jefferson, A., Hoffman, A., and Lark, R. (2014). Simulation of the capillary flow of an autonomic healing agent in discrete cracks in cementitious materials. *Cement and Concrete Research, 58*, 35-44.

Ghosh, S. K. (2006). Functional coatings and microencapsulation: a general perspective. *Functional coatings*, 1-28.

Gilabert, F., Van Tittelboom, K., Van Stappen, J., Cnudde, V., De Belie, N., and Van Paepegem, W. (2017). Integral procedure to assess crack filling and mechanical contribution of polymer-based healing agent in encapsulation-based self-healing concrete. *Cement and Concrete Composites, 77*, 68-80.

Gilford III, J., Hassan, M. M., Rupnow, T., Barbato, M., Okeil, A., and Asadi, S. (2014). Dicyclopentadiene and sodium silicate microencapsulation for self-healing of concrete. *Journal of materials in civil engineering, 26*(5), 886-896.

Glukhovskij, V., Zaitsev, Y., and Pakhomov, V. (1983). Slag-alkaline cements and concretes-structure, properties, technological and economical aspects of the use. *Silicates industriels, 48*(10), 197-200.

Granger, S., Loukili, A., Pijaudier-Cabot, G., and Chanvillard, G. (2007). Experimental characterization of the self-healing of cracks in an ultra high performance

cementitious material: Mechanical tests and acoustic emission analysis. *Cement and Concrete Research, 37*(4), 519-527.

Gruyaert, E., Debbaut, B., Snoeck, D., Díaz, P., Arizo, A., Tziviloglou, E., Schlangen, E. and De Belie, N. (2016). Self-healing mortar with pH-sensitive superabsorbent polymers: testing of the sealing efficiency by water flow tests. *Smart Materials and Structures, 25*(8), 084007.

Gruyaert, E., Van Tittelboom, K., Sucaet, J., Anrijs, J., Van Vlierberghe, S., Dubruel, P., De Geest, B.G., Remon, J.P. and De Belie, N. (2016). Capsules with evolving brittleness to resist the preparation of self-healing concrete. *Materiales de Construcción, 66*(323), 092.

Guan, X., Zhang, C., Li, Y., and Zhao, S. (2020). Effect of exposure conditions on self-healing behavior of engineered cementitious composite incorporating limestone powder. *Cement and Concrete Composites, 114*, 103808.

Gwon, S., Ahn, E., and Shin, M. (2019). Self-healing of modified sulfur composites with calcium sulfoaluminate cement and superabsorbent polymer. *Composites Part B: Engineering, 162*, 469-483.

Hammes, F., and Verstraete, W. (2002). Key roles of pH and calcium metabolism in microbial carbonate precipitation. *Reviews in environmental science and biotechnology, 1*(1), 3-7.

Hazelwood, T., Jefferson, A. D., Lark, R. J., and Gardner, D. R. (2014). Long-term stress relaxation behavior of predrawn poly (ethylene terephthalate). *Journal of Applied Polymer Science, 131*(23).

Herbert, E. N., and Li, V. C. (2013). Self-healing of microcracks in engineered cementitious composites (ECC) under a natural environment. *Materials, 6*(7), 2831-2845.

Hewlett, P., and Liska, M. (2019). *Lea's chemistry of cement and concrete*: Butterworth-Heinemann.

Hia, I. L., Chan, E.-S., Chai, S.-P., and Pasbakhsh, P. (2018). A novel repeated self-healing epoxy composite with alginate multicore microcapsules. *Journal of Materials Chemistry A, 6*(18), 8470-8478.

Hilloulin, B., Legland, J.-B., Lys, E., Abraham, O., Loukili, A., Grondin, F., Durand, O., and Tournat, V. (2016). Monitoring of autogenous crack healing in cementitious materials by the nonlinear modulation of ultrasonic coda waves, 3D microscopy and X-ray microtomography. *Construction and Building Materials, 123*, 143-152.

Hilloulin, B., Van Tittelboom, K., Gruyaert, E., De Belie, N., and Loukili, A. (2015). Design of polymeric capsules for self-healing concrete. *Cement and Concrete Composites, 55*, 298-307.

Homma, D., Mihashi, H., and Nishiwaki, T. (2009). Self-healing capability of fibre reinforced cementitious composites. *Journal of Advanced Concrete Technology, 7*(2), 217-228.

Hong, G., and Choi, S. (2017). Rapid self-sealing of cracks in cementitious materials incorporating superabsorbent polymers. *Construction and Building Materials, 143*, 366-375.

Hong, S.-G., Kim, M.-S., and Moon, J. (2018). Effect of Gel-Polymerized Superabsorbent Polymers—SAPs on Concrete Freeze-Thaw Resistance. *Special Publication, 326*, 86.81-86.10.

Hu, M., Guo, J., Xu, Y., Fan, J., Cao, L., Wang, M., and Feng, Y. (2018). Influence of triethanolamine on reactivity of hydrated matrix in sodium silicate self-healing system and the mechanism. *Construction and Building Materials, 185*, 445-452.

Hu, M., Guo, J., Yu, Y., Cao, L., and Xu, Y. (2017). Research advances of microencapsulation and its prospects in the petroleum industry. *Materials, 10*(4), 369.

Hu, Z.-X., Hu, X.-M., Cheng, W.-M., Zhao, Y.-Y., and Wu, M.-Y. (2018). Performance optimization of one-component polyurethane healing agent for self-healing concrete. *Construction and Building Materials, 179*, 151-159.

Huang, H., Ye, G., and Damidot, D. (2014). Effect of blast furnace slag on self-healing of microcracks in cementitious materials. *Cement and Concrete Research, 60*, 68-82.

Huang, H., Ye, G., Qian, C., and Schlangen, E. (2016). Self-healing in cementitious materials: Materials, methods and service conditions. *Materials and Design, 92*, 499-511.

Huang, H., Ye, G., and Shui, Z. (2014). Feasibility of self-healing in cementitious materials–By using capsules or a vascular system? *Construction and Building Materials, 63*, 108-118.

Huang, T., Zhang, Y., and Yang, C. (2016). Multiscale modelling of multiple-cracking tensile fracture behaviour of engineered cementitious composites. *Engineering Fracture Mechanics, 160*, 52-66.

Huang, X., Ge, J., Kaewunruen, S., and Su, Q. (2020). The self-sealing capacity of environmentally friendly, highly damped, fibre-reinforced concrete. *Materials, 13*(2), 298.

Hung, C.-C., and Su, Y.-F. (2016). Medium-term self-healing evaluation of engineered cementitious composites with varying amounts of fly ash and exposure durations. *Construction and Building Materials, 118*, 194-203.

Hung, C.-C., Su, Y.-F., and Hung, H.-H. (2017). Impact of natural weathering on medium-term self-healing performance of fiber reinforced cementitious composites with intrinsic crack-width control capability. *Cement and Concrete Composites, 80*, 200-209.

Hung, C.-C., Su, Y.-F., and Su, Y.-M. (2018). Mechanical properties and self-healing evaluation of strain-hardening cementitious composites with high volumes of hybrid pozzolan materials. *Composites Part B: Engineering, 133*, 15-25.

Huseien, G. F., Mirza, J., Ariffin, N. F., and Hussin, M. W. (2015). Synthesis and characterization of self-healing mortar with modified strength. *Jurnal Teknologi, 76*(1).

Jackson, A. C., Bartelt, J. A., and Braun, P. V. (2011). Transparent self-healing polymers based on encapsulated plasticizers in a thermoplastic matrix. *Advanced Functional Materials, 21*(24), 4705-4711.

Jiang, Z., Li, W., and Yuan, Z. (2015). Influence of mineral additives and environmental conditions on the self-healing capabilities of cementitious materials. *Cement and Concrete Composites, 57*, 116-127.

Jiang, Z., Yuan, Z., and Li, W. (2019). Acoustic emission analysis of characteristics of healing products in steam-cured cementitious materials with mineral additives. *Construction and Building Materials, 201*, 807-817.

Jin, H., Mangun, C. L., Griffin, A. S., Moore, J. S., Sottos, N. R., and White, S. R. (2014). Thermally stable autonomic healing in epoxy using a dual-microcapsule system. *Advanced Materials, 26*(2), 282-287.

Jonkers, H. M., Thijssen, A., Muyzer, G., Copuroglu, O., and Schlangen, E. (2010). Application of bacteria as self-healing agent for the development of sustainable concrete. *Ecological engineering, 36*(2), 230-235.

Joseph, C., Jefferson, A. D., Isaacs, B., Lark, R., and Gardner, D. (2010). Experimental investigation of adhesive-based self-healing of cementitious materials. *Magazine of Concrete Research, 62*(11), 831-843.

Juenger, M. C., and Siddique, R. (2015). Recent advances in understanding the role of supplementary cementitious materials in concrete. *Cement and Concrete Research, 78*, 71-80.

Kalender, W. A. (2006). X-ray computed tomography. *Physics in Medicine and Biology, 51*(13), R29.

Kalyoncu, R. S. (1997). Coal combustion products. *Minerals Yearbook, 1*, 30.

Kanellopoulos, A., Giannaros, P., and Al-Tabbaa, A. (2016). The effect of varying volume fraction of microcapsules on fresh, mechanical and self-healing properties of mortars. *Construction and Building Materials, 122*, 577-593.

Kanellopoulos, A., Giannaros, P., Palmer, D., Kerr, A., and Al-Tabbaa, A. (2017). Polymeric microcapsules with switchable mechanical properties for self-healing concrete: synthesis, characterisation and proof of concept. *Smart Materials and Structures, 26*(4), 045025.

Kanellopoulos, A., Qureshi, T., and Al-Tabbaa, A. (2015). Glass encapsulated minerals for self-healing in cement based composites. *Construction and Building Materials, 98*, 780-791.

Kang, S.-H., Hong, S.-G., and Moon, J. (2018a). Importance of monovalent ions on water retention capacity of superabsorbent polymer in cement-based solutions. *Cement and Concrete Composites, 88*, 64-72.

Kang, S.-H., Hong, S.-G., and Moon, J. (2018b). Shrinkage characteristics of heat-treated ultra-high performance concrete and its mitigation using superabsorbent polymer based internal curing method. *Cement and Concrete Composites, 89*, 130-138.

Khaliq, W., and Ehsan, M. B. (2016). Crack healing in concrete using various bio influenced self-healing techniques. *Construction and Building Materials, 102*, 349-357.

Khushnood, R. A., Qureshi, Z. A., Shaheen, N., and Ali, S. (2020). Bio-mineralized self-healing recycled aggregate concrete for sustainable infrastructure. *Science of The Total Environment, 703*, 135007.

Kim, D. W., Kim, K. S., Seo, Y. G., Lee, B.-J., Park, Y. J., Youn, Y. S., Kim, J.O., Yong, C.S., Jin, S.G. and Choi, H.G. (2015). Novel sodium fusidate-loaded film-forming hydrogel with easy application and excellent wound healing. *International journal of pharmaceutics, 495*(1), 67-74.

Kim, M., Kang, S.-H., Hong, S.-G., and Moon, J. (2019). Influence of Effective Water-to-Cement Ratios on Internal Damage and Salt Scaling of Concrete with Superabsorbent Polymer. *Materials, 12*(23), 3863.

Kishi, T. (2007). *Self healing behaviour by cementitious recrystallization of cracked concrete incorporating expansive agent.* Paper presented at the First International Conference on Self Healing Materials, Noordwijk, The Netherlands, 2007. 4.

Kohli, R., and Mittal, K. Developments in Surface Contamination and Cleaning, Volumes 1–12: Elsevier.

Korkmaz, K. A., and Al-Durzi, L. (2016). An Analytical Approach for Self-Healing Capability of Cementitious and Polymeric Materials. *Journal of Construction and Building Materials, 1*(1).

Kosarli, M., Bekas, D. G., Tsirka, K., Baltzis, D., Vaimakis-Tsogkas, D. T., Orfanidis, S., Papavassiliou, G. and Paipetis, A.S. (2019). Microcapsule-based self-healing materials: Healing efficiency and toughness reduction vs. capsule size. *Composites Part B: Engineering, 171*, 78-86.

Kua, H. W., Gupta, S., Aday, A. N., and Srubar III, W. V. (2019). Biochar-immobilized bacteria and superabsorbent polymers enable self-healing of fiber-reinforced concrete after multiple damage cycles. *Cement and Concrete Composites*.

Kuang, Y., and Ou, J. (2008). Self-repairing performance of concrete beams strengthened using superelastic SMA wires in combination with adhesives released from hollow fibers. *Smart Materials and Structures, 17*(2), 025020.

Lee, H., Wong, H., and Buenfeld, N. (2010). Potential of superabsorbent polymer for self-sealing cracks in concrete. *Advances in Applied Ceramics, 109*(5), 296-302.

Lee, H., Wong, H., and Buenfeld, N. (2016). Self-sealing of cracks in concrete using superabsorbent polymers. *Cement and Concrete Research, 79*, 194-208.

Lee, K.-J., Lee, J.-H., Jung, C.-Y., and Choi, E. (2018). Crack-closing performance of NiTi and NiTiNb fibers in cement mortar beams using shape memory effects. *Composite Structures, 202*, 710-718.

Lee, Y. S., and Park, W. (2018). Current challenges and future directions for bacterial self-healing concrete. *Applied microbiology and biotechnology, 102*(7), 3059-3070.

Lefever, G., Snoeck, D., Aggelis, D. G., De Belie, N., Van Vlierberghe, S., and Van Hemelrijck, D. (2020). Evaluation of the Self-Healing Ability of Mortar Mixtures Containing Superabsorbent Polymers and Nanosilica. *Materials, 13*(2), 380.

Li, D., Chen, B., Chen, X., Fu, B., Wei, H., and Xiang, X. (2020). Synergetic effect of superabsorbent polymer (SAP) and crystalline admixture (CA) on mortar macro-crack healing. *Construction and Building Materials, 247*, 118521.

Li, G., Liu, S., Niu, M., Liu, Q., Yang, X., and Deng, M. (2020). Effect of granulated blast furnace slag on the self-healing capability of mortar incorporating crystalline admixture. *Construction and Building Materials, 239*, 117818.

Li, H., Liu, Z., and Ou, J. (2006). Behavior of a simple concrete beam driven by shape memory alloy wires. *Smart Materials and Structures, 15*(4), 1039.

Li, H., Qiu, K., Zhou, F., Li, L., and Zheng, Y. (2016). Design and development of novel antibacterial Ti-Ni-Cu shape memory alloys for biomedical application. *Scientific Reports, 6*, 37475.

Li, V. C. (2003). On engineered cementitious composites (ECC). *Journal of Advanced Concrete Technology, 1*(3), 215-230.

Li, V. C., Lim, Y. M., and Chan, Y.-W. (1998). Feasibility study of a passive smart self-healing cementitious composite. *Composites Part B: Engineering, 29*(6), 819-827.

Li, V. C., Wang, S., and Wu, C. (2001). Tensile strain-hardening behavior of polyvinyl alcohol engineered cementitious composite (PVA-ECC). *ACI Materials Journal-American Concrete Institute, 98*(6), 483-492.

Li, W., Dong, B., Yang, Z., Xu, J., Chen, Q., Li, H., Xing, F., and Jiang, Z. (2018). Recent advances in intrinsic self-healing cementitious materials. *Advanced Materials, 30*(17), 1705679.

Li, W., Jiang, Z., and Yang, Z. (2017). Acoustic characterization of damage and healing of microencapsulation-based self-healing cement matrices. *Cement and Concrete Composites, 84*, 48-61.

Li, Z., de Souza, L. R., Litina, C., Markaki, A. E., and Al-Tabbaa, A. (2020). A novel biomimetic design of a 3D vascular structure for self-healing in cementitious materials using Murray's law. *Materials and Design, 190*, 108572.

Liu, H., Huang, H., Wu, X., Peng, H., Li, Z., Hu, J., and Yu, Q. (2019). Effects of external multi-ions and wet-dry cycles in a marine environment on autogenous self-healing of cracks in cement paste. *Cement and Concrete Research, 120*, 198-206.

Liu, H., Zhang, Q., Gu, C., Su, H., and Li, V. (2017). Self-healing of microcracks in Engineered Cementitious Composites under sulfate and chloride environment. *Construction and Building Materials, 153*, 948-956.

Liu, J., Farzadnia, N., Shi, C., and Ma, X. (2019). Effects of superabsorbent polymer on shrinkage properties of ultra-high strength concrete under drying condition. *Construction and Building Materials, 215*, 799-811.

Liu, S., Bundur, Z. B., Zhu, J., and Ferron, R. D. (2016). Evaluation of self-healing of internal cracks in biomimetic mortar using coda wave interferometry. *Cement and Concrete Research, 83*, 70-78.

Lothenbach, B., Scrivener, K., and Hooton, R. (2011). Supplementary cementitious materials. *Cement and Concrete Research, 41*(12), 1244-1256.

Łukowski, P., and Adamczewski, G. (2013). Self-repairing of polymer-cement concrete. *Bulletin of the Polish Academy of Sciences: Technical Sciences, 61*(1), 195-200.

Luo, M., and Qian, C. (2016). Influences of bacteria-based self-healing agents on cementitious materials hydration kinetics and compressive strength. *Construction and Building Materials, 121*, 659-663.

Lv, L., Guo, P., Liu, G., Han, N., and Xing, F. (2020). Light induced self-healing in concrete using novel cementitious capsules containing UV curable adhesive. *Cement and Concrete Composites, 105*, 103445.

Ma, X., Yuan, Q., Liu, J., and Shi, C. (2019). Effect of water absorption of SAP on the rheological properties of cement-based materials with ultra-low w/b ratio. *Construction and Building Materials, 195*, 66-74.

Maes, M., Van Tittelboom, K., and De Belie, N. (2014). The efficiency of self-healing cementitious materials by means of encapsulated polyurethane in chloride containing environments. *Construction and Building Materials, 71*, 528-537.

Mao, W., Litina, C., and Al-Tabbaa, A. (2020). Development and application of novel sodium silicate microcapsule-based self-healing oil well cement. *Materials, 13*(2), 456.

Mason, W. T. (1999). *Fluorescent and luminescent probes for biological activity: a practical guide to technology for quantitative real-time analysis*: Elsevier.

Mazzoni, G., Stimilli, A., Cardone, F., and Canestrari, F. (2017). Fatigue, self-healing and thixotropy of bituminous mastics including aged modified bitumens and different filler contents. *Construction and Building Materials, 131*, 496-502.

Mechtcherine, V., Schroefl, C., Wyrzykowski, M., Gorges, M., Lura, P., Cusson, D., Margeson, J., De Belie, N., Snoeck, D., Ichimiya, K. and Igarashi, S.I. (2017). Effect of superabsorbent polymers (SAP) on the freeze–thaw resistance of concrete: results of a RILEM interlaboratory study. *Materials and Structures, 50*(1), 14.

Mechtcherine, V., Snoeck, D., Schröfl, C., De Belie, N., Klemm, A. J., Ichimiya, K., Moon, J., Wyrzykowski, M., Lura, P., Toropovs, N., and Assmann, A. (2018). Testing superabsorbent polymer (SAP) sorption properties prior to implementation in concrete: results of a RILEM Round-Robin Test. *Materials and Structures, 51*(1), 28.

Mignon, A., De Belie, N., Dubruel, P., and Van Vlierberghe, S. (2019). Superabsorbent polymers: A review on the characteristics and applications of synthetic, polysaccharide-based, semi-synthetic and 'smart'derivatives. *European Polymer Journal*.

Mignon, A., Graulus, G.-J., Snoeck, D., Martins, J., De Belie, N., Dubruel, P., and Van Vlierberghe, S. (2015). pH-sensitive superabsorbent polymers: a potential candidate material for self-healing concrete. *Journal of materials science, 50*(2), 970-979.

Mignon, A., Snoeck, D., Dubruel, P., Van Vlierberghe, S., and De Belie, N. (2017). Crack mitigation in concrete: superabsorbent polymers as key to success? *Materials, 10*(3), 237.

Mihashi, H., Kaneko, Y., Nishiwaki, T., and Otsuka, K. (2000). Fundamental study on development of intelligent concrete characterized by self-healing capability for strength. *Transactions of the Japan Concrete Institute, 22*, 441-450.

Misra, S. K. (2013). Shape memory alloy reinforced self-healing metal matrix composites.

Mostavi, E., Asadi, S., Hassan, M. M., and Alansari, M. (2015). Evaluation of self-healing mechanisms in concrete with double-walled sodium silicate microcapsules. *Journal of materials in civil engineering, 27*(12), 04015035.

Muhammad, N. Z., Shafaghat, A., Keyvanfar, A., Majid, M. Z. A., Ghoshal, S., Yasouj, S. E. M., Ganiyu, A.A., Kouchaksaraei, M.S., Kamyab, H., Taheri, M.M. and Shirdar, M.R. (2016). Tests and methods of evaluating the self-healing efficiency of concrete: A review. *Construction and Building Materials, 112*, 1123-1132.

Neville, A. M. (1995). *Properties of concrete* (Vol. 4): Longman London.

Nguyễn, H. H., Choi, J.-I., Song, K.-I., Song, J.-K., Huh, J., and Lee, B. Y. (2018). Self-healing properties of cement-based and alkali-activated slag-based fiber-reinforced composites. *Construction and Building Materials, 165*, 801-811.

Nguyen, T. H., Ghorbel, E., Fares, H., and Cousture, A. (2019). Bacterial self-healing of concrete and durability assessment. *Cement and Concrete Composites, 104*, 103340.

Nishiwaki, T., Koda, M., Yamada, M., Mihashi, H., and Kikuta, T. (2012). Experimental study on self-healing capability of FRCC using different types of synthetic fibers. *Journal of Advanced Concrete Technology, 10*(6), 195-206.

Ohama, Y. (1997). Recent progress in concrete-polymer composites. *Advanced Cement Based Materials, 5*(2), 31-40.

Okafor, N. (2011). *Environmental microbiology of aquatic and waste systems*: Springer Science and Business Media.

Pacheco-Torgal, F., Khatib, J., Colangelo, F., and Tuladhar, R. (2018). *Use of recycled plastics in eco-efficient concrete*: Woodhead Publishing.

Paine, K., Al-Tabbaa, A., Gardner, D., and Jefferson, A. (2019a). *Resilient materials for life: Biomimetic self-healing and self-diagnosing concretes.* Paper presented at the UKIERI Concrete Congress Concrete; The Global Builder: Jalandhar, India.

Paine, K., Al-Tabbaa, A., Gardner, D., and Jefferson, A. (2019b). *Resilient materials for life: Biomimetic self-healing and self-diagnosing concretes.* Paper presented at the UKIERI Concrete Congress, Concrete: The Global Builder: Working together for durable and sustainable infrastructure.

Palin, D., Jonkers, H., and Wiktor, V. (2016). Autogenous healing of sea-water exposed mortar: Quantification through a simple and rapid permeability test. *Cement and Concrete Research, 84*, 1-7.

Pang, B., Zhou, Z., Hou, P., Du, P., Zhang, L., and Xu, H. (2016). Autogenous and engineered healing mechanisms of carbonated steel slag aggregate in concrete. *Construction and Building Materials, 107*, 191-202.

Park, B., and Choi, Y. C. (2018). Self-healing capability of cementitious materials with crystalline admixtures and super absorbent polymers (SAPs). *Construction and Building Materials, 189*, 1054-1066.

Park, B., and Choi, Y. C. (2020). Effect of healing products on the self-healing performance of cementitious materials with crystalline admixtures. *Construction and Building Materials*, 121389.

Priniotakis, G., Bouguessir, H., Harkati, E., Rokbi, M., and Vassilliadis, S. (2018). *Environmental durability of externally natural fabrics reinforced polymer concrete.* Paper presented at the IOP conference series: materials science and engineering.

Pungrasmi, W., Intarasoontron, J., Jongvivatsakul, P., and Likitlersuang, S. (2019). Evaluation of microencapsulation techniques for MICP bacterial spores applied in self-healing concrete. *Sci Rep, 9*(1), 1-10.

Qiu, J., He, S., and Yang, E.-H. (2019). Autogenous healing and its enhancement of interface between micro polymeric fiber and hydraulic cement matrix. *Cement and Concrete Research, 124*, 105830.

Qiu, J., Tan, H. S., and Yang, E.-H. (2016). Coupled effects of crack width, slag content, and conditioning alkalinity on autogenous healing of engineered cementitious composites. *Cement and Concrete Composites, 73*, 203-212.

Qureshi, T., Kanellopoulos, A., and Al-Tabbaa, A. (2016). Encapsulation of expansive powder minerals within a concentric glass capsule system for self-healing concrete. *Construction and Building Materials, 121*, 629-643.

Qureshi, T., Kanellopoulos, A., and Al-Tabbaa, A. (2018). Autogenous self-healing of cement with expansive minerals-I: Impact in early age crack healing. *Construction and Building Materials, 192*, 768-784.

Qureshi, T., Kanellopoulos, A., and Al-Tabbaa, A. (2019). Autogenous self-healing of cement with expansive minerals-II: Impact of age and the role of optimised expansive minerals in healing performance. *Construction and Building Materials, 194*, 266-275.

Rajasegar, M., and Kumaar, C. M. (2021). Hybrid effect of poly vinyl alcohol, expansive minerals, nano-silica and rice husk ash on the self-healing ability of concrete. *Materials Today: Proceedings, 45*, 5944-5952.

Ramalingam, M., and Ramakrishna, S. (2017). *Nanofiber composites for biomedical applications*: Woodhead Publishing.

Reddy, T. C. S., and Ravitheja, A. (2019). Macro mechanical properties of self healing concrete with crystalline admixture under different environments. *Ain Shams Engineering Journal, 10*(1), 23-32.

Reddy, T. C. S., Ravitheja, A., and Sashidhar, C. (2020). Micromechanical Properties of Self-Healing Concrete with Crystalline Admixture and Silica Fume. *ACI Materials Journal, 117*(3), 63-74.

Reinhardt, H.-W., and Jooss, M. (2003). Permeability and self-healing of cracked concrete as a function of temperature and crack width. *Cement and Concrete Research, 33*(7), 981-985.

Roig-Flores, M., Moscato, S., Serna, P., and Ferrara, L. (2015). Self-healing capability of concrete with crystalline admixtures in different environments. *Construction and Building Materials, 86*, 1-11.

Roig-Flores, M., Pirritano, F., Serna, P., and Ferrara, L. (2016). Effect of crystalline admixtures on the self-healing capability of early-age concrete studied by means of permeability and crack closing tests. *Construction and Building Materials, 114*, 447-457.

Ruan, S., Qiu, J., Weng, Y., Yang, Y., Yang, E.-H., Chu, J., and Unluer, C. (2019). The use of microbial induced carbonate precipitation in healing cracks within reactive magnesia cement-based blends. *Cement and Concrete Research, 115*, 176-188.

Sabir, B., Wild, S., and O'farrell, M. (1998). A water sorptivity test for martar and concrete. *Materials and Structures, 31*(8), 568-574.

Sahmaran, M., Yildirim, G., and Erdem, T. K. (2013). Self-healing capability of cementitious composites incorporating different supplementary cementitious materials. *Cement and Concrete Composites, 35*(1), 89-101.

Saini, V., von Tapavicza, M., Eloo, C., Braesch, K., Wack, H., Nellesen, A., Schmidt, A.M. and García, S.J. (2018). Superabsorbent polymer additives for repeated barrier restoration of damaged powder coatings under wet-dry cycles: A proof-of-concept. *Progress in Organic Coatings, 122*, 129-137.

Saleem, B., Hussain, A., Khattak, A., and Khan, A. (2021). Performance evaluation of bacterial self-healing rigid pavement by incorporating recycled brick aggregate. *Cement and Concrete Composites, 117*, 103914.

Sam, A. R. M., Ariffin, N. F., Hussin, M. W., Lee, H. S., Ismail, M. A., Lim, N. H. A. S., Khalid, N.H.A., Samadi, M., Mirza, J. and Majid, M.Z.A. (2015). Performance of epoxy resin as self-healing agent. *Jurnal Teknologi, 77*(16).

Sánchez, L., Cuevas, J., Ramírez, S., De León, D. R., Fernández, R., Villa, R. V. D., and Leguey, S. (2006). Reaction kinetics of FEBEX bentonite in hyperalkaline conditions resembling the cement–bentonite interface. *Applied Clay Science, 33*(2), 125-141.

Sangadji, S. (2017). Can self-healing mechanism helps concrete structures sustainable? *Procedia engineering, 171*, 238-249.

Šavija, B., Feiteira, J., Araújo, M., Chatrabhuti, S., Raquez, J.-M., Van Tittelboom, K., Gruyaert, E., De Belie, N. and Schlangen, E. (2017). Simulation-aided design of tubular polymeric capsules for self-healing concrete. *Materials, 10*(1), 10.

Schlangen, E. (2005). Self-healing phenomena in cement-based materials. *RILEM. See http://www. rilem. net/tcDetails. php*.

Seifan, M., Samani, A. K., and Berenjian, A. (2016). Bioconcrete: next generation of self-healing concrete. *Applied microbiology and biotechnology, 100*(6), 2591-2602.

Seifan, M., Sarmah, A. K., Ebrahiminezhad, A., Ghasemi, Y., Samani, A. K., and Berenjian, A. (2018). Bio-reinforced self-healing concrete using magnetic iron oxide nanoparticles. *Applied microbiology and biotechnology, 102*(5), 2167-2178.

Seifan, M., Sarmah, A. K., Samani, A. K., Ebrahiminezhad, A., Ghasemi, Y., and Berenjian, A. (2018). Mechanical properties of bio self-healing concrete containing immobilized bacteria with iron oxide nanoparticles. *Applied microbiology and biotechnology, 102*(10), 4489-4498.

Sengul, O. (2014). Use of electrical resistivity as an indicator for durability. *Construction and Building Materials, 73*, 434-441.

Shaheen, N., Khushnood, R. A., Khaliq, W., Murtaza, H., Iqbal, R., and Khan, M. H. (2019). Synthesis and characterization of bio-immobilized nano/micro inert and reactive additives for feasibility investigation in self-healing concrete. *Construction and Building Materials, 226*, 492-506.

Sharma, R., and Khan, R. A. (2017). Sustainable use of copper slag in self compacting concrete containing supplementary cementitious materials. *Journal of Cleaner Production, 151*, 179-192.

Sharma, T., Alazhari, M., Heath, A., Paine, K., and Cooper, R. (2017). Alkaliphilic Bacillus species show potential application in concrete crack repair by virtue of rapid spore production and germination then extracellular calcite formation. *Journal of applied microbiology, 122*(5), 1233-1244.

Sherir, M. A., Hossain, K. M., and Lachemi, M. (2016). Self-healing and expansion characteristics of cementitious composites with high volume fly ash and MgO-type expansive agent. *Construction and Building Materials, 127*, 80-92.

Sherir, M. A., Hossain, K. M., and Lachemi, M. (2017). The influence of MgO-type expansive agent incorporated in self-healing system of Engineered cementitious Composites. *Construction and Building Materials, 149*, 164-185.

Sherir, M. A., Hossain, K. M., and Lachemi, M. (2018). Permeation and transport properties of self-healed cementitious composite produced with MgO expansive agent. *Journal of materials in civil engineering, 30*(11), 04018291.

Siddique, R., and Cachim, P. (2018). *Waste and Supplementary Cementitious Materials in Concrete: Characterisation, Properties and Applications*: Woodhead Publishing.

Sierra-Beltran, M. G., Jonkers, H., and Schlangen, E. (2014). Characterization of sustainable bio-based mortar for concrete repair. *Construction and Building Materials, 67*, 344-352.

Silva, D., Fernandes, A., Nunes, T., Colaço, R., and Serro, A. (2015). The effect of albumin and cholesterol on the biotribological behavior of hydrogels for contact lenses. *Acta biomaterialia, 26*, 184-194.

Sisomphon, K., Copuroglu, O., and Koenders, E. (2012). Self-healing of surface cracks in mortars with expansive additive and crystalline additive. *Cement and Concrete Composites, 34*(4), 566-574.

Sisomphon, K., Copuroglu, O., and Koenders, E. (2013). Effect of exposure conditions on self healing behavior of strain hardening cementitious composites incorporating various cementitious materials. *Construction and Building Materials, 42*, 217-224.

Snoeck, D., Dewanckele, J., Cnudde, V., and De Belie, N. (2016). X-ray computed microtomography to study autogenous healing of cementitious materials promoted by superabsorbent polymers. *Cement and Concrete Composites, 65*, 83-93.

Snoeck, D., Pel, L., and De Belie, N. (2020). Autogenous healing in cementitious materials with superabsorbent polymers quantified by means of NMR. *Sci Rep, 10*(1), 1-6.

Snoeck, D., Van Tittelboom, K., Steuperaert, S., Dubruel, P., and De Belie, N. (2014). Self-healing cementitious materials by the combination of microfibres and superabsorbent polymers. *Journal of Intelligent Material Systems and Structures, 25*(1), 13-24.

Song, M., Jeon, S., and Song, Y. (2011). *The change of osmosis pressure by crack self-healing of cementitious materials.* Paper presented at the Proceedings of 3rd International Conference on Self Healing Materials, Bath, UK.

Souza, L., and Al-Tabbaa, A. (2018). Microfluidic fabrication of microcapsules tailored for self-healing in cementitious materials. *Construction and Building Materials, 184*, 713-722.

Stuckrath, C., Serpell, R., Valenzuela, L. M., and Lopez, M. (2014). Quantification of chemical and biological calcium carbonate precipitation: performance of self-healing in reinforced mortar containing chemical admixtures. *Cement and Concrete Composites, 50*, 10-15.

Su, Y.-F., Huang, C., Jeong, H., Nantung, T., Olek, J., Baah, P., and Lu, N. (2020). Autogenous healing performance of internal curing agent-based self-healing cementitious composite. *Cement and Concrete Composites, 114*, 103825.

Su, Y., Qian, C., Rui, Y., and Feng, J. (2020). Exploring the coupled mechanism of fibers and bacteria on self-healing concrete from bacterial extracellular polymeric substances (EPS). *Cement and Concrete Composites*, 103896.

Suleiman, A., and Nehdi, M. (2018). Effect of environmental exposure on autogenous self-healing of cracked cement-based materials. *Cement and Concrete Research, 111*, 197-208.

Suleiman, A. R., and Nehdi, M. (2021). Effect of autogenous crack self-healing on mechanical strength recovery of cement mortar under various environmental exposure. *Scientific Reports*, *11*(1), 1-14.

Suleiman, A. R., Nelson, A. J., and Nehdi, M. L. (2019). Visualization and quantification of crack self-healing in cement-based materials incorporating different minerals. *Cement and Concrete Composites, 103*, 49-58.

Sun, L., Liang, D., Gao, Q., and Zhou, J. (2013). Analysis on factors affecting the self-repair capability of SMA wire concrete beam. *Mathematical Problems in Engineering, 2013*.

Sun, X., Miao, L., Wu, L., Wang, C., and Chen, R. (2020). The method of repairing microcracks based on microbiologically induced calcium carbonate precipitation. *Advances in Cement Research, 32*(6), 262-272.

Taha, M. M. R. (2018). *International Congress on Polymers in Concrete (ICPIC 2018): Polymers for Resilient and Sustainable Concrete Infrastructure*: Springer.

Tan, L., Reeksting, B., Ferrandiz-Mas, V., Heath, A., Gebhard, S., and Paine, K. (2019). *Application of calcium nitrate as calcium source on self-healing concrete with non-ureolytic bacteria.* Paper presented at the 7th International Conference on Self-Healing Materials.

Tang, W., Kardani, O., and Cui, H. (2015). Robust evaluation of self-healing efficiency in cementitious materials–A review. *Construction and Building Materials, 81*, 233-247.

Tayebani, B., Hosseinibalam, N., and Mostofinejad, D. (2019). Influential Effect of Self-Healing Treatment on Water Absorption and Electrical Resistance of Normal and Light Weight Aggregate Concretes. *International Journal of Civil and Environmental Engineering, 13*(4), 195-199.

TC, R. (1999). Recommendations of TC 116-PCD, Tests for gas permeability of concrete. B. Measurement of the gas permeability of concrete by the RILEM-CEMBUREAU method. *Mater. and Struct., 32*, 176-178.

Teall, O. (2016). *Crack closure and enhanced autogenous healing of structural concrete using shape memory polymers.* Cardiff University.

Teall, O., Davies, R., Pilegis, M., Kanellopoulos, A., Sharma, T., Paine, K., Jefferson, A., Lark, R., Gardner, D. and Al-Tabbaa, A. (2016). *Self-healing concrete full-scale site trials.* Paper presented at the Proceedings of the 11th fib International PhD Symposium in Civil Engineering.

Teall, O., Pilegis, M., Davies, R., Sweeney, J., Jefferson, T., Lark, R., and Gardner, D. (2018). A shape memory polymer concrete crack closure system activated by electrical current. *Smart Materials and Structures, 27*(7), 075016.

Thomas, S., and Maria, H. J. (2016). *Progress in rubber nanocomposites*: Woodhead Publishing.

Tomczak, K., Jakubowski, J., and Kotwica, Ł. (2020). Self-Sealing Process Evaluation Method Using Ultrasound Technique in Cement Composites with Mineral Additives. *Materials, 13*(15), 3336.

Tsangouri, E., Gilabert, F. A., De Belie, N., Van Hemelrijck, D., Zhu, X., and Aggelis, D. G. (2019). Concrete fracture toughness increase by embedding self-healing capsules using an integrated experimental approach. *Construction and Building Materials, 218*, 424-433.

Tsangouri, E., Lelon, J., Minnebo, P., Asaue, H., Shiotani, T., Van Tittelboom, K., De Belie, N., Aggelis, D.G. and Van Hemelrijck, D. (2019). Feasibility study on real-scale, self-healing concrete slab by developing a smart capsules network and assessed by a plethora of advanced monitoring techniques. *Construction and Building Materials, 228*, 116780.

Tziviloglou, E., Wiktor, V., Jonkers, H., and Schlangen, E. (2016). Bacteria-based self-healing concrete to increase liquid tightness of cracks. *Construction and Building Materials, 122*, 118-125.

Van Belleghem, B., Van den Heede, P., Van Tittelboom, K., and De Belie, N. (2017). Quantification of the service life extension and environmental benefit of chloride exposed self-healing concrete. *Materials, 10*(1), 5.

Van Tittelboom, K., and De Belie, N. (2013). Self-healing in cementitious materials—A review. *Materials, 6*(6), 2182-2217.

Van Tittelboom, K., De Belie, N., De Muynck, W., and Verstraete, W. (2010). Use of bacteria to repair cracks in concrete. *Cement and Concrete Research, 40*(1), 157-166.

Van Tittelboom, K., De Belie, N., Lehmann, F., and Grosse, C. U. (2012). Acoustic emission analysis for the quantification of autonomous crack healing in concrete. *Construction and Building Materials, 28*(1), 333-341.

Van Tittelboom, K., De Belie, N., Van Loo, D., and Jacobs, P. (2011). Self-healing efficiency of cementitious materials containing tubular capsules filled with healing agent. *Cement and Concrete Composites, 33*(4), 497-505.

Van Tittelboom, K., Gruyaert, E., Rahier, H., and De Belie, N. (2012). Influence of mix composition on the extent of autogenous crack healing by continued hydration or calcium carbonate formation. *Construction and Building Materials, 37*, 349-359.

Van Tittelboom, K., Tsangouri, E., Van Hemelrijck, D., and De Belie, N. (2015). The efficiency of self-healing concrete using alternative manufacturing procedures and more realistic crack patterns. *Cement and Concrete Composites, 57*, 142-152.

Van Tittelboom, K., Wang, J., Araújo, M., Snoeck, D., Gruyaert, E., Debbaut, B., Derluyn, H., Cnudde, V., Tsangouri, E., Van Hemelrijck, D. and De Belie, N. (2016). Comparison of different approaches for self-healing concrete in a large-scale lab test. *Construction and Building Materials, 107*, 125-137.

Vijay, K., and Murmu, M. (2019). Effect of calcium lactate on compressive strength and self-healing of cracks in microbial concrete. *Frontiers of Structural and Civil Engineering, 13*(3), 515-525.

Wang, C., Bu, Y., Guo, S., Lu, Y., Sun, B., and Shen, Z. (2019). Self-healing cement composite: Amine-and ammonium-based pH-sensitive superabsorbent polymers. *Cement and Concrete Composites, 96*, 154-162.

Wang, J.-Y., De Belie, N., and Verstraete, W. (2012). Diatomaceous earth as a protective vehicle for bacteria applied for self-healing concrete. *Journal of industrial Microbiology and biotechnology, 39*(4), 567-577.

Wang, J., Dewanckele, J., Cnudde, V., Van Vlierberghe, S., Verstraete, W., and De Belie, N. (2014). X-ray computed tomography proof of bacterial-based self-healing in concrete. *Cement and Concrete Composites, 53*, 289-304.

Wang, J., Mignon, A., Snoeck, D., Wiktor, V., Van Vliergerghe, S., Boon, N., and De Belie, N. (2015). Application of modified-alginate encapsulated carbonate producing bacteria in concrete: a promising strategy for crack self-healing. *Frontiers in microbiology, 6*, 1088.

Wang, J., Snoeck, D., Van Vlierberghe, S., Verstraete, W., and De Belie, N. (2014). Application of hydrogel encapsulated carbonate precipitating bacteria for approaching a realistic self-healing in concrete. *Construction and Building Materials, 68*, 110-119.

Wang, J., Soens, H., Verstraete, W., and De Belie, N. (2014). Self-healing concrete by use of microencapsulated bacterial spores. *Cement and Concrete Research, 56*, 139-152.

Wang, J., Van Tittelboom, K., De Belie, N., and Verstraete, W. (2012). Use of silica gel or polyurethane immobilized bacteria for self-healing concrete. *Construction and Building Materials, 26*(1), 532-540.

Wang, M. L., Lynch, J. P., and Sohn, H. (2014). *Sensor technologies for civil infrastructures, volume 2: Applications in structural health monitoring*: Elsevier.

Wang, W., Zhong, T., Wang, X., and He, Z. (2019). *Research Status of Self-healing Concrete.* Paper presented at the IOP Conference Series: Earth and Environmental Science.

Wang, X., Fang, C., Li, D., Han, N., and Xing, F. (2018). A self-healing cementitious composite with mineral admixtures and built-in carbonate. *Cement and Concrete Composites, 92*, 216-229.

Wang, X., Yang, Z., Fang, C., Han, N., Zhu, G., Tang, J., and Xing, F. (2019). Evaluation of the mechanical performance recovery of self-healing cementitious materials–its methods and future development: a review. *Construction and Building Materials, 212*, 400-421.

White, S. R., Blaiszik, B. J., Kramer, S. L., Olugebefola, S. C., Moore, J. S., and Sottos, N. R. (2011). Self-healing Polymers and Composites: Capsules, circulatory systems and chemistry allow materials to fix themselves. *American Scientist, 99*(5), 392-399.

White, S. R., Sottos, N. R., Geubelle, P. H., Moore, J. S., Kessler, M. R., Sriram, S., Brown, E.N. and Viswanathan, S. (2001). Autonomic healing of polymer composites. *Nature, 409*(6822), 794-797.

Wiktor, V., and Jonkers, H. M. (2011). Quantification of crack-healing in novel bacteria-based self-healing concrete. *Cement and Concrete Composites, 33*(7), 763-770.

Williams, S. L., Sakib, N., Kirisits, M. J., and Ferron, R. D. (2016). Flexural Strength Recovery Induced by Vegetative Bacteria Added to Mortar. *ACI Materials Journal, 113*(4).

Wong, H. S. (2018). Concrete with superabsorbent polymer *Eco-Efficient Repair and Rehabilitation of Concrete Infrastructures* (pp. 467-499): Elsevier.

Wu, H.-L., Zhang, D., Du, Y.-J., and Li, V. C. (2020). Durability of Engineered Cementitious Composite exposed to Acid Mine Drainage. *Cement and Concrete Composites*, 103550.

Wu, M., Hu, X., Zhang, Q., Cheng, W., Xue, D., and Zhao, Y. (2020). Application of bacterial spores coated by a green inorganic cementitious material for the self-healing of concrete cracks. *Cement and Concrete Composites, 113*, 103718.

Xiao, X., Yu, L., Xie, F., Bao, X., Liu, H., Ji, Z., and Chen, L. (2017). One-step method to prepare starch-based superabsorbent polymer for slow release of fertilizer. *Chemical Engineering Journal, 309*, 607-616.

Xu, J., and Wang, X. (2018). Self-healing of concrete cracks by use of bacteria-containing low alkali cementitious material. *Construction and Building Materials, 167*, 1-14.

Xu, J., and Yao, W. (2014). Multiscale mechanical quantification of self-healing concrete incorporating non-ureolytic bacteria-based healing agent. *Cement and Concrete Research, 64*, 1-10.

Xue, C., Li, W., Li, J., Tam, V. W., and Ye, G. (2019). A review study on encapsulation-based self-healing for cementitious materials. *Structural concrete, 20*(1), 198-212.

Xue, C., Li, W., Luo, Z., Wang, K., and Castel, A. Effect of chloride ingress on self-healing recovery of smart cementitious composite incorporating crystalline admixture and MgO expansive agent. *Cement and Concrete Research, 139*, 106252.

Yang, E.-H., Yang, Y., and Li, V. C. (2007). Use of high volumes of fly ash to improve ECC mechanical properties and material greenness. *ACI Materials Journal, 104*(6), 620.

Yang, H., He, Z., Shao, Y., and Li, L. (2018). Improving freeze-thaw resistance and strength gain of roller compacted fly ash concretes with modified absorbent polymer. *Journal of materials in civil engineering, 30*(3), 04018010.

Yang, J., Huang, J., He, X., Su, Y., and Oh, S.-K. (2020). Shrinkage properties and microstructure of high volume ultrafine phosphorous slag blended cement mortars with superabsorbent polymer. *Journal of Building Engineering, 29*, 101121.

Yang, J., Liu, L., Liao, Q., Wu, J., Li, J., and Zhang, L. (2019). Effect of superabsorbent polymers on the drying and autogenous shrinkage properties of self-leveling mortar. *Construction and Building Materials, 201*, 401-407.

Yang, Y., Lepech, M., and Li, V. C. (2005). Self-healing of ECC under cyclic wetting and drying.

Yang, Y., Yang, E.-H., and Li, V. C. (2011). Autogenous healing of engineered cementitious composites at early age. *Cement and Concrete Research, 41*(2), 176-183.

Yang, Z., Hollar, J., He, X., and Shi, X. (2011). A self-healing cementitious composite using oil core/silica gel shell microcapsules. *Cement and Concrete Composites, 33*(4), 506-512.

Yao, Y., Zhu, Y., and Yang, Y. (2012). Incorporation superabsorbent polymer (SAP) particles as controlling pre-existing flaws to improve the performance of engineered cementitious composites (ECC). *Construction and Building Materials, 28*(1), 139-145.

Yıldırım, G., Khiavi, A. H., Yeşilmen, S., and Şahmaran, M. (2018). Self-healing performance of aged cementitious composites. *Cement and Concrete Composites, 87*, 172-186.

Yildirim, G., Sahmaran, M., Balcikanli, M., Ozbay, E., and Lachemi, M. (2015). Influence of cracking and healing on the gas permeability of cementitious composites. *Construction and Building Materials, 85*, 217-226.

Yoo, D.-Y., Banthia, N., Fujikake, K., Borges, P. H., and Gupta, R. (2017). Advanced Cementitious Materials: Mechanical Behavior, Durability, and Volume Stability: Hindawi.

Young, T., and Hirst, M. (2012). *Innovation in aeronautics*: Elsevier.

Yuan, B., Yang, Y., Wang, Y., and Zhang, K. (2017). Self-healing efficiency of EVA-modified cement for hydraulic fracturing wells. *Construction and Building Materials, 146*, 563-570.

Yuan, L., Huang, S., Gu, A., Liang, G., Chen, F., Hu, Y., and Nutt, S. (2013). A cyanate ester/microcapsule system with low cure temperature and self-healing capacity. *Composites Science and Technology, 87*, 111-117.

Yuan, Z.-c., Jiang, Z.-w., and Chen, Q. (2019). Permeability modeling of self-healing due to calcium carbonate precipitation in cement-based materials with mineral additives. *Journal of Central South University, 26*(3), 567-576.

Zhang, D., Wu, H., Li, V. C., and Ellis, B. R. (2020). Autogenous healing of Engineered Cementitious Composites (ECC) based on MgO-fly ash binary system activated by carbonation curing. *Construction and Building Materials, 238*, 117672.

Zhang, J., Liu, Y., Feng, T., Zhou, M., Zhao, L., Zhou, A., and Li, Z. (2017). Immobilizing bacteria in expanded perlite for the crack self-healing in concrete. *Construction and Building Materials, 148*, 610-617.

Zhang, J., Wang, Z., and Ju, X. (2013). Application of ductile fiber reinforced cementitious composite in jointless concrete pavements. *Composites Part B: Engineering, 50*, 224-231.

Zhang, J., Zhou, A., Liu, Y., Zhao, B., Luan, Y., Wang, S., Yue, X. and Li, Z. (2017). Microbial network of the carbonate precipitation process induced by microbial consortia and the potential application to crack healing in concrete. *Scientifc Reports, 7*(1), 14600.

Zhang, L., Suleiman, A., and Nehdi, M. (2020). Self-healing in fiber-reinforced alkali-activated slag composites incorporating different additives. *Construction and Building Materials, 262*, 120059.

Zhang, W., Wang, D., and Han, B. (2020). Self-healing concrete-based composites *Self-Healing Composite Materials* (pp. 259-284): Elsevier.

Zheng, T., and Qian, C. (2020). Self-healing of later-age cracks in cement-based materials by encapsulation-based bacteria. *Journal of materials in civil engineering, 32*(11), 04020341.

Zheng, T., Su, Y., Qian, C., and Zhou, H. (2020). Low alkali sulpho-aluminate cement encapsulated microbial spores for self-healing cement-based materials. *Biochemical Engineering Journal, 163*, 107756.

Zhu, Y., Zhang, Z., Chen, X., Zou, D., Guan, X., and Dong, B. (2020). Non-destructive methods to evaluate the self-healing behavior of engineered cementitious composites (ECC). *Construction and Building Materials, 230*, 116753.

Chapter 3

3 CRACK SELF-HEALING IN NAOH-ACTIVATED SLAG-BASED COMPOSITES INCORPORATING CALCIUM HYDROXIDE[1]

This chapter explores the crack self-healing capability of NaOH-activated slag composites using a portfolio of testing methods, including electrical conductivity, mercury intrusion porosimetry, inductively coupled plasma optical emission spectroscopy, scanning electron microscopy (SEM) coupled with energy-dispersive X-ray spectroscopy, and X-ray microcomputed tomography. Experimental results indicate that alkali-activated slag-based composites incorporating calcium hydroxide achieved higher level of self-healing than control specimens without calcium hydroxide. X-ray micro-computed tomography coupled with three-dimensional image analysis demonstrated that the observed self-healing was a surface mechanism, only occurring at surface cracks. Calcium carbonate was found to be the main self-healing product in all test specimens. Leaching experimental results indicated that the concentration of Ca^{2+} ions in the AAM matrix plays a critical role in calcium carbonate precipitation, and thus in the self-healing potential.

3.1 INTRODUCTION

Cracking in concrete structures is among the predominant factors contributing to structural deterioration. It provides a preferential pathway for aggressive substances such as chloride ions to ingress into the concrete matrix, thus compromising the service life of concrete structures (Nguyễn *et al*., 2018). To mitigate this problem, conventional repair methods are commonly deployed (Breugel 2007). While such methods are laborious and costly, they become impractical when cracks are not visible or difficult to access. For instance, the European Union spent an annual budget of £215 million on reinforced concrete bridges requiring maintenance, strengthening, and rehabilitation (Pacheco-

[1] A version of this chapter was published in the *ASCE Journal of Materials in Civil Engineering* (2021).

Torgal *et al*., 2012). Similarly, in the UK, more than 45% of the annual construction expenditure has been consumed by repair and maintenance. Thus, developing cost-effective and robust techniques to mitigate cracks in concrete structures has paramount economic and sustainability implications.

Recently, the ability to endow materials such as polymers, metals, ceramics, and cementitious composites with self-healing behaviour has attracted much attention (Yıldırım *et al*., 2018; Yıldırım *et al.*, 2015; Suryanto *et al*., 2015; Liu *et al*., 2017). For instance, Gagné and Argouges (2012) found that pre-cracked cement mortars exhibited autogenous healing properties when stored in a curing room at high relative humidity. Dong *et al*., (2017) showed that the self-healing efficiency of mortar was dramatically improved by incorporating epoxy laden urea-formaldehyde microcapsules. Tittelboom *et al*., (2012) reported that blast furnace slag improved the autogenous crack sealing efficiency of mortar samples in water curing conditions. Qureshi *et al*., (2019) investigated the self-healing performance of cementitious materials added with expansive minerals. Their results showed that incorporation of expansive minerals resulted in higher self-healing capability. Suleiman *et al*., (2019) reported that the type of mineral admixture used and environmental exposure conditions play an important role in the autogenous self-healing of cracks in cement-based materials. Luo *et al*., (2015) used a spore-forming alkali-resistant bacteria solution in concrete to improve its self-healing properties. Their results showed that pre-cracked specimens incorporating a microbial self-healing solution could heal cracks of up to 0.3 mm in width.

Alkali-activated materials (AAMs), including the low-calcium aluminosilicates referred to as geopolymers are sustainable and robust contenders to replace OPC in diverse applications (Shi *et al*., 2003; Shi *et al*., 2011; Provis, 2018). They can be made using a wide range of solid aluminosilicate precursors activated by alkaline solutions (Provis and Bernal, 2014; Luukkonen *et al*., 2017). Such solid precursors are usually reclaimed industrial by-products or agricultural waste, including metallurgical slag, fly ash, and rice husk ash (Provis and Van Deventer, 2014). AAMs exhibit distinguished performance including superior resistance to acid and sulfate attacks, resistance to high temperature (Zhang *et al*., 2015; Rashad and Ouda, 2016; Rashad *et al*., 2016), immobilization of

toxic and nuclear wastes (Lancellotti *et al*., 2015; Geddes *et al*., 2018), and durability to freezing-thawing cycles (Topçu *et al*., 2018). However, numerous studies have reported that AAMs are more vulnerable to drying shrinkage than their OPC counterparts, which may trigger cracking issues (Krizan and Zivanovic, 2002; Atiş *et al*., 2009; Song *et al*., 2016). This drawback could hinder the commercial-scale deployment of AAMs. Thus, exploring self-healing mechanisms in AAMs and developing effective strategies to improve their crack self-healing efficiency is paramount.

Much effort has recently been devoted to a wide range of research on self-healing of OPC-based materials. In contrast, little is known about the self-healing potential of AAM, despite that it has been hailed as an essential part of future construction materials (Juenger *et al*., 2011; Part *et al*., 2015; Provis, 2018). Indeed, very few studies addressing the effects of various additives on the crack self-healing efficiency of AAMs could be retrieved in the open literature (Zhang *et al*., 2020).

The effects of incorporating $Ca(OH)_2$ on the engineering properties of AAMs have been reported in numerous references. For instance, Alonso *et al*. (2001) found that a highly alkaline environment favored the formation of amorphous sodium aluminosilicate gel by the activation of metakaolin in the presence of $Ca(OH)_2$ in metakaolin-based AAM systems. An increased content of $Ca(OH)_2$ within a proper range was found to promote the formation of higher amounts of C-S-H gel, favoring the evolution of higher mechanical strength and a denser binder structure overtime (Dombrowski *et al*., 2007). While there has been substantial research on the mechanical properties and microstructure of AAMs incorporating $Ca(OH)_2$, there is dearth of research efforts that have been devoted to the self-healing capability of AAMs incorporating $Ca(OH)_2$.

Therefore, this chapter investigates the effectiveness of $Ca(OH)_2$ in enhancing the autogenous crack self-healing of alkali-activated slag-based composites. To gain insight into the self-healing mechanism, mercury intrusion porosimetry (MIP), X-ray microcomputed tomography augmented with three-dimensional image analysis, and scanning electron microscopy (SEM) coupled with energy-dispersive X-ray spectroscopy

(EDX) have been deployed to quantify the pore size distribution, investigate self-healing and crack depth, and characterize the nature of potential healing products.

3.2 EXPERIMENTAL PROGRAM

3.2.1 Materials and mixture proportions

Ground granulated blast furnace slag (GGBFS) was used as the precursor along with sodium hydroxide pellets as the alkali activator. Silica sand with a specific gravity of 2.65 was used to make the mortar specimens. The chemical composition and physical properties of the slag and silica sand were determined by X-ray fluorescence and given in **Table 3-1**. The particle size distribution of the GGBFS (measured using a Malvern Panalytical particle size analyzer) and silica sand are shown in **Figure 3-1**. **Table 3-2** lists the mixture proportions. The water-to-binder ratio of all mixtures was 0.45. The GGBFS was activated through a 10 M NaOH solution. To prepare the NaOH solution, a clean volumetric flask was filled halfway with distilled water. 400g NaOH was then slowly added in the flask since this large amount of NaOH could trigger much heat, thereby causing damage to the flask. After shaking the flask for 2 min, more water was added to reach the 1.0-liter mark and upon mixing a 10 M NaOH standard solution was obtained. 840 g solution was taken out and mixed until it reached room temperature. 15 g Polyvinyl alcohol (PVA) fibers were also added to the AAM mixture to control cracking and promote self-healing. 10 g MasterGlenium 7500 superplasticizer (SP) from BASF was used to enhance workability. Two alkali-activated GGBFS mortar mixtures were modified by incorporating 7% (by GGBFS mass) of $Ca(OH)_2$, in powder form. The selection of 7% $Ca(OH)_2$ was determined based on the findings of (Yang *et al*., 2012), which indicated good development of mechanical strength. However, the incorporation of $Ca(OH)_2$ above 10% by weight relative to the precursor caused a considerable reduction of compressive strength at the long-term age (Yang *et al*., 2010), which is not proper for practical application of alkali-activated slag-based materials.

Table 3-1: Physical and chemical properties of GGBFS and silica sand

Components/property	GGBFS	Silica sand
Silicon oxide (SiO_2) (%)	33.70	99.70
Aluminum oxide (Al_2O_3) (%)	12.80	0.14
Ferric oxide (Fe_2O_3) (%)	0.96	0.016
Calcium oxide (CaO) (%)	45.40	0.01
Magnesium oxide (MgO) (%)	1.00	0.01
Specific gravity	2.90	2.65
Blaine fineness (m^2/kg)	399	--
Loss on ignition (LOI) at 1000 °C	2.72	--

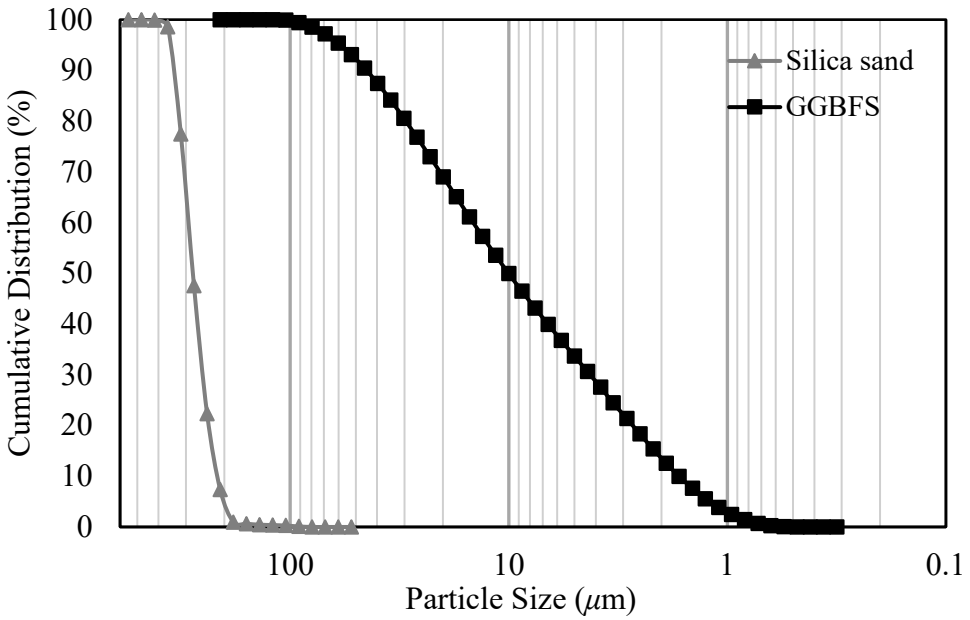

Figure 3-1: The particle size distribution of GGBFS and silica sand.

Table 3-2: Mixture design of tested mortars

Mix	Description	GGBFS	$Ca(OH)_2$	Extra Water	Silica sand	SP	Fibre
0-Slag	Control	5000 g	-	1650g	10000g	10g	15g
CH-Slag	$Ca(OH)_2$	4650g	350g	1650g	10000g	10g	15g

3.2.2 Mortar preparation

All solid ingredients were first dry mixed in a 10L-Hobart mixer for three minutes. The sodium hydroxide solution was then added, and mixing resumed for one minute at 150 rpm, followed by adding the water and SP with subsequent two minutes mixing at 250 rpm. Finally, PVA fibres were added gradually at 150 rpm mixing to achieve adequate fibre dispersion. All fresh mixtures were then cast into cylindrical molds with 100 mm diameter and 50 mm height and disk molds with 50 mm diameter and 15 mm height. Molds were vibrated for two minutes to remove any entrapped air, then covered with plastic sheets. All mortar specimens were demolded after 24 hours and then moved to a standard curing room with a relative humidity >95% and T = 19 ± 1 °C for 14 days.

3.2.3 Specimen pre-cracking and environmental exposure

All disc-shaped specimens were pre-cracked at the age of 14 days using a screw jack to introduce a single surface crack of about 50-500 μm in width. The crack width can be controlled through a calibration ruler according to the method mentioned in (Roig-Flores *et al*., 2015). Cracks were categorized into three groups with average crack width of 50-150 μm, 150-300 μm, and 300-500 μm, respectively. After pre-cracking, surface crack width was measured using a digital microscope. All specimens were submerged in de-ionized water at a constant temperature of 20 °C. The Barnstead Easypure RoDi water purification system was deployed to provide purified water for water curing.

3.2.4 Experimental procedures self-Healing tests

3.2.4.1 Electrical conductivity and ICP-OES

Previous studies (Homma *et al*., 2009; Sisomphon *et al*., 2012; Huang *et al*., 2013; Stuckrath *et al*., 2014; Huang *et al*., 2015; Jiang *et al*., 2015) reported that calcium ions dissolved from the cementitious matrix and the pH value of the curing environment were highly related to the formation of self-healing products. In this study, a Vista Pro Inductively Coupled Plasma Optical Emission Spectroscopy (ICP-OES) was used to measure the concentration of calcium ions. Two 14 day-cured cylindrical specimens from each mixture were half-broken, followed by immersion in an equal amount of deionized

water. The pH value and electrical conductivity of the solution were measured using a Fisherbrand™ accumet™ AB200 pH/Conductivity Benchtop Meter.

3.2.4.2 Mercury Intrusion Porosimetry (MIP)

The samples for MIP testing were extracted from test specimens for each mixture using an electrical jigsaw, without creating additional cracks that could affect the measured porosity. To preserve the pore structure, fragments from cracked specimens were first immersed in an isopropanol solvent exchange for two days to remove water, followed by drying at 50°C until reaching constant mass (Shi, 2016). The pore size distribution was then analyzed using a Micrometrics AutoPore IV 9520 Series mercury intrusion porosimeter, assuming a contact angle of 140o, surface tension of 0.48 N/m and an applied pressure ranging from 0 to 414 MPa (Kaufmann, 2010) at 25°C, as per ASTM D4404 (2004).

3.2.4.3 Microscopic observation

Crack closure in the disc-shaped specimens was monitored using a Jiusion digital microscope to evaluate surface self-healing efficiency (Park and Choi, 2018). Three random locations were measured for each specimen. The crack closure ratio (Qiu *et al*., 2016), as defined by **Eq. 3-1**, was calculated:

$$CCR(\%) = (w_0 - w_t)/w_0 \qquad \text{Eq. 3-1}$$

where; *CCR* = crack closure ratio; w_0 = initial crack width; and w_t = crack width after curing at time *t*.

3.2.4.4 X-ray microcomputed tomography

The healing of internal cracks was investigated using a Nikon XT H 225 ST X-ray microcomputed tomography (μCT) scanner. A series of sequential high-resolution 2D X-ray images were captured and then reconstructed to generate a 3D volumetric representation of the object via a 3D rendering software (Dragonfly 4.0). This software refines the analysis and characterization of material samples to assist in understanding the

structures and physical properties of different materials. The resolution was 56μ voxel size in the 3-D image. The parameters were set as follows: 225 kV, 130 μA, 29.3 watts; 1 panel gain = 24; 3142 projections; 150 frames/projection on shading correction; 2.5 mm Cu filter; 55 min scanning.

3.2.4.5 SEM coupled with energy-dispersive X-ray spectroscopy (EDS)

The small disc-shaped specimens were dried in a desiccator for a week, followed by surface gold-coating. A Hitachi SU3500 Field-Emission SEM operated at a voltage of 20.0 kV was employed to analyze the morphology near the mouth of cracks. To determine the elemental composition of the self-healing products, EDX was also used via a Quantax 400 software.

3.3 EXPERIMENTAL RESULTS AND DISCUSSION

3.3.1 CCR analysis and ICP-OES results

Surface cracks of specimens, before and after water submersion, were examined via a digital microscope. Binary images were obtained using OriginPro 8.5 via its image processing function. For the control specimens (0-Slag), the change in surface crack width was inconspicuous; however, self-healing products having a crystal-like material form sprouting from both sides of the crack were found in the typical pre-cracked CH-Slag specimens.

The surface crack width reduction was used as an indicator to quantitatively evaluate self-healing capacity. The surface crack width was observed after 4, 8, 16, and 32 days of curing. **Figure 3-2** plots the reduction of surface cracks of specimens submerged in water. A 45-degree reference line was marked to represent zero self-healing, and a complete self-healing is achieved if the dots are on the X-axis. It can be observed in **Figure 3-2 (a)** that CH-Slag cracks with initial width ranging from 50 μm to 100 μm exhibited the highest reduction within 32 days. However, cracks with larger width achieved partial healing with residual crack width. Slight downward movement of each dot was observed (**Figure 3-2 (b)**), indicating that the self-healing capacity in 0-Slag specimens was comparatively lower. **Figure 3-3** illustrates a typical relationship between

the crack closure ratio and the initial crack width. To quantify the degree of crack closure versus initial crack width, the crack closure ratio at a certain crack width was obtained using a non-linear fitting curve. Cracks with smaller initial width achieved higher crack closure. From **Figure 3-3**, the crack closure ratio dropped sharply when the initial crack width increased from 50 μm to 100 μm, followed by a gradual decrease with further increasing the width.

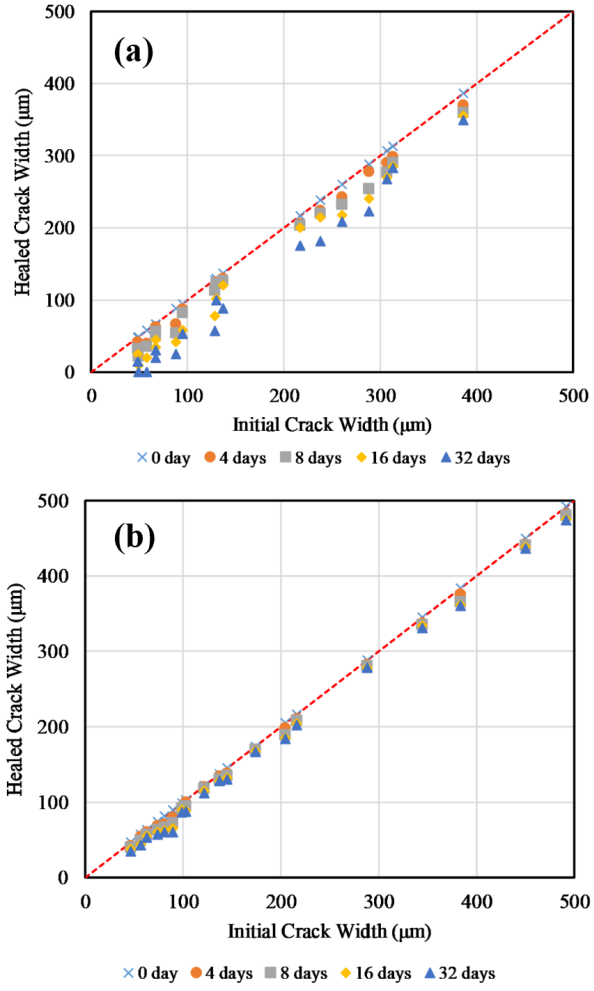

Figure 3-2：Crack width reduction of (a) CH-Slag, and (b) 0-Slag specimens.

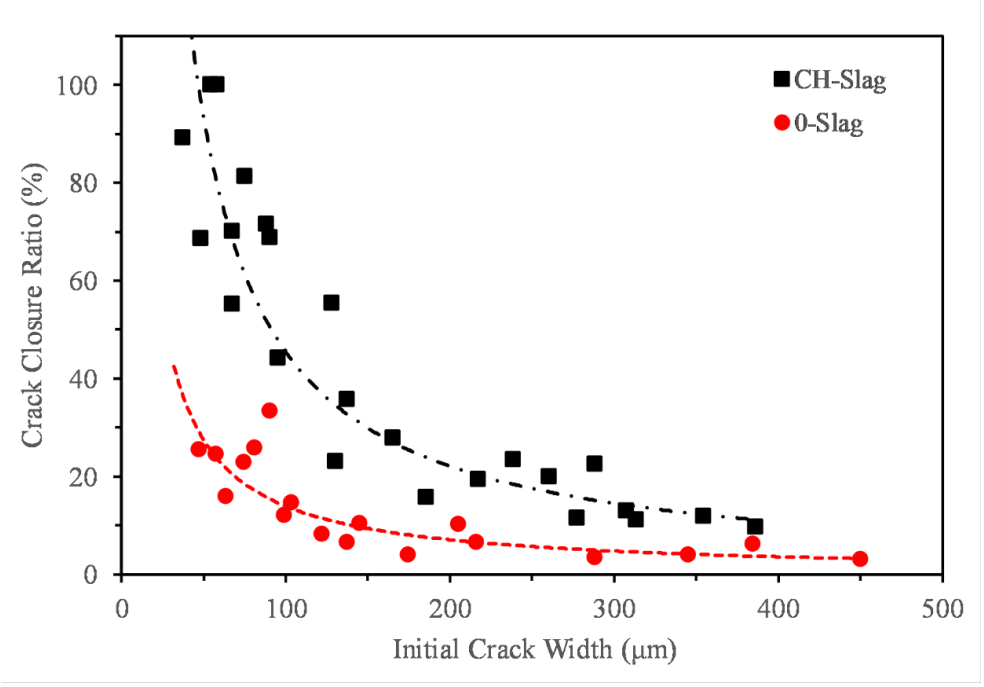

Figure 3-3: Typical relationship between crack width and crack closure ratio at a certain initial crack width in CH-Slag and 0-Slag specimens.

The self-healing behaviour of 0-Slag and CH-Slag specimens can be explained by ICP-OES test results. As shown in **Table 3-3**, mixture CH-Slag had larger Ca^{2+} dissolution compared to that of mixture 0-Slag. It was observed that the higher the concentration of Ca^{2+} leached from the specimen, the higher was its self-healing capability. This is consistent with studies by Suleiman *et al.* (2019) and Sisomphon *et al.* (2012) that leached Ca^{2+} from the matrix would promote autogenous self-healing via calcium carbonate precipitation. The higher Ca^{2+} concentration can be explained by the incorporation of $Ca(OH)_2$. $Ca(OH)_2$ had not been much consumed due to the low solubility of $Ca(OH)_2$ at the high pH level before the occurrence of cracking, implying that it remained largely unaffected by the reaction process (Provis, 2014). Therefore, when geopolymerization stabilized after the activation of NaOH, $Ca(OH)_2$ dissolved in the curing water, thereby increasing the Ca^{2+} concentration. The self-healing also depends on the availability of moisture, time, chemistry of the pore solution, width of original crack, kinetics of nucleation and growth of healing compounds, and other parameters (Qiu *et al.*, 2016; Luo *et al.*, 2015). Therefore, in this study, the limitation of

self-healing could not be directly related to a specific parameter such as the depletion of $Ca(OH)_2$.

Table 3-3: Calcium concentrations in water after 16 days submersion

Mix	Ca^{2+} concentration (mg/L)
CH-Slag	3.164
0-Slag	0.956

3.3.2 MIP results and pore structure analyses

The pore structure development was investigated using MIP. The cumulative mercury intrusion curves of water submerged CH-Slag and 0-Slag specimens measured at ages of 14, 21, 28, and 60 days are shown in **Figure 3-4**. Both types of specimens continued to achieve pore volume reduction and pore size refinement with longer curing time, leading to microstructural densification, with CH-Slag specimens achieving better performance than 0-Slag specimens. For instance, the cumulative volume of capillary pores with diameter ranging from 0.03 to 0.2 μm decreased by nearly 37% and 23% after two months in CH-Slag and 0-Slag specimens, respectively. Also, CH-Slag specimens showed more reduction in pore volume with diameters ranging from 0.4 to 0.8 μm during 32 days of water submersion (**Figure 3-5 (a)**) after cracking compared to that of 0-Slag specimens. **Figure 3-5 (b)** illustrates the corresponding logarithmic differential intruded pore volume versus pore diameter for the two specimens. Generally, there were two main peaks in the two logarithmic differential curves, representing two pore systems: gel pores and capillary pores (Aligizki, 2005; Guo *et al*., 2013). Gel pores are generated by the formation of calcium aluminosilicate hydrates (C-A-S-H) and have pore size diameter ranging from 0.5 nm to 0.01 μm (Ma *et al*., 2013). Capillary pores are formed in the space not filled by hydration products, and their pore size diameter typically ranges from 0.01 μm to 10 μm (Neville, 1995; Dong *et al*., 2017). As shown in **Figure 3-5 (b)**, the two peaks of pore size for CH-Slag specimens were ahead of that of 0-Slag specimens, indicating that CH-Slag exhibited more reduction in porosity and refinement in pore size distribution compared to that of 0-Slag.

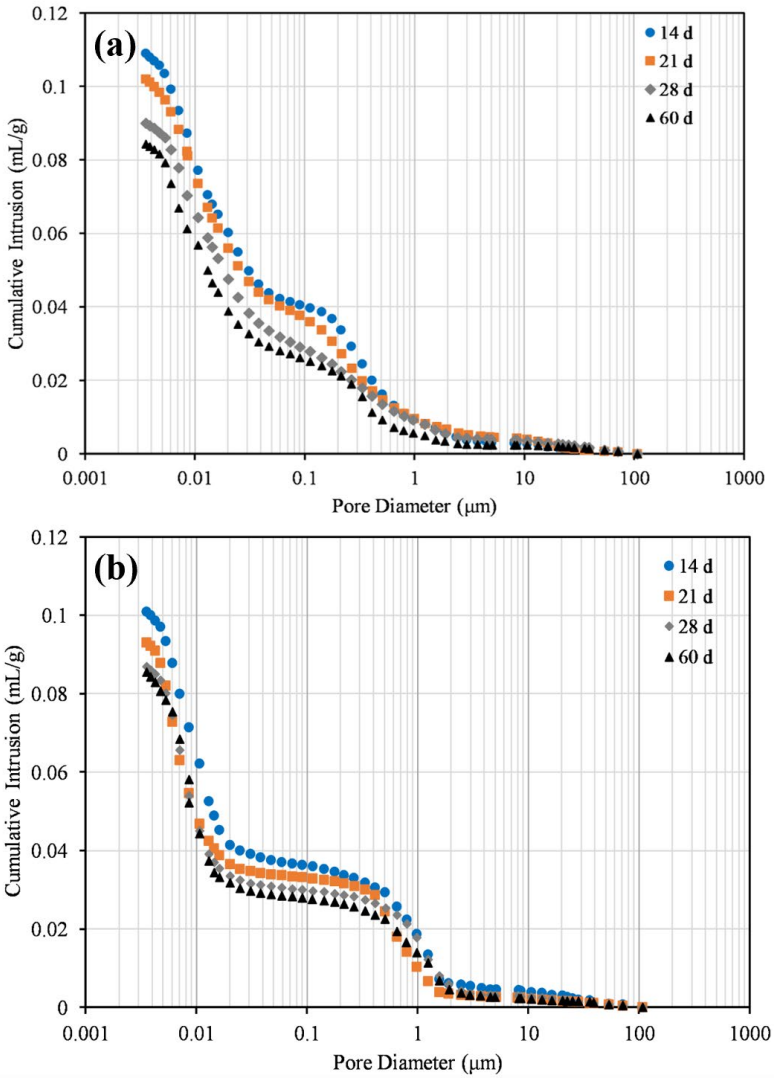

Figure 3-4: Cumulative intruded pore volume vs. pore diameter for cracked specimens: (a) CH-Slag, and (b) 0-Slag specimens.

The reduction in pore volume and refinement of pore size can be attributed to the combined effects of ongoing hydration (Tang *et al*., 2019) and carbonation of $Ca(OH)_2$ (Soja *et al*., 2018). The additional solid volume produced by these synergistic effects filled space in the pore structure, resulting in a reduction of pore volume and refinement of pore structure (Shah *et al*., 2018). As compared with 0-Slag specimens in **Figure 3-5**, more reduction in porosity was observed in CH-Slag specimens, which provides evidence that the incorporation of $Ca(OH)_2$ could act as a trigger for enhancing the refinement of the pore structure of the alkali-activated slag-based composites. This hypothesis can be

further explained by the ICP-OES results. The higher concentration of Ca^{2+} released from CH-Slag specimens was much higher than that from 0-Slag specimens, likely due to the incorporation of $Ca(OH)_2$, which can play a significant role in the carbonation, thereby promoting both self-healing and pore refinement.

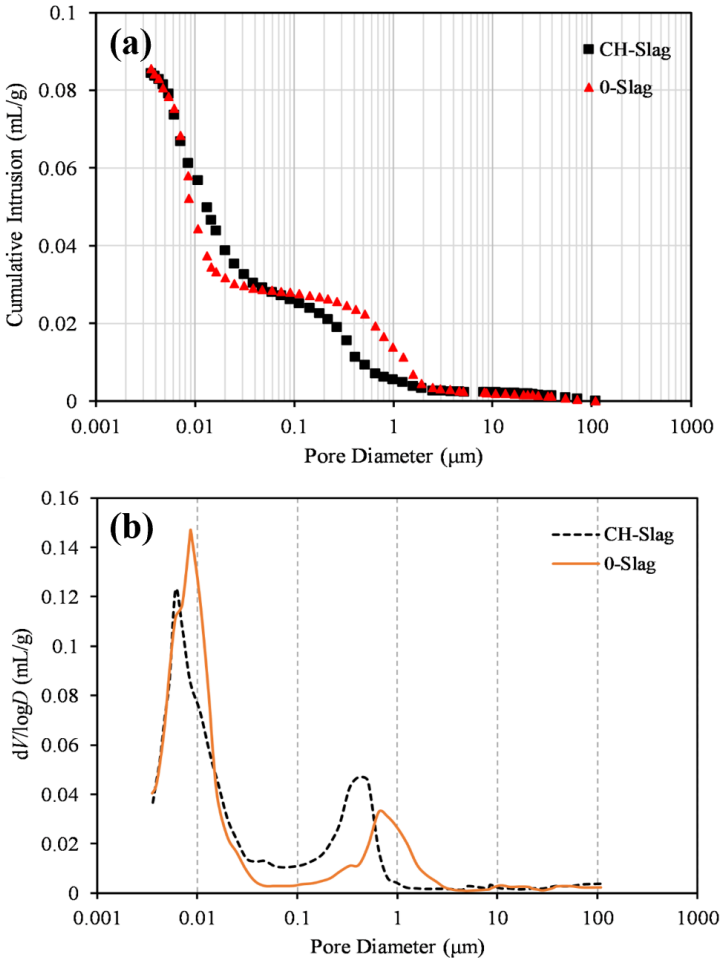

Figure 3-5: Pore size distribution of CH-Slag and 0-Slag at the age of 60 days: (a) cumulative intruded pore volume vs. pore diameter, and (b) logarithmic differential intrusion vs. pore diameter.

3.3.3 SEM analyses

SEM micrographs of self-healing compounds in water-submerged CH-Slag and 0-Slag specimens are shown in **Figure 3-6**. Cubic and prismatic shapes formed in the crack of the CH-Slag specimen. EDS results in **Table 3-4** show that those crystals were composed

of three main elements, namely, C, Ca, and O, indicating the existence of calcium carbonate. **Figure 3-6 (b)** shows that irregular crystals occupied the surface of the crack in the 0-Slag specimen with EDS results in **Table 3-3**, indicating sharp peaks of calcium, oxygen, and carbon. Interestingly, a small amount of silicon and aluminum was determined, indicating that some C-A-S-H may exist in the crack as the reaction product of alkali-activation of the slag. In both types of mixtures, the calcium, oxygen, and carbon contents were predominant, indicating that calcium carbonate was the main self-healing product in both CH-Slag and 0-Slag specimens. This is consistent with the observation of Nguyễn *et al*. (2018) that calcium carbonate was the primary self-healing material for alkali-activated slag composite due to abundant Ca^{2+} leaching from the matrix and diffusion of carbonates.

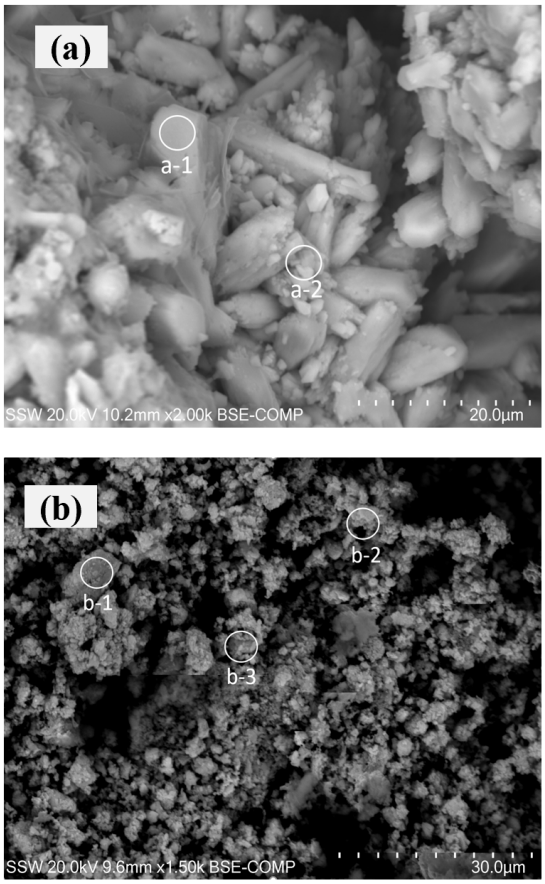

Figure 3-6: SEM images with EDS pattern of products within the cracks of (a) CH-Slag, and (b) 0-Slag specimens.

Table 3-4: Chemical compositions of healing materials of CH-Slag and 0-Slag

Position	Element composition (%)					
	C	O	Mg	Al	Si	Ca
a-1	14.31	51.60	0.29	0.19	0.21	32.2
a-2	13.24	49.53	0.10	0.41	0.13	36.0
b-1	18.8	54.35	0.12	0.71	0.71	25.32
b-2	17.09	52.52	0.09	0.82	0.72	28.76
b-3	19.12	54.06	0.15	0.93	1.1	24.64

3.3.4 Electrical conductivity and pH values

Figure 3-7 shows the electrical conductivity and pH values of water in which specimens were submerged at ages of 2, 4, 8, 16, and 32 days. For both types of specimens, the electrical conductivity and pH values increased over the curing period. Electrical conductivity was primarily related to the concentration of total dissolved ions in the curing water, while pH values were dependent on the number of hydroxyl ions leaching from the matrix. CH-Slag curing water had higher pH values and electrical conductivity at all curing periods, indicating that more Ca^{2+} ions were leached and dissolved in water, which agrees with results in **Table 3-3**. Higher pH value generally promotes the precipitation of calcium carbonate (Sisomphon *et al*., 2012; Wang *et al*., 2014). According to **Eq. 3-2**, carbonic acid (H_2CO_3) derived from the dissolution of carbon dioxide (CO_2) reacts with hydroxyl ions to produce carbonate ions. Higher pH shifts carbonate acid equilibrium, resulting in the formation of more carbonate ions (Achal and Mukherjee, 2015). The formation of calcium carbonate dependent on the pH value can be described by **Eq. 3-3**:

$$2OH^- + H_2CO_3 \leftrightarrow CO_3^{2-} + 2H_2O \qquad \text{Eq. 2}$$

$$Ca^{2+} + CO_3^{2-} \rightarrow CaCO_3 \ (pH_{water} > 8) \qquad \text{Eq. 3}$$

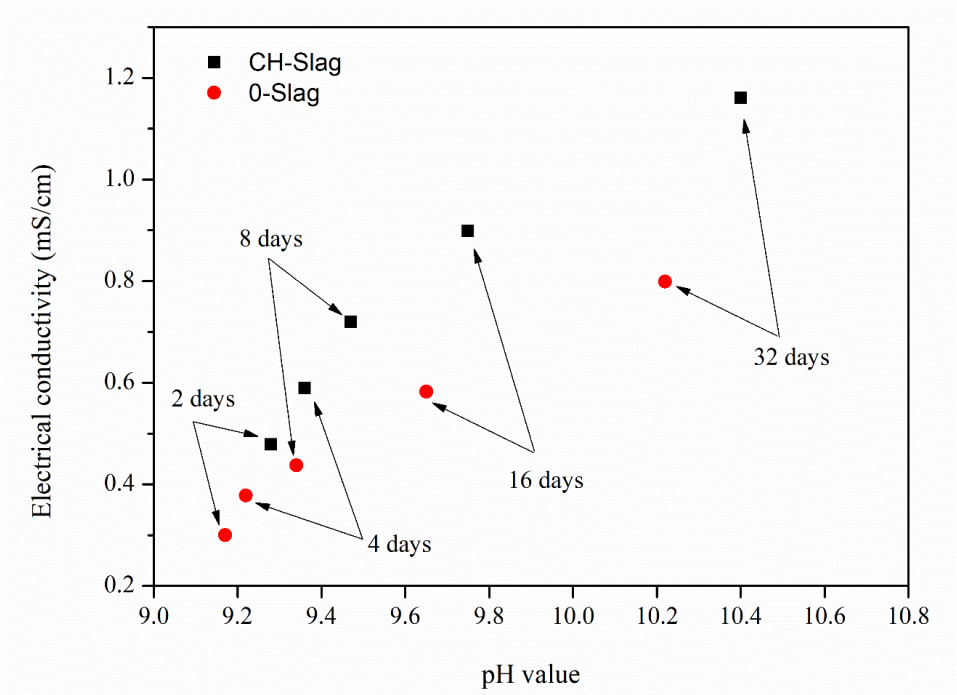

Figure 3-7: Electrical conductivity vs. pH of water for the submerged specimens.

3.3.5 X-ray computed tomography

X-ray μCT data can provide a detailed visualization of self-healing as a function of crack depth via 3D reconstruction analysis. **Figure 3-8** illustrates X-ray tomography images of CH-Slag specimens after two months of water submersion. Only CH-Slag specimens with crack width ranging from 50 to 150 μm were chosen for X-ray μCT analysis since they exhibited noticeable self-healing through visual observation. To better understand the internal self-healing condition of the specimen, various densities of the specimen were distinguished by yellow, orange, and red colors to depict the denser parts, while the porosity and crack were colored in black. The Z-axis sectional 2D image and the 3D images from X-axis sectional view in **Figure 3-8** show that the crack near the surface was almost completely healed. In contrast, the crack close to the specimen center remained unchanged, suggesting that no significant self-healing occurred.

This phenomenon can be primarily attributed to the precipitation of calcium carbonate on the surface of the crack, preventing the diffusion of carbonate ions (CO_3^{2-}) from forming the self-healing material in the interior of the crack (Wang *et al.*, 2018). The

concentration of CO_3^{2-} on the surface of cracks would be much higher than that deeper in the crack (Li *et al*., 2018). Previous studies revealed similar results in cementitious composites incorporating different minerals. For instance, Suleiman *et al*. (2019) investigated the self-healing efficiency of cement-based materials, which was promoted by adding metakaolin, bentonite, and calcium carbonate micro-filler in two environmental exposures. X-ray μCT analysis showed that self-healing product was mostly localized at the crack mouth. Similarly, Wang *et al*. (2014) used encapsulated bacterial spores for enhancing self-healing capability of the concrete specimens. Their results showed that precipitation of calcium carbonate was mainly restricted to surface cracks.

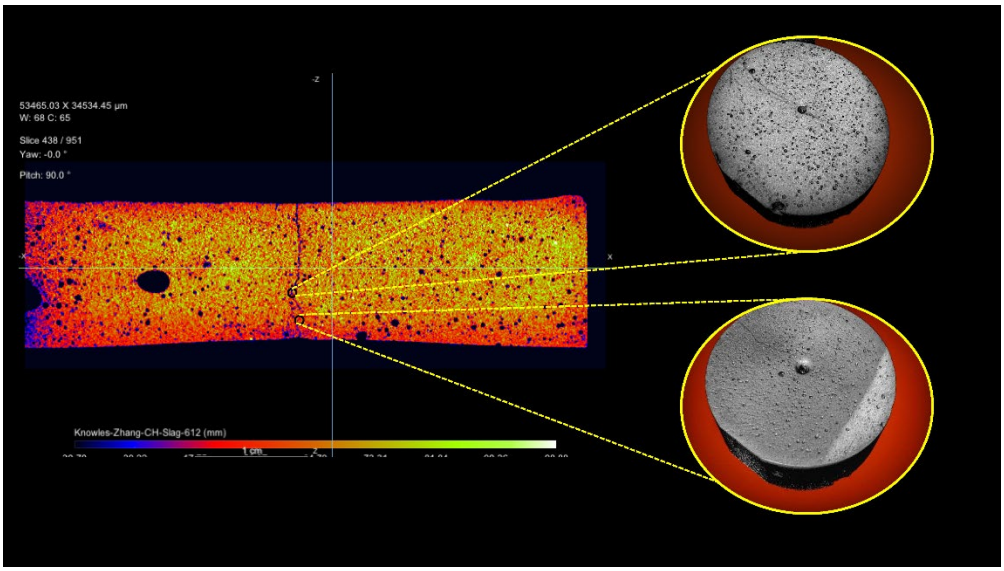

Figure 3-8: X-ray μCT scanning images showing cracks at different positions.

3.3.6 Self-healing mechanism in AAM incorporating calcium hydroxide

Based on the results corroborated by different tests in the present study, the mechanism of crack closing in the alkali-activated slag composite incorporating $Ca(OH)_2$ was schematically illustrated in **Figure 3-9**. When the alkali-activated slag mortar specimen is submerged in water, the dissolvable Ca^{2+} ions are gradually leached from the matrix. By incorporating $Ca(OH)_2$, the Ca^{2+} concentration increases significantly. CO_2 from the atmosphere dissolves in the curing water and transfers into H_2CO_3; however, H_2CO_3 is

unstable and easily converts to CO_3^{2-} and HCO_3^-. The decomposition of H_2CO_3 accelerates due to the alkaline environment. Calcium carbonate is then formed near the surface of the crack, preventing the further diffusion of CO_3^{2-} to the interior of crack. Consequently, the majority of calcium carbonate precipitation occurs at the crack surface, while little precipitation can be observed in the interior crack (Wang *et al*., 2018).

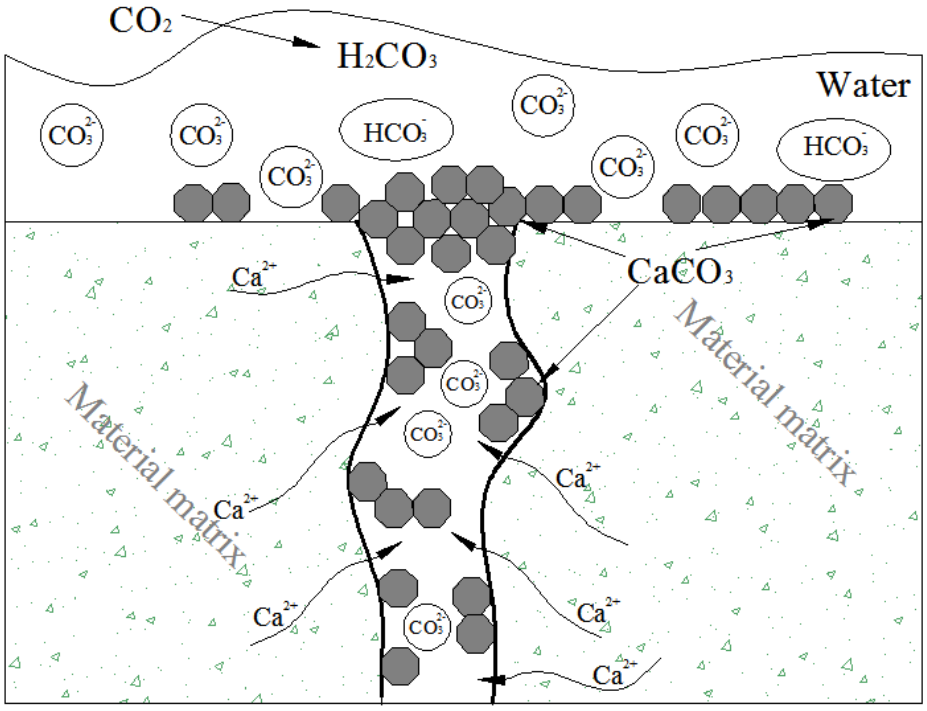

Figure 3-9: Schematic illustration of the self-healing mechanism of alkali-activated slag-based composites.

3.4 CONCLUSIONS

In the present study, the potential of using $Ca(OH)_2$ to enhance the self-healing capability of cracks in alkali-activated slag-based mortars was explored using a portfolio of testing methods. Based on the experimental results, the following conclusions can be drawn:

1) The crack self-healing ability of the alkali-activated slag composites cured by water submersion can be considerably improved by incorporating $Ca(OH)_2$.
2) The crack sealing ratio was affected by the initial crack width. The larger the crack, the lower was the crack sealing ratio.

3) MIP results showed that incorporation of $Ca(OH)_2$ in the alkali-activated slag-based composite system contributed to reducing porosity and refining the pore size, resulting in microstructural densification.
4) The primary self-healing product formed in the cracks was $CaCO_3$.
5) X-ray μCT coupled with three-dimensional image analysis showed that the self-healing product was mainly restricted to the surface of the crack.
6) The insights into the investigations of self-healing efficiency in AAMs with additives provided by this research extend our knowledge of understanding the behaviour of AAMs.

3.5 REFERENCES

Aligizaki, K. K. (2005). *Pore structure of cement-based materials: testing, interpretation and requirements*: CRC Press.

Arbi, K., Nedeljković, M., Zuo, Y., and Ye, G. (2016). A review on the durability of alkali-activated fly ash/slag systems: advances, issues, and perspectives. *Industrial and Engineering Chemistry Research, 55*(19), 5439-5453.

Atiş, C. D., Bilim, C., Çelik, Ö., and Karahan, O. (2009). Influence of activator on the strength and drying shrinkage of alkali-activated slag mortar. *Construction and Building Materials, 23*(1), 548-555.

D, A. (2004). Standard test for determination of pore volume distribution of soil and rock by MIP: ASTM International.

Dong, B., Fang, G., Wang, Y., Liu, Y., Hong, S., Zhang, J., Lin, S., and Xing, F. (2017). Performance recovery concerning the permeability of concrete by means of a microcapsule based self-healing system. *Cement and Concrete Composites, 78*, 84-96.

Dong, H., Gao, P., and Ye, G. (2017). Characterization and comparison of capillary pore structures of digital cement pastes. *Materials and Structures, 50*(2), 154.

Gagné, R., and Argouges, M. (2012). A study of the natural self-healing of mortars using air-flow measurements. *Materials and Structures, 45*(11), 1625-1638.

Geddes, D., Ke, X., Bernal, S., Hayes, M., and Provis, J. (2018). Metakaolin-Based Geopolymers for Nuclear Waste Encapsulation *Calcined Clays for Sustainable Concrete* (pp. 183-188): Springer.

Guo, Y., Qian, J., and Wang, X. (2013). Pore structure and influence of recycled aggregate concrete on drying shrinkage. *Mathematical Problems in Engineering, 2013*.

Hager, M. D., Greil, P., Leyens, C., van der Zwaag, S., and Schubert, U. S. (2010). Self-healing materials. *Advanced Materials, 22*(47), 5424-5430.

Homma, D., Mihashi, H., and Nishiwaki, T. (2009). Self-healing capability of fibre reinforced cementitious composites. *Journal of Advanced Concrete Technology, 7*(2), 217-228.

Huang, H., and Ye, G. (2015). Self-healing of cracks in cement paste affected by additional Ca2+ ions in the healing agent. *Journal of Intelligent Material Systems and Structures, 26*(3), 309-320.

Huang, H., Ye, G., and Damidot, D. (2013). Characterization and quantification of self-healing behaviors of microcracks due to further hydration in cement paste. *Cement and Concrete Research, 52*, 71-81.

Jiang, Z., Li, W., and Yuan, Z. (2015). Influence of mineral additives and environmental conditions on the self-healing capabilities of cementitious materials. *Cement and Concrete Composites, 57*, 116-127.

Juenger, M., Winnefeld, F., Provis, J. L., and Ideker, J. (2011). Advances in alternative cementitious binders. *Cement and Concrete Research, 41*(12), 1232-1243.

Kaufmann, J. (2010). Pore space analysis of cement-based materials by combined Nitrogen sorption–Wood's metal impregnation and multi-cycle mercury intrusion. *Cement and Concrete Composites, 32*(7), 514-522.

Krizan, D., and Zivanovic, B. (2002). Effects of dosage and modulus of water glass on early hydration of alkali–slag cements. *Cement and Concrete Research, 32*(8), 1181-1188.

Lagerblad, B. (2005). Carbon dioxide uptake during concrete life cycle–state of the art. *Swedish Cement and Concrete Research Institute CBI, Stockholm*.

Lancellotti, I., Barbieri, L., and Leonelli, C. (2015). Use of alkali-activated concrete binders for toxic waste immobilization *Handbook of Alkali-Activated Cements, Mortars and Concretes* (pp. 539-554): Elsevier.

Li, W., Dong, B., Yang, Z., Xu, J., Chen, Q., Li, H., Xing, F, and Jiang, Z. (2018). Recent advances in intrinsic self-healing cementitious materials. *Advanced Materials, 30*(17), 1705679.

Liu, H., Zhang, Q., Gu, C., Su, H., and Li, V. (2017). Influence of microcrack self-healing behavior on the permeability of Engineered Cementitious Composites. *Cement and Concrete Composites, 82*, 14-22.

Luo, M., Qian, C.-x., and Li, R.-y. (2015). Factors affecting crack repairing capacity of bacteria-based self-healing concrete. *Construction and Building Materials, 87*, 1-7.

Luukkonen, T., Abdollahnejad, Z., Yliniemi, J., Kinnunen, P., and Illikainen, M. (2017). One-part alkali-activated materials: A review. *Cement and Concrete Research*, 103, 21-34.

Ma, Y., Hu, J., and Ye, G. (2013). The pore structure and permeability of alkali activated fly ash. *Fuel, 104*, 771-780.

Mellado, A., Pérez-Ramos, M. I., Monzó, J., Borrachero, M. V., and Payá, J. (2017). Resistance to acid attack of alkali-activated binders: simple new techniques to measure susceptibility. *Construction and Building Materials, 150*, 355-366.

Neville, A. M. (1995). *Properties of concrete* (Vol. 4): longman London.

Nguyễn, H. H., Choi, J.-I., Song, K.-I., Song, J.-K., Huh, J., and Lee, B. Y. (2018). Self-healing properties of cement-based and alkali-activated slag-based fiber-reinforced composites. *Construction and Building Materials, 165*, 801-811.

Pacheco-Torgal, F., Abdollahnejad, Z., Miraldo, S., Baklouti, S., and Ding, Y. (2012). An overview on the potential of geopolymers for concrete infrastructure rehabilitation. *Construction and Building Materials, 36*, 1053-1058.

Park, B., and Choi, Y. C. (2018a). Quantitative evaluation of crack self-healing in cement-based materials by absorption test. *Construction and Building Materials, 184*, 1-10.

Park, B., and Choi, Y. C. (2018b). Self-healing capability of cementitious materials with crystalline admixtures and super absorbent polymers (SAPs). *Construction and Building Materials, 189*, 1054-1066.

Part, W. K., Ramli, M., and Cheah, C. B. (2015). An overview on the influence of various factors on the properties of geopolymer concrete derived from industrial by-products. *Construction and Building Materials, 77*, 370-395.

Provis, J., and Van Deventer, J. (2014). Alkali Activated Materials: State-of-the-Art Report, RILEM TC.

Provis, J. L. (2014). *Alkali Activated Materials: State-of-the-art-Report*. Dordrecht: Springer.

Provis, J. L. (2018). Alkali-activated materials. *Cement and Concrete Research, 114*, 40-48.

Provis, J. L., and Bernal, S. A. (2014). Geopolymers and related alkali-activated materials. *Annual Review of Materials Research, 44*, 299-327.

Qiu, J., Tan, H. S., and Yang, E.-H. (2016). Coupled effects of crack width, slag content, and conditioning alkalinity on autogenous healing of engineered cementitious composites. *Cement and Concrete Composites, 73*, 203-212.

Qureshi, T., Kanellopoulos, A., and Al-Tabbaa, A. (2019). Autogenous self-healing of cement with expansive minerals-II: Impact of age and the role of optimised expansive minerals in healing performance. *Construction and Building Materials, 194*, 266-275.

Rashad, A. M., and Ouda, A. S. (2016). An investigation on alkali-activated fly ash pastes modified with quartz powder subjected to elevated temperatures. *Construction and Building Materials, 122*, 417-425.

Rashad, A. M., Zeedan, S. R., and Hassan, A. A. (2016). Influence of the activator concentration of sodium silicate on the thermal properties of alkali-activated slag pastes. *Construction and Building Materials, 102*, 811-820.

Roig-Flores, M., Moscato, S., Serna, P., and Ferrara, L. (2015). Self-healing capability of concrete with crystalline admixtures in different environments. *Construction and Building Materials, 86*, 1-11.

Shah, V., Scrivener, K., Bhattacharjee, B., and Bishnoi, S. (2018). Changes in microstructure characteristics of cement paste on carbonation. *Cement and Concrete Research, 109*, 184-197.

Shi, C., Jiménez, A. F., and Palomo, A. (2011). New cements for the 21st century: The pursuit of an alternative to Portland cement. *Cement and Concrete Research, 41*(7), 750-763.

Shi, C., Roy, D., and Krivenko, P. (2003). *Alkali-activated cements and concretes*: CRC press.

Shi, Z. (2016). Durability of Portland Cement–Calcined Clay–Limestone Blends.

Sisomphon, K., Copuroglu, O., and Koenders, E. (2012). Self-healing of surface cracks in mortars with expansive additive and crystalline additive. *Cement and Concrete Composites, 34*(4), 566-574.

Soja, W., Maraghechi, H., Georget, F., and Scrivener, K. (2018). *Changes of microstructure and diffusivity in blended cement pastes exposed to natural carbonation.* Paper presented at the MATEC Web of Conferences.

Song, C., Choi, Y. C., and Choi, S. (2016). Effect of internal curing by superabsorbent polymers–internal relative humidity and autogenous shrinkage of alkali-activated slag mortars. *Construction and Building Materials, 123*, 198-206.

Stuckrath, C., Serpell, R., Valenzuela, L. M., and Lopez, M. (2014). Quantification of chemical and biological calcium carbonate precipitation: performance of self-

healing in reinforced mortar containing chemical admixtures. *Cement and Concrete Composites, 50*, 10-15.

Suleiman, A., and Nehdi, M. (2018). Effect of environmental exposure on autogenous self-healing of cracked cement-based materials. *Cement and Concrete Research*, 111, 197-208.

Suleiman, A. R., Nelson, A. J., and Nehdi, M. L. (2019). Visualization and quantification of crack self-healing in cement-based materials incorporating different minerals. *Cement and Concrete Composites, 103*, 49-58.

Suryanto, B., Wilson, S. A., McCarter, W. J., and Chrisp, T. M. (2015). Self-healing performance of engineered cementitious composites under natural environmental exposure. *Advances in Cement Research, 28*(4), 211-220.

Tahri, W., Abdollahnejad, Z., Pacheco-Torgal, F., and Aguiar, J. (2016). Performance on an Alkali-Activated Cement-Based Binder (AACB) for Coating of an OPC Infrastructure Exposed to Chemical Attack: A Case Study. *Handbook of Low Carbon Concrete*, 335.

Van Breugel, K. (2007). *Is there a market for self-healing cement-based materials.* Paper presented at the Proceedings of the first international conference on self-healing materials.

Van Tittelboom, K., Gruyaert, E., Rahier, H., and De Belie, N. (2012). Influence of mix composition on the extent of autogenous crack healing by continued hydration or calcium carbonate formation. *Construction and Building Materials, 37*, 349-359.

Wang, J., Soens, H., Verstraete, W., and De Belie, N. (2014). Self-healing concrete by use of microencapsulated bacterial spores. *Cement and Concrete Research, 56*, 139-152.

Wang, X., Fang, C., Li, D., Han, N., and Xing, F. (2018). A self-healing cementitious composite with mineral admixtures and built-in carbonate. *Cement and Concrete Composites, 92*, 216-229.

Xueqian, Y., Lin, L., Haoyu, D., and Sainan, Q. (2018). *Changes in Pore Characteristics of Alkali-activated Slag Paste after Freeze-thaw Cycles.* Paper presented at the IOP Conference Series: Materials Science and Engineering.

Yıldırım, G., Keskin, Ö. K., Keskin, S. B., Şahmaran, M., and Lachemi, M. (2015). A review of intrinsic self-healing capability of engineered cementitious composites: Recovery of transport and mechanical properties. *Construction and Building Materials, 101*, 10-21.

Yıldırım, G., Khiavi, A. H., Yeşilmen, S., and Şahmaran, M. (2018). Self-healing performance of aged cementitious composites. *Cement and Concrete Composites, 87*, 172-186.

Yıldırım, G., Şahmaran, M., and Anıl, Ö. (2018). *Determination of Self-Healing Performance of Cementitious Composites Under Elevated CO2 Concentration by Resonant Frequency and Crack Opening Measurements.* Paper presented at the Proceedings of 3rd International Sustainable Buildings Symposium (ISBS 2017).

Zhang, Z., Provis, J. L., Reid, A., and Wang, H. (2015). Mechanical, thermal insulation, thermal resistance and acoustic absorption properties of geopolymer foam concrete. *Cement and Concrete Composites, 62*, 97-105.

Zhu, H., Zhang, Z., Zhu, Y., and Tian, L. (2014). Durability of alkali-activated fly ash concrete: chloride penetration in pastes and mortars. *Construction and Building Materials, 65*, 51-59.

Chapter 4

4 SELF-HEALING IN FIBRE-REINFORCED ALKALI-ACTIVATED SLAG COMPOSITES INCORPORATING DIFFERENT ADDITIVES[2]

This chapter deploys a wide array of experimental techniques to investigate the self-healing properties of PVA fibre-reinforced alkali-activated slag-based composites incorporating crystalline additives (CA) and bentonite minerals (BN). X-ray microcomputed tomography (μCT) with three-dimensional image segmentation and analysis, scanning electron microscopy with energy dispersive X-ray (SEM-EDS) analysis, inductively coupled plasma optical emission spectroscopy (ICP-OES), optical microscopy, and water sorptivity measurements were used to visualize, quantify, and identify the nature of healing compounds. While specimens incorporating CA exhibited significant self-healing, less self-healing was observed in specimens incorporating bentonite. X-ray μCT results indicated that the healing mechanism mainly occurred at surface of cracks and calcium carbonate was the prevalent self-healing product formed. It was found that rising the pH and concentration of calcium ions of the curing medium and using polyvinyl alcohol (PVA) fibres in the mixture acted synergistically to accelerate crack self-healing in alkali-activated slag composites.

4.1 INTRODUCTION

Owing to its versatility, concrete has gained worldwide recognition, becoming the most widely used material after water (Ding *et al*., 2016; Juenger *et al*., 2011). Yet, concrete is susceptible to various sources of cracking due to diverse mechanisms (Li *et al*., 2018). The occurrence of cracks compromises the durability and integrity of reinforced concrete structures since cracks provide an open path for moisture and aggressive substances including carbon dioxide, sulfates, and chloride ions to ingress into the cementitious matrix and initiate degradation such as reinforcing steel corrosion, sulfate attack, alkali-

[2] A version of this chapter was published in the *Construction and Building Materials (2020)*

aggregate reactions, and damage by freezing and thawing cycles (Suleiman *et al*., 2019). While conventional crack repair techniques such as epoxy injection can mitigate risks associated with cracks, such practice is often laborious and costly, and maybe impractical in hard to access areas or when cracks are not visible. For instance, in the US, it is estimated that over $1.6 trillion will be needed by 2021 for 27% of the highway concrete bridges in need of maintenance and retrofitting (Tahri *et al*., 2016). Therefore, if self-healing behaviour inherent to concrete structures can become an autonomous feature, the associated economic and sustainability benefits can be immense.

Biological systems such as animal organs can self-heal wounds and restore their original functionality upon damage (Chen *et al*., 2016). Inspired by nature to solve engineering problems, scientists devoted much effort to a variety of research on self-healing from macromolecular compounds (Ma *et al*., 2019) to electronic materials (Markvicka *et al*., 2018) and metals (Ferguson *et al*., 2014). Self-healing was also found in cementitious materials and can be divided into autogenous healing and autonomous healing (Wu *et al*., 2012). Autogenous healing can be defined as an inherent ability to seal cracks automatically without any intervention, for instance via carbonation of $Ca(OH)_2$ and formation of $CaCO_3$, hydration of unreacted cement and other cementitious materials, and swelling of hydrated cementitious products (C-S-H) (Reinhardt *et al*., 2013). For instance, Suleiman and Nehdi (2018) investigated the self-healing of cracks in cement-based composites under different environmental exposures and found that the main self-healing product was calcium carbonate. By contrast, autonomous healing refers to the mechanism that is triggered by artificial healing substances, which can be achieved by microcapsules containing polymeric adhesive agents such as epoxy, or microbially induced calcium carbonate precipitation (MICP) (Gardner *et al*., 2014).

Several techniques have been explored to improve the self-healing capacity of cementitious materials (Li *et al*., 2012). For example, Jiang *et al*. (2015) investigated the feasibility of enhancing the self-healing in cementitious materials by incorporating various minerals additives. They observed an improved healing efficiency using a combination of minerals. Nguyen *et al*. (2019) used *Bacillus subtilis* as a microbial adjuvant to improve crack self-healing and found that cracks with width of up to 400 μm

were completely sealed. Du *et al*. (2019) used microcapsules with toluene-di-isocyanate (TDI) as a healing agent and paraffin as shell material. Compressive strength could be restored and increased by 28.2%, while surface cracks with width below 400 μm were filled within 6 hours.

Crystalline additive (CA), an admixture with hydrophilic nature containing reactive silica and crystalline catalysts, has potential for reducing the permeability of concrete by reacting with some of its compounds (Senft *et al*., 1999). The deployment of CA for enhancing the self-healing efficiency of concrete has been intensively investigated since the reaction products of CAs deposit in cracks, thereby contributing to sealing (Ferrara *et al*., 2016). For instance, Sisomphon *et al*. (2012) explored the self-healing of surface cracks in mortars that incorporate CA. They found that more Ca^{2+} leached out from mortars incorporating CA, which enhanced precipitation of calcium carbonate as a self-healing product. Roig-Flores *et al*. (2015) found that specimens with 4% by-weigh-of-cement of CA and cured by water submersion exhibited best self-healing capability. Azarsa *et al*. (2019) conducted investigations on the effect of CA on mechanical strength, self-healing, and durability properties of concrete. Their results showed that water permeability decreased by three times, and the self-healing efficiency increased considerably by adding CA into the concrete mixture.

Bentonite (BN) has been also employed as a self-healing promoter owing to its swelling properties in contact with water, thereby sealing cracks (Qureshi *et al*., 2016). Another mechanism was reported by Ekaputri *et al*. (2018) that BN promoted precipitation of calcite crystals by providing additional calcium ions. Previous studies showed that crack healing could be achieved by either embedding capsules containing BN or incorporating BN powders in mortars (Qureshi *et al*., 2016; Sánchez *et al*., 2006). Qureshi *et al*. (2018) confirmed that the cement mix with BN exhibited limited improvement in crack sealing compared to a combination of expansive minerals.

Recently, Alkali-activated materials (AAM) have emerged as a strong contender to replace Ordinary Portland cement (OPC) concrete in diverse applications. This binder system is derived from the reaction of a solid aluminosilicate precursor with a

concentrated alkaline aqueous solution that encompasses alkali hydroxide, carbonates, silicate, sulfate, etc. (Shi *et al*., 2003; Provis and Bernal, 2014; Luukkonen *et al*., 2017). The solid precursor containing aluminosilicate can be a beneficiated industrial or mining by-product, such as fly ash from coal combustion or metallurgical slag from iron production, etc. (Provis and Deventer, 2014). Apart from the reduction of CO_2 emissions from OPC production (Ding *et al*. 2016), alkali-activated materials (AAMs) have shown enhanced resistance to chemical attack (Zhu *et al*., 2014; Arbi *et al*., 2016; Mellado *et al*., 2017) and high-temperature (Zhang *et al*., 2015; Rashad and Ouda, 2016a; Rashad and Ouda, 2016b), and to better immobilize toxic substances such as nuclear waste (Geddes *et al*., 2018; Lancellotti *et al*., 2015). However, numerous studies have revealed that the risk of early-age cracking caused by drying shrinkage in AAMs was considerably higher than that in OPC concrete (Atiş *et al*., 2009; Song *et al*., 2016). This shortcoming could jeopardize wider implementation of AAMs in various construction applications. Thus, exploring the ability to endow AAMs with crack self-healing ability has paramount importance.

While there is abundant research on self-healing of OPC-based materials, there are few studies devoted to the self-healing behaviour of AAMs, despite their use in full-scale construction projects (Provis and Bernal, 2014). While the efficacy of CA and BN as self-healing additives in OPC-based materials has been well documented, there are no studies devoted to the self-healing of AAMs incorporating CA and BN. Thus, this chapter explores, for the first time, the effectiveness of CA and BN in fibre-reinforced alkali-activated slag composites using various techniques including microscopy, inductively coupled plasma optical emission spectroscopy (ICP-OES), and X-ray micro-computed tomography (μ-CT) coupled with 3D image segmentation and analysis. Moreover, the recovery of transport property was investigated using a water absorption test. The self-healing products were characterized via scanning electron microscopy (SEM) coupled with energy-dispersive X-ray spectroscopy (EDS) analysis.

4.2 EXPERIMENTAL PROCEDURES

4.2.1 Materials

Ground granulated blast furnace slag (GGBFS) was used as the AAM precursor. Sodium hydroxide pellets were used as alkali activator. The CA and BN self-healing admixtures were obtained from industrial suppliers. The chemical composition and physical properties of the slag, as determined by X-ray fluorescence, are given in **Table 4-1**. The particle size distribution of the GGBFS was measured using a Malvern laser diffraction particle analyzer (**Figure 4-1**). The GGBFS was activated using a 5M sodium hydroxide solution. Polyvinyl alcohol (PVA) fibres, with mechanical properties shown in **Table 4-2**, were used to control cracks and improve self-healing as recommended by Feng *et al*. (2019) who observed that the presence of PVA fibres contributed to calcium carbonate nucleation. A superplasticizer (SP) was used to achieve good workability. Two different additives, namely CA and Na-bentonite in powder form, were added to the mixture. The mixture proportions are shown in **Table 4-3**.

Table 4-1: Physical and chemical properties of GGBFS

Components/property	GGBFS
Silicon oxide (SiO_2) (%)	33.70
Aluminum oxide (Al_2O_3) (%)	12.80
Ferric oxide (Fe_2O_3) (%)	0.96
Calcium oxide (CaO) (%)	45.40
Magnesium oxide (MgO) (%)	1.00
Specific gravity	2.90
Blaine fineness (m^2/kg)	399
Loss on ignition (LOI) at 1000 °C	2.72

Table 4-2: Mechanical properties of PVA fibres

Mechanical properties	Ultimate tensile strength (MPa)	Diameter (mm)	Density (kg/m^3)	Length (mm)	Young's modulus (GPa)	Elongation (%)
PVA	1620	0.039	1300	12	43	6

Table 4-3: Mixture design of the mortars

Mix	GGBFS	Additives	Extra water	NaOH solution	SP
0-AAS	100	0	7.5	22.5	0.2
CA-AAS	95	5	7.5	22.5	0.2
BN-AAS	95	5	7.5	22.5	0.2

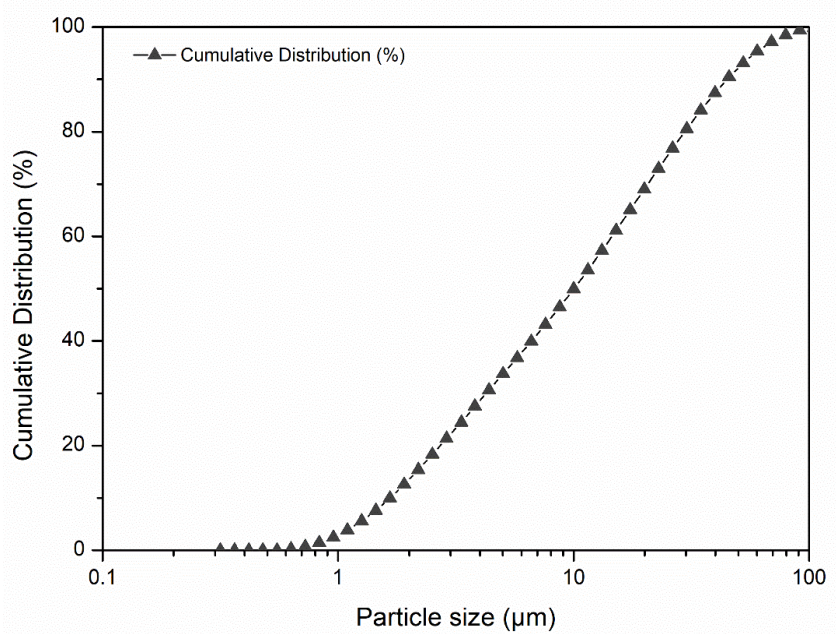

Figure 4-1: Particle size distribution of GGBFS.

4.2.2 Mixing procedure and specimen preparation

All solid ingredients were first dry-mixed using a 10L-Hobart mixer for two minutes. A 5M sodium hydroxide solution was added to the dry mixture at a low mixing speed over two minutes, followed by adding additional water and SP at a medium mixing speed for another two minutes to achieve the required rheology of fresh mortar. Finally, 0.5% PVA fibres by volume were slowly added into the mixture at low mixing speed and then mixed resumed at medium speed for two minutes to achieve good fibre dispersion. The fresh mixture was then cast into various types of molds. Cylindrical specimens with 50-mm diameter and 100-mm height were made for tensile strength, pH, electrical conductivity, and concentration of calcium ions measurements. Cubic specimens (50×50×50-mm) were prepared for compressive strength measurement. Larger disc-shaped specimens with 100-

mm diameter and 50-mm height were used for the water absorption test. Small disc-shaped specimens with 50-mm diameter and 15-mm height were used for crack width measurements, X-ray computed tomography analyses, and analysis of self-healing products. All molds were consolidated using a vibrating table and sealed using plastic films. All mortar specimens were demoulded after 24h and subsequently moved to a standard curing room with relative humidity >95% and T=20 ± 1 °C.

4.2.3 Crack creation and incubation

Small disc-shaped specimens were pre-cracked at the age of 7 days using a screw jack to introduce a surface crack of about 50-300 μm in width, as shown in **Figure 4-2**. Small disc-shaped specimens were divided into three groups based on different crack widths. The crack widths for the three groups include average crack width in the range of 50-100 μm, 100-200 μm, and 200-300 μm, respectively. The crack width could be controlled through a calibration ruler according to the method mentioned in (Roig-Flores *et al*., 2015). Similarly, larger disc-shaped specimens were subjected to a splitting test to create cracks with width 100 ± 20 μm as per (Suleiman and Nehdi, 2018). After pre-cracking, surface crack width was measured using a digital microscope. All cracked specimens were submerged in deionized water at a constant temperature of 20 °C. The Barnstead Easypure RoDi water purification system was employed to provide deionized water for water curing (**Figure 4-3**).

Figure 4-2: Cracking specimens using a screw jack.

Figure 4-3: Water purification system.

4.2.4 Test procedures

4.2.4.1 pH value, electrical conductivity and calcium ion concentration

Previous studies reported that calcium ions leaching from the matrix and the pH value of the curing environment play an essential role in the precipitation of calcium carbonate, which contributes to the self-healing of cracks (Jiang *et al*., 2015; Sisomphon *et al*., 2012; Huang and Ye, 2015; Homma *et al*., 2009; Huang *et al*., 2013; Stuckrath *et al*., 2014). To quantify the amount of leached calcium ions, a Vista Pro ICP-OES was used (**Figure 4-4**). All 7-day cured cylindrical samples were immersed in the same amount of deionized water. Before immersion, the three specimens were half-cut. The pH value and electrical conductivity were measured using Fisherbrand™ accumet™ AB200 pH/Conductivity Benchtop Meter (**Figure 4-5**).

Figure 4-4: Vista-Pro ICP-OES system.

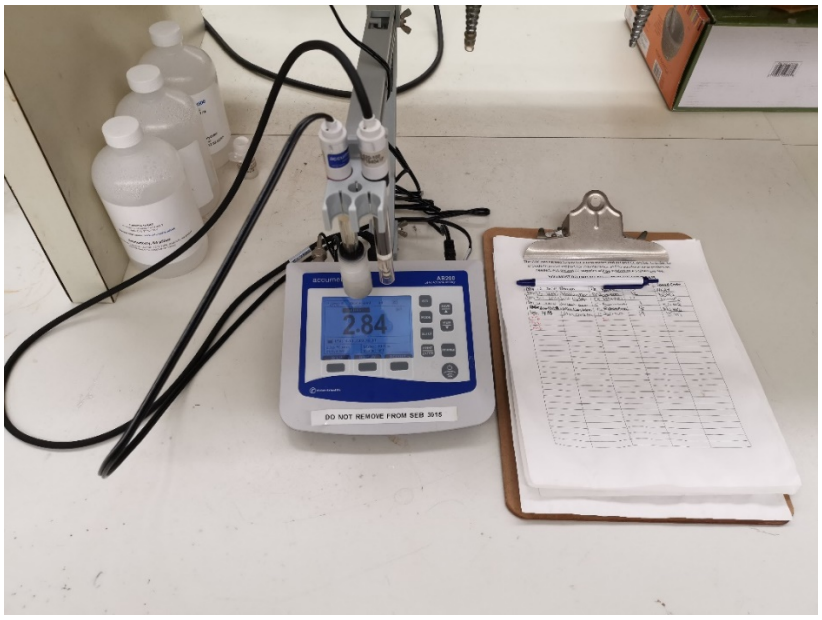

Figure 4-5: Fisherbrand™ accumet™ AB200 pH/Conductivity Benchtop Meter.

4.2.4.2 Quantification of crack-sealing through visual observation

The change in crack width on the surface of the disc-shaped specimens (before and after healing) was investigated using a digital Jiusion microscope with magnification ranging from 50× to 200× as a direct method to assess the crack self-healing efficiency, similar to previous studies by Park *et al*. (2018a and 2018b) and Ferrara *et al*. (2016). Three locations on both sides of each specimen were examined. The crack sealing ratio was calculated using **Eq. 4-1** (Qiu *et al*., 2016).

$$CSR(\%) = (w_0 - w_t)/w_0 \qquad \text{Eq. 4-1}$$

where *CSR* = crack sealing ratio; w_0 = initial crack width; w_t = crack width after curing at time *t*.

4.2.4.3 Mechanical tests

At 7, 14, and 28 days after casting, the compressive strength was measured on three cubic specimens from each mixture, according to ASTM C109 (ASTM International 2008). The tensile test was conducted using a displacement control method with a loading speed of 0.05 mm/min, as per the Brazilian method (Dai *et al*., 2010).

4.2.4.4 Water absorption test

The water absorption test was performed according to ASTM C1585 (ASTM International 2011) on 7-day old specimens, which were placed in an oven at 50 ± 2°C till constant mass. The split test was then used to create 100 ± 20 µm cracks. The side surface of each sample was sealed using silicone, while the bottom surface was allowed to be in contact with water to a depth of 3-5 mm (**Figure 4-6**). The specimen mass was recorded at 10-minute intervals up to 6 hours. The rate of water absorption was measured before and upon cracking, and after self-healing. Absorption was calculated via **Eq. 4-2**. The sorptivity coefficient, I was estimated as the slope of the best fit line plotted against the square root of time ($s^{1/2}$), according to **Eq. 4-3**.

$$I = \frac{m_t}{a*d} \qquad \text{Eq. 4-2}$$

where: I = the absorption in mm/s; m_t = the change in specimen mass in grams, at the time t in s; a = the exposed area of the specimen, in mm^2; d = the density of the water in g/mm^3.

$$S = \frac{I}{\sqrt{t}} \qquad \text{Eq. 4-3}$$

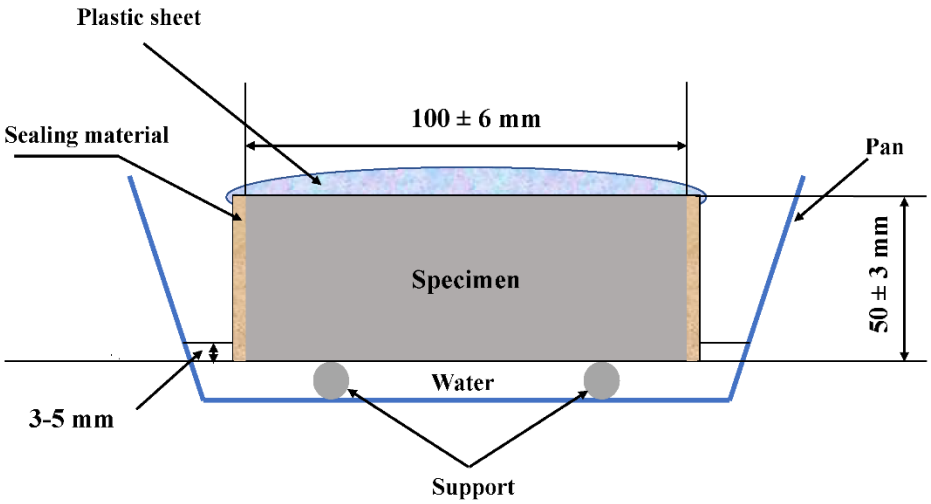

Figure 4-6: Schematic of water absorption test.

4.2.4.5 X-ray microcomputed tomography

To visualize the self-healing process, a micro-focus µCT scanner, Nikon XT H 225 ST (Nikon Corporation) was used (**Figure 4-7**). A series of sequential high-resolution 2D X-ray images were captured as the object was rotated through 360° to generate a 3D CT volume. These images were then reconstructed to generate a 3D volumetric representation of the object via a 3D rendering software named Dragonfly 4.0. The resolution was 56µ voxel size in the 3-D image. The parameters were set as follows: 225 kV, 130 µA, 29.3 watts; 1 panel gain = 24; 3141 projections; 150 frames/projection on shading correction; 2.5 mm Cu filter - fast CT - 60 min scanning.

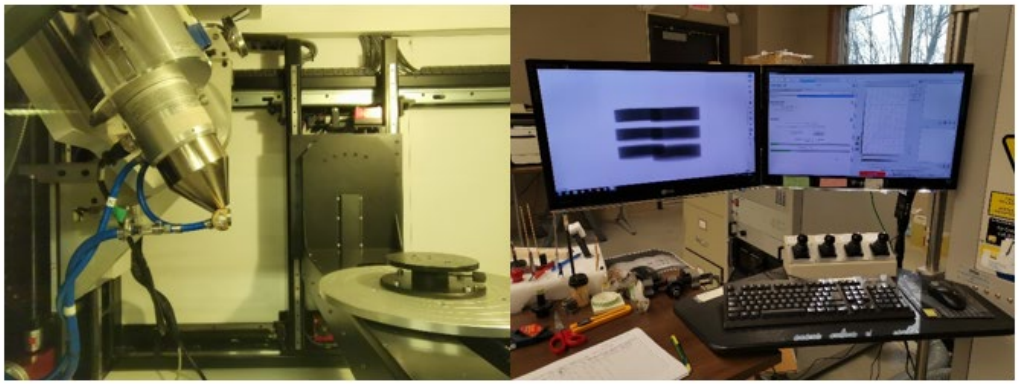

Figure 4-7: X-ray µCT scanning setup.

4.2.4.6 Characterization of self-healing products using SEM-EDS

Self-healing specimens were dried in a desiccator for a week, followed by surface gold-coating to enhance conductivity. A Hitachi SU3900 Field-Emission SEM with advanced functionalities for automated measurement and wide-angle camera navigation operated at a voltage of 20 kV was employed to analyze the morphology within the mouth of the cracks (**Figure 4-8**). To determine the elemental composition of the self-healing products, EDS was used via a Quantax 400 software.

Figure 4-8: SEM coupled with EDS analysis.

4.3 EXPERIMENTAL RESULTS AND DISCUSSION

4.3.1 CSR and ICP-OES results

Surface cracks on specimens before and after the self-healing process were investigated using a digital microscope. Binary images were obtained using OriginPro 8.5 with its image processing function (**Figure 4-9**). For CA-AAS specimens, the mouth of surface cracks was filled with self-healing products, and the crack width was decreased considerably. Notably, crack width of around 130 μm in CA-AAS specimens submerged in water could be completely sealed in 30 days. However, 0-AAS and BN-AAS specimens exhibited less self-healing. The crack sealing ratio was used as an indicator to evaluate self-healing efficiency. **Figure 4-10 (a)** plots a typical relationship between the crack sealing ratio and the initial crack width. It can be observed that CA-AAS specimens achieved the highest efficiency of crack width reduction among the three types of specimens. In addition, smaller cracks showed higher self-healing efficiency. To quantitatively compare the self-healing capability of the three specimen groups, the crack sealing ratio was estimated using nonlinear curve fitting. **Figure 4-10 (b)** shows the crack sealing ratio of different specimen groups having initial crack width of 50 μm, 100 μm, and 150 μm, respectively. CA-AAS specimens had the highest potential of crack width reduction, while BN reduced the self-healing efficiency compared to the control specimen 0-AAS. This result is consistent with Suleiman *et al*. (2019) who observed that the crack healing efficiency of cementitious composite incorporating BN was lower than that of the reference specimen. The self-healing efficiency of three types of specimens

was correlated with ICP-OES results. As shown in **Table 4-4**, the concentration of calcium ions in the leaching water of CA-AAS specimens was much higher than that for 0-AAS and BN-AAS specimens, indicating a higher potential for self-healing efficiency. This finding is in line with Feng *et al*. (2019) and Sisomphon *et al*. (2012) who observed that high-leaching calcium ions would promote self-healing efficiency by enhancing precipitation of calcium carbonate.

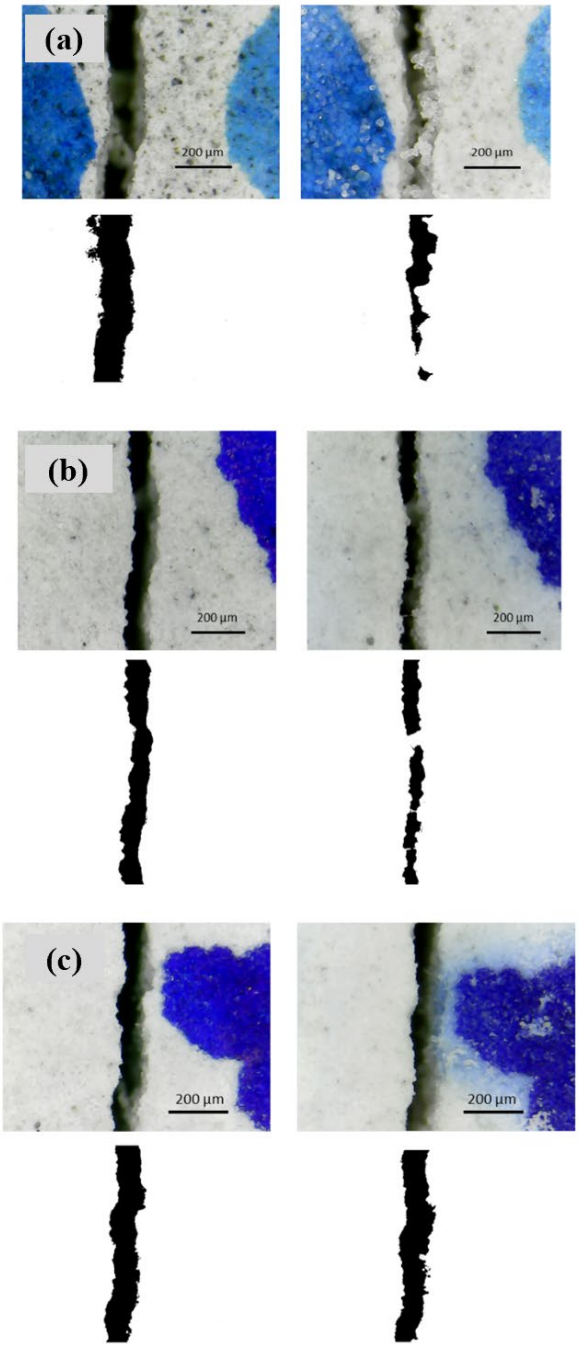

Figure 4-9: Surface and binary images of specimens from different mixtures before and after water submersion: (a) CA-AAS specimen; (b) 0-AAS specimen; (c) BN-AAS specimen.

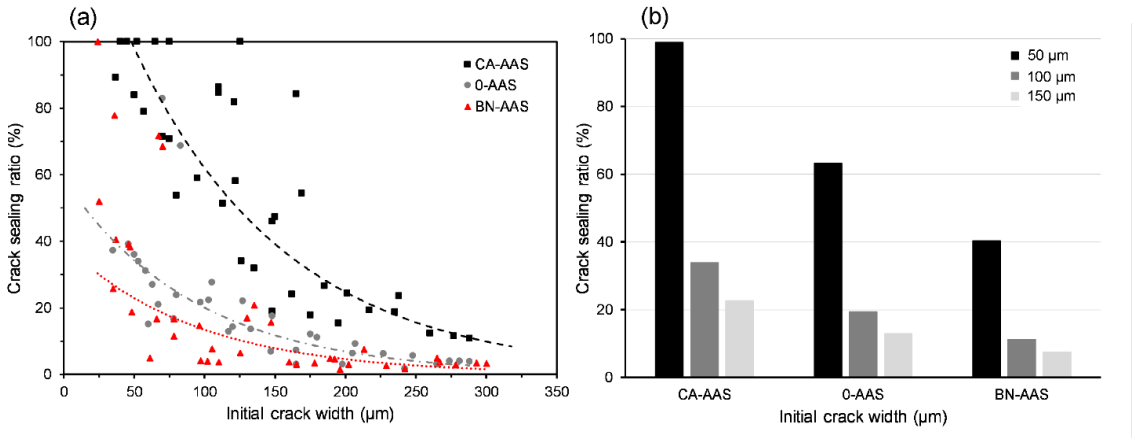

Figure 4-10: Relationship between initial crack width and crack sealing ratio for the three mixtures: (a) non-linear fitting of the typical relationship between crack sealing ratio and initial crack width; (b) effect of original crack width on crack sealing ratio determined from Figure 4-10 (a).

Table 4-4: Calcium concentrations in water after 16 days submersion

Mix	Ca^{2+} concentration (mg/L)
CH-Slag	3.164
0-Slag	0.956

4.3.2 Mechanical properties

The compressive and splitting tensile strengths of specimens from different mixtures at 7, 14, and 28 days increased over time as expected (**Figure 4-11**). Usually, the splitting tensile strength of alkali-activated slag-based concrete is around 17% of the corresponding compressive strength (Thomas and Peethamparan, 2015); however, the tensile strength of the tested mixtures was 20%-22% of the corresponding compressive strength. This could be attributed to the desirable interfacial bonding provided by PVA fibres (Li *et al*., 2002; Peyvandi *et al*., 2013). 5% CA addition had a positive effect on the development of mechanical properties compared to the control 0-AAS. The compressive strength of CA-AAS was 20-25% higher than that of 0-AAS at 14 days, and the splitting tensile strength was 14-24% higher than the reference group at 14 days. In contrast, the substitution of 5% BN caused a slight reduction in both compressive strength and splitting tensile strengths. The increase in both compressive strength and tensile strength

by incorporating CA may be explained by a filler effect that can reinforce the cementitious matrix through refining the microstructure (Azarsa *et al*. 2019). The decrease in both compressive strength and tensile strength with BN could account for the water-absorbing and soft nature of BN, and lower participation in pozzolanic reaction, thereby negatively affecting the strength development of alkali-activated slag composites (Qureshi *et al*., 2016). Previous studies by Akbar *et al*. (2013) and Mirza *et al*. (2009) also stated that the incorporation of BN in concrete caused a reduction of compressive strength.

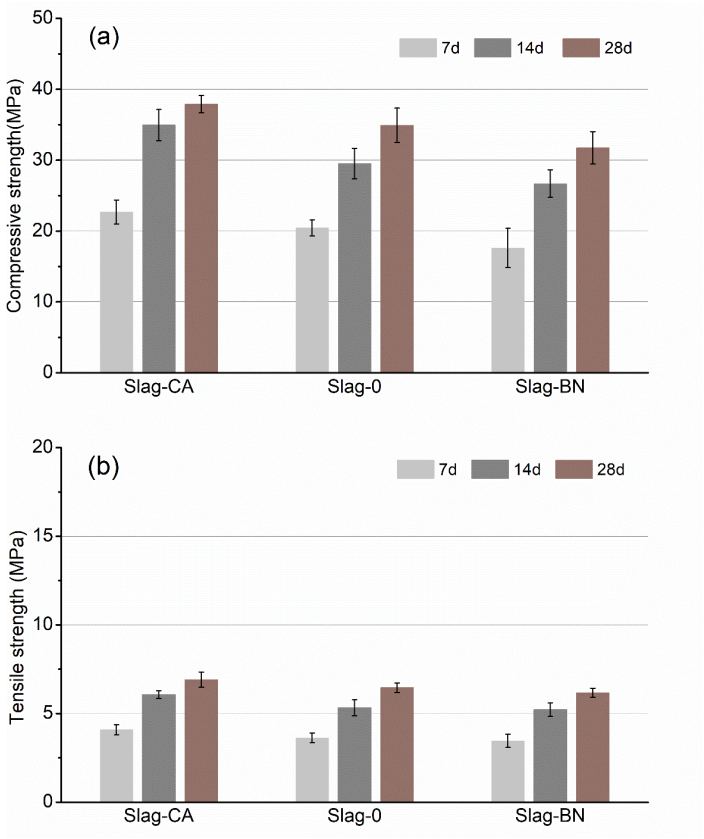

Figure 4-11: Mechanical properties development: (a) compressive strength, and (b) tensile strength.

4.3.3 Water absorption

Figure 4-12 plots the capillary water absorption test results of specimens from the three mixtures before and upon cracking, and after water submersion. The sorptivity coefficient was fitted using linear regression. For each type of uncracked specimen at 7-d, CA-AAS

had minimum water absorption (**Figure 4-12 (a)**), which is likely due to incorporation of CA, a synthetic cementitious material containing reactive silica and crystalline catalysts, used as a concrete permeability reducer (Sisomphon *et al*., 2012; Whitney, 2008). Cement compounds such as C_3S react with CA components to produce modified C-S-H and pore-blocking precipitates, which decrease water absorption (Roig-Flores *et al*., 2016). A slightly higher water absorption compared to that of the control 0-AAS was observed for BN-AAS. As shown in **Figure 4-12 (b)**, water absorption increased more rapidly in cracked specimens. The sorptivity index of the uncracked 0-AAS specimen, for instance, was 0.03396 mm/$\sqrt{sec}$ (**Figure 4-12 (a)**). In contrast, it was 0.0573 mm/$\sqrt{sec}$ for the cracked specimen, likely because the crack acted as a capillary pipe for water absorption and restoration (Park and Choi, 2018). It can be observed in **Figure 4-12 (c)** that the sorptivity coefficient in specimens from the three mixtures after 14-d water curing decreased markedly, especially for the CA-AAS specimens, indicating the more significant self-healing in CA-AAS specimens. To quantitatively determine the self-healing efficiency, the sorptivity coefficient reduction ratio, as defined by **Eq. 4-4**, was calculated for each specimen at cracking and after healing.

$$\gamma = \frac{s_1 - s_2}{s_1} \times 100\% \qquad \text{Eq. 4-4}$$

where s_1 and s_2 refer to the sorptivity coefficient at cracking and after conditioning, respectively. Results in **Figure 4-12(d)** indicate that cracked specimens incorporating CA achieved a much higher reduction in the sorptivity coefficient compared to that of specimens from the other two mixes.

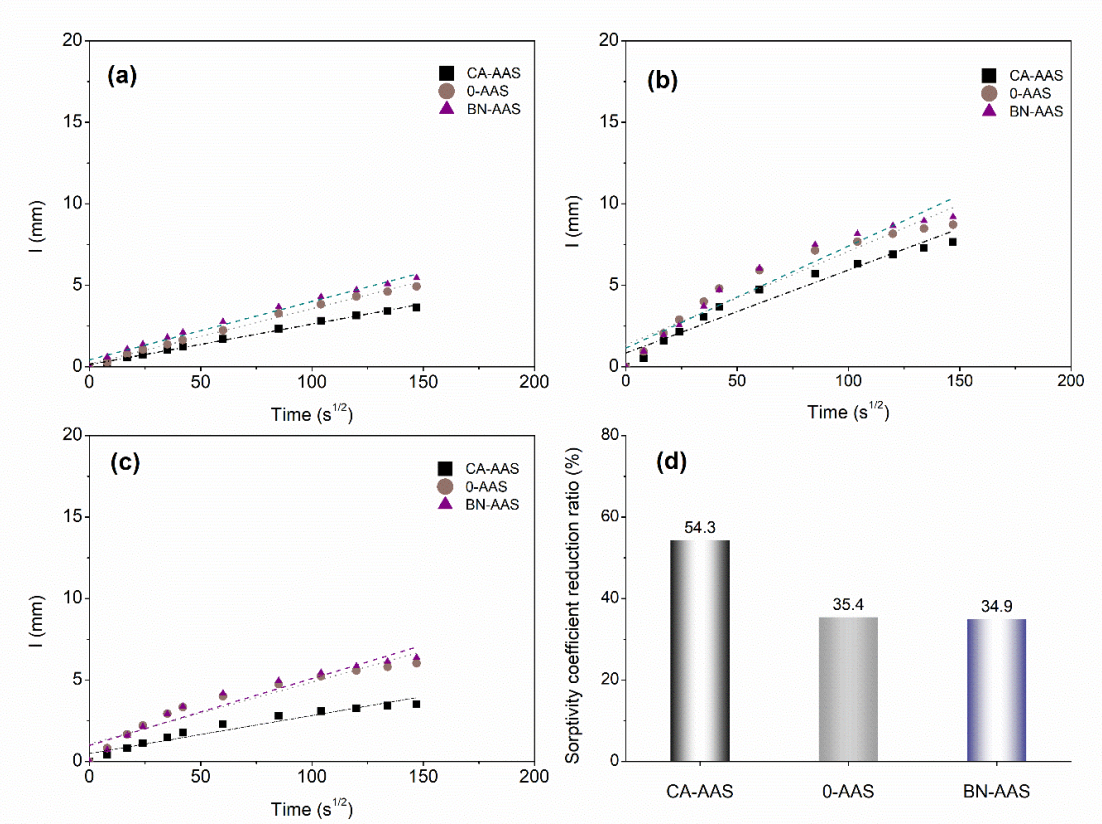

Figure 4-12: Change in water absorption of cracked specimens exposed to water (a) before cracking, (b) upon cracking, (c) after curing, and (d) sorptivity coefficient reduction ratio of the specimen groups.

4.3.4 Self-healing compounds

The morphology of self-healing compounds formed within and on the surface of cracks was assessed by SEM analysis. Massive precipitates which are different from the cementitious matrix outside of the crack boundary, grew within the crack mouth, and the 120 μm gap was nearly filled (**Figure 4-13 (a)**). Various irregular polyhedron-like, cube-like, and prism-like crystals, together with a few gel-like particles, formed a solid bulk expanding toward each other and finally making a dense bridge of crystals over the crack. In contrast, some small amorphous crystal materials and plenty of irregular polyhedron-like crystals were intermingled within the crack mouth in the 0-AAS and BN-AAS specimens, as shown in **Figure 4-13 (b)** and **(c)**.

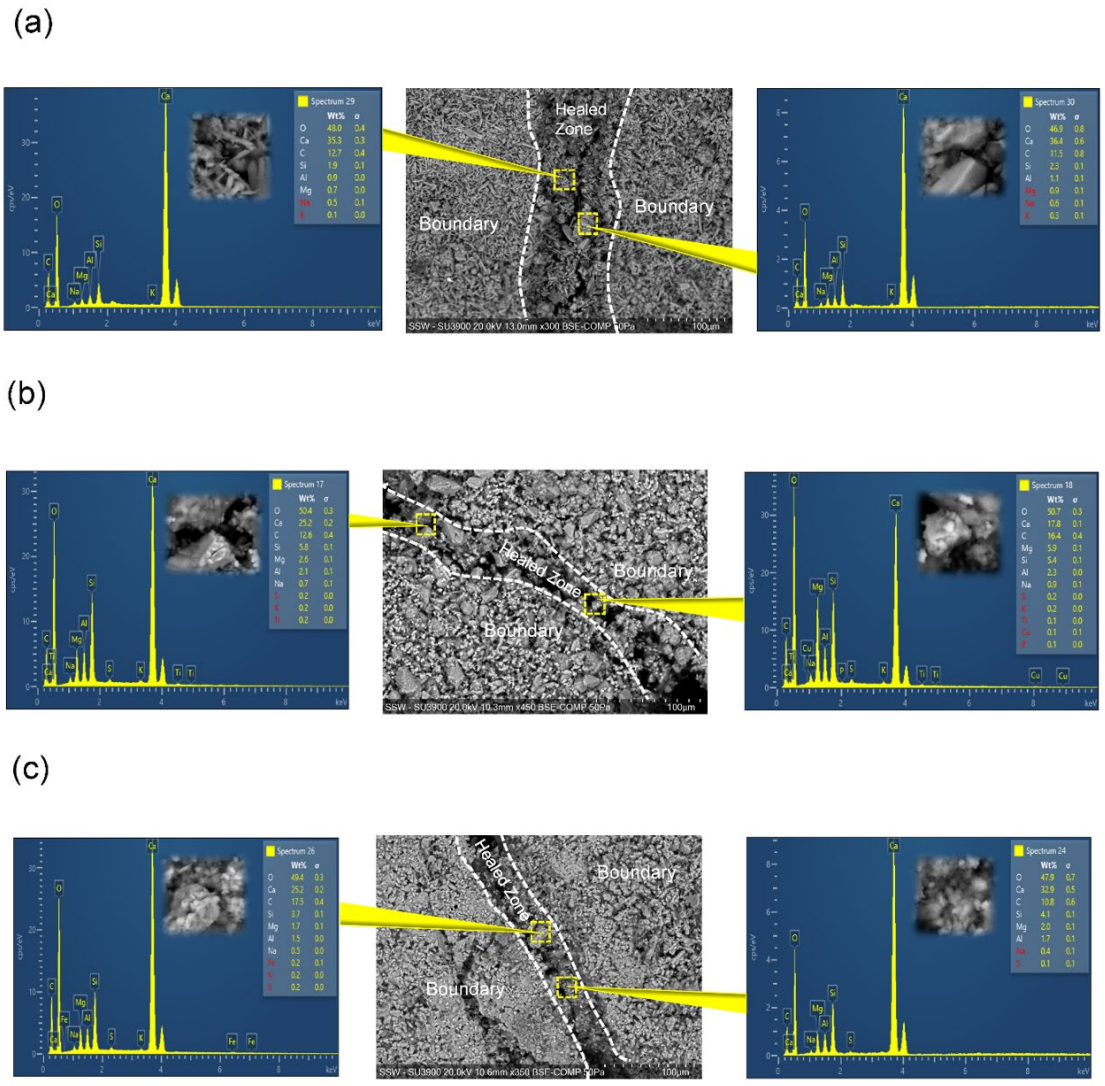

Figure 4-13: SEM images with EDS pattern of self-healing products within the cracks of (a) CA-AAS, (b) 0-AAS, and (c) BN-AAS.

To further confirm the chemical composition of self-healing products, elemental EDS analysis was conducted. The healing products at the surface cracks in all specimens were mainly dominated by Ca, O, and C according to the spectrum maps, confirming that the self-healing materials were primarily composed of $CaCO_3$. Noticeably, a small amount of silicon and aluminum was also found, which suggests the presence of calcium-alumino-silicate-hydrate (C-A-S-H) as a hydration product of alkali-activated slag. This finding is in agreement with the study conducted by Nguyễn *et al*. (2019), which concluded that the

dominant healing material of sodium activator-based alkali-activated slag composites was CaCO3. It is noted that the observed magnesium content could arise from the raw GGBFS or is possibly from magnesite ($MgCO_3$), or brucite ($Mg(OH)_2$) (Nguyễn *et al*., 2019).

Figure 4-14 shows the morphology of self-healing materials covering PVA fibres. In the CA-AAS and the BN-AAS specimens, irregular polyhedron-like crystals were packed more densely than in the 0-AAS specimens. Interestingly, small needle-like crystal clusters were scattered on the surface of PVA fibres in the CA-AAS and the 0-AAS specimens, as shown in **Figure 4-14 (a)** and **(b)**. The self-healing products on the boundary of the crack were attracted by the PVA fibre and grew towards it (**Figure 4-14 (b)**), suggesting a trend to bridge the gap. It can be hypothesized that PVA fibres induced precipitation of self-healing products by acting as nucleation sites. According to this hypothesis, the PVA fibre-induced bridging of cracks could promote self-healing efficiency of alkali-activated slag-based composites, indicating that self-healing was determined by coupled factors through synergistic action (Qiu *et al*., 2016).

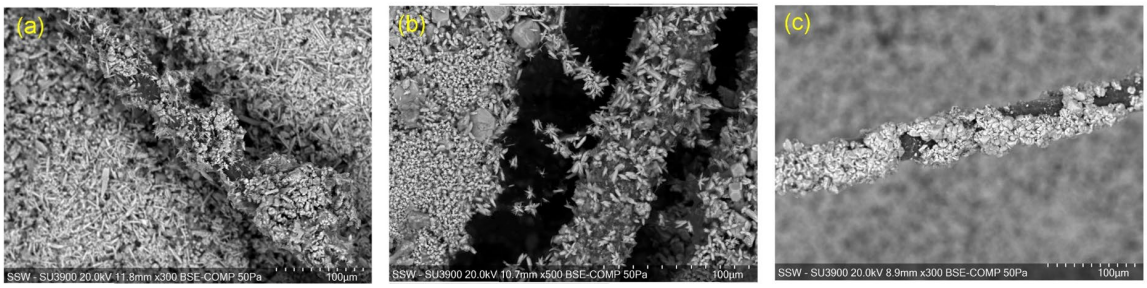

Figure 4-14: Healing products covering PVA fibre for (a) CA-AAS, (b) 0-AAS, and (c) BN-AAS specimens.

4.3.5 X-ray microcomputed tomography

Figure 4-15 illustrates the change in the crack area of fully healed CA-AAS specimen upon cracking and after healing, and the two corresponding reconstructed slices extracted from the same distance (2 mm) from the top surface. X-ray μCT analysis provided detailed visualization of self-healing as a function of crack depth via a large quantity of 2D reconstructed images. Only the CA-AAS specimen with a crack width ranging from

50 to 100 µm was chosen for X-ray µCT analysis since it exhibited full self-healing after 2 months of water submersion. Different densities of CA-AAS specimen were distinguished by different colors; yellow and orange depict the denser parts, while the porosity and the crack were colored in blue. Additionally, crack images from the reconstructed slices were converted to binary images for better comparison. The depth within 1.5 mm from the top surface was partially sealed with self-healing products, suggesting that the majority of self-healing products precipitated in the region close to the specimen surface (Fan and Li, 2014). The precipitation of self-healing products on the surface of the crack could be responsible for obstructing moisture ingress deeper into the specimen and preventing self-healing from reaching the interior of the crack (Wang *et al*. 2018). Similar results were reported in Portland cementitious composites, for instance, by Suleiman and Nehdi (2018) who investigated crack sealing of cement-based mortars incorporating 20% fly ash. Micro-focus X-ray CT showed that the sealing precipitates occurred only close to the surface of the specimen. Fan and Li (2014) also found that the region of the crack near the surface (usually 0-150 µm) was more likely healed in a short time; however, self-healing was negligible in the crack at greater depth.

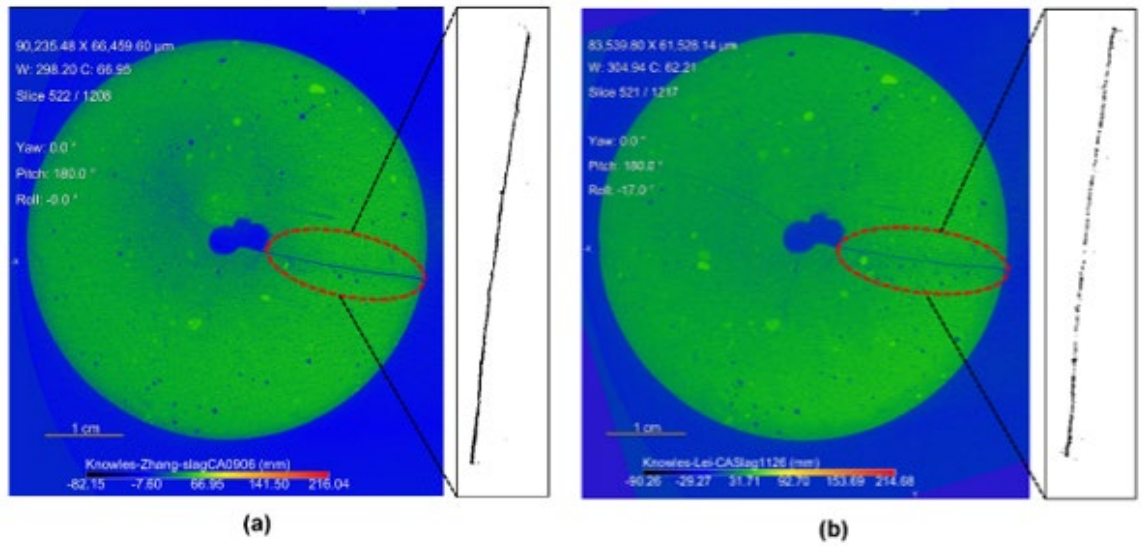

Figure 4-15: X-ray µCT scanning images of the CA-AAS specimen with modified binary images demonstrating interior cracks: (a) upon cracking and (b) after healing.

4.3.6 Coupled effect of calcium ions, pH, and PVA fibre on self-healing

As presented in **Table 4-4**, the concentration of calcium ions leached in curing water of CA-AAS specimens with best self-healing performance was the highest, indicating that calcium carbonate precipitation as a healing compound required calcium ions supply, from the alkali-activated slag-based composite. It was hypothesized that the incorporation of CA boosts the dissolution of calcium ions, which promotes the formation of calcium carbonate (Sisomphon *et al*., 2012).

The electrical conductivity and pH values of the curing water at 7, 14, and 28 days increased with increasing curing time for all specimens (**Figure 4-16**). The electrical conductivity was primarily related to the concentration of total dissolved ions in the curing water, while pH values were dependent on the number of hydroxyl ions leaching from the matrix. The curing water of CA-AAS specimens showed higher pH and electrical conductivity values at all curing periods compared to that of the other two mixtures. More Ca^{2+} leaching and higher pH promote the precipitation of calcium carbonate (Sisomphon *et al*., 2012; Wang *et al*., 2014; Zhang *et al*., 2017), which stimulated crack self-healing. According to **Eq. 4-5**, carbonic acid (H_2CO_3), derived from the dissolution of carbon dioxide (CO_2), reacts with hydroxyl ions to form carbonates. Higher pH shifts carbonate acid equilibrium, converting to the formation of carbonate ions (Zhang *et al*., 2017; Vchal *et al*., 2015).

$$2OH^- + H_2CO_3 \leftrightarrow CO_3^{2-} + 2H_2O \qquad \text{Eq. 4-5}$$

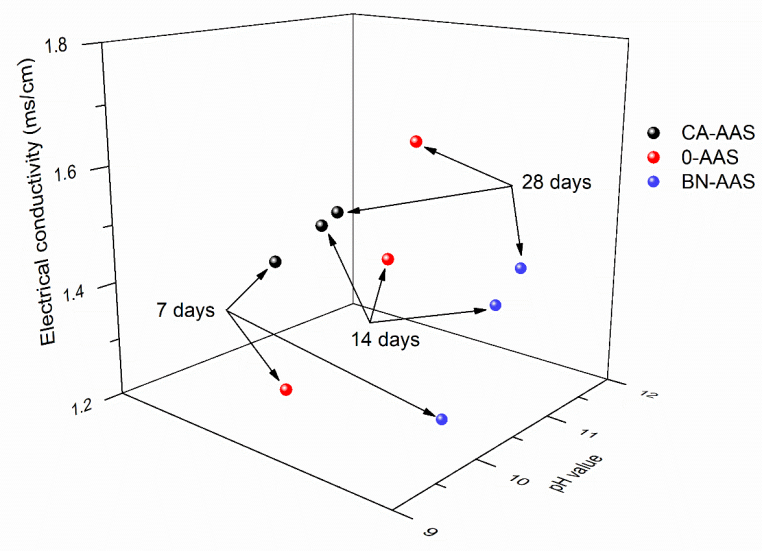

Figure 4-16: Electrical conductivity vs. pH of curing water for the submerged specimens.

As shown in **Figure 4-14**, fibres were covered with calcium carbonate, indicating that PVA fibres may play a role in the precipitation of calcium carbonate. The intermolecular forces between PVA fibre molecules and the surrounding aqueous solution include Van der Waals forces, ionic bonding, and hydrogen bonding (Kihara, 1978). The hydroxyl group in the vinyl alcohol molecular structure, a strong polar group, contributes most to fibre's bond polarity (**Figure 4-17**), resulting in a tendency to attract electrons via the functional group (Feng *et al*., 2019) and potential to attract Ca^{2+} (Homma *et al*., 2009). Moreover, hydroxyls in the PVA molecular structure tend to form hydrogen bonds in aqueous solutions, having strong interaction with water (Guan *et al*., 2017; Meng *et al*., 2017). Water is the carrier for Ca^{2+} and CO_3^{2-}, and through interaction with water, the hydroxyl group can provide a site, in which ions can rest. When carbonates form, Ca^{2+} ions will be attracted due to the strong electrostatic forces supporting the hypothesis that the PVA molecular structure promotes the formation of self-healing products by offering preferential nucleation sites for calcium carbonation.

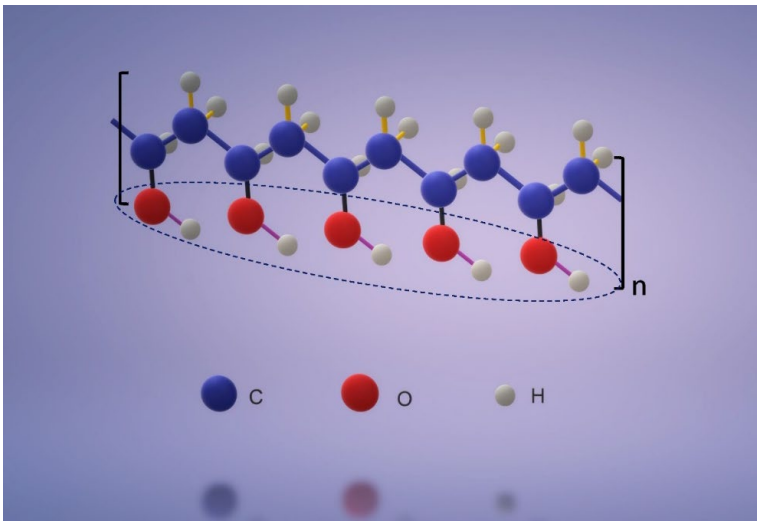

Figure 4-17: Molecular structure of polyvinyl alcohol (PVA).

Based on the results of this study and the discussion above, the mechanism of crack self-healing in PVA fibre-reinforced alkali-activated slag-based composites is schematically illustrated in **Figure 4-18**. When the PVA fibre-reinforced alkali-activated slag-based composite is exposed to water, some Ca^{2+} ions from the matrix gradually leach to the curing water. The concentration of Ca^{2+} increases by incorporating CA during the mixing process. CO_2 from the atmosphere dissolves in the curing water, converting to H_2CO_3. However, H_2CO_3 decomposes into CO_3^{2-} and HCO_3^- due to its instability. Therefore, the concentration of CO_3^{2-} and HCO_3^- in the surface water gets higher than that inside the crack. Accordingly, a significant amount of calcium carbonate precipitates near the surface of cracks, blocking the pathway of diffusion of CO_3^{2-} to the interior of the cracks. Consequently, little precipitation of calcium carbonate can be observed inside of the cracks (Sisomphon *et al*., 2012). Moreover, the high pH value in the curing water provides an alkaline environment, which favors calcium carbonate precipitation through shifting the carbonate acid equilibrium. In addition, the PVA fibres near the crack mouth provide preferential nucleation sites for calcium carbonate precipitation.

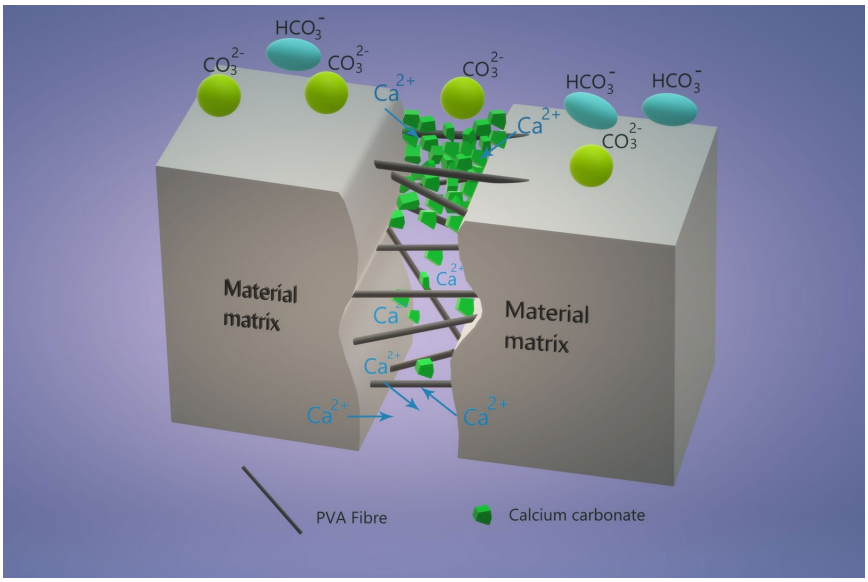

Figure 4-18: Schematic illustration of the self-healing mechanism of PVA fibre-reinforced alkali-activated slag-based composites incorporating CA.

4.4 CONCLUSIONS

In the present study, the potential of crack self-healing in alkali-activated slag composites incorporating crystalline additive (CA) and bentonite (BN) has been investigated using a wide array of test methods. Based on the experimental results, the following conclusions can be drawn:

1) Specimens incorporating CA achieved the highest crack sealing ratio among the three mixtures investigated, and surface cracks with smaller width achieved better self-healing potential.

2) Fibre-reinforced alkali-activated slag composites incorporating CA reached higher compressive and tensile strength compared to that of control mixtures. In contrast, BN mixtures had slightly decreased mechanical properties.

3) Sorptivity decreased by 54.3% for pre-cracked CA-AAS after 15-d water curing, which was more than that of pre-cracked 0-AAS and BN-AAS specimens.

4) Mobilizing a portfolio of test methods including SEM-EDS, ICP-OES, and X-ray μCT can provide synergistic information, which better characterizes and quantifies crack self-healing in fibre-reinforced alkali-activated slag composites.

5) The main self-healing compound identified in cracks of specimens from all mixtures was calcium carbonate.

6) High pH of the curing environment and the presence of high concentration of calcium ions and PVA fibres seem to act synergistically in accelerating precipitation of calcium carbonate as a crack healing compound.

4.5 REFERENCE

Achal, V., and Mukherjee, A. (2015). A review of microbial precipitation for sustainable construction. *Construction and Building Materials, 93*, 1224-1235.

Akbar, J., Alam, B., Ashraf, M., Afzal, S., Ahmad, A., and Shahzada, K. (2013). Evaluating the Effect of Bentonite on Strength and Durability of High Performance Concrete. *International Journal Advanced Structural Geotechnical Engineering, 2*, 1-5.

Arbi, K., Nedeljković, M., Zuo, Y., and Ye, G. (2016). A review on the durability of alkali-activated fly ash/slag systems: advances, issues, and perspectives. *Industrial and Engineering Chemistry Research, 55*(19), 5439-5453.

Atiş, C. D., Bilim, C., Çelik, Ö., and Karahan, O. (2009). Influence of activator on the strength and drying shrinkage of alkali-activated slag mortar. *Construction and Building Materials, 23*(1), 548-555.

Azarsa, P., Gupta, R., and Biparva, A. (2019). Assessment of self-healing and durability parameters of concretes incorporating crystalline admixtures and Portland Limestone Cement. *Cement and Concrete Composites, 99*, 17-31.

Chen, J., Dong, Q., Ma, X., Fan, T.-H., and Lei, Y. (2016). Repetitive Biomimetic Self-healing of Ca^{2+}-Induced Nanocomposite Protein Hydrogels. *Scientific Report, 6*, 30804.

Dai, F., Chen, R., Iqbal, M., and Xia, K. (2010). Dynamic cracked chevron notched Brazilian disc method for measuring rock fracture parameters. *International Journal of Rock Mechanics and Mining Sciences, 47*(4), 606-613.

De Rooij, M., Van Tittelboom, K., De Belie, N., and Schlangen, E. (2013). *Self-healing phenomena in cement-Based materials: state-of-the-art report of RILEM*

technical committee 221-SHC: self-Healing phenomena in cement-Based materials (Vol. 11): Springer.

Ding, Y., Dai, J.-G., and Shi, C.-J. (2016). Mechanical properties of alkali-activated concrete: A state-of-the-art review. *Construction and Building Materials, 127*, 68-79.

Du, W., Yu, J., Gu, Y., Li, Y., Han, X., and Liu, Q. (2019). Preparation and application of microcapsules containing toluene-di-isocyanate for self-healing of concrete. *Construction and Building Materials, 202*, 762-769.

Ekaputri, J., Anam, M., Luan, Y., Fujiyama, C., Chijiwa, N., and Setiamarga, D. (2018). Application of GGBFS and Bentonite to Auto-Healing Cracks of Cement Paste. *JACEE (Journal of Advanced Civil and Environmental Engineering), 1*(1), 38-48.

Fan, S., and Li, M. (2014). X-ray computed microtomography of three-dimensional microcracks and self-healing in engineered cementitious composites. *Smart Materials and Structures, 24*(1), 015021.

Feng, J., Su, Y., and Qian, C. (2019). Coupled effect of PP fiber, PVA fiber and bacteria on self-healing efficiency of early-age cracks in concrete. *Construction and Building Materials, 228*, 116810.

Ferguson, J., Schultz, B. F., and Rohatgi, P. K. (2014). Self-healing metals and metal matrix composites. *Jom, 66*(6), 866-871.

Ferrara, L., Krelani, V., and Moretti, F. (2016a). Autogenous healing on the recovery of mechanical performance of High Performance Fibre Reinforced Cementitious Composites (HPFRCCs): Part 2–Correlation between healing of mechanical performance and crack sealing. *Cement and Concrete Composites, 73*, 299-315.

Ferrara, L., Krelani, V., and Moretti, F. (2016b). On the use of crystalline admixtures in cement based construction materials: from porosity reducers to promoters of self healing. *Smart Materials and Structures, 25*(8), 084002.

Gardner, D., Jefferson, A., Hoffman, A., and Lark, R. (2014). Simulation of the capillary flow of an autonomic healing agent in discrete cracks in cementitious materials. *Cement and Concrete Research, 58*, 35-44.

Geddes, D., Ke, X., Bernal, S., Hayes, M., and Provis, J. (2018). Metakaolin-based geopolymers for nuclear waste encapsulation *Calcined clays for sustainable concrete* (pp. 183-188): Springer.

Guan, Y., Li, W., Zhang, Y., Shi, Z., Tan, J., Wang, F., and Wang, Y. (2017). Aramid nanofibers and poly (vinyl alcohol) nanocomposites for ideal combination of strength and toughness via hydrogen bonding interactions. *Composites Science and Technology, 144*, 193-201.

Homma, D., Mihashi, H., and Nishiwaki, T. (2009). Self-healing capability of fibre reinforced cementitious composites. *Journal of Advanced Concrete Technology, 7*(2), 217-228.

Huang, H., and Ye, G. (2015). Self-healing of cracks in cement paste affected by additional Ca2+ ions in the healing agent. *Journal of Intelligent Material Systems and Structures, 26*(3), 309-320.

Huang, H., Ye, G., and Damidot, D. (2013). Characterization and quantification of self-healing behaviors of microcracks due to further hydration in cement paste. *Cement and Concrete Research, 52*, 71-81.

Jiang, Z., Li, W., and Yuan, Z. (2015). Influence of mineral additives and environmental conditions on the self-healing capabilities of cementitious materials. *Cement and Concrete Composites, 57*, 116-127.

Juenger, M., Winnefeld, F., Provis, J. L., and Ideker, J. (2011). Advances in alternative cementitious binders. *Cement and Concrete Research, 41*(12), 1232-1243.

Kihara, T. (1978). *Intermolecular forces*: Wiley New York.

Lancellotti, I., Barbieri, L., and Leonelli, C. (2015). Use of alkali-activated concrete binders for toxic waste immobilization *Handbook of Alkali-Activated Cements, Mortars and Concretes* (pp. 539-554): Elsevier.

Li, V. C., and Herbert, E. (2012). Robust self-healing concrete for sustainable infrastructure. *Journal of Advanced Concrete Technology, 10*(6), 207-218.

Li, V. C., Wu, C., Wang, S., Ogawa, A., and Saito, T. (2002). Interface tailoring for strain-hardening polyvinyl alcohol-engineered cementitious composite (PVA-ECC). *Materials Journal, 99*(5), 463-472.

Li, W., Dong, B., Yang, Z., Xu, J., Chen, Q., Li, H., Xing, F., and Jiang, Z. (2018). Recent advances in intrinsic self-healing cementitious materials. *Advanced Materials, 30*(17), 1705679.

Luukkonen, T., Abdollahnejad, Z., Yliniemi, J., Kinnunen, P., and Illikainen, M. (2017). One-part alkali-activated materials: A review. *Cement and Concrete Research*.

Ma, X., Shi, C., Huang, X., Liu, Y., and Wei, Y. (2019). Effect of natural melanin nanoparticles on a self-healing cross-linked polyurethane. *Polymer Journal, 51*(6), 547.

Markvicka, E. J., Bartlett, M. D., Huang, X., and Majidi, C. (2018). An autonomously electrically self-healing liquid metal–elastomer composite for robust soft-matter robotics and electronics. *Nature materials, 17*(7), 618-624.

Mellado, A., Pérez-Ramos, M. I., Monzó, J., Borrachero, M. V., and Payá, J. (2017). Resistance to acid attack of alkali-activated binders: simple new techniques to measure susceptibility. *Construction and Building Materials, 150*, 355-366.

Meng, X., Zeng, N., Zhang, J., Jiang, L., and Dan, Y. (2017). Polyvinyl alcohol-based hydrophilic monoliths from water-in-oil high internal phase emulsion template. *Journal of colloid and interface science, 497*, 290-297.

Mirza, J., Riaz, M., Naseer, A., Rehman, F., Khan, A., and Ali, Q. (2009). Pakistani bentonite in mortars and concrete as low cost construction material. *Applied Clay Science, 45*(4), 220-226.

Nguyễn, H. H., Choi, J.-I., Kim, H.-K., and Lee, B. Y. (2019). Effects of the type of activator on the self-healing ability of fiber-reinforced alkali-activated slag-based composites at an early age. *Construction and Building Materials, 224*, 980-994.

Nguyen, T. H., Ghorbel, E., Fares, H., and Cousture, A. (2019). Bacterial self-healing of concrete and durability assessment. *Cement and Concrete Composites, 104*, 103340.

Park, B., and Choi, Y. C. (2018a). Quantitative evaluation of crack self-healing in cement-based materials by absorption test. *Construction and Building Materials, 184*, 1-10.

Park, B., and Choi, Y. C. (2018b). Self-healing capability of cementitious materials with crystalline admixtures and super absorbent polymers (SAPs). *Construction and Building Materials, 189*, 1054-1066.

Peyvandi, A., Soroushian, P., and Jahangirnejad, S. (2013). Enhancement of the structural efficiency and performance of concrete pipes through fiber reinforcement. *Construction and Building Materials, 45*, 36-44.

Provis, J. L., and Bernal, S. A. (2014). Geopolymers and related alkali-activated materials. *Annual Review of Materials Research, 44*, 299-327.

Provis, J. L., and van Deventer, J. S. J. (2013). *Alkali Activated Materials: State-of-the-Art Report, RILEM TC 224-AAM*: Springer Netherlands.

Qiu, J., Tan, H. S., and Yang, E.-H. (2016). Coupled effects of crack width, slag content, and conditioning alkalinity on autogenous healing of engineered cementitious composites. *Cement and Concrete Composites, 73*, 203-212.

Qureshi, T., Kanellopoulos, A., and Al-Tabbaa, A. (2016). Encapsulation of expansive powder minerals within a concentric glass capsule system for self-healing concrete. *Construction and Building Materials, 121*, 629-643.

Qureshi, T., Kanellopoulos, A., and Al-Tabbaa, A. (2018). Autogenous self-healing of cement with expansive minerals-I: Impact in early age crack healing. *Construction and Building Materials, 192*, 768-784.

Rashad, A. M., and Ouda, A. S. (2016). An investigation on alkali-activated fly ash pastes modified with quartz powder subjected to elevated temperatures. *Construction and Building Materials, 122*, 417-425.

Rashad, A. M., Zeedan, S. R., and Hassan, A. A. (2016). Influence of the activator concentration of sodium silicate on the thermal properties of alkali-activated slag pastes. *Construction and Building Materials, 102*, 811-820.

Roig-Flores, M., Moscato, S., Serna, P., and Ferrara, L. (2015). Self-healing capability of concrete with crystalline admixtures in different environments. *Construction and Building Materials, 86*, 1-11.

Roig-Flores, M., Pirritano, F., Serna, P., and Ferrara, L. (2016). Effect of crystalline admixtures on the self-healing capability of early-age concrete studied by means of permeability and crack closing tests. *Construction and Building Materials, 114*, 447-457.

Sánchez, L., Cuevas, J., Ramírez, S., De León, D. R., Fernández, R., Villa, R. V. D., and Leguey, S. (2006). Reaction kinetics of FEBEX bentonite in hyperalkaline conditions resembling the cement–bentonite interface. *Applied Clay Science, 33*(2), 125-141.

Senft, S., Gallegos, S., Manson, D. P., and Gonzales, C. (1999). *Chemical admixtures for concrete*: Crc Press.

Shi, C., Roy, D., and Krivenko, P. (2003). *Alkali-activated cements and concretes*: CRC press.

Sisomphon, K., Copuroglu, O., and Koenders, E. (2012). Self-healing of surface cracks in mortars with expansive additive and crystalline additive. *Cement and Concrete Composites, 34*(4), 566-574.

Song, C., Choi, Y. C., and Choi, S. (2016). Effect of internal curing by superabsorbent polymers–internal relative humidity and autogenous shrinkage of alkali-activated slag mortars. *Construction and Building Materials, 123*, 198-206.

Standard, A. (2008). ASTM C109-standard test method for compressive strength of hydraulic cement mortars. *ASTM International, West Conshohocken, PA*.

Standard, A. (2011). C1585. *Standard Test Method for Measurement of Rate of Absorption of Water by Hydraulic-Cement Concretes. ASTM International, West Conshohocken, Pennsylvania*.

Stuckrath, C., Serpell, R., Valenzuela, L. M., and Lopez, M. (2014). Quantification of chemical and biological calcium carbonate precipitation: performance of self-healing in reinforced mortar containing chemical admixtures. *Cement and Concrete Composites, 50*, 10-15.

Suleiman, A., and Nehdi, M. (2018). Effect of environmental exposure on autogenous self-healing of cracked cement-based materials. *Cement and Concrete Research, 111*, 197-208.

Suleiman, A. R., Nelson, A. J., and Nehdi, M. L. (2019). Visualization and quantification of crack self-healing in cement-based materials incorporating different minerals. *Cement and Concrete Composites, 103*, 49-58.

Tahri, W., Abdollahnejad, Z., Pacheco-Torgal, F., and Aguiar, J. (2016). Performance on an Alkali-Activated Cement-Based Binder (AACB) for Coating of an OPC Infrastructure Exposed to Chemical Attack: A Case Study. *Handbook of Low Carbon Concrete*, 335.

Thomas, R. J., and Peethamparan, S. (2015). Alkali-activated concrete: Engineering properties and stress–strain behavior. *Construction and Building Materials, 93*, 49-56.

Wang, J., Soens, H., Verstraete, W., and De Belie, N. (2014). Self-healing concrete by use of microencapsulated bacterial spores. *Cement and Concrete Research, 56*, 139-152.

Wang, X., Fang, C., Li, D., Han, N., and Xing, F. (2018). A self-healing cementitious composite with mineral admixtures and built-in carbonate. *Cement and Concrete Composites, 92*, 216-229.

Whitney, D. P. (2008). Chemical admixtures. *Concrete Construction Engineering Handbook. 2nd*, 3-1.

Wu, M., Johannesson, B., and Geiker, M. (2012). A review: Self-healing in cementitious materials and engineered cementitious composite as a self-healing material. *Construction and Building Materials, 28*(1), 571-583.

Yıldırım, G., Şahmaran, M., and Anıl, Ö. (2018). *Determination of Self-Healing Performance of Cementitious Composites Under Elevated CO2 Concentration by Resonant Frequency and Crack Opening Measurements.* Paper presented at the Proceedings of 3rd International Sustainable Buildings Symposium (ISBS 2017).

Zhang, J., Zhou, A., Liu, Y., Zhao, B., Luan, Y., Wang, S., Yue, X., and Li, Z. (2017). Microbial network of the carbonate precipitation process induced by microbial consortia and the potential application to crack healing in concrete. *Scientific Report, 7*(1), 1-10.

Zhang, Z., Provis, J. L., Reid, A., and Wang, H. (2015). Mechanical, thermal insulation, thermal resistance and acoustic absorption properties of geopolymer foam concrete. *Cement and Concrete Composites, 62*, 97-105.

Zhang, Z., Qian, S., and Ma, H. (2014). Investigating mechanical properties and self-healing behavior of micro-cracked ECC with different volume of fly ash. *Construction and Building Materials, 52*, 17-23.

Zhu, H., Zhang, Z., Zhu, Y., and Tian, L. (2014). Durability of alkali-activated fly ash concrete: chloride penetration in pastes and mortars. *Construction and Building Materials, 65*, 51-59.

Chapter 5

5 CRACK SELF-HEALING IN ALKALI-ACTIVATED SLAG COMPOSITES INCORPORATING IMMOBILIZED BACTERIA: EFFECT OF ENVIRONMENTAL EXPOSURE[3]

This chapter investigates the potential of *S. pasteurii* bacteria to impart crack self-healing in alkali-activated slag-based composites. Porous expanded glass granules made from recycled glass were used, for the first time, as bacterial and nutrient carriers. Scanning electron microscopy, Raman spectroscopy, capillary water absorption, and inductively coupled plasma optical emission spectroscopy were deployed to investigate self-healing efficiency in the bio-green concrete under various environmental exposure. Crack width up to 111 μm for moist-dry cured specimens incorporating bacteria were completely healed within 90 days, while no self-healing was observed in the control specimens. The sorptivity coefficient in specimens incorporating *S. pasteurii* bacteria was also much lower. SEM-EDS combined with Raman spectroscopy indicated that the dominant self-healing product was calcite. This study elucidates crack remediation in AAMs and demonstrates the potential of this novel biogenic self-healing system in green concrete structures.

5.1 INTRODUCTION

The compelling demand for curtailing carbon dioxide emissions from the manufacturing process of ordinary portland cement (OPC) has motivated researchers to develop alternative cement-free concrete or "green concrete," thereby mitigating the negative environmental impacts of OPC production. For instance, owing to their lower carbon footprints and enhanced sustainability features, alkali-activated materials (AAMs), geopolymers, and other aluminosilicate binders, have emerged as strong contenders to replace OPC-based construction materials in diverse applications (Zhang *et al*., 2020; Zhang *et al*., 2018).

[3] A version of this chapter was submitted to the *Composites: Part B Engineering*.

Indeed, several studies have reported that the amount of CO_2 emissions from the unit production of AAM is about one-fifth of that from OPC production (Habert *et al*., 2011). AAMs are formed through reactions between aluminosilicate sources and concentrated aqueous alkaline solutions. Aluminosilicate precursors often consist of industrial wastes or by-products (i.e., rice husk ash, fly ash, slag, metakaolin, etc.), thereby alleviating the landfilling and disposal costs of such byproducts. The activator alkali medium for aluminosilicates is commonly made of alkali hydroxide, silicate, or carbonate (Li *et al*., 2019; Ling *et al*., 2019).

Several studies have reported that AAMs can achieve better performance than that of conventional OPC-based materials. For example, Khan *et al*. (2016) developed fly ash-slag geopolymer composites with 108 MPa compressive strength at 28 days via optimizing the activator ratios and curing regimes. Ali *et al*. (2017) reported that alkali-activated concrete achieved superior spalling resistance in fire. Aiken *et al*. (2018) revealed that geopolymer binders showed superior sulfuric acid resistance compared to their OPC counterparts. The application of AAMs for the immobilization of toxic metals was explored by Nikolić *et al*. (2017). They found that hexavalent chromium (Cr (VI)) could be effectively immobilized in alkali-activated fly ash-based composites. In addition, mechanical activation of fly ash resulted in an increase in efficiency of Cr immobilization.

AAMs have been used in several real-life projects including the Brisbane West Wellcamp Airport (Shill *et al*., 2020), the University of Queensland's Global Change Institute (GCI) (Albitar *et al*., 2015), and a high-rise residential building in Chongqing, China (Tang *et al*., 2019).

Nonetheless, AAMs are quasi-brittle materials and demonstrated susceptibility to numerous causes of cracking (Song *et al*., 2016). Previous studies have shown that AAMs exhibit higher drying and autogenous shrinkage than that of OPC-based materials, thus increasing the likelihood of cracking (Ma and Ye, 2015). For instance, Atiş *et al*. (2009) reported that sodium silicate-activated slag mortars exhibited considerably higher drying shrinkage, which reached up to six times that of OPC-based materials.

Cracking-initiated deteriorations pose serious threats to the safety and service life of engineering structures, allowing more rapid ingress of chloride and sulfate ions, and other

hostile substances. This can result in increased damage due to reinforcing steel corrosion, sulfate attack, freeze-thaw damage, and alkali-aggregate expansion. Such damage exacerbates life cycle maintenance and repair costs. However, the implementation of repair is not only associated with about prohibitively high costs but can be difficult if cracks are too fine to be detected or not accessible (Zhang *et al*., 2020). The increasing concern regarding the resilience of AAM infrastructure requires smart and autonomic approaches to address the issue of cracking-initiated deterioration. In this context, smart AAMs with the ability to repair cracks autonomously without human intervention are highly desirable.

Self-healing, a bio-inspired phenomenon observed in biological systems, can enable a material to heal from the infliction of damage (e.g., crack formation) and restore its original functionalities (Fang *et al*., 2021). Accordingly, substantial research has explored in recent years the self-healing behaviour of a variety of materials, from metals to cement-based materials and ceramics. The self-healing of cement-based materials was first discovered by the French Academy of Science in 1836 (Lauer, 1956). Based on extensive research, it is believed that the autogenous healing of cracks in cement-based materials originates from both physical and chemical processes, such as swelling of C-S-H, carbonation of calcium hydroxide, and further hydration of unreacted cement particles (Roig-Flores *et al*., 2021). However, numerous studies have shown that complete autogenous healing of cement-based materials cannot normally be observed in cracks having a width of more than 300 μm. To address this challenge, numerous approaches have been implemented to endow cement-based materials with remarkably enhanced self-healing capability, from the incorporation of superabsorbent polymers (SAP) (Gwon *et al*., 2019), encapsulated expansive minerals (Ren *et al*., 2021), to the microbially induced calcium carbonate precipitation (MICCP) (Su *et al*., 2020).

MICCP, a ubiquitous microbial metabolic activity in nature, is performed by alkaliphilic bacteria involving a ureolytic process to induce calcium carbonate ($CaCO_3$) formation (Pungrasmi *et al*., 2019; Skorupa *et al*., 2019). MICCP has been widely employed in numerous engineering applications, such as industrial wastewater treatment (Hammes *et al*., 2003), soil stabilization (Lauchnor *et al*., 2013), and metal remediation (Kurmaç, 2009). Recently, MICCP has attracted much attention as a novel approach to repair cracks in cementitious materials. This technique could confer new possibilities to mitigate cracks in

concrete structures, thereby prolonging structural service life. Extensive research on MICCP in cement-based materials has been undertaken. For instance, Wiktor and Jonkers (Wiktor and Jonkers, 2011) introduced *B. alkalinitrilicus* endospores into concrete to remediate microcracks. They found that the maximum width of completely healed cracks in specimens incorporating the bacteria was 460 μm, which was considerably larger than that in reference specimens (180 μm). Similarly, the crack self-healing capability was studied by Nguyen *et al.* (2019) using *B. subtilis*, which showed that the microbial adjuvant in concrete mixtures resulted in a marked decrease in porosity, thereby leading to an increase in mechanical properties as well as reduces mass transport properties. Complete sealing of crack widths of up to 400 μm was observed after 44 days. Yet, it remains challenging for ureolytic micro-organisms to tolerate the harsh environmental stressors in cementitious matrices characterized by very high pH, oxygen depletion, and desiccation. Such environmental factors affect the ureolytic activity, thereby jeopardizing the implementation of the MICCP process for crack self-healing (Seifan and Berenjian, 2018). For example, Jonker *et al*. (2010) directly mixed a group of genus *Bacillus* alkaliphilic spore-forming bacteria with the cement paste. No active bacterial spores were observed after 4 months.

The increasing concern regarding microbial survival and their associated long-term autonomous repair of cracks has led to the advent of novel techniques to protect the bacteria. Encapsulation or immobilization of the micro-organisms has been proposed as a preferable method to provide a protective carrier, thus increasing the viability of the bacteria. The encapsulation and immobilization approaches include lightweight porous aggregates (LWAs) (Wiktor and Jonkers, 2011), silica gel (Wang *et al*., 2012), polyurethane (Bang *et al*., 2001), modified sodium alginate (Wang *et al*., 2015), and hydrogel (Wang *et al*., 2014a). For instance, Alazhari *et al*. (2018) immobilized *B. pseudofirmus* spores and their nutrients with coated expanded perlite. The results suggest that 20% coated expanded perlite partial replacement for fine aggregates could achieve crack self-healing when calcium sources (e.g. calcium acetate) were sufficient. Wang *et al.* (2014a) encapsulated *B. sphaericus* spores into hydrogels to investigate the crack self-healing efficiency. It was shown that mortar specimens incorporating hydrogel-encapsulated microorganisms exhibited crack width self-healing of up to 500 μm. In addition, the water permeability in the bacterial specimens decreased by 15-55% compared to that of the reference specimens. In recent work, Zamani *et al*. (2020) synthesized a polyurea polymer to provide encapsulation of *B. pseudofirmus* for facilitating

MICCP. It was concluded that the polyurea microcapsules succeeded to provide protection and nutrients for the microorganisms to germinate and precipitate calcium carbonate.

While crack self-healing in cement-based materials has been a topic of extensive research, very few studies have so far investigated the self-healing of AAMs (Nguyễn *et al*., 2018; San Nicolas *et al*., 2014; Zhang *et al*., 2020). Although the efficacy of MICCP in cement-based materials has been well-documented and understood, there remains doubts and ongoing controversy regarding whether MICCP is applicable and viable in AAM systems. As such, systematic and rigorous research is needed to acquire a better understanding of the efficiency of the MICCP technique implemented in AAM and to elucidate the crack self-healing capability of AAMs, thereby potentially prolonging the service life of alkali activated concrete structures.

In the present study, ground granulated blast furnace slag (GGBFS) was used as a precursor for the preparation of alkali-activated concrete. Porous expanded glass granules (EG) from the recycled glass industry were used, for the first time, as a carrier of spores and nutrients to protect the bacteria and trigger crack self-healing. In addition, the effect of different environmental exposures on self-healing was investigated. This study provides a new understanding of MICCP in the crack remediation of AAMs and demonstrates the potential of this novel EG-based biogenic self-healing system in green concrete structures.

5.2 MATERIALS AND METHODS

5.2.1 Bacterial strain selection and growth media

The matrix of fresh AAMs is highly alkaline due to the existence of alkaline activators. The pH value of the capillary solution within the matrix is usually above 12. As such, the bacteria incorporated into the AAM matrix should be alkalinity tolerant. The microorganisms should also be oxygen-tolerant since AAMs are oxic due to oxygen ingress through capillary pores. Therefore, aerobic alkaliphilic spore-forming microorganisms within the bacterial genus *Bacillus* were considered. According to the statistical percentage of bio-based cementitious materials incorporating bacteria in the last decade, *S. pasteurii* was one of the most widely used microorganisms in a variety of cement-based materials. Gram-positive bacterium *S. pasteurii* (ATCC 11859) was used

in the present study. The *S. pasteurii* was cultured in a liquid medium consisting of yeast extract (20.0 g/L), $(NH_4)_2SO_4$ (10.0g/L), and tris buffer (0.13 M). The nutrients were sourced from Fisher Scientific International, Inc. All ingredients were dissolved in distilled water and then autoclaved separately at 120 °C for 20 min before preparing the growth media. After combining all nutrient solutions, the pH value of the medium was adjusted to 9 by adding 1M HCl solution. *S. pasteurii* cells were inoculated in the medium and incubated aerobically in a shaking incubator with 180 rpm at 30 ± 2 °C. Sample aliquots were taken from the media periodically and inoculated on agar petri dishes. **Figure 5-1** schematically depicts the process of culturing *S. pasteurii*.

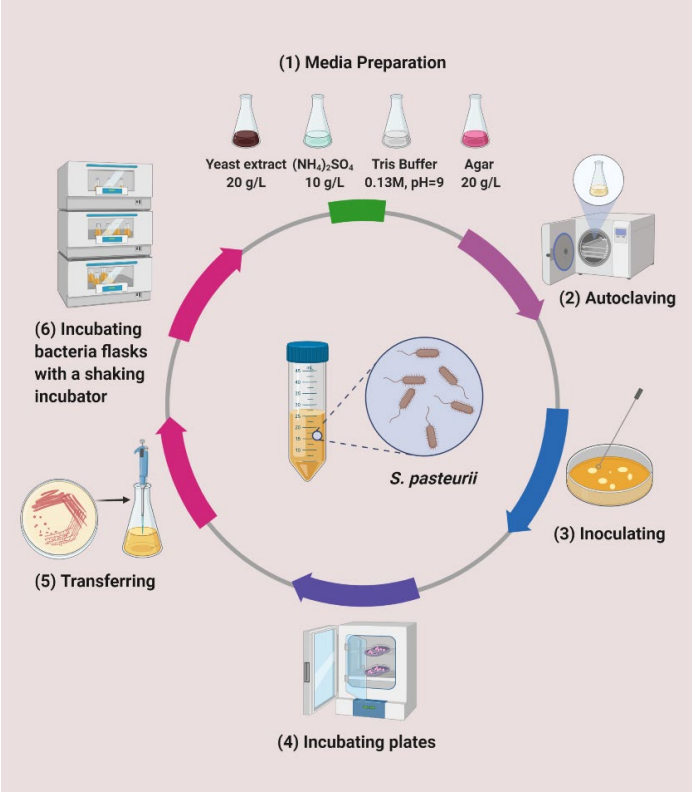

Figure 5-1: Schematic illustration of *S. pasteurii* culture.

5.2.2 Determination of *S. pasteurii* concentration

The concentration of the bacterial solution was calculated based on optical density measurement at 600 nm (OD_{600}) using a SPECTRONIC™ 200 spectrophotometer (Thermo Scientific™). OD_{600} measurement is preferable since the 600 nm wavelength causes little damage to the bacteria and does not hinder its growth. For this purpose, the medium without *S. pasteurii* was selected as blank. Thus, the OD_{600} value of a quantity of 0.5 mL blank solution was set as zero. 0.5 mL of the medium with the bacteria was taken each time at intervals and serially diluted (10^0-10^5) in broth tubes (see **Figure 5-2**). Thereafter, it was vortexed to achieve homogeneity before measuring OD_{600}. During the dilution, each 0.5 mL sample was inoculated on petri dishes simultaneously for viable plate counts, representing colony-forming units (CFU/mL). The absorbance of the cells was correlated with CFU counts. CFUs were counted after 3-d. Each count and reading of OD_{600} was triplicated. The concentration of the microorganisms can be determined via **Eq. 5-1** using the results shown in **Figure 5-3,** where, Y is the absorbance reading at OD_{600}, and X is the CFU per mL. The final concentration (10^7 CFU/ml) of *S. pasteurii* in the medium was determined, and the preparation was ready for mixing.

$$Y = 2\text{E-}7X + 0.0154 \qquad \text{Eq. 5-1}$$

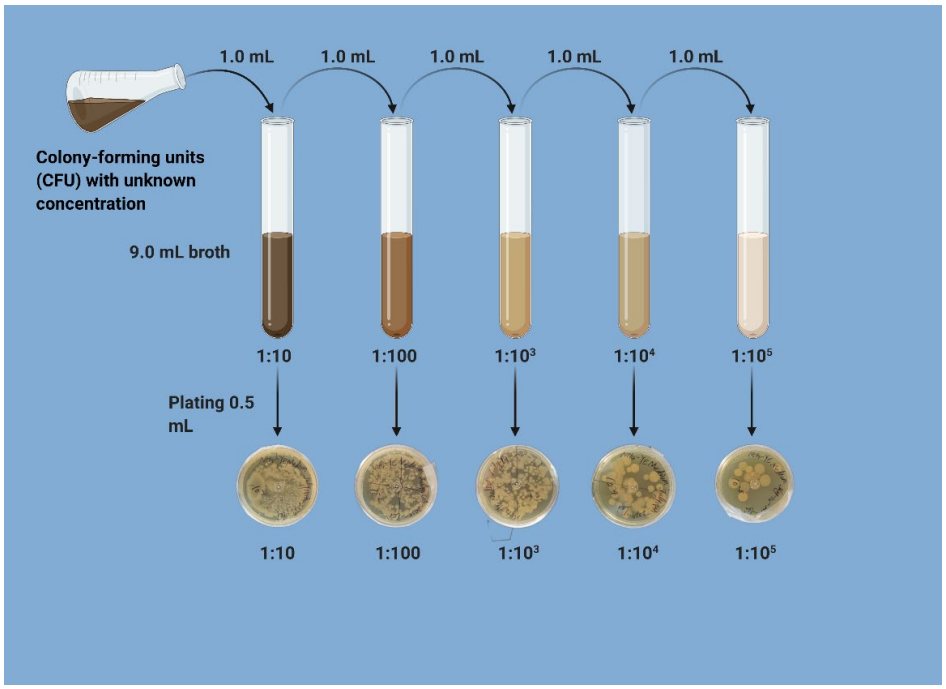

Figure 5-2: Schematic of serial dilution.

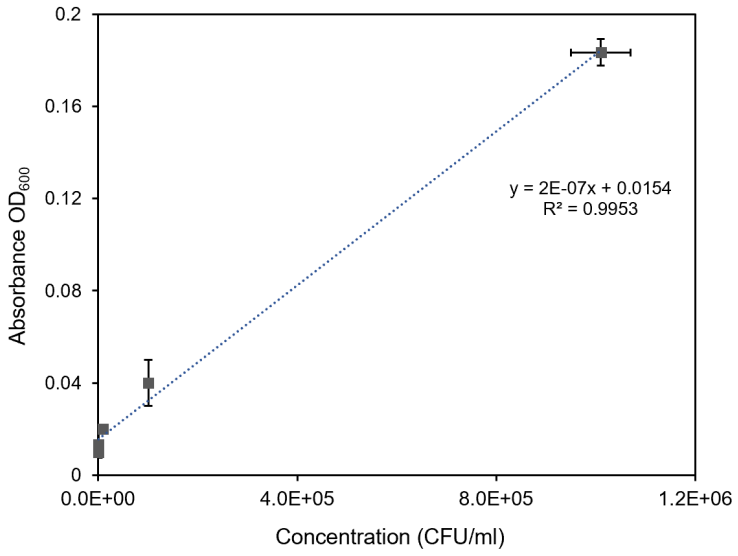

Figure 5-3: Correlation between cell concentration and absorbance at OD600.

5.2.3 Raw materials

In this study, ground granulated blast furnace slag (GGBFS) sourced from Lafarge, Canada was used as the AAM precursor to produce the binders. Its chemical composition and physical properties are given in **Table 5-1**. The particle size distribution of the GGBFS obtained via a Malvern laser diffraction particle analyzer is shown in **Figure 5-4**. The alkali-activation of the GGBFS was carried out using a combination of sodium hydroxide pellets (analytical specification) and sodium silicate solution ($Na_2O(SiO_2)x \cdot xH_2O$) consisting of with 8% Na_2O, 27% SiO_2, and 65% H_2O by mass. The silica modulus of the sodium silicate solution (M_s = molar SiO_2/Na_2O) ratio was 3.5. E-Glass (EG) was used as the carrier for *S. pasteurii* spores and nutrients. It is made from recycled glass to enhance sustainability. EG exhibits excellent characteristics regarding high porosity and ultra-lightweight. The morphology of EG is depicted in **Figure 5-5**. Two types of grain sizes for EG were used in this study. EG with grain size of 0.5-1 mm consisted of 25% of the total weight, and EG with grain size of 1-2.5 mm occupied 75% of the total weight. River sand was used as aggregate. The properties of both EG and river sand are given in **Table 5-2**. Polyvinyl alcohol (PVA) fibres were incorporated into the mixture to control cracks and enhance the crack self-healing. A polycarboxylate-based superplasticizer (SP) with a specific gravity of 1.06 was used to achieve a suitable flowability of alkali-activated concrete. The physical and mechanical properties of the mixtures are provided in **Table 5-3**.

Table 5-1: Chemical and physical properties of GGBFS

Properties	Item	GGBFS
Chemical	Silicon oxide (SiO_2) (%)	35.42
	Aluminum oxide (Al_2O_3) (%)	9.65
	Ferric oxide (Fe_2O_3) (%)	0.41
	Calcium oxide (CaO) (%)	45.40
	Magnesium oxide (MgO) (%)	1.00
	Sulfur trioxide (SO_3) (%)	3.11
	Sodium oxide (%)	0.33
	Specific gravity	2.90
Physical	Blaine fineness (m^2/kg)	399
	Retained on 0.045 mm (%)	0.40
	Slag activity index (%)	104

Table 5-2: Properties of EG and river sand

	Bulk density (kg/m^3)	Specific gravity	Maximum aggregate size
River sand	1.67	2.65	2
EG (0.5-1	0.27	0.38	1
EG (1-2.5	0.22	0.5	2.5

Table 5-3: Mechanical properties of PVA fibres

Mechanical properties	Ultimate tensile strength (MPa)	Diameter (mm)	Density (kg/m^3)	Length (mm)	Young's modulus (GPa)	Elongation (%)
PVA	1620	0.039	1300	12	43	6

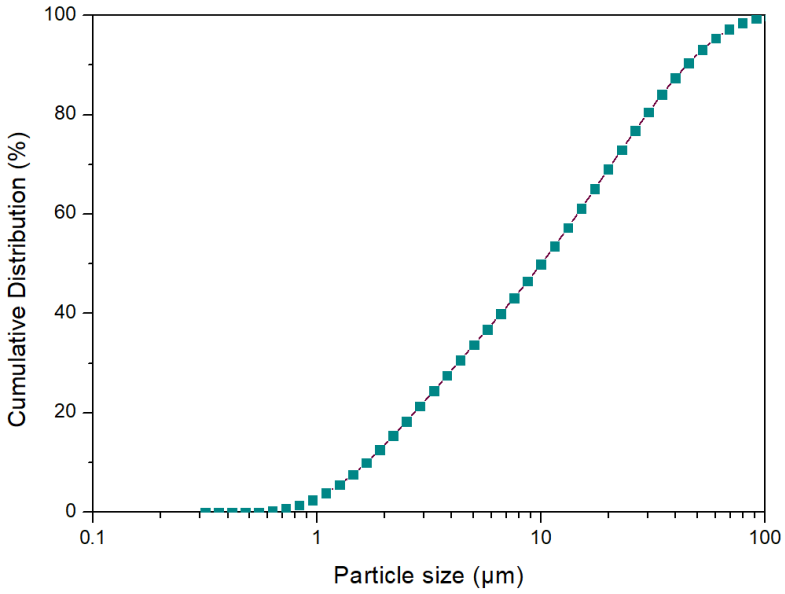

Figure 5-4: Particle size distribution of GGBFS used in this study.

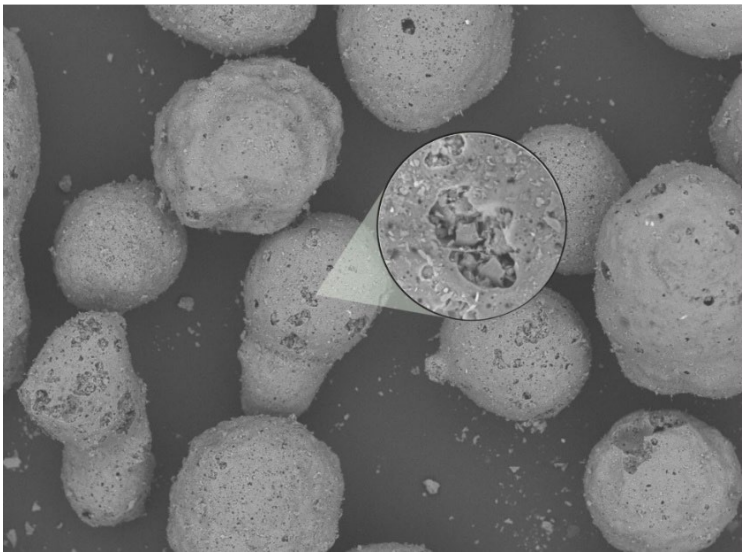

Figure 5-5: Morphology of EG particles using a scanning electron microscope.

5.2.4 Immobilizing bacteria in EG

The bacterial solution, urea, and calcium lactate were immobilized into EG through the vacuum impregnation method. Figure 6 illustrates the vacuum impregnation system. EG particles were placed inside a chamber connected with a vacuum gauge to evacuate air inside of the chamber. Then the valve of the separation funnel was opened to permit the impregnating liquid to flow into the chamber. In the first treatment, EG was first impregnated with a combination of calcium lactate solution (60 g/L) and urea solution (20 g/L), followed by vacuum impregnation with the *S. pasteurii* spore suspension. In the second treatment, the EG was only impregnated with the calcium lactate solution and urea solution. After each impregnation, EG particles were dried for 2-d at 30 °C until the mass change was within 0.5%.

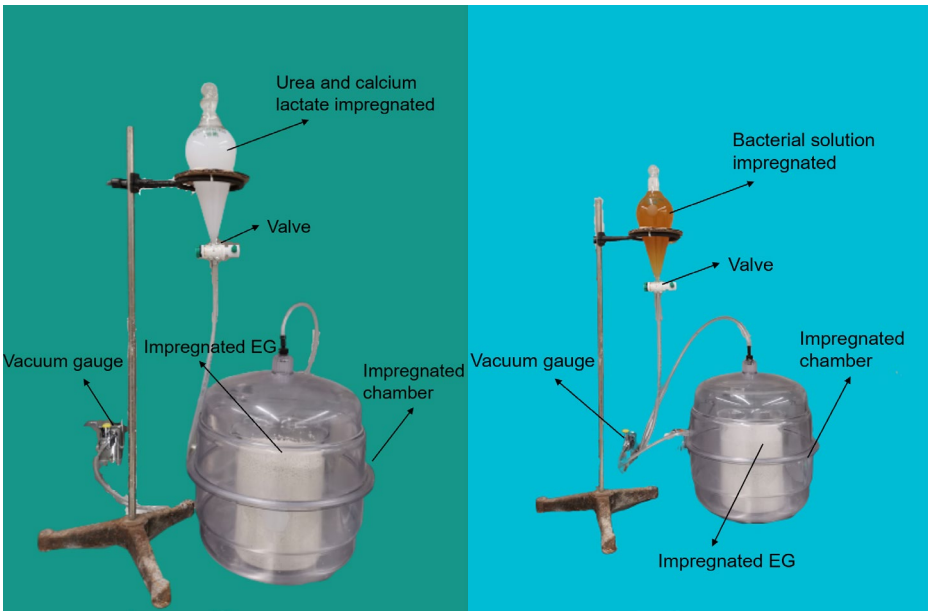

Figure 5-6: Vacuum impregnation setup.

5.2.5 Mixture design and specimen preparation

Five types of alkali-activated slag-based (AAS) composites were prepared, including (a) normal green concrete incorporating EG (referred as EG-N); (b) green concrete incorporating EG with only the media, urea, and calcium lactate (referred as EG-MUC); (c) bacterial green concrete incorporating EG with urea and calcium lactate (referred as EG-B); (d) bacterial green concrete adding urea and calcium lactate directly (referred as 0-B); and (e) normal green concrete (referred as 0-N). The five mixture proportions are given in **Table 5-4**.

For each mixture, 157g of NaOH pellets were first dissolved in 392 mL water to prepare 10M liquidous activator. A cover was used to prevent carbonation. The solution was obtained after being shaken for 5 min. Then it was ready cooled until the temperature decreased to room temperature (20 ± 2 °C). A planetary mixer (Hobart, Canada) was used for mixing to obtain homogeneous AAS composites. After 1 min of pre-mixing of the raw materials, except for EG, the activators were supplied at a low mixing speed of 165 rpm. The mixing continued at 165 rpm for 1 min after adding 1465g of water containing the SP and at a medium speed of 300 rpm for another 3 min. Finally, all EG particles

were added, and the mixing resumed for another 2 min at 165 rpm to avoid crushing the EG particles.

The fresh mixtures were cast in different types of molds intended for various tests. Small disk-shaped specimens (50-mm diameter and 15-mm height) were prepared for surface crack width observations and analysis of self-healing compounds. Large disk-shaped specimens (100-mm diameter and 50-mm height) were made for water absorption tests. Cubic 50-mm specimens were cast for measuring compressive strength, electrical conductivity, pH, and concentration of calcium ions. Cylindrical specimens (50-mm diameter and 100-mm height) were made for split tensile tests. All filled molds were vibrated then sealed with covers to prevent water evaporation. After 24h, all specimens were demolded and subsequently moist-cured at a controlled temperature of 20 ± 1 °C and ≥ 98 % RH for 14-d.

Table 5-4: AAS composite mixture proportions

Mixture ID	Slag (g)	Sand (g)	EG (g)	NaOH (g)	Sodium silicate (g)	Water (g)	Fibre (g)	SP (g)	Bacteria (ml)	Calcium lactate and urea (ml)
EG-N	4500	6500	250	157	285	1857	30	22.5	-	-
EG-MUC	4500	6500	250	157	285	1857	30	22.5	-	150
EG-B	4500	6500	250	157	285	1857	30	22.5	300	150
0-B	4500	6750	-	157	285	1407	30	22.5	300	150
0-N	4500	6750	-	157	285	1857	30	22.5	-	-

5.2.6 Creation of cracks and environmental exposures

After 14-d of incubation in the curing room, small disk-shaped specimens were pre-cracked using a screw jack. The effect of incubation conditions on the self-healing development in alkali-activated slag-based composites was investigated. The pre-cracked EG-B specimens were exposed to two environmental exposures: (1) 22 ± 1°C with immersion in deionized water; and (2) exposure at 30 ± 1 °C under wetting-drying cycles. The Barnstead Easypure RoDi water purification system was used to provide deionized water. The second group specimens were immersed in deionized water within a digitally

controlled walk-in environmental chamber (Burnsco Technologies INC., Canada) and subjected to a temperature of 30 ± 1 °C and RH of 80%. The specimens were taken out of the chamber every 2-d and then exposed to the air at RH of 80% for 3h. The rest of the specimens were only subjected to the former exposure.

5.2.7 Experimental procedures

Various testing conditions, including various pH levels (9, 10, 11, 12, and 13), were prepared to investigate the viability of *S. pasteurii*. The schematic of the viability test is shown in **Figure 5-7**. First, the bacteria were incubated in a shaking incubator for 3-d at 130 rpm and 30 °C before transfer into the prepared bacterial medium. Each falcon tube was then filled with 9 mL medium. The pH values ranged from 9 to 13 and were adjusted using HCl or NaOH solutions. After injecting 1-mL microbes into the pH-modified medium, all falcon tubes were covered and moved to a shaking incubator for another 2-d at 130 rpm and 30 °C. The OD_{600} was finally measured.

Ureolytic activity can be determined by electrical conductivity since *S. pasteurii* containing urease transforms non-conductive urea into conductive ammonium and carbonates (Tian *et al*., 2018). **Figure 5-8** depicts the testing procedure for the test. 0.18g urea and 0.72g calcium lactate were added into each tube before transferring the 1-mL bacterial solution. Similar to the above-mentioned viability test, the electrical conductivity of the solution in each falcon tube was measured using an AB200 pH/Conductivity Benchtop Meter (Thermo Fisher Scientific, USA) before and after the incubation.

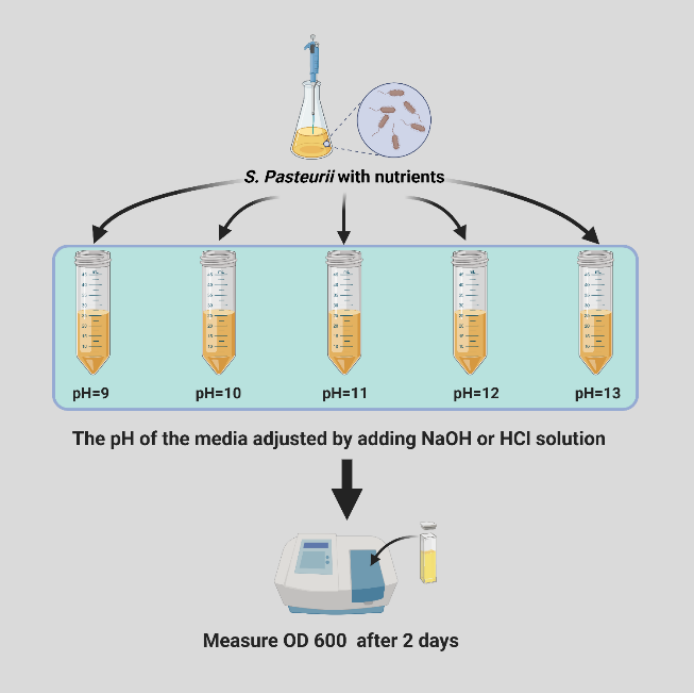

Figure 5-7: Schematic of bacterial viability test.

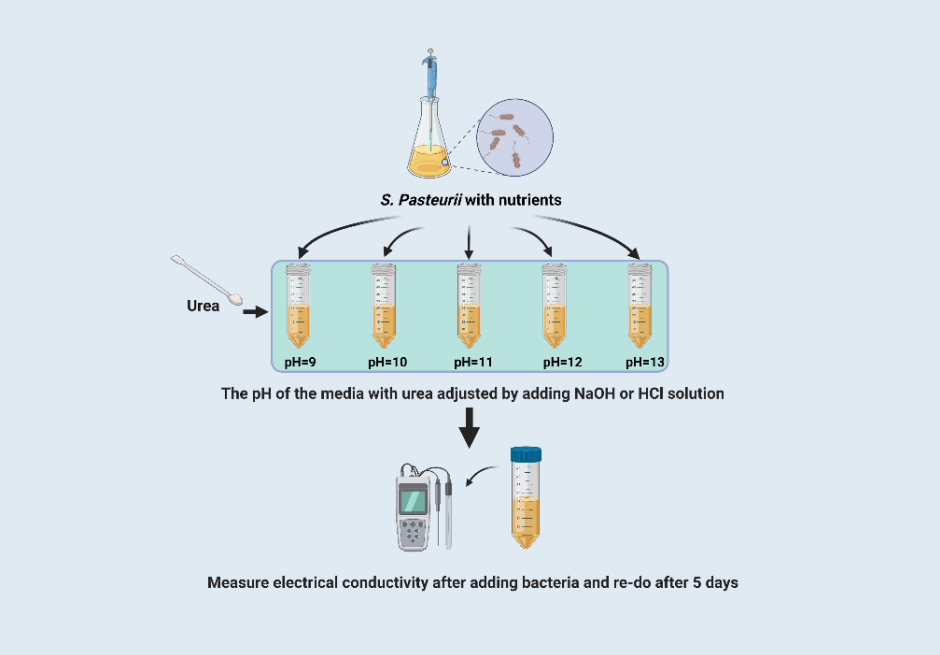

Figure 5-8: Schematic of the ureolytic activity test.

Several studies have revealed that calcium ions dissolved from the cementitious matrix and the pH value of the surrounding environment play a critical role in calcium precipitation, thereby facilitating crack self-healing (Feng *et al*., 2019; Huang *et al*., 2013; Jiang *et al*., 2015; Sisomphon *et al*., 2012; Zhang *et al*., 2020). In this study, cylindrical specimens from each batch were half-broken at the age of 14-d using a split tensile test. Then the specimens were cured under deionized water. The concentration of calcium ions was quantified at time intervals using a Vista Pro inductively coupled plasma optical emission spectroscopy (ICP-OES) (Agilent Technologies Inc., USA). The pH value and electrical conductivity were analyzed using the pH/conductivity benchtop meter accordingly. To determine both compressive strength and split tensile strength, cubic specimens (50 × 50 × 50-mm) and cylindrical specimens (50-mm diameter and 100-mm height) were tested at 7, 14, and 28-d, according to ASTM C109 and ASTM C496. All tests were performed using three identical specimens, and the average values with the standard deviation were reported.

The width change of the surface cracks was monitored using a digital microscope (Jiusion, China). Multiple locations along the crack on both surfaces of small disc-shaped specimens were selected and marked for measurement. All marked positions were examined before the exposure conditions and after 90-d of healing. The crack closure ratio (*CCR*) was calculated using **Eq. 5-2**, where; *CCR* = crack closure ratio; w_0 = initial crack width; and w_t = crack width after environmental exposures at time *t*:

$$CCR\ (\%) = (w_0 - w_t) / w_0 \qquad \text{Eq. 5-2}$$

To quantify the resistance of specimens after incubations to water penetration, the water absorption test (**Figure 5-9**), based on ASTM C1585, was carried out on large disc-shaped specimens at the age of 90-d. Before the test, all specimens were dried using a ventilated oven at 50 °C until the mass change was less than 0.1% during 72-h. The side surface of all specimens was coated with silicone to ensure that only one surface could be in contact with water. The specimens were then placed in 5-mm deep water, and the mass of the specimens was recorded at regular time intervals after drying the wet surface with a damp towel. Absorption was calculated by **Eq. 5-3**. The sorptivity coefficient, defined

as the slope of the curve of absorption, I versus the square root of time, $t^{1/2}$, was used to characterize the sorptivity capacity, as calculated using **Eq. 5-4**. The mass change within 6-h was recorded since the cumulative water absorption increases considerably in the first 6-h, and the trend approaches linear behaviour.

$$I = \frac{m_t}{a \times d} \quad \text{Eq. 5-3}$$

$$S = \frac{I}{\sqrt{t}} \quad \text{Eq. 5-4}$$

where, m_t = mass change (g) in the specimen at a time t; a = cylinder area in contact with water in mm^2; and d = density of the water in g/mm^3.

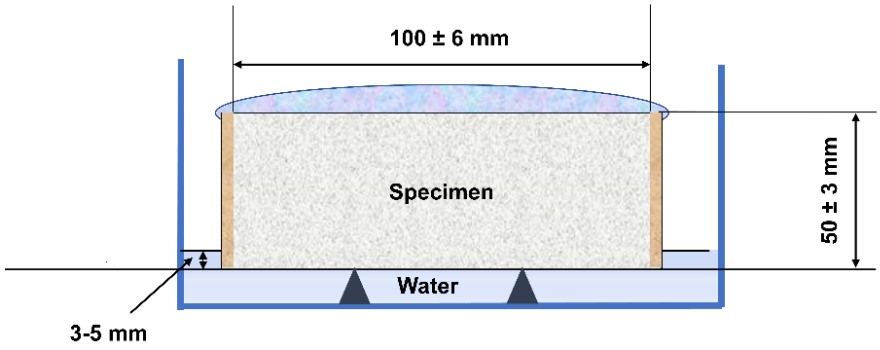

Figure 5-9: Schematic of water absorption test.

Characteristics of the healing compounds were analyzed using a Hitachi TM3030Plus electron microscope at an accelerating voltage of 15 kV coupled with EDS. Specimens for SEM-EDS were dried in a vacuum desiccator for 2-d before gold-coating treatment. Moreover, a confocal Renishaw InVia Reflex Raman spectrometer with a 50× objective lens was employed to identify the polymorphs of the healing compound within the crack mouth and the surface of PVA fibres. Raman spectra were collected in the 139-1800 cm^{-1} spectral range with a 765 nm excitation wavelength. During measurements, three accumulations of 5s exposure were used.

5.3 EXPERIMENTAL RESULTS

5.3.1 Bacterial survivability and urease activity

Figure 5-10 shows the concentrations of *S. pasteurii* spores after 2-d exposure under various pH levels. The viability of the microorganisms was highly affected by pH values since their concentration dramatically decreased when the pH values increased from 9 to 13. Remarkably, few bacteria survived under pH 13. This demonstrates that a conducive pH for *S. pasteurii* multiplication was around 9 within the explored range of 9 to 13, and any pH value higher than 9 would negatively affect bacteria viability. A carrier for protecting the bacteria from the high pH environment is therefore essential to maintain bacterial survival. **Figure 5-11** depicts the kinetics of urea hydrolysis by *S. pasteurii* exposed to different pH levels. The correlation between the solution electrical conductivity before and after urea hydrolysis and the pH range of 9-13 demonstrates strong dependence on the pH level, with the highest increase in electrical conductivity observed at pH = 9. It can be observed in **Figure 5-11** that the increase in electrical conductivity at pH = 9 was around 120%. However, the conductivity dropped rapidly when the pH increased beyond 9.

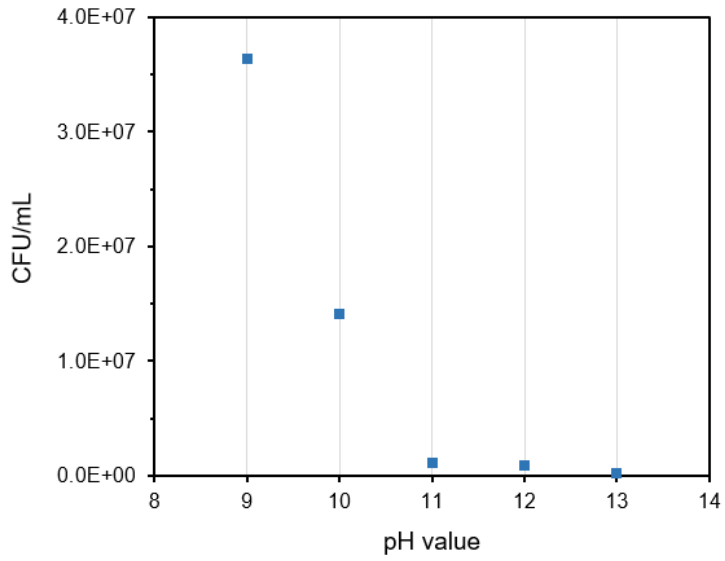

Figure 5-10: Concentrations of *S. pasteurii* spores exposed to different pH levels for 2-d.

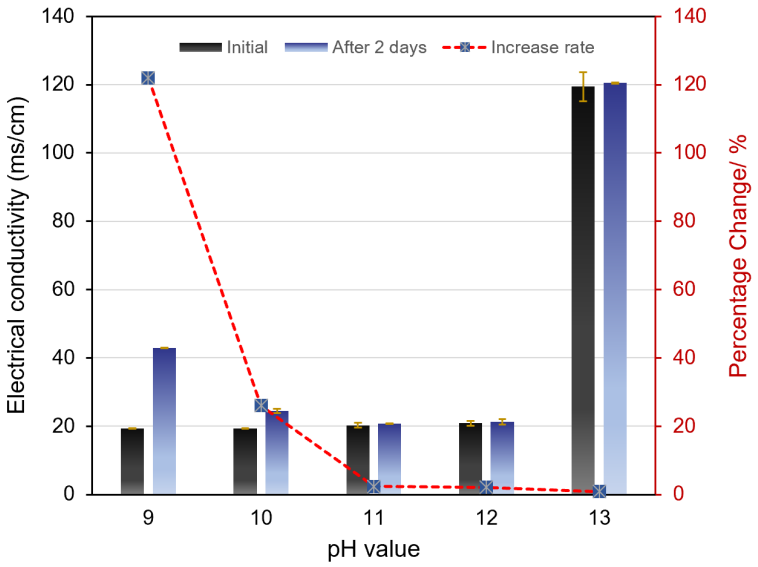

Figure 5-11: Change of electrical conductivity reflecting urease activity under various pH levels.

5.3.2 Crack closure ratio

Figure 5-12 displays the microscopic observation of surface cracks in various types of specimens upon cracking and after 90-d of exposure to different environmental conditions. In addition, binarization was used via Origin 8.5 Pro (Zhang *et al*., 2020) to extract the target area (crack area), thereby better distinguishing the cracks from exterior materials. As for the bacteria-based specimens (EG-B), considerable self-healing was observed near the crack mouth; however, reference specimens (EG-N) and specimens incorporating bacterial culture media and nutrients (EG-MUC) exhibited limited crack self-healing potential. As shown in **Figure 5-12 (a)** and **(b)**, the type of environmental exposure plays an important role in crack self-healing efficiency since the specimens subjected to relatively higher temperature and wet-dry cycles in the environmental chamber showed more precipitates filling the crack. The relationship between the crack closure ratio and initial crack width for four mixtures is depicted in **Figure 5-13 (a)**. All specimens showed a comparable trend regarding this relationship, whereby the larger the initial crack width, the lower was the crack closure ratio. In addition, the bio-specimens showed much higher crack healing since many cracks widths under 100 µm achieved 100% crack closure ratio. The crack closure ratio versus an initial crack width of 50 µm,

100 μm, and 150 μm was determined by a fitted curve as shown in **Figure 5-13 (b)**. The specimens exposed to a relatively higher temperature and wet-dry cycles (EG-B-Environmental chamber) achieved a higher crack closure ratio than that of specimens subjected to water submersion under room temperature (EG-B-Water). For example, the crack closure ratio was 58.6% when the initial crack width was 150 μm in group EG-B-Environmental chamber, which is 10% larger compared with the ratio in group EG-B-Water. In addition, the specimens incorporating nutrients (EG-MUC) did not attain significant improvement in surface crack self-healing, indicating less than 10% increase in the crack sealing ratio compared to that for EG-N specimens when the crack width was 150 μm.

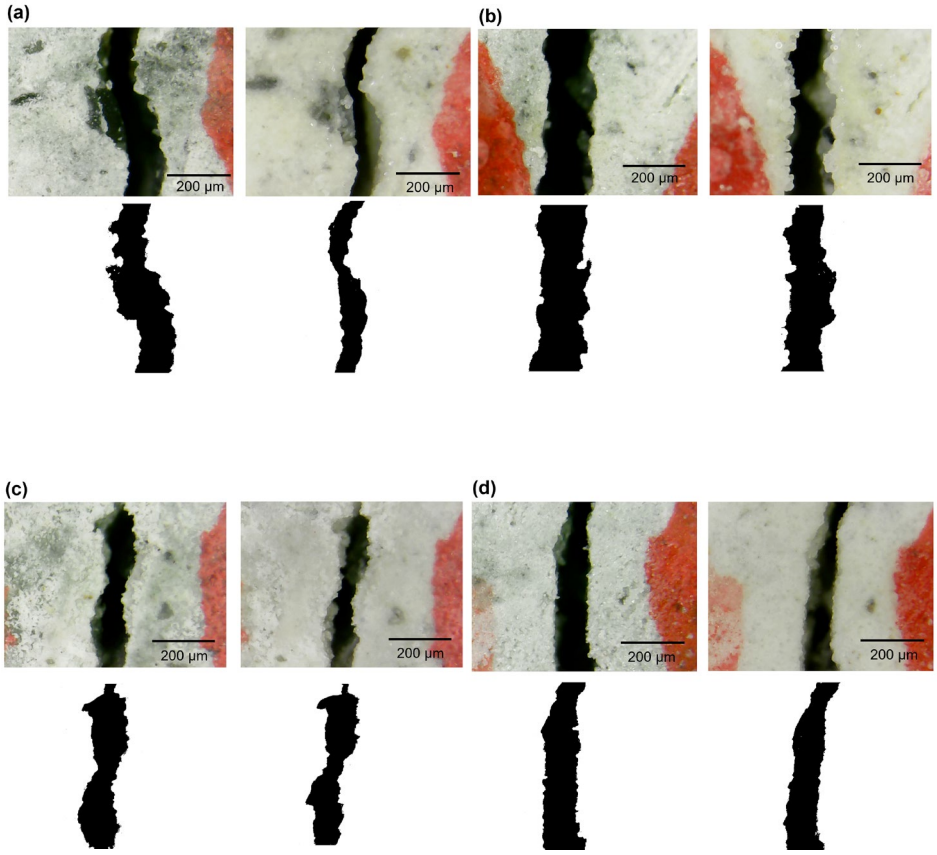

Figure 5-12: Typical photomicrographs and corresponding binary figures showing crack healing before and after 90-d incubations: (a) EG-B (Environmental chamber); (b) EG-B (Water); (c) EG-MUC; and (d) EG-N.

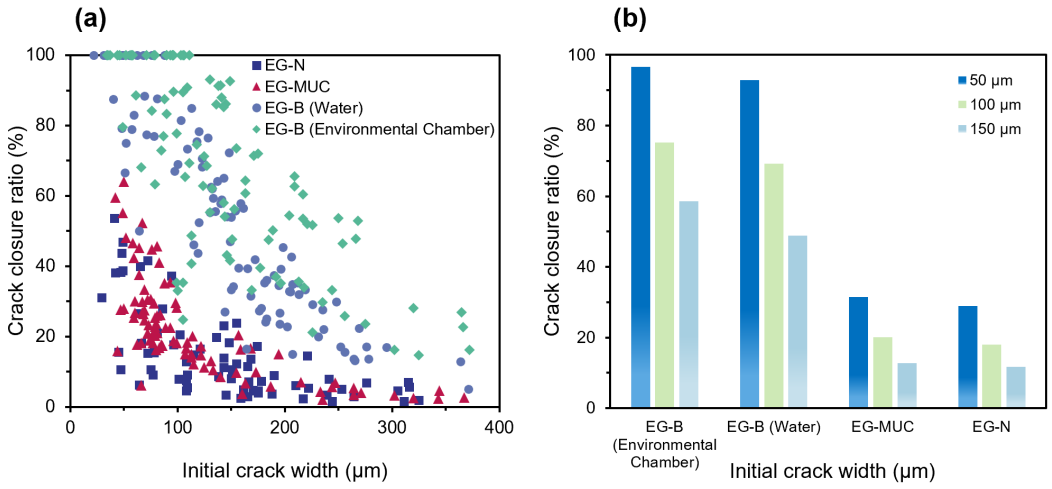

Figure 5-13: Relationship between initial crack width and crack closure ratio for the four groups: (a) non-linear fitting of the typical relationship between crack closure ratio and initial crack width; (b) effect of original crack width on crack closure ratio determined from Figure 5-13 (a).

5.3.3 Mechanical properties

Figure 5-14 depicts the influence of the EG aggregates and the bacteria spores on the compressive strength and splitting tensile strength at 7, 14, and 28-d. Incorporating EG had a negative effect on both the compressive and splitting tensile strengths. It can be observed that the mechanical properties of the EG-N, EG-B, and EG-MUC specimens were significantly lower than that of the 0-B and 0-N specimens. Direct addition of the bacterial solution in mixtures (e.g., 0-B) also negatively affected the mechanical properties compared with that of control neat composites (e.g., 0-N). For example, the compressive and splitting tensile strengths of group 0-B specimens were 7.1% and 7.0% lower than that of 0-N specimens, respectively at the age of 28 days. In contrast, the bacteria immobilized into EG compensated for the decrease in the mechanical properties caused by the combination of bacterial nutrients and increased slightly at later ages (28-d). For instance, the splitting tensile strength at 28-d of EG-B was around 5.4% higher than that of EG-MUC.

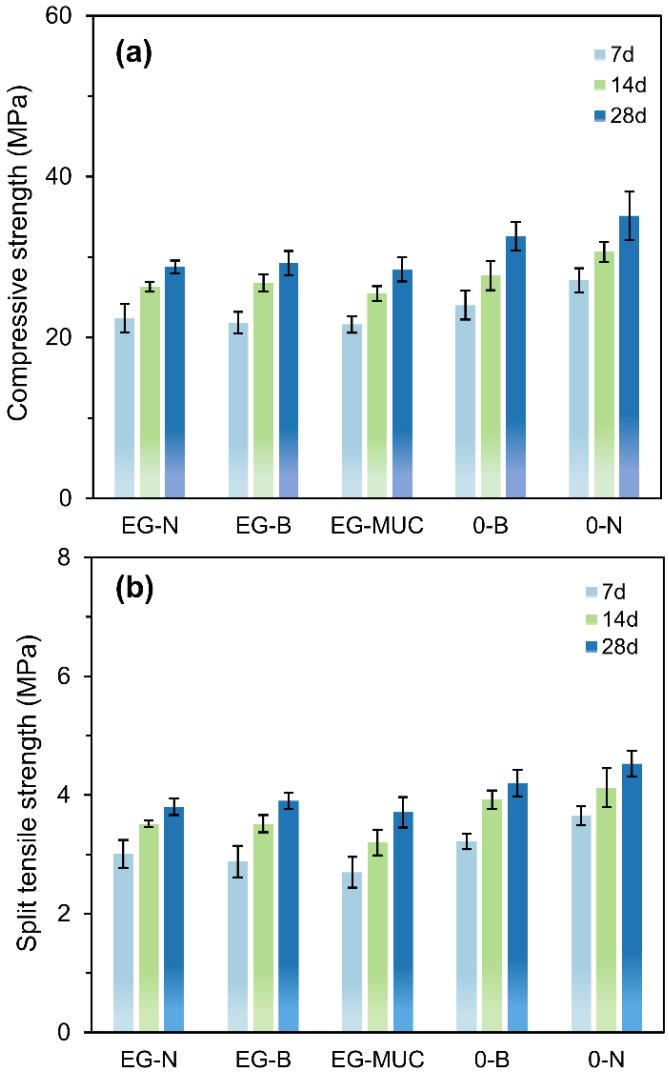

Figure 5-14: Mechanical properties: (a) compressive strength, and (b) splitting tensile strength; error bars represent the standard deviation for triplicate specimens.

5.3.4 Capillary water absorption

Figure 5-15 illustrates the influence of MICCP and environmental exposure conditions on the capillary water absorption after 90-d. The addition of bacteria as a self-healing mechanism decreased capillary water absorption of the tested specimens. For example, the specimens treated with bacteria (EG-B) attained a significant decrease in the sorptivity coefficient compared with that of the reference specimens (EG-N). The specimens treated with nutrients, urea, and calcium lactate (EG-MUC) did incur significant improvement in water-tightness since both the EG-MUC and EG-N specimens had similar slope (0.0106 mm/ $sec^{1/2}$), indicating comparable rate of water absorption. The results also demonstrate that environmental exposure performed an essential role in improving capillary water absorption. As can be observed in **Figure 5-15**, the specimens exposed to a higher temperature and wet-dry cycles (EG-B-Environmental chamber) achieved a slight reduction in water absorption compared with that of the specimens immersed in water (EG-B-water) under normal room temperature. For instance, the sorptivity coefficient of the EG-B-Environmental chamber was 0.0068 mm/ $sec^{1/2}$, about 11.7% lower than that of EG-B-Water, which was 0.0077 mm/ $sec^{1/2}$.

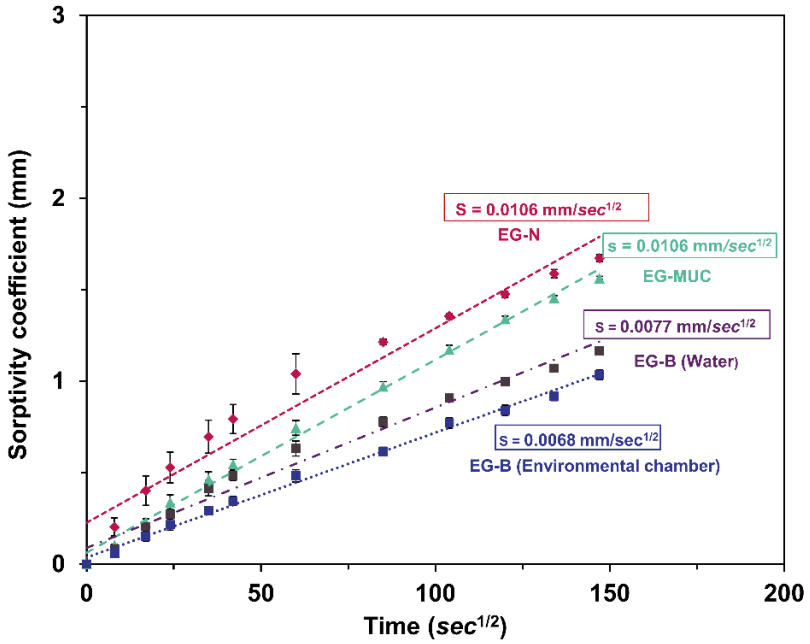

Figure 5-15: Effect of MICCP and incubation method on water absorption of alkali-activated slag-based mortars.

5.3.5 SEM-EDS results

Figures 5-16 and **5-17** show SEM images of typical self-healing compound within cracks and on the surface of PVA fibres located near cracks for four different mixtures. It can be observed that the self-healing products in the bacterial specimen groups (EG-B-Environmental chamber and EG-B-Water submersion), were distinct from their bacteria free counterparts (EG-N and EG-MUC) and appeared much denser and compact. In addition, the crystal size for MICCP specimens was larger than that under the autogenous healing process. This is consistent with findings of Mitchell *et al*. (2006a and 2013) who found that calcium carbonate crystals formed via MICCP were typically larger and less soluble than those precipitated under the same conditions of abiotic solution phase. **Figures 5-16 (a)** and **(b)** indicate that higher incubation temperature and water-dry cycles could accelerate the metabolism of *S. pasteurii*, thereby resulting in more densely stacked crystal growth with clusters resembling deformed lamellar rhombohedra. Some cubic and needle-like amorphous crystals were loosely intermingled within cracks. In **Figure 5-17**, all PVA fibres in the four specimen groups were covered by cubic and irregular polyhedron-like crystals, indicating the beneficial role played by PVA fibres as nucleation sites. EDS conducted via Quantax 400 software (Zhang *et al*., 2020) revealed that the self-healing compounds within cracks, as labelled in **Figures 5-16** and **5-17,** were comprised of three main elements: calcium, carbon, and oxygen, suggesting the existence of calcium carbonate as the dominant self-healing product. Noticeably, a little amount of silicon and aluminum (**Table 5-5**) was found in EG-N and EG-MUC and may arise from calcium-alumino-silicate-hydrate (C-A-S-H) as the hydration product of alkali-activated slag. This is in line with the observations by Nguyễn *et al*. (2019).

Table 5-5: Chemical compositions of the healing materials

Position	Atomic element composition (%)						
	Ca	C	O	Al	Si	Mg	Na
P1	30.07	20.01	49.91	-	-	-	-
P2	32.31	14.89	51.98	-	0.42	0.4	-
P3	21.24	21.92	45.68	0.22	8.79	1.98	0.17
P4	20.21	22.68	48.6	0.37	7.05	1.09	-
P5	28.84	20.04	50.71	-	0.41	-	-
P6	20.63	26.97	52.33	-	0.07	-	-
P7	18.34	26.98	54.33	-	0.35	-	-
P8	17.55	27.39	53.59	0.13	0.4	0.94	-

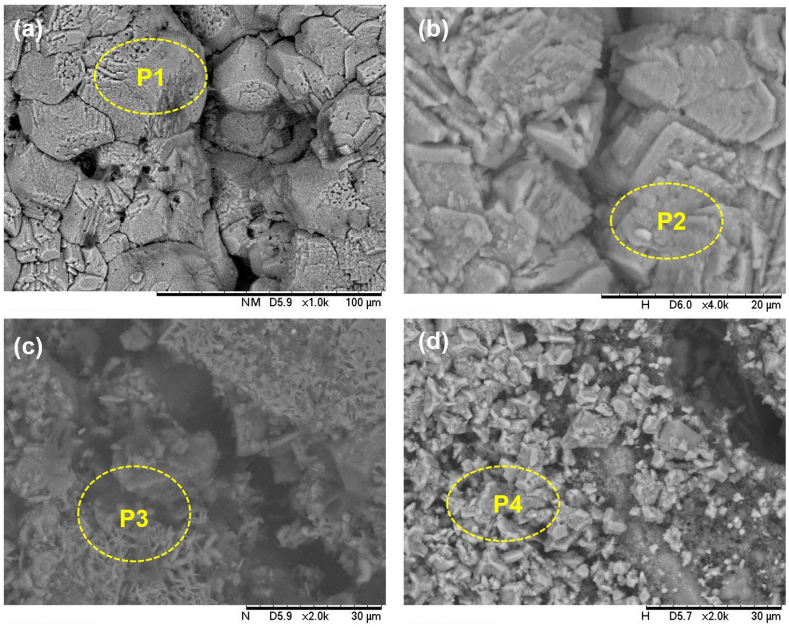

Figure 5-16: SEM images of self-healing compounds within cracks of (a) EG-B-Environmental chamber, (b) EG-B-Water submersion, and (c) EG-N, and (d) EG-MUC.

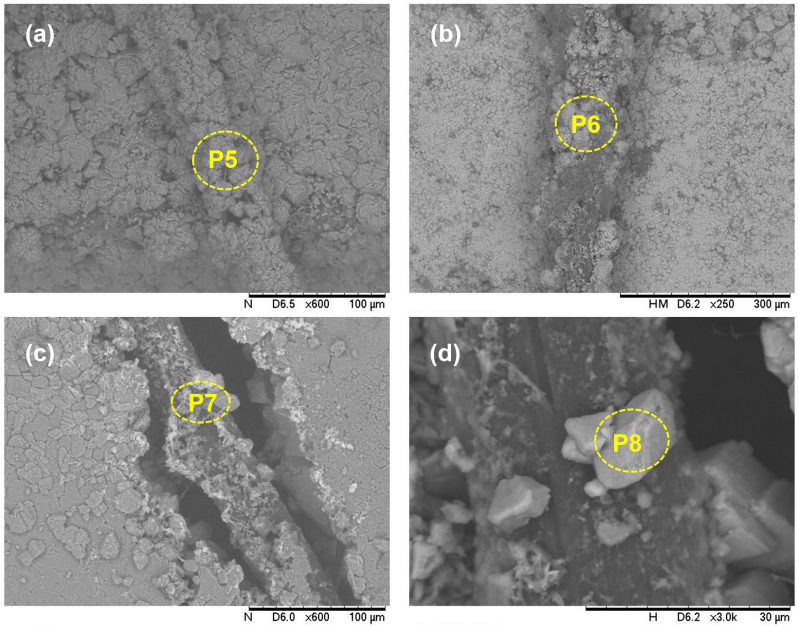

Figure 5-17: Crystals covering PVA fibres for (a) EG-B-Environmental chamber, (b) EG-B-Water submersion, and (c) EG-N, and (d) EG-MUC.

5.3.6 Raman spectra

Raman spectroscopy is widely used as a powerful and non-destructive tool for molecule identification as it provides structural fingerprints. For instance, it is can distinguish between different polymorphs of $CaCO_3$. **Figure 5-18** presents stacked Raman spectra of self-healing products within cracks and on the surface of PVA fibres in 5 specimen groups. Wavenumbers (also called Raman shifts) of $CaCO_3$ polymorphs have several ranges of peaks. In the Raman spectra for all specimen cases, four peaks at Raman shifts were characterized. The highest intensity at 1086 cm^{-1} corresponding to the symmetric stretching mode (v_1 vibration) of the carbonate group was identified. In addition, three other minor bands were identified representing two external lattice modes and in-plan bending mode (v_4 vibration) at 157 cm^{-1}, 282 cm^{-1}, and 712 cm^{-1}, respectively. These regions confirm the most prominent features of calcite, which precisely match previously identified calcite reference bands (DeCarlo, 2018; Saracho *et al*., 2020; White, 2009).

Raman spectra also help distinguish calcite from aragonite and vaterite by comparing lattice modes and the v_4 vibration mode. According to Dandeu *et al*. (2006), vaterite had broad Raman bands, particularly at both ~100 cm^{-1} and 300 cm^{-1}. Likewise, White (2009) reported that Raman peaks for aragonite were located at ~207 cm^{-1} and 704 cm^{-1} due to the external lattice mode and internal $v4$ vibration, being distinct from that of calcite. The minor variation in Raman band positions may be attributed to the effects of natural impurities, optical scattering, and trace metal (Gunasekaran *et al*., 2006; White, 2009). It should be noted that Raman bands cannot be used to quantify the amount of the testing sample straightforwardly due to different Raman scattering efficacies showing in different species (White, 2009).

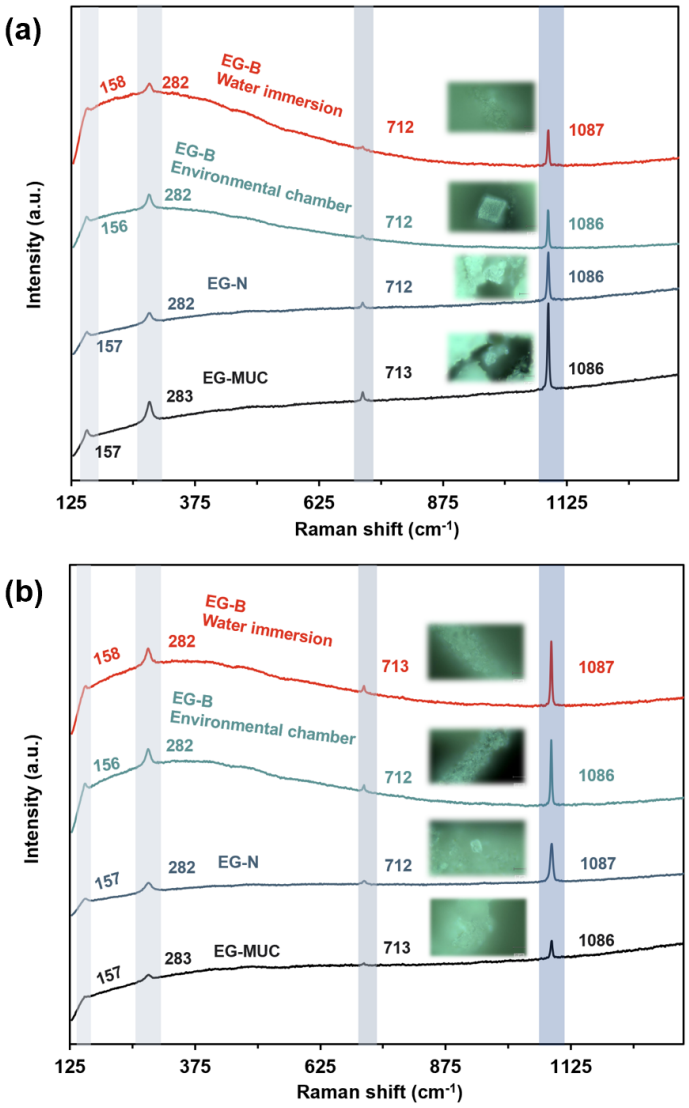

Figure 5-18: Raman spectra of calcium carbonate as the main self-healing product: (a) within cracks; and (b) on the surface of PVA fibres.

5.3.7 Calcium leaching, pH, and electrical conductivity in the curing media

Figure 5-19 shows the concentration of calcium ions in the water submerging the three types of specimens at the ages of 4, 8, 16, and 32-d. Compared with EG-N and EG-MUC, the curing medium of the specimens incorporating *S. pasteurii* impregnated-EG (EG-B) exhibited much higher concentration of dissolved calcium ions, with a peak concentration of 22.6 mg/L. In contrast, the highest concentration of leached calcium observed in both groups EG-N and EG-MUC was less than 3 mg/L at the age of 8-d. The calcium ions concentration for EG-MUC was similar to that for the reference specimen (EG-N) at all ages. **Figure 5-20** shows the electrical conductivity and pH values of the curing medium hosting the specimens at the ages of 4, 8, 16, and 32-d. There was an upward trend in both electrical conductivity and pH values for all groups with respect to the submersion period. It can be observed that the pH value in the water immersing EG-B specimens was higher than that of the other two groups at all ages. The pH values and electrical conductivity are highly related to the dissolved hydroxide ions and total leached ions in the solution.

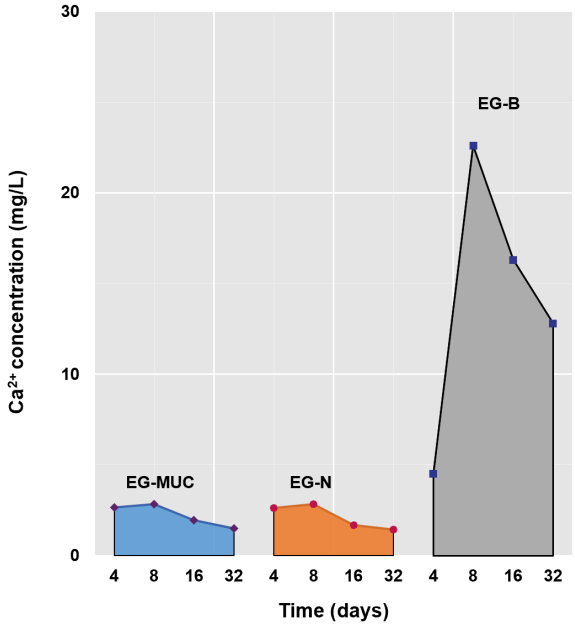

Figure 5-19: The concentration of Ca^{2+} in the curing media vs. time of submersion.

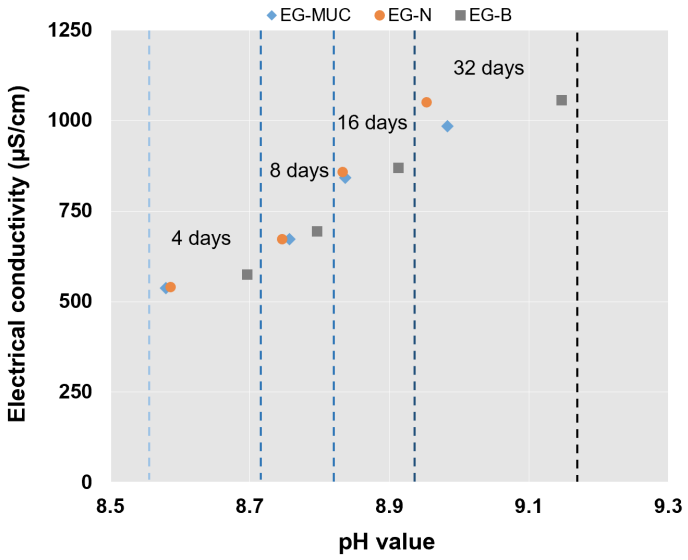

Figure 5-20: The electrical conductivity vs. pH of the curing media.

5.4 DISCUSSION

5.4.1 Role of *S. pasteurii* on calcium carbonate precipitation

In this study, *S. pasteurii* was involved in two main reactions, namely, metabolic conversion of calcium lactate and urea hydrolysis, thereby inducing calcium carbonate deposition. In the first reaction, calcium lactate, as an organic calcium source, was decomposed and metabolically converted into calcium carbonate precipitates in the presence of oxygen, according to the **Eq. 5-5** (Jonkers *et al*., 2010):

$$CaC_6H_{10}O_6 + 6O_2 \rightarrow CaCO_3 \downarrow + CO_2 \uparrow + 5H_2O \quad \text{Eq. 5-5}$$

$$CO_2 + H_2O \rightarrow H_2CO_3 \quad \text{Eq. 5-6}$$

$$2OH^- + H_2CO_3 \leftrightarrow CO_3^{2-} + 2H_2O \quad \text{Eq. 5-7}$$

$$Ca^{2+} + CO_3^{2-} \rightarrow CaCO_3 \downarrow \quad \text{Eq. 5-8}$$

In addition, extra CO_2 was released simultaneously during the decomposition of calcium lactate via bacterial metabolism, thereby substantially enhancing precipitation of calcium carbonate. Based on **Eq. 5-6**, metabolically released CO_2 molecules were converted to

carbonic acid (H_2CO_3) by dissolving in water. Then hydroxyl ions, owing to high pH values (**Figure 5-20)** in the matrix, reacted with H_2CO_3 to form carbonates, according to **Eq. 5-7**. It should be noted that higher pH values shifted the equilibrium to the formation of carbonates (Zhang *et al*., 2017; Zhang *et al*., 2020). Calcium carbonate precipitates were derived by the reaction between carbonates and calcium ions leaching from the AAS matrix (**Figure 5-19)**, as per **Eq. 5-8**.

The urea hydrolysis is governed by an enzyme urease within *S. pasteurii* including a series of reactions, shown in **Eqs. 5-9** to **5-13**. 1-mol of urea hydrolyzed intracellularly by urease results in the production of 1 mol of carbamate and 1 mol of ammonia, followed by being spontaneously hydrolyzed to form another 1 mol of ammonia and 1 mol of carbonic acid. Then these products are converted to bicarbonate by carbonic anhydrase (CA) and 2 mol ammonium and 2 mol hydroxyl ions by ammonia hydrolysis (Castro-Alonso *et al*., 2019).

$$CO(NH_2)_2 + H_2O \xrightarrow{\text{Urease}} NH_2COOH + NH_3 \quad \text{Eq. 5-9}$$

$$NH_2COOH + H_2O \rightarrow H_2CO_3 + NH_3 \quad \text{Eq. 5-10}$$

$$H_2CO_3 \leftrightarrow HCO_3^- + H^+ \quad \text{Eq. 5-11}$$

$$2NH_3 + 2H_2O \leftrightarrow 2NH_4^+ + 2OH^- \quad \text{Eq. 5-12}$$

$$HCO_3^- + H^+ + 2NH_4^+ + 2OH^- \leftrightarrow CO_3^{2-} + 2NH_4^+ + 2H_2O \quad \text{Eq. 5-13}$$

Finally, the concentration of carbonate increases, inducing an increase in the supersaturation level, thus triggering calcium carbonate precipitation around the *S. pasteurii* cell wall when the soluble calcium ions are sufficient in the surrounding environment (**Eqs. 5-14** and **5-15**).

$$Ca^{2+} + Cell \rightarrow Cell - Ca^{2+} \quad \text{Eq. 5-14}$$

$$Cell - Ca^{2+} + CO_3^{2-} \rightarrow Cell - CaCO_3 \quad \text{Eq. 5-15}$$

According to the equations shown above, calcium carbonate precipitation is governed by several key factors, namely, the urease, the concentration of inorganic carbon source, dissolved calcium ions, and available nucleation sites (Hammes and Verstraete, 2002; Torgal *et al*., 2015). It is essential that bacteria like *S. pasteurii* function as nucleation sites for continuous and stable calcium carbonate precipitation. *S. pasteurii* has a special cell envelope as gram-positive bacteria, acting as nucleation sites. As shown in **Figure 5-21**, *S. pasteurii* is surrounded by multiple layers of peptidoglycan cell wall where small-grain precipitates can be induced and reside in this region (Seifan and Berenjian, 2018). In addition, the negatively charged cell wall owing to the presence of functional groups in teichoic acids, such as phosphate and carboxyl groups, (Scott and Barnett, 2006) can attract metal cations (Ca^{2+}) and bind them onto the cell surfaces. The special cell envelope would accelerate bio-mineralization when an increase of carbonates occurs.

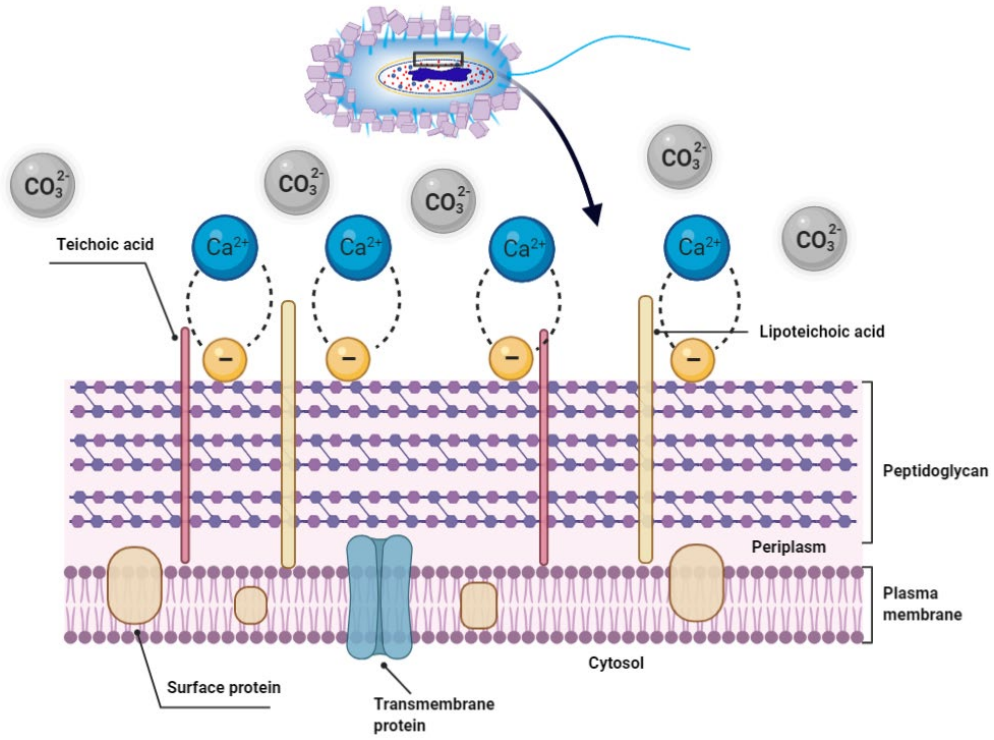

Figure 5-21: Schematic illustration of interactions between calcium ions and the gram-positive cell wall of *S. pasteurii*.

5.4.2 Effect of EG-immobilized *S. pasteurii* on properties of AAM

To maintain the viability of S. pasteurii and facilitate self-healing capability, immobilization of the bacteria using EG granules as a protective carrier was introduced. As can be observed in **Figure 5-14**, the addition of EG caused a reduction in mechanical properties. This was attributed to the relatively lower intrinsic strength of EG since it is lightweight and highly porous. However, all the specimens incorporated with EG attained satisfactory mechanical strengths suitable for structural concrete. The slight increase in mechanical properties when incorporating nutrients-impregnated EG is likely the result of calcium carbonate precipitation. It was also found for EG-N and EG-MUC specimens that nutrients hindered continued strength development. Similar results were reported in normal concrete by Bolobova and Kondrashchenko (2000) who observed that yeast extract delayed cement hydration. Similarly, Bundur *et al*. (2015) reported that incorporating bacterial nutrients resulted in lower compressive strength than that of control mortars. Directly adding a bacterial solution in mixtures (0-B) also decreased the mechanical properties due to the much lower survival rate of S. pasteurii in contact with the highly alkaline environment. The nutrients with killed cells hindered geopolymerization, thus delaying strength development. Considering the water absorption results, the bacteria have significantly affected capillary water absorption results of alkali-activated slag-based specimens. This can be explained by the blockage of capillary pores by MICCP (Wu *et al*., 2020). After *S. pasteurii* spores together with nutrients and precipitation sources were impregnated into EG, the bacteria engaged in ureolytic and bio-mineralization reactions, further reducing the total porosity of specimens and blocking water transport channels.

5.4.3 Crack self-healing and ions diffusion

As can be observed in **Figure 5-13 (b)**, The crack closure ratio in specimens without *S. pasteurii* (EG-N) was in the range of 11.7-28.9% for crack width from 50 μm to 150 μm after 90-d of water submersion. In contrast, the specimens made with the bacteria (EG-B) exhibited considerable improvement in crack sealing, with a maximum crack width of 111 μm completely healed after the 90-d incubation. The crack self-healing efficiency shown in **Figure 5-13** had a strong correlation with the ICP-OES results. The higher the

calcium ions leaching from the specimen, the higher was the surface crack self-healing ratio. This indicates that the concentration of diffused calcium ions was an essential parameter contributing to calcium carbonate precipitation (Xu and Wang, 2018). Similar results were reported by (Suleiman *et al*., 2019). The utilization of calcium for precipitating either abiotic calcium carbonate or biogenic calcium carbonate may explain why Ca^{2+} concentrations at 8-d in all specimen groups started to decline (Su *et al*., 2020).

5.4.4 Influence of environmental exposures on MICCP

The various environmental exposures significantly influenced the self-healing performance in bacterial series of specimens. As can be observed in **Figure 5-13 (a)**, crack widths under 100 μm were inclined to be healed when the bio-green concrete specimens were cured in the environmental chamber compared with their counterparts immersed in water. On the other hand, higher temperature increased the ureolysis degree and converted calcium lactate more efficiently, thereby facilitating calcium carbonate precipitation. Similar findings were reported by Nemati *et al*. (2005) who showed that microbial activities improved when the temperature at 19 °C raised to 30 °C. On the other hand, wet-dry cycles are essential for aerobic *S. pasteurii* to accelerate MICCP. When the bacterial specimens were immersed in water, all the matrix can fully absorb the surrounding water and maintain the water during the dry stage, especially that the RH in the environmental chamber was 80%. More oxygen can ingress into the inside of specimens compared with the continuous submersion stage. Aerobic *S. pasteurii* exposed to more oxygen could achieve more efficient crack self-healing. The finding that wet-dry cycles facilitate MICCP is consistent with previous work by Wang *et al*. (2014), where specimens with microencapsulated ureolytic bacteria exposed to wet-dry cycles achieved the highest self-healing capability.

5.4.5 Polymorphology of calcium carbonate within cracks

The anhydrous morphology of calcium carbonate due to bio-mineralization is an essential feature that affects the efficiency of MICCP (Seifan and Berenjian, 2018). The properties of the three anhydrous crystalline phases (calcite, vaterite, and aragonite) are listed in **Table 6**. Ostwald's rule suggests that the least stable polymorph crystallizes first (Rodriguez-Navarro

et al., 2012). In addition, it should be noted that a more stable polymorph has a lower solubility index (Bundur *et al*., 2017). As shown in **Table 6**, the order of solubility index for the three polymorphs from lowest to highest is calcite, aragonite, and vaterite. This indicates that the crystallization order for calcium carbonate from the least stable to the most thermodynamically stable polymorph is vaterite, aragonite, and calcite. Considering precipitation kinetics, the crystal polymorphs are influenced by numerous parameters such as temperature, ion concentration, pH, etc. (Bundur *et al*., 2017; Tai and Chen, 1998). The polymorphs of calcium carbonate are much dependent on temperature. Aragonite precipitates at higher temperatures, preferably above 40°C, whereas calcite and vaterite are predominant phases at lower temperatures (Flaten *et al*., 2009; Ogino *et al*., 1987). Vaterite and calcite, therefore, were expected as two final polymorphous compositions in this study since the temperature in all exposure conditions were at or below 30 °C. Compared with calcite, vaterite, however, is a metastable and intermediate form that transforms readily and irreversibly into calcite in an aqueous solution (Flaten *et al*., 2009; Warren *et al*., 2001; Wiktor and Jonkers, 2011). Raman spectra results indicate that the calcite with thermodynamical stability was the only polymorph in the calcium carbonate. This finding is consistent with the work by Díaz-Dosque *et al*. (2008), where agglomerations of calcium carbonate crystals via bio-mineralization were initially the vaterite phase, followed by subsequently stabilizing as calcite.

Table 5-6: Comparison of physical properties in calcite, vaterite, and aragonite

Properties	**Calcite**	**Vaterite**	**Aragonite**
Solubility (K_{sp})	4.83×10^{-9}	1.66×10^{-8}	7.24×10^{-9}
Specific gravity	2.71	2.54	2.93
Mohs hardness	3	3	3.5-4
Crystal system	Trigonal	Hexagonal	Orthorhombic
Color	Colorless or white, yellow, red, orange, blue, green, grey, etc.	Colorless	White, red, yellow, orange, green, purple, grey, blue and brown
Luster	Vitreous to pearly on cleavage surfaces	Sub-vitreous, waxy	Vitreous, resinous on fracture surfaces
Coordination number	6	6	9

5.4.6 Effect of PVA fibres on calcium carbonate precipitation

As can be observed in **Figure 5-17**, PVA fibres were covered with calcium carbonate crystals. This implies that PVA fibres can facilitate the precipitation of calcium carbonate by providing preferential nucleation sites. The effect of PVA fibres on improving precipitation of self-healing products can be attributed to two mechanisms, namely, the unique molecular structure of hydroxyls and the template effect of crystalline polymers (Feng *et al*., 2019). PVA fibre molecules interact with ions in the surrounding aqueous environment through intermolecular forces, including Van der Waals forces, ionic bonds, and hydrogen bonds (Kihara, 1978). A hydroxy group, as indicated in **Figure 5-22**, has polarity strengths due to electronegativity, thereby attracting calcium ions via the organic functional group and accelerating the precipitation of calcium carbonate (Homma *et al*., 2009). In addition, the hydroxyl group structure appears to form hydrogen bonds in aqueous solutions, interacting strongly with water (Guan *et al*., 2017; Meng *et al*., 2017). The OH radical provides a site where calcium carbonate can nucleate since water is the carrier for both calcium ions and carbonates. In terms of nanoscale, similar lattice spacing may reduce the interfacial nucleation energy and stimulate priority crystal orientation along one lattice direction owing to the template effect (Hosoda *et al*., 2003). **Figure 5-23** depicts unit cell parameters on the *a*-*b* plane of crystalline PVA and different polymorphs of calcium carbonate crystals. The PVA unit cell parameters along the *b*-axis were close to that of calcite; however, the parameters of vaterite and aragonite crystals at both axes differed from that of PVA. It therefore can be hypothesized that calcite could crystallize on the PVA *a*-*b* plane with a preferential orientation at the *b*-axis (Feng *et al*., 2019).

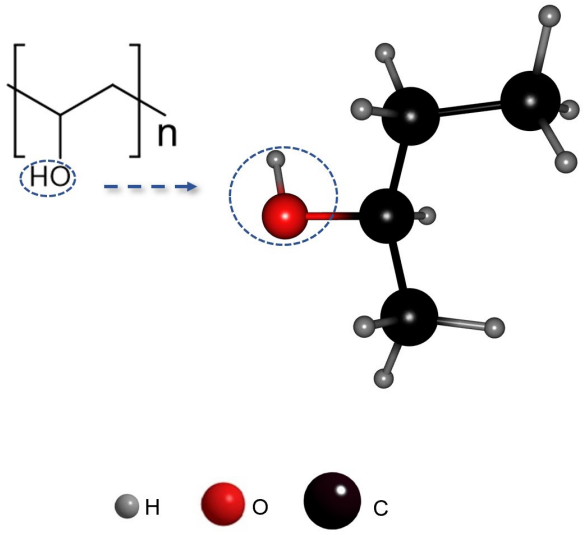

Figure 5-22: Molecular structure of vinyl alcohol.

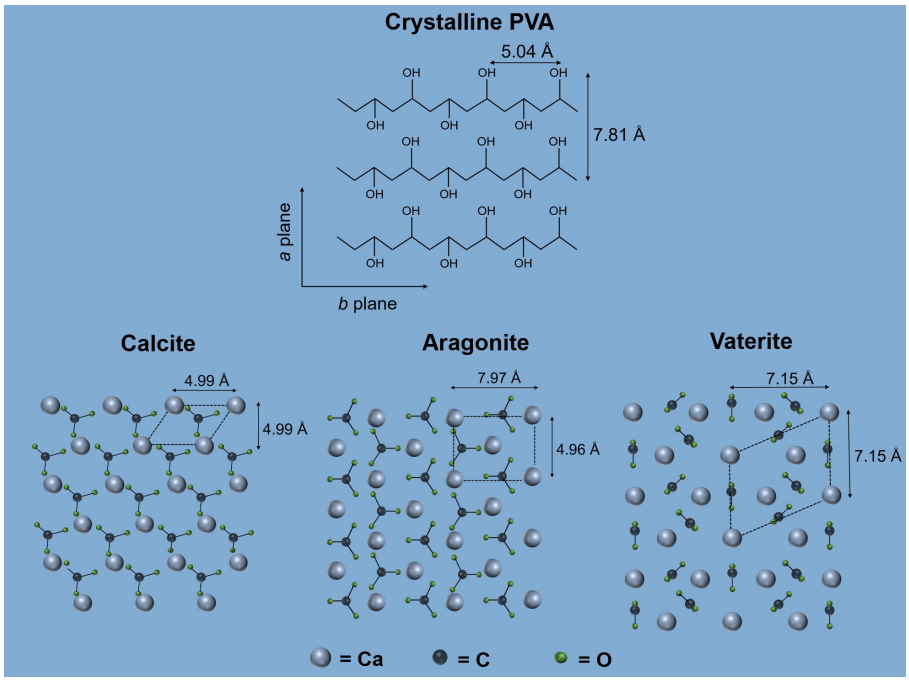

Figure 5-23: Schematic illustrations of the crystal structure of one layer of PVA and $CaCO_3$ on the ab plane. The unit cells are marked with the dashed lines.

5.4.7 Synergistic effect of crack self-healing

Based on the abovementioned discussion, the synergistic mechanisms of bacteria immobilized fibre-reinforced alkali-activated slag concrete involved in the calcium carbonate precipitation contributing to crack self-healing are schematically illustrated in **Figure 5-24**. In this study, both autogenous self-healing and microbial autonomic self-healing were involved. According to **Eqs. 5-8** and **5-9**, the carbonates were derived from the CO_2 dissolving in alkaline water, and then reacted with calcium ions leaching from the matrix, facilitating calcium carbonate precipitation. In addition, the mixture with the bacteria had higher pH value than the control mixture, likely owing to the hydrolysis of urea, thus rising pH in the curing medium and favoring the formation of calcium carbonate (Edvardsen, 1999). This autogenous self-healing could occur in all types of specimens in this study since leaching calcium ions were available in all mixtures, as indicated in **Figure 5-19**. Significant improvements by MICCP autonomic self-healing were manifested through surface crack observations and capillary water absorption tests in this study. When cracks occurred, water and oxygen penetrated the fresh cracks and activated the immobilized *S. pasteurii* spores in the EG near cracks. The microbial self-healing was then triggered via urea hydrolysis and metabolic conversion of calcium lactate into calcium carbonate, as mentioned **in Section 5.4.1**. In addition, the PVA fibres provided preferential nucleation sites for calcium carbonate precipitation, further creating synergistic self-healing.

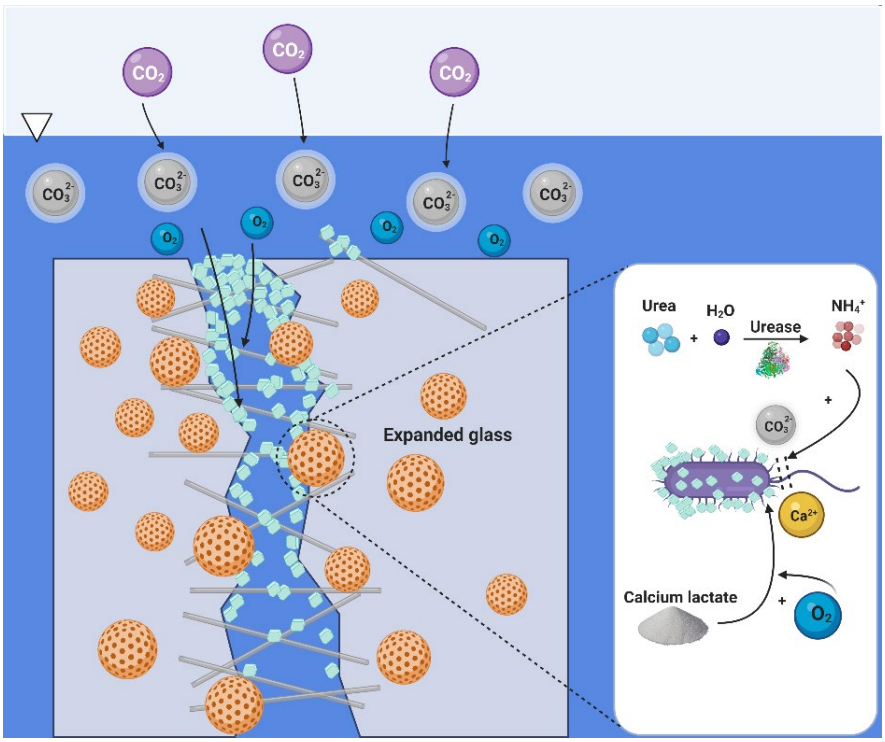

Figure 5-24: Schematic illustration of the self-healing mechanism of *S. pasteurii* immobilized PVA fibre-reinforced alkali-activated slag composites.

5.5 CONCLUSIONS

This study explored the potential of *S. pasteurii*, a type of bacteria able to survive in highly alkaline environments, to act as a crack self-healing agent in bio-green concrete. Based on the experimental results and pertinent discussion, the following conclusions can be drawn:

(1) Results indicate that the crack self-healing ability of bio-green concrete incorporating *S. pasteurii* impregnated EG was substantially enhanced.

(2) Compared to water submersion under normal temperature, the condition of higher temperature coupled with water-dry cycles could accelerate the metabolism of *S. pasteurii*, resulting in enhanced crack self-healing.

(3) The specimens incorporating bacteria immobilized EG compensated for the decrease in mechanical properties caused by the addition of bacterial nutrients and EG.

(4) The bacterial cell surfaces with negatively charged groups attracted calcium ions for the precipitation of calcium carbonate, thereby enhancing self-healing.

(5) The specimens treated with bacteria exhibited significant decrease in the water sorptivity coefficient compared with that of the reference specimens without bacteria.

(6) SEM-EDS confirmed the presence of calcium carbonate as the dominant self-healing compound. In addition, the morphology of calcium carbonate was further identified via Raman spectra.

(7) PVA fibres acted as preferential crystal nucleation sites for calcium carbonate precipitation.

(8) In an alkaline environment and through *S. pasteurii* driven-ureolysis, calcium ions converted from the organic calcium source and acted synergistically in contributing to precipitation of calcium carbonate to heal surface cracks in fibre-reinforced alkali-activated slag-based concrete.

5.6 REFERENCES

Aiken, T. A., Kwasny, J., Sha, W., and Soutsos, M. N. (2018). Effect of slag content and activator dosage on the resistance of fly ash geopolymer binders to sulfuric acid attack. *Cement and Concrete Research, 111*, 23-40.

Alazhari, M., Sharma, T., Heath, A., Cooper, R., and Paine, K. (2018). Application of expanded perlite encapsulated bacteria and growth media for self-healing concrete. *Construction and Building Materials, 160*, 610-619.

Albitar, M., Ali, M. M., Visintin, P., and Drechsler, M. (2015). Effect of granulated lead smelter slag on strength of fly ash-based geopolymer concrete. *Construction and Building Materials, 83*, 128-135.

Ali, A. M., Sanjayan, J., and Guerrieri, M. (2017). Performance of geopolymer high strength concrete wall panels and cylinders when exposed to a hydrocarbon fire. *Construction and Building Materials, 137*, 195-207.

Atiş, C. D., Bilim, C., Çelik, Ö., and Karahan, O. (2009). Influence of activator on the strength and drying shrinkage of alkali-activated slag mortar. *Construction and Building Materials, 23*(1), 548-555.

Bang, S. S., Galinat, J. K., and Ramakrishnan, V. (2001). Calcite precipitation induced by polyurethane-immobilized Bacillus pasteurii. *Enzyme and microbial technology, 28*(4-5), 404-409.

Bolobova, A., and Kondrashchenko, V. (2000). Use of yeast fermentation waste as a biomodifier of concrete. *Applied Biochemistry and Microbiology, 36*(3), 205-214.

Bundur, Z. B., Amiri, A., Ersan, Y. C., Boon, N., and De Belie, N. (2017). Impact of air entraining admixtures on biogenic calcium carbonate precipitation and bacterial viability. *Cement and Concrete Research, 98*, 44-49.

Bundur, Z. B., Kirisits, M. J., and Ferron, R. D. (2015). Biomineralized cement-based materials: Impact of inoculating vegetative bacterial cells on hydration and strength. *Cement and Concrete Research, 67*, 237-245.

Castro-Alonso, M. J., Montañez-Hernandez, L. E., Sanchez-Muñoz, M. A., Macias Franco, M. R., Narayanasamy, R., and Balagurusamy, N. (2019). Microbially Induced Calcium Carbonate Precipitation (MICP) and Its Potential in Bioconcrete: Microbiological and Molecular Concepts. *Frontiers in Materials, 6*. doi: 10.3389/fmats.2019.00126

Dandeu, A., Humbert, B., Carteret, C., Muhr, H., Plasari, E., and Bossoutrot, J.-M. (2006). Raman spectroscopy–a powerful tool for the quantitative determination of the composition of polymorph mixtures: application to CaCO3 polymorph mixtures. *Chemical Engineering & Technology: Industrial Chemistry-Plant Equipment-Process Engineering-Biotechnology, 29*(2), 221-225.

DeCarlo, T. M. (2018). Characterizing coral skeleton mineralogy with Raman spectroscopy. *Nature communications, 9*(1), 1-3.

Díaz-Dosque, M., Aranda, P., Darder, M., Retuert, J., Yazdani-Pedram, M., Arias, J. L., and Ruiz-Hitzky, E. (2008). Use of biopolymers as oriented supports for the stabilization of different polymorphs of biomineralized calcium carbonate with complex shape. *Journal of Crystal Growth, 310*(24), 5331-5340.

Edvardsen, C. (1999). Water permeability and autogenous healing of cracks in concrete *Innovation in concrete structures: Design and construction* (pp. 473-487): Thomas Telford Publishing.

Fang, Y., Xu, J., Gao, F., Du, X., Du, Z., Cheng, X., and Wang, H. (2021). Self-healable and recyclable polyurethane-polyaniline hydrogel toward flexible strain sensor. *Composites Part B: Engineering, 219*, 108965.

Feng, J., Su, Y., and Qian, C. (2019). Coupled effect of PP fiber, PVA fiber and bacteria on self-healing efficiency of early-age cracks in concrete. *Construction and Building Materials, 228*, 116810.

Flaten, E. M., Seiersten, M., and Andreassen, J.-P. (2009). Polymorphism and morphology of calcium carbonate precipitated in mixed solvents of ethylene glycol and water. *Journal of Crystal Growth, 311*(13), 3533-3538.

Guan, Y., Li, W., Zhang, Y., Shi, Z., Tan, J., Wang, F., and Wang, Y. (2017). Aramid nanofibers and poly (vinyl alcohol) nanocomposites for ideal combination of strength and toughness via hydrogen bonding interactions. *Composites Science and Technology, 144*, 193-201.

Gunasekaran, S., Anbalagan, G., and Pandi, S. (2006). Raman and infrared spectra of carbonates of calcite structure. *Journal of Raman Spectroscopy: An International Journal for Original Work in all Aspects of Raman Spectroscopy, Including Higher Order Processes, and also Brillouin and Rayleigh Scattering, 37*(9), 892-899.

Gwon, S., Ahn, E., and Shin, M. (2019). Self-healing of modified sulfur composites with calcium sulfoaluminate cement and superabsorbent polymer. *Composites Part B: Engineering, 162*, 469-483.

Habert, G., De Lacaillerie, J. D. E., and Roussel, N. (2011). An environmental evaluation of geopolymer based concrete production: reviewing current research trends. *Journal of Cleaner Production, 19*(11), 1229-1238.

Hammes, F., Seka, A., de Knijf, S., and Verstraete, W. (2003). A novel approach to calcium removal from calcium-rich industrial wastewater. *Water research, 37*(3), 699-704.

Hammes, F., and Verstraete, W. (2002). Key roles of pH and calcium metabolism in microbial carbonate precipitation. *Reviews in environmental science and biotechnology, 1*(1), 3-7.

Homma, D., Mihashi, H., and Nishiwaki, T. (2009). Self-healing capability of fibre reinforced cementitious composites. *Journal of Advanced Concrete Technology, 7*(2), 217-228.

Hosoda, N., Sugawara, A., and Kato, T. (2003). Template effect of crystalline poly (vinyl alcohol) for selective formation of aragonite and vaterite CaCO3 thin films. *Macromolecules, 36*(17), 6449-6452.

Huang, H., Ye, G., and Damidot, D. (2013). Characterization and quantification of self-healing behaviors of microcracks due to further hydration in cement paste. *Cement and Concrete Research, 52*, 71-81.

Jiang, Z., Li, W., and Yuan, Z. (2015). Influence of mineral additives and environmental conditions on the self-healing capabilities of cementitious materials. *Cement and Concrete Composites, 57*, 116-127.

Jonkers, H. M., Thijssen, A., Muyzer, G., Copuroglu, O., and Schlangen, E. (2010). Application of bacteria as self-healing agent for the development of sustainable concrete. *Ecological engineering, 36*(2), 230-235.

Khan, M. Z. N., Hao, Y., and Hao, H. (2016). Synthesis of high strength ambient cured geopolymer composite by using low calcium fly ash. *Construction and Building Materials, 125*, 809-820.

Kihara, T. (1978). *Intermolecular forces*: Wiley New York.

Kurmaç, Y. (2009). The impact of toxicity of metals on the activity of ureolytic mixed culture during the precipitation of calcium. *Journal of Hazardous Materials, 163*(2-3), 1063-1067.

Lauchnor, E. G., Schultz, L. N., Bugni, S., Mitchell, A. C., Cunningham, A. B., and Gerlach, R. (2013). Bacterially induced calcium carbonate precipitation and strontium coprecipitation in a porous media flow system. *Environmental science & technology, 47*(3), 1557-1564.

Lauer, K. R. (1956). *Autogenous healing of cement paste.* Paper presented at the Journal Proceedings.

Li, N., Shi, C., Zhang, Z., Wang, H., and Liu, Y. (2019). A review on mixture design methods for geopolymer concrete. *Composites Part B: Engineering, 178*, 107490.

Ling, Y., Wang, K., Li, W., Shi, G., and Lu, P. (2019). Effect of slag on the mechanical properties and bond strength of fly ash-based engineered geopolymer composites. *Composites Part B: Engineering, 164*, 747-757.

Ma, Y., and Ye, G. (2015). The shrinkage of alkali activated fly ash. *Cement and Concrete Research, 68*, 75-82.

Meng, X., Zeng, N., Zhang, J., Jiang, L., and Dan, Y. (2017). Polyvinyl alcohol-based hydrophilic monoliths from water-in-oil high internal phase emulsion template. *Journal of colloid and interface science, 497*, 290-297.

Nemati, M., Greene, E., and Voordouw, G. (2005). Permeability profile modification using bacterially formed calcium carbonate: comparison with enzymic option. *Process Biochemistry, 40*(2), 925-933.

Nguyễn, H. H., Choi, J.-I., Kim, H.-K., and Lee, B. Y. (2019). Effects of the type of activator on the self-healing ability of fiber-reinforced alkali-activated slag-based composites at an early age. *Construction and Building Materials, 224*, 980-994.

Nguyễn, H. H., Choi, J.-I., Song, K.-I., Song, J.-K., Huh, J., and Lee, B. Y. (2018). Self-healing properties of cement-based and alkali-activated slag-based fiber-reinforced composites. *Construction and Building Materials, 165*, 801-811.

Nguyen, T. H., Ghorbel, E., Fares, H., and Cousture, A. (2019). Bacterial self-healing of concrete and durability assessment. *Cement and Concrete Composites, 104*, 103340.

Nikolić, V., Komljenović, M., Džunuzović, N., Ivanović, T., and Miladinović, Z. (2017). Immobilization of hexavalent chromium by fly ash-based geopolymers. *Composites Part B: Engineering, 112*, 213-223.

Ogino, T., Suzuki, T., and Sawada, K. (1987). The formation and transformation mechanism of calcium carbonate in water. *Geochimica et Cosmochimica Acta, 51*(10), 2757-2767.

Pungrasmi, W., Intarasoontron, J., Jongvivatsakul, P., and Likitlersuang, S. (2019). Evaluation of microencapsulation techniques for MICP bacterial spores applied in self-healing concrete. *Scientific Reports, 9*(1), 1-10.

Ren, J., Wang, X., Li, D., Han, N., Dong, B., and Xing, F. (2021). Temperature adaptive microcapsules for self-healing cementitious materials. *Composites Part B: Engineering, 223*, 109138.

Rodriguez-Navarro, C., Jroundi, F., Schiro, M., Ruiz-Agudo, E., and González-Muñoz, M. T. (2012). Influence of substrate mineralogy on bacterial mineralization of calcium carbonate: implications for stone conservation. *Applied and environmental microbiology, 78*(11), 4017-4029.

Roig-Flores, M., Formagini, S., and Serna, P. (2021). Self-healing concrete-What Is it Good For? *Materiales de Construcción, 71*(341), e237-e237.

San Nicolas, R., Bernal, S. A., de Gutiérrez, R. M., van Deventer, J. S., and Provis, J. L. (2014). Distinctive microstructural features of aged sodium silicate-activated slag concretes. *Cement and Concrete Research, 65*, 41-51.

Saracho, A. C., Haigh, S. K., Hata, T., Soga, K., Farsang, S., Redfern, S. A., and Marek, E. (2020). Characterisation of CaCO 3 phases during strain-specific ureolytic precipitation. *Scientific Reports, 10*(1), 1-12.

Scott, J. R., and Barnett, T. C. (2006). Surface proteins of gram-positive bacteria and how they get there. *Annual Review in Microbiology, 60*, 397-423.

Seifan, M., and Berenjian, A. (2018). Application of microbially induced calcium carbonate precipitation in designing bio self-healing concrete. *World Journal of Microbiology and Biotechnology, 34*(11), 168.

Shill, S. K., Al-Deen, S., Ashraf, M., and Hutchison, W. (2020). Resistance of fly ash based geopolymer mortar to both chemicals and high thermal cycles simultaneously. *Construction and Building Materials, 239*, 117886.

Sisomphon, K., Copuroglu, O., and Koenders, E. (2012). Self-healing of surface cracks in mortars with expansive additive and crystalline additive. *Cement and Concrete Composites, 34*(4), 566-574.

Skorupa, D. J., Akyel, A., Fields, M. W., and Gerlach, R. (2019). Facultative and anaerobic consortia of haloalkaliphilic ureolytic micro-organisms capable of precipitating calcium carbonate. *Journal of applied microbiology, 127*(5), 1479-1489.

Song, C., Choi, Y. C., and Choi, S. (2016). Effect of internal curing by superabsorbent polymers–internal relative humidity and autogenous shrinkage of alkali-activated slag mortars. *Construction and Building Materials, 123*, 198-206.

Su, Y., Qian, C., Rui, Y., and Feng, J. (2020). Exploring the coupled mechanism of fibers and bacteria on self-healing concrete from bacterial extracellular polymeric substances (EPS). *Cement and Concrete Composites*, 103896.

Suleiman, A. R., Nelson, A. J., and Nehdi, M. L. (2019). Visualization and quantification of crack self-healing in cement-based materials incorporating different minerals. *Cement and Concrete Composites, 103*, 49-58.

Tai, C. Y., and Chen, F. B. (1998). Polymorphism of CaCO3, precipitated in a constant-composition environment. *AIChE Journal, 44*(8), 1790-1798.

Tang, Z., Li, W., Hu, Y., Zhou, J. L., and Tam, V. W. (2019). Review on designs and properties of multifunctional alkali-activated materials (AAMs). *Construction and Building Materials, 200*, 474-489.

Tian, K., Wu, Y., Zhang, H., Li, D., Nie, K., and Zhang, S. (2018). Increasing wind erosion resistance of aeolian sandy soil by microbially induced calcium carbonate precipitation. *Land Degradation & Development, 29*(12), 4271-4281.

Torgal, F. P., Labrincha, J. A., Diamanti, M. V., Yu, C.-P., and Lee, H.-K. (2015). *Biotechnologies and biomimetics for civil engineering*: Springer.

Wang, J., Mignon, A., Snoeck, D., Wiktor, V., Van Vliergerghe, S., Boon, N., and De Belie, N. (2015). Application of modified-alginate encapsulated carbonate producing bacteria in concrete: a promising strategy for crack self-healing. *Frontiers in microbiology, 6*, 1088.

Wang, J., Snoeck, D., Van Vlierberghe, S., Verstraete, W., and De Belie, N. (2014). Application of hydrogel encapsulated carbonate precipitating bacteria for approaching a realistic self-healing in concrete. *Construction and Building Materials, 68*, 110-119.

Wang, J., Soens, H., Verstraete, W., and De Belie, N. (2014). Self-healing concrete by use of microencapsulated bacterial spores. *Cement and Concrete Research, 56*, 139-152.

Wang, J., Van Tittelboom, K., De Belie, N., and Verstraete, W. (2012). Use of silica gel or polyurethane immobilized bacteria for self-healing concrete. *Construction and Building Materials, 26*(1), 532-540.

Warren, L. A., Maurice, P. A., Parmar, N., and Ferris, F. G. (2001). Microbially mediated calcium carbonate precipitation: implications for interpreting calcite precipitation and for solid-phase capture of inorganic contaminants. *Geomicrobiology Journal, 18*(1), 93-115.

White, S. N. (2009). Laser Raman spectroscopy as a technique for identification of seafloor hydrothermal and cold seep minerals. *Chemical Geology, 259*(3-4), 240-252.

Wiktor, V., and Jonkers, H. M. (2011). Quantification of crack-healing in novel bacteria-based self-healing concrete. *Cement and Concrete Composites, 33*(7), 763-770.

Wu, M., Hu, X., Zhang, Q., Cheng, W., Xue, D., and Zhao, Y. (2020). Application of bacterial spores coated by a green inorganic cementitious material for the self-healing of concrete cracks. *Cement and Concrete Composites, 113*, 103718.

Xu, J., and Wang, X. (2018). Self-healing of concrete cracks by use of bacteria-containing low alkali cementitious material. *Construction and Building Materials, 167*, 1-14.

Zamani, M., Nikafshar, S., Mousa, A., and Behnia, A. (2020). Bacteria encapsulation using synthesized polyurea for self-healing of cement paste. *Construction and Building Materials, 249*, 118556.

Zhang, J., Zhou, A., Liu, Y., Zhao, B., Luan, Y., Wang, S., Yue, X. and Li, Z. (2017). Microbial network of the carbonate precipitation process induced by microbial consortia and the potential application to crack healing in concrete. *Scientific Reports, 7*(1), 1-10.

Zhang, L., Suleiman, A., and Nehdi, M. (2020). Self-healing in fiber-reinforced alkali-activated slag composites incorporating different additives. *Construction and Building Materials, 262*, 120059.

Zhang, P., Wang, K., Li, Q., Wang, J., and Ling, Y. (2020). Fabrication and engineering properties of concretes based on geopolymers/alkali-activated binders-A review. *Journal of Cleaner Production, 258*, 120896.

Zhang, P., Zheng, Y., Wang, K., and Zhang, J. (2018). A review on properties of fresh and hardened geopolymer mortar. *Composites Part B: Engineering, 152*, 79-95.

Zhang, W., Zheng, Q., Ashour, A., and Han, B. (2020). Self-healing cement concrete composites for resilient infrastructures: A review. *Composites Part B: Engineering, 189*, 107892.

Chapter 6

6 CRACK SELF-HEALING IN ALKALI-ACTIVATED SLAG COMPOSITES INCORPORATING IMMOBILIZED BACTERIA: EFFECT OF CALCIUM SOURCES[4]

This chapter investigates the self-healing efficiency of alkali-activated slag-based composites using bacteria immobilized in expanded glass granules made from recycled glass. The effect of different calcium sources on the reaction kinetics, mechanical properties, capillary water absorption, and final self-healing compounds was also investigated. The results revealed that the bio-based specimens attained a remarkably enhanced crack healing ratio, while no obvious self-healing was observed in abiotic control samples. Furthermore, the sorptivity coefficient decreased significantly by incorporating bacteria. Scanning electron microscopy with energy dispersive X-ray (SEM-EDX) analysis and Raman spectroscopy confirmed that calcite was the dominant self-healing product. This study suggests that using calcium lactate as the calcium source is advantageous owing to economic and sustainability considerations.

6.1 INTRODUCTION

Concrete is the world's most widely used construction material and has been a backbone of urbanization, industrialization and modernization owing to its versatility and the wide availability of its raw materials (Alyousef *et al*., 2020; Li *et al*., 2018; Yıldırım *et al*., 2015; Wang *et al*., 2019). An essential part of concrete, ordinary portland cement (OPC) has been the most extensively used binding material in most concrete structures. Global cement production has grown consistently at an annual rate of about 9% over the past decades and is estimated to reach 6.1 billion metric tons in 2050 (Ranjbar and Zhang, 2020; Arman *et al*., 2019). Nevertheless, the high production of OPC is now facing the challenge of massive carbon dioxide (CO_2) emissions, mainly due to the thermal

[4] A version of this chapter was submitted to the *Construction and Building Materials*.

decomposition of its limestone, the primary raw material in cement manufacturing (Provis and Bernal, 2014). It has been reported that OPC production contributed to roughly 12% of the total CO_2 emissions in 2020 (Dange and Suryawanshi, 2017). Increasing levels of CO_2 into the atmosphere cause accelerated climate change. Annual greenhouse gas emissions in 2019 hit a record high with a sharp increase in OPC production globally, raising concerns about the associated environmental impacts. Therefore, pursuing an eco-friendly alternative to OPC is of great importance to mitigate environmental pollution and achieve sustainability goals.

Alkali-activated materials (AAMs), which are inorganic polymers derived from the geopolymerization of certain industrial by-products or mining wastes containing siliceous-aluminous resources, and activated with aqueous alkaline activators, provide a sustainable way for lowing the CO_2 footprint of concrete through clinker-free cement production and utilization of wastes (Bajpai *et al*., 2020; Li *et al*., 2020; Singh and Middendorf, 2020; Rożek *et al*., 2019; Thakur *et al*., 2019). Such siliceous-aluminous raw materials originate from steel slag (Katpady *et al*., 2020; Xiang *et al*., 2019), metakaolin (Sun *et al*., 2019; Shi *et al*., 2020), fly ash (Cai *et al*., 2020; Noushini *et al*., 2020), rice husk ash (Nuaklong *et al*., 2020; He *et al*., 2017), volcanic pumice (Grillo *et al*., 2019; Li *et al*., 2019), red mud (Li *et al*., 2019; Hu *et al*., 2018), etc. Compared to OPC-based materials, AAMs have demonstrated unconventionally superior performance regarding high strength given proper curing (Ali *et al*., 2017; Hajimohammadi *et al*., 2019), high-temperature resistance (Celik *et al*., 2018; Sha *et al*., 2020; Zhang *et al*., 2020), acid resistance (Aiken *et al*., 2018; Mehta *et al*., 2017), and superior immobilization of heavy metals (Sevim and Demir, 2019), attracting considerable attention. Furthermore, several full-scale construction projects built using AAMs have marked the milestone that AAMs can be commercialized and successfully deployed in real-world structures (Janik, 2017; Poulet and Cyr, 2016; Shill *et al*., 2020). However, AAMs are susceptible to cracking due to their inherent brittleness (Atiş *et al*., 2009; Song *et al*., 2016; Thomas *et al*., 2017). Cracking has been a primary threat to the structural integrity, serviceability, and safety of AAMs, thereby impeding their broader commercial applications. Moreover, an *in-situ* crack repair can be hazardous and difficult due to inaccessibility. In addition, conventional repair methods are typically onerous, laborious,

and time-consuming, thus causing enormous financial burdens (Yıldırım *et al*., 2015). As a result, the sustainable development of AAM applications calls for the development of self-healing AAMs, thereby repairing cracks autonomously without human interventions and facilitating the creation of resilient AAMs.

Self-healing is one of the most extraordinary external stimuli-responsive properties stemming from biological systems, where the healing processes are autogenously triggered after the occurrence of damage, thereby restoring the original functions and properties (Chen *et al*., 2016; Kang *et al*., 2019). Animal skin, for example, can self-heal wounds autonomously in response to damage. This phenomenon has inspired scientists to explore the self-healing of a variety of smart materials, from functional metals (Markvicka *et al*., 2018; Hager, 2017; Ferguson *et al*., 2014) to polymer composites (White *et al*., 2001; Thakur and Kessler, 2015) and ceramics (Ozaki *et al*., 2016; Greil, 2019; Farle *et al*., 2016).

It was found that OPC-based materials are capable of self-repairing cracks. For instance, Yıldırım *et al*. (2018) investigated the self-healing behaviour of aged engineered cementitious composites (ECC), and indicated that the presence of water played a crucial role in enhancing autogenous healing. Similarly, Suleiman and Nehdi (2018) reported that pre-cracked mortars submerged in water achieved more self-healing than mortars exposed to cyclic temperature and relative humidity. Over the past decades, numerous approaches have been explored to improve the self-healing capability of OPC-based materials, including swelling additives (Jiang *et al*., 2015; Buller *et al*., 2019; Wang *et al*., 2018), shape memory alloys (SMA) (Bonilla *et al*., 2018; Alam *et al*., 2007), crystalline admixtures (Roig-Flores *et al*., 2016; Azarse *et al*., 2019; Borg *et al*., 2018), microcapsules with healing agents (Wang *et al*., 2019; Dong *et al*., 2017), superabsorbent polymers (SAP) (Chindasiriphan *et al*., 2020; Gwon *et al*., 2019; Mechtcherine *et al*., 2018; Snoeck *et al*., 2020), microbially induced calcium carbonate precipitation (MICP) (Alazhari *et al*., 2018; Feng *et al*., 2019), etc.

MICP is a carbonate-induced bio-mineralization process usually performed by alkali-tolerant bacteria via metabolic activities (Zhang *et al*., 2017; Jena *et al*., 2020; Choi *et al*.,

2020). As a novel technology for the self-repairing of cracks in OPC-based materials, MICP has been attracting much attention. A growing body of literature has investigated the crack self-healing efficiency of OPC-based materials using MICP. For instance, Nguyen *et al*. (2019) incorporated *Bacillus subtilis*, yeast extract, and peptone as a microbial adjuvant to enhance self-healing capability. It was found that surface cracks with width of 400 μm were filled. Hence, a decrease in porosity, increase in both dynamic modulus and mechanical strength were reported. To increase the viability of microorganisms by implementing a carrier, Zhang *et al*. (2017) conducted detailed research on quantifying the self-healing efficiency of concrete by expanded perlite (EP)-immobilized *B. cohnii*. The results showed that specimens with added EP-immobilized bacteria exhibited effective crack-healing, and crack widths up to 790 μm can be fully healed.

Ureolytic *S. pasteurii*, formerly known as *B. pasteurii*, is one of the most commonly used bacteria applied in cement-based materials for crack self-healing owing to their capability of forming spores under harsh environments (Nguyen *et al*., 2019). Incorporated calcium sources play an essential role in facilitating calcium carbonate precipitation. The use of several calcium sources such as calcium chloride (Jonkers *et al*., 2008), calcium lactate (Wiktor and Jonkers, 2011), calcium gluconate (Ducasse-Lapeyrusse *et al*., 2017), and calcium acetate (Alazhari *et al*., 2018) has been reported in applications of concrete crack self-healing. Yet, significantly less research effort has been devoted to the effect of different calcium sources on crack self-healing efficiency.

Despite the remarkable progress achieved in the self-healing of OPC-based materials, very few studies have addressed the self-healing of AAMs. In addition, no systematic research concerning the enhancement of crack self-healing of AAMs using MICP has been published. To help bridge these research gaps, in this study, we experimentally investigated the effects of different calcium sources on the reaction kinetics, mechanical properties, capillary water absorption, and final self-healing compounds of AAMs made from activated slag. This work broadens the horizon for novel biogenic self-healing in AAMs and sheds light on understanding other behaviour involving the self-healing process.

6.2 MATERIALS AND METHODS

6.2.1 Preparation of bacterial strain

In this study, alkaliphilic and spore-forming bacterium *S. pasteurii* (ATCC 11859) was used as a self-healing agent. The cells were initially stored in 20% (v/v) glycerol at −75 °C. The *S. pasteurii* were cultured in deionized water containing 20.0 g/L yeast extract, 10.0 g/L $(NH_4)_2SO_4$, and 0.13M tris buffer (pH = 9.0). The abovementioned nutrients were obtained from Thermo Fisher Scientific, Canada. All the ingredients were autoclaved separately at 120 °C for 15 mins. The bacterial solution was incubated at 30 ± 2 °C and agitated at 180 rpm after transferring the *S. pasteurii* to the medium in a sterilized fume hood. Sample aliquots taken from the liquid cultures were inoculated on agar petri dishes in preparation for future bacterial cultivation. The procedures for culturing *S. pasteurii* are schematically illustrated in **Figure 6-1**.

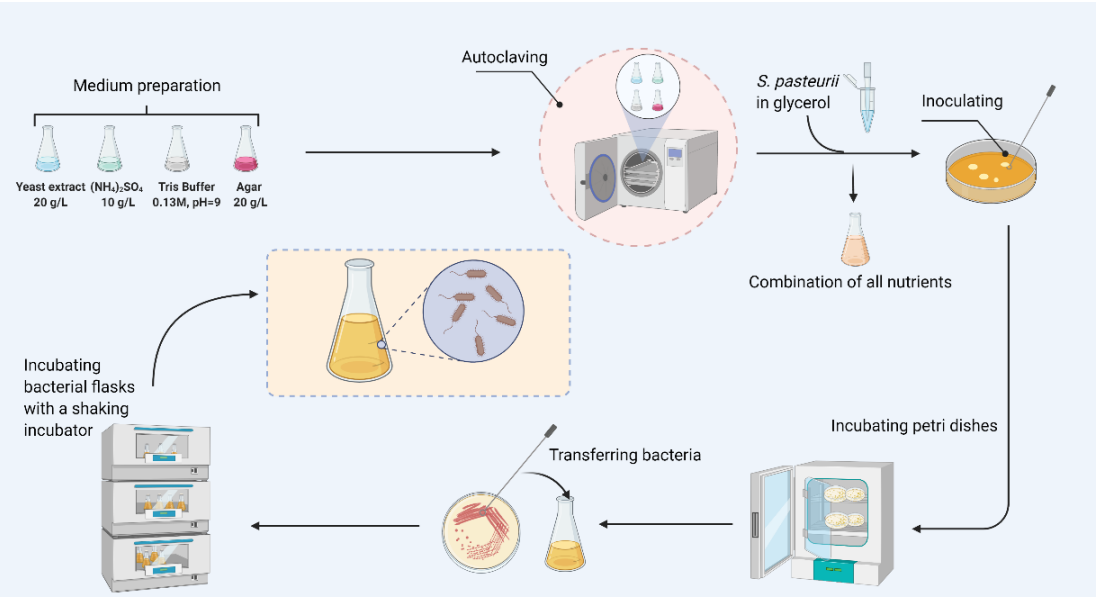

Figure 6-1: Schematic illustration of *S. pasteurii* culture.

The growth of *S. pasteurii* was monitored by measuring the optical density at a wavelength of 600 nm (OD_{600}) with a SPECTRONIC™ 200 spectrophotometer (Thermo Scientific™). The number of cells as per OD_{600} under the previous culture conditions was

determined by the plate counting method via serial dilutions, as shown in **Figure 6-2**. The concentration was determined through the relationship between the CFU/mL and corresponding absorbance reading at OD_{600}, as shown in **Figure 6-3**. The concentration of 10^7 CFU/mL was used in the subsequent mixtures.

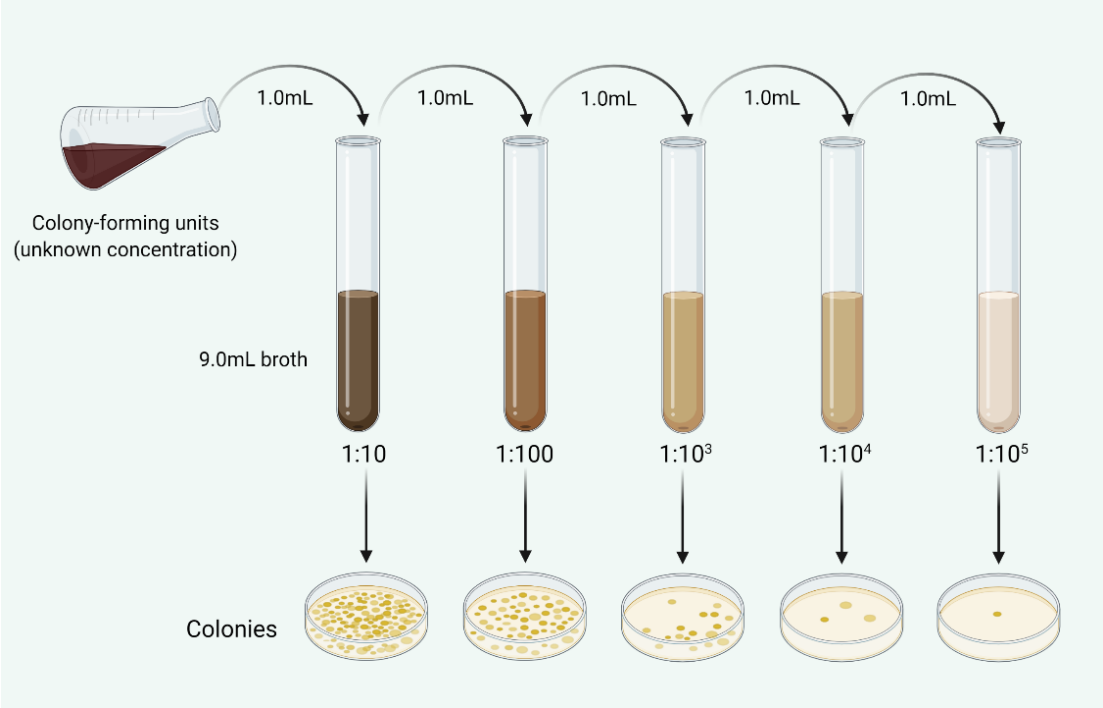

Figure 6-2: Schematic of serial dilutions.

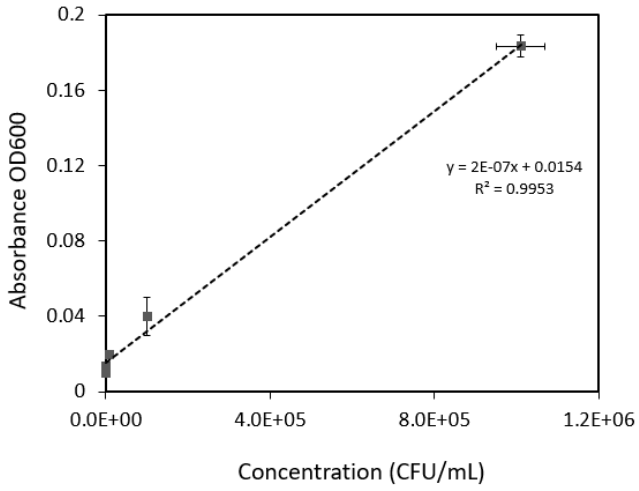

Figure 6-3: Correlation between bacterial cell concentration and the corresponding absorbance at OD600.

6.2.2 Materials and sample preparation

Ground granulated blast furnace slag (BFS), supplied by Lafarge (Canada), was used as the solid precursor. Its oxide compositions and physical properties are given in **Table 6-1**. The particle size distribution of the BFS was determined using a Malvern laser diffraction particle analyzer, as shown in **Figure 6-4**. Sodium silicate solution ($Na_2O(SiO_2)x \cdot xH_2O$) consisting of 8% Na_2O, 27% SiO_2, and 65% H_2O by mass and sodium hydroxide pellets, both supplied by Sigma-Aldrich, were used as activators in each mixture. Porous and superlight expanded glass (EG) (**Figure 6-5**) from recycling glass waste served as a reservoir for *S. pasteurii* cells and nutrients to endure the harsh alkali-activated slag (AAB) environment. River sand was used as aggregate. The properties of both EG and river sand are summarized in **Table 6-2**. Polyvinyl alcohol (PVA) fibres were added to control cracks. A polycarboxylate-based superplasticizer (SP) (BASF, Canada) was used to achieve adequate workability of AAB-based composites. Both physical and mechanical properties of the mixtures are listed in **Table 6-3**.

Table 6-1: Chemical and physical properties of BFS

Components/property	BFS
Silicon oxide (SiO_2) (%)	35.42
Aluminum oxide (Al_2O_3) (%)	9.65
Ferric oxide (Fe_2O_3) (%)	0.41
Calcium oxide (CaO) (%)	45.40
Magnesium oxide (MgO) (%)	1.00
Specific gravity	2.90
Blaine fineness (m^2/kg)	399
Loss on ignition (LOI) at 1000 °C	2.72

Table 6-2: Properties of EG and river sand used in this study

Properties (unit)	River sand	EG
Size (mm)	-	1-2
Dry loose bulk density (kg/m^3)	1670	230
Fineness modulus	2.4	3.81
Compressive strength (MPa)	-	⩾ 1.6

Table 6-3: Mechanical properties of PVA fibres

Mechanical properties	Ultimate tensile strength (MPa)	Diameter (mm)	Density (kg/m^3)	Length (mm)	Young's modulus (GPa)	Elongation (%)
PVA	1620	0.039	1300	12	43	6

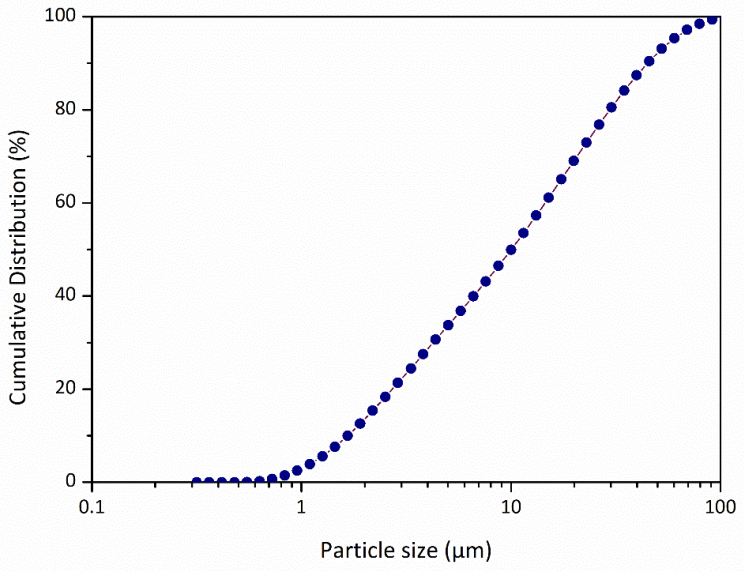

Figure 6-4: Particle size distribution of BFS.

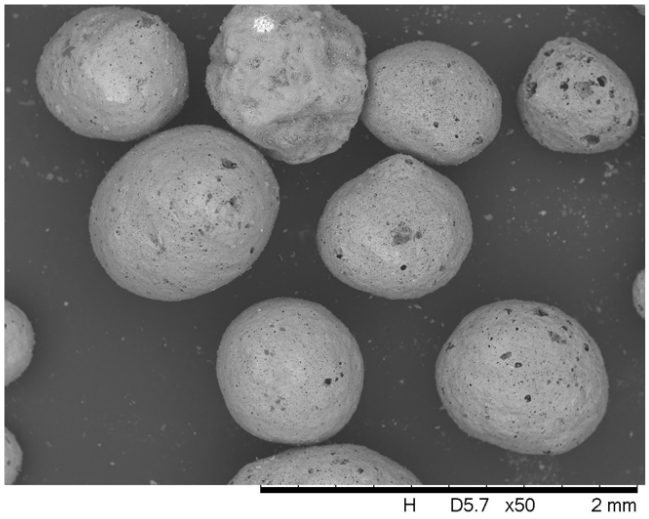

Figure 6-5: Morphology of EG particles using scanning electron microscope.

6.2.3 Impregnation procedures

S. pasteurii spores with two types of calcium sources, namely, calcium lactate and calcium chloride, were immobilized into EG separately via a vacuum impregnation system. As can be observed in **Figure 6-6**, the vacuum system was connected to an impregnated chamber and a funnel. The bacterial solution and the calcium-based solutions were filled into the funnel, and EG was loaded into the vacuum chamber. For the first group, EG was first impregnated with the calcium lactate solution, followed by impregnating *S. pasteurii* spores. For the second group, EG was first impregnated with a combination of a urea and calcium chloride solution, followed by impregnating *S. pasteurii* spores. EG was dried at 30°C after each impregnation until the mass change was under 0.5%.

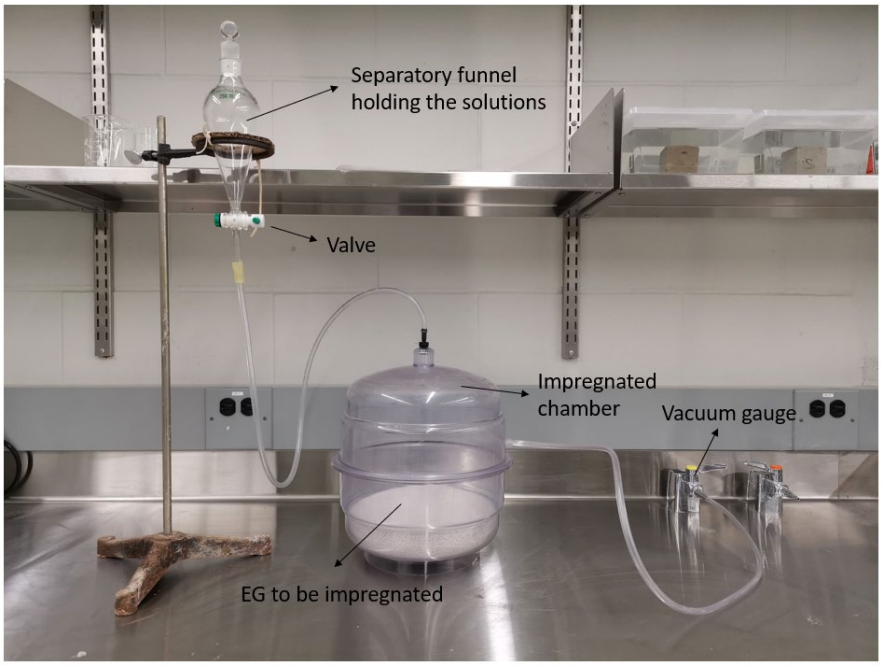

Figure 6-6: Vacuum impregnation setup.

6.2.4 Mixture design

The mixture design of PVA fibre-reinforced alkali activated slag (AAS) based composite mixtures is listed in **Table 6-4**. The water/binder ratio was kept at a constant value of 0.44. NaOH pellets were first added to 400 g water to prepare the alkaline solution. This liquid activator was ready for mixing when the temperature cooled down to room temperature (20 ± 2 °C). The fresh mixtures were cast in molds with different shapes for various experimental purposes. All molds filled with fresh mixes were vibrated and then covered to prevent water evaporation. After 1-d, all specimens were moved into a curing room at a controlled temperature of 20 ± 1 °C and ⩾ 98% RH for 7-d after demolding.

Table 6-4: AAS composite mixture design

Component (g)	R-0	R-EG	CL-EG	CC-EG
Slag	4500	4500	4500	4500
Sand	4950	4500	4500	4500
EG	0	450	450	450
NaOH	140.25	140.25	140.25	140.25
Sodium silicate	285	285	285	285
Water	1767	1767	1767	1767
PVA Fibre	45	45	45	45
SP	26	26	26	26
Bacteria	-	-	450	450
Calcium lactate	-	-	27	-
$CaCl_2$	-	-	-	13.75
Urea	-	-	-	7.43

6.2.5 Creation of cracks and incubation

Small disk-shaped specimens (50-mm diameter and 15-mm height) were pre-cracked using a screw jack according to (Suleiman *et al*., 2019) after 7-d of moist curing. Subsequently, all samples were subject to water submersion in a digitally controlled walk-in environmental chamber (Burnsco Technologies INC., Canada) at a temperature of 30 ± 1 °C.

6.2.6 Experimental methods

6.2.6.1 Visual observation of surface crack

In this study, the surface crack width was monitored before and after the incubation using a digital microscope (Jiusion, China). The spots with varied crack width were marked. The crack healing ratio can be calculated via **Eq. 6-1**.

$$\text{Crack healing ratio } \% = [(w_0 - w_t)/w_0] \times 100 \qquad \text{Eq. 6-1}$$

where w_0 = initial crack width; and w_t = crack width after curing at t.

6.2.6.2 Reaction heat

The reaction heat of bacterial AAS paste with different calcium sources was monitored using an eight-channel TAM-Air isothermal calorimeter (TA Instruments, USA) at 23 ±

0.2 °C. The calorimeter was calibrated before the testing. All test samples were manually mixed in ampoules via a plastic stirrer, and all ampoules were subsequently placed into the channels. Based on the abovementioned water to binder ratio in **Table 6-4**, a total mass of 4.46 g of each mixture was weighed into each ampoule. The resulting heat flow and the corresponding accumulative heat were normalized by the binder (GGBFS) mass. Heat evolution was recorded for 96 h.

6.2.6.3 Mechanical properties

Cubic specimens from each mixture were subjected to a compression test performed using a 200 kN capacity automatic compression machine (ELE International, UK) as per ASTM C109. Split tensile strength was appraised on cylindrical specimens as per ASTM C496. All samples were tested at ages of 7, 14, and 28d after demolding. For each mixture, both compression and splitting tensile tests were performed in triplicates, and the average values with standard deviation were reported.

6.2.6.4 Water absorption test

The capillary water absorption test was conducted according to ASTM C1585-13 provisions on 5-month-old large disc-shaped specimens to compare their resistance to water penetration. All specimens were initially dried in a ventilated oven at 50 °C until the mass changed was less than 0.1%. The side surface was sealed with waterproof tape to ensure unidirectional water contact. The top surface was covered by a plastic sheet secured using rubber bands to prevent evaporation. The water depth was 3-5 mm. At regular time intervals (1 min, 5 min, 10 min, 20 min, 30 min, 1h, 2h, 3h, 4h, 5h, and 6h), all specimens were removed out of the water and surface dried with a towel before weighing. The rate of water absorption, defined as the mass change (g) divided by the sectional area contacted with water (mm^2) and the density of the water (g/mm^3), was plotted against the square root of time t ($s^{1/2}$). Therefore, the sorptivity coefficient was determined through the slope of the plots between absorption I (mm) and the square root of time t ($s^{1/2}$).

6.2.6.5 Mercury Intrusion Porosimetry (MIP)

To explore the effect of the bacteria on the pore structure of the AAS composites, the pore size distribution of all specimens at the age of 5 months was investigated using MIP (Micrometrics AutoPore IV 9500). First, fragments of approximately 1 cm^3 were sectioned from the crushed small disc-shaped specimens, followed by immersion in isopropanol for 24h to prevent further alkali-activation. The fragments were then dried inside a vacuum desiccator until constant mass. Pressure ranging from 0.14 to 414 MPa was applied with a contact angle of 140° and surface tension of 0.484 N/m as per ASTM D4404 (Standard Test Method for Determination of Pore Volume and Pore Volume Distribution of Soil and Rock by Mercury Intrusion Porosimetry).

6.2.6.6 SEM-EDS analysis

The morphology and characteristics of the self-healing products which formed within cracks were analyzed using scanning electron microscopy (SEM) (Hitachi TM 3030Plus) coupled with Energy-dispersive X-ray spectroscopy (EDS). Images of the self-healing products were captured with an accelerating voltage of 15 kv and an operating current of 20 μA.

6.2.6.7 Raman spectroscopy

Raman spectroscopy has become widely used as a powerful and non-destructive tool for molecule identification since it can provide structural fingerprints. Raman spectroscopy measurements were performed using a Renishaw InVia Reflex Raman spectrometer at the Surface Science Centre, Western University. Raman spectra were collected using three accumulations of 5s exposure acquired with a laser excitation of 633 nm. A 50× objective lens with a numerical aperture (NA) of 0.6 was used on a 1 μm^2 laser-focusing area of the sample site. The laser power was kept at 1.5 mW.

6.3 RESULTS AND DISCUSSION

6.3.1 Visualisation and quantification of surface crack self-healing

Figure 6-7 depicts photographic images of surface cracks from the three types of samples before and after environmental exposure. The images were also converted into binary sections using the Origin 8.5 software (OriginLab Corporation, Northampton, MA, USA) with its image processing function. The targeted cracking area was extracted and marked in black color to easily distinguish the surrounding matrix cracks. As shown in **Figure 6-7 (a)**, no obvious crack self-healing occurred in the control specimen series (R-EG). The crack width of the surface did not change much, and very few crystalline products formed within the crack. In contrast, the crack width in CL-EG and CC-EG specimens showed enhanced crack self-healing. The cracks were covered with massive crystals, which appeared as self-healing products.

The self-healing efficiency of the surface cracks of abiotic control and bacteria-based specimens was quantified. **Figure 6-8** presents the crack healing ratio as per **Eq. 6-1**. A typical relationship between the crack healing ratio and initial crack width was plotted. It can be observed that specimen groups CL-EG and CC-EG attained great potential in crack width reduction. Most surface cracks under 100 μm were entirely healed after 5-months of curing. Interestingly, the maximum crack width that can be completely healed in CC-EG specimens was 141 μm in comparison to 134 μm in CL-EG specimens. However, the crack healing ratio decreased substantially when no bacteria was incorporated. It was observed that cracks with smaller widths attained higher self-healing efficiency. Visual inspection and quantification indicate that the addition of *S. pasteurii* contributed to crack self-healing enhancement through enhanced depositing of minerals within the crack mouth. Previous studies showed similar results. For example, Jadhav *et al*. (2018) incorporated *S. pasteurii* solution into metakaolin-based geopolymer to engage self-healing. They found that the pre-cracked bacteria-containing specimens with average crack width of 89 ± 3 μm could be completely healed after conditioning. Similarly, Bhaskar *et al*. (2017) investigated the potential of porous zeolite-immobilized bacteria into cementitious mortars for repairing surface cracks. It was reported that *S. pasteurii*

and *S. ureae*-immobilized specimens showed much more pronounced crack self-healing than abiotic control specimens.

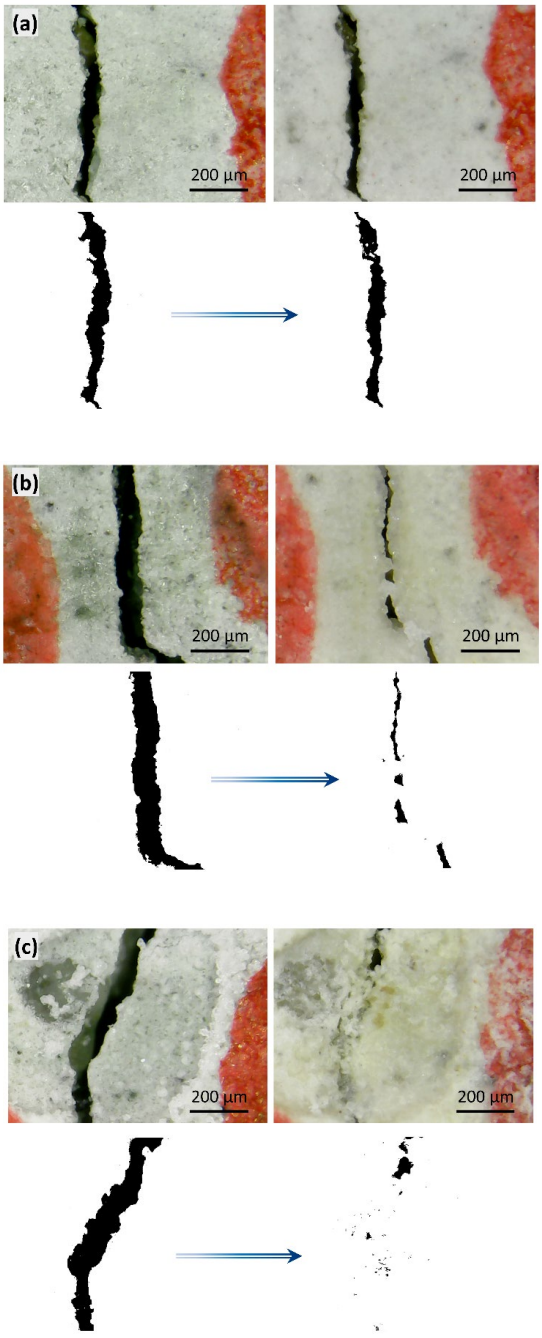

Figure 6-7: Typical photomicrographs and corresponding binary images showing crack healing after 5-months of environmental exposure: (a) R-EG; (b) CL-EG; and (c) CC-EG specimens.

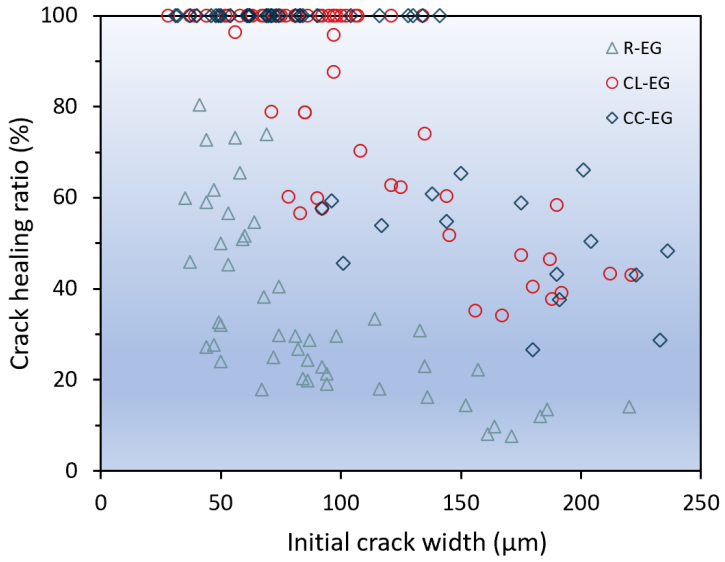

Figure 6-8: Crack healing ratio (%) as a function of initial crack width for bio-based and reference specimens.

6.3.2 Influence of the bacteria and calcium sources on AAS reaction kinetics

The calorimetric curves for AAS paste incorporated with different calcium additives compared to the reference sample are presented in **Figure 6-9**. It can be observed that the heat flow curves of all AAS pastes were similar to that of identical OPC hydration including five distinctive stages: initial hydrolysis, induction, acceleration, deceleration, and steady phase (Jansen *et al*., 2012; Neville, 1995). The first exothermic peak appeared immediately in all pastes when activators reacted with the slag, which links to the first stage of polymerization (destruction-coagulation) (Shi *et al*., 2003; Provis and Deventer, 2009). It was found that the incorporation of the bacteria, calcium lactate, and calcium chloride prolonged the induction period. The second exothermic peak is closely related to the formation and polymerization of activated slag gels (Yao *et al*., 2009; Chithiraputhiran and Neithalath, 2013), indicating the acceleration period of the reaction. A retarding effect was found in the three mixtures with additives. The main reason for the delayed induction period and the second exothermic peak when adding *S. pasteurii* could be the yeast extract. This organic nutrient in the bacterial solution containing sugar and carbohydrates can be considered a reaction retarder that negatively affected the

geopolymerization of the slag paste. Similar results were reported by Bundur *et al*. (2015) who found that *S. pasteurii* solution consisting of urea-yeast extract nutrient caused severe retardation of cement paste hydration. Similarly, calcium chloride and calcium lactate acted as retarders to prolong the dormant period and the second hydration peak. **Figure 9(b)** shows the cumulative heat for all pastes. This plot suggests that all pastes reached a very similar extent of reaction after 96-hr of hydration.

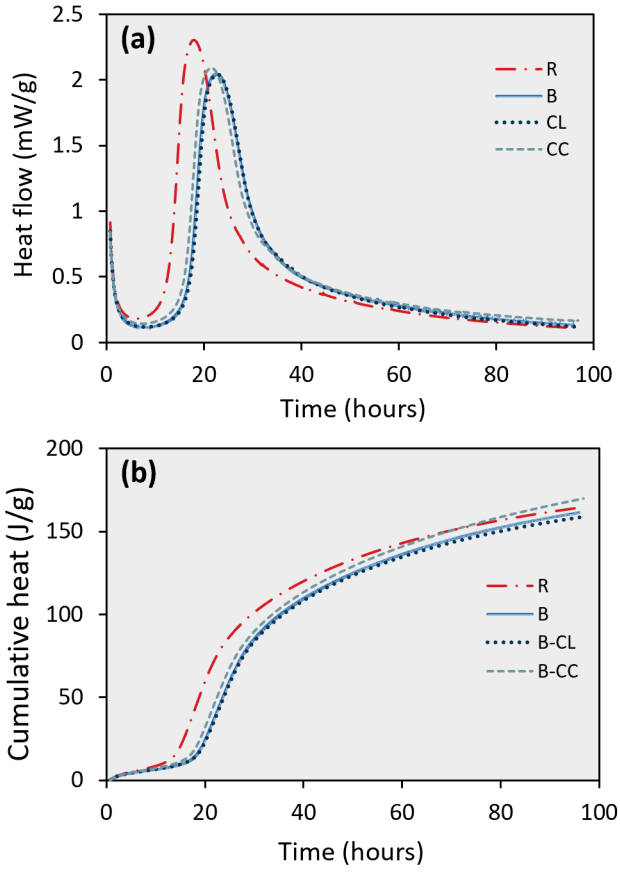

Figure 6-9: React heat from bacterial AAS paste with calcium lactate and calcium chloride and pure paste: (a) heat flow; (b) cumulative heat.

6.3.3 Mechanical properties

Figure 6-10 compares the compressive strength and split tensile strength of all mixtures at different ages of 7, 14, and 28d. The partial replacement of sand by EG caused a reduction in mechanical properties. For example, the compressive strength and the splitting tensile strength of the specimens incorporating EG (R-EG) were 30% and 20% lower than that of the R-0 specimens at the age of 28d. This was attributed to EG's comparatively low strength given the super-lightweight and high porosity. All specimens incorporating EG, however, demonstrated sufficient strengths by optimizing the EG ratio and activators design. As shown in **Figure 6-10 (a)**, a slight increase in the compressive strength was observed in the bacterial samples with two types of calcium sources (CC-EG and CL-EG) in comparison to the control group (R-EG). For instance, at 14d, bacterial specimens containing calcium lactate (CL-EG) and calcium chloride (CC-EG) reached 7% and 12% increase in compressive strength, respectively higher than that R-EG specimens. Similarly, the splitting tensile strength of the samples with two types of calcium sources at 28d was slightly improved compared to that of the reference group. A slight improvement in strength development was likely due to the deposition of self-healing products from *S. pasteurii*, therefore filling mortar pores and enhancing both compressive strength and split tensile strength. This was confirmed by previous references (Ramakrishnan *et al*., 1998; Ghosh *et al*., 2005; Achal *et al*., 2009; Khushnood *et al*., 2020).

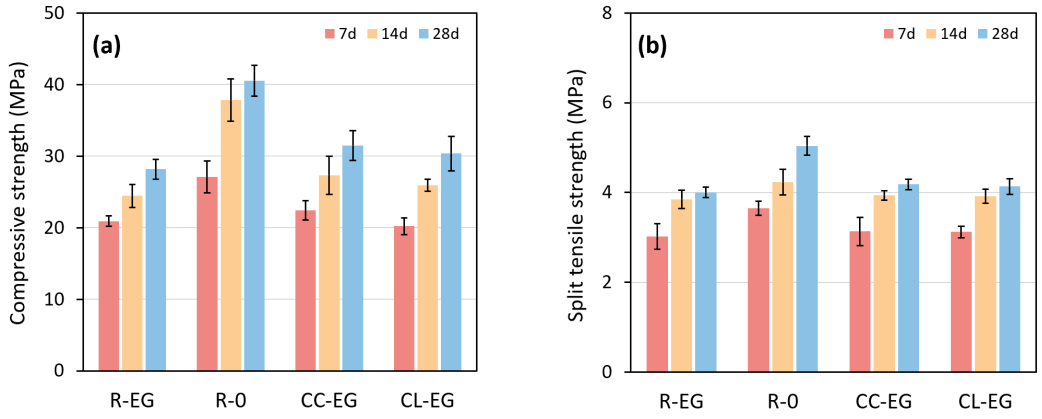

Figure 6-10: Mechanical properties development in all mixtures: (a) compressive strength, and (b) tensile strength.

6.3.4 Capillary water absorption

Figure 6-11 quantitatively illustrates the influence of different calcium sources on the water absorption of bacterial specimens. The curves were fitted by linear regression to determine the sorptivity coefficient *k*. It was found that the *S. pasteurii* treated specimens achieved a significant decrease in capillary water absorption. For example, the reference specimen (R-EG) exhibited the highest sorptivity coefficient of 0.0056 mm/$sec^{1/2}$. In contrast, the sorptivity coefficient of the bacterial specimens incorporating different calcium sources (CL-EG and CC-EG) was 0.0028 mm/$sec^{1/2}$ and 0.0035 mm/$sec^{1/2}$, respectively. It can be hypothesized that MICP played an essential role in reducing the sorptivity coefficient by blocking some capillary pores. A similar result was reported by Chahal *et al*. (2012), who found that the inclusion of *S. pasteurii* resulted in a markable decrease in the water uptake compared to that in the reference specimens by depositing a layer of calcium carbonate crystals on and within the pores of the concrete specimens. In terms of the two types of calcium sources, the sorptivity coefficient of the bacterial specimens made with calcium lactate (CL-EG) was slightly smaller than that of those with calcium chloride (CC-EG), indicating that calcium lactate appeared to facilitate more calcium carbonate precipitation, thereby contributing to a decrease in sorptivity. The transport properties of the specimens are influenced by the capillary pore size volume and connectivity, which can be further verified via MIP.

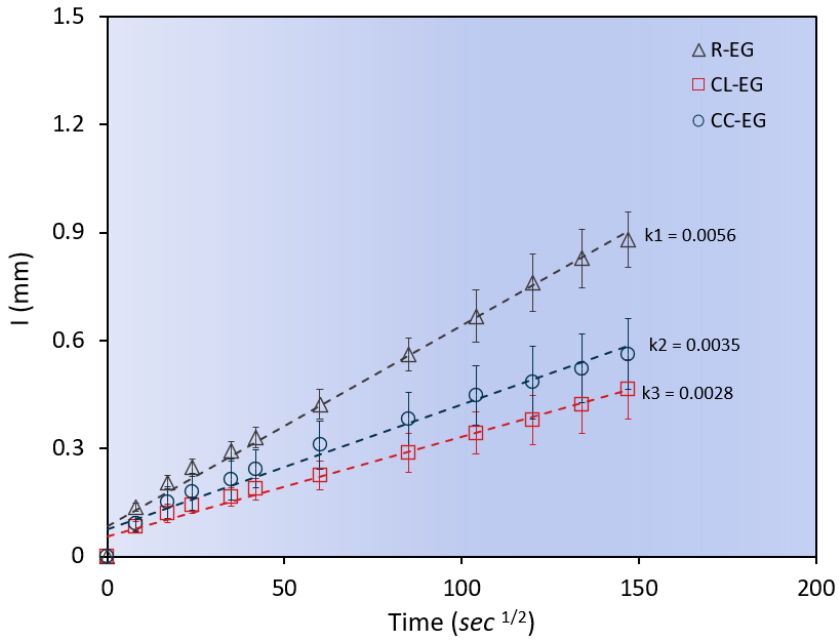

Figure 6-11: Capillary water absorption of specimens in each series as a function of time.

6.3.5 MIP results and pore structure

Figure 6-12 compares the MIP curves of samples from the three mixtures cured for 5 months. The specimens incorporating immobilized *S. pasteurii* with two types of calcium sources (CL-EG and CC-EG) resulted in significant pore volume reduction and pore size refinement after 5 months. For example, the cumulative intruded pores volume of CL-EG and CC-EG was 0.077 mL/g and 0.086 mL/g, respectively. In contrast, the total mercury intrusion volume of the reference sample (R-EG) was 0.125 mL/g. Interestingly, the MIP curves of CL-EG overlapped with that of CC-EG in the range of 0.01-100 µm referring to capillary pores (Zhang *et al*., 2021). However, for pores ranging from 0.001-0.01 µm, the CL-EG exhibited more noticeable reduction in porosity than that of the CC-EG.

Thus, the MIP results indicate that MICP resulted in the precipitation of self-healing products, thereby filling capillary pores and achieving lower porosity. This understanding is consistent with the work of Su *et al*. (2019) where calcium carbonate-formed bacteria (*B. mucilaginosus*) into concrete densified the microstructure by precipitating minerals. The pore structure is highly related to the permeability and diffusivity of hardened alkali-

activated materials (Ma *et al*., 2013). In the present study, the refined pore structure of the bio-composites can govern the transport properties, hence tightening the water uptake. The MIP results were then cross-checked with the sorptivity coefficient, as shown in **Figure 6-13**. It can be observed that the relationship of the sorptivity coefficient and the cumulative intrusion volume referring to porosity showed a linear trend, which in turn explains the results of the water absorption test. The lower the porosity, the lower is the permeability.

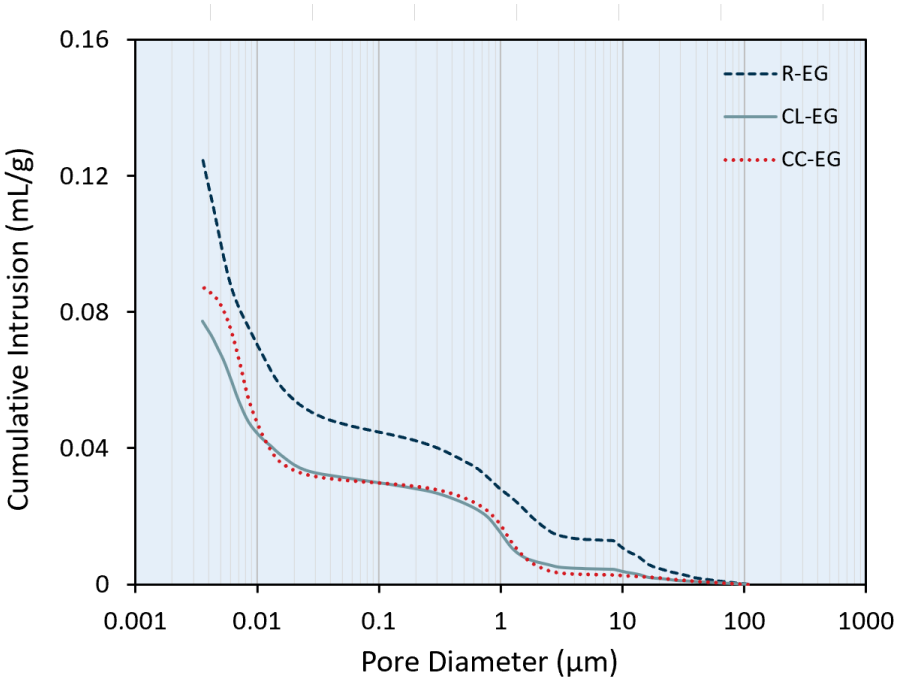

Figure 6-12: Cumulative intruded pore volume vs. pore diameter for the three types of samples after 5-months of water submersion.

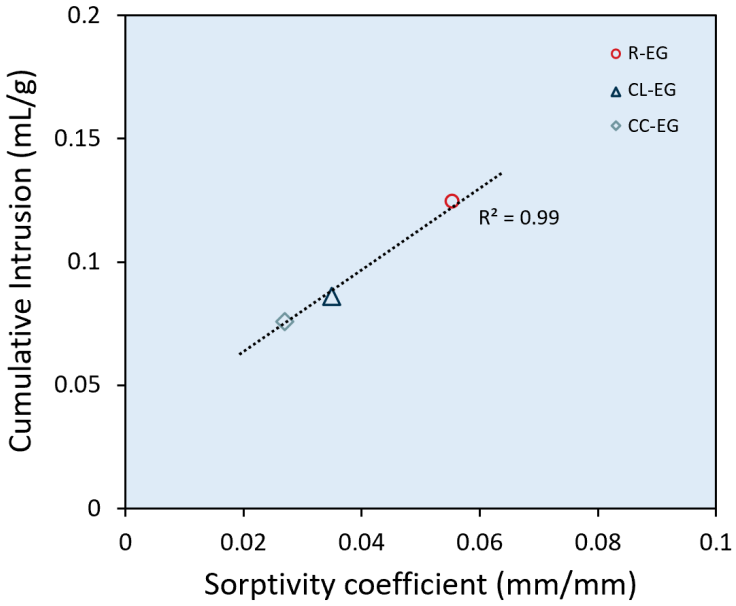

Figure 6-13: Cumulative intruded pore volume vs. pore diameter for the three types of samples after 5-months of water submersion.

6.3.6 SEM-EDS

The morphology of the self-healing compounds in the pre-cracked disc-shaped specimens after environmental exposure was examined by SEM analysis. As can be observed in **Figure 6-14 (a)**, lamellar rhombohedral crystals, forming massive crystal clusters, deposited within the crack of the CL-EG. Similarly, stacked crystals in the cracks of the CC-EG specimen and resembling rhombohedra are shown in **Figure 6-14 (b)**. Compared to the morphology of the mineral precipitates in CC-EG specimens, precipitates with relatively larger crystal size in specimens CL-EG appeared more compact with denser crystal clusters. In contrast, some cubic and irregular polyhedron-like mineral particles were intermingled within the crack of specimens R-EG (**Figure 6-14 (c)**). To further investigate the chemical compositions of the self-healing products, EDX via the Quantax 400 software (Bruker, Germany 2021) was employed. **Figure 14** also depicts the EDX spectra at the marked spots. As shown in **Figure 14 (a) and (b)**, the main elements of the compounds at the surface cracks of all specimens were O, Ca, and C, suggesting that the dominant self-healing product was calcium carbonate-based minerals. This finding is consistent with previous studies (Jadhav *et al*., 2018; Bhaskar *et al*., 2017; Bayati and

Saadabadi, 2021; Williams *et al*., 2017), where *S. pasteurii* facilitated the precipitation of calcium carbonate via metabolic activities, thereby healing surface cracks in cement-based materials and AAS composites. In R-EG specimens (see **Figure 6-14 (c)**), apart from the calcium carbonate as the primary self-healing material, a certain amount of silicon and aluminum was also observed, indicating the presence of calcium-alumino-silicate-hydrate (C-A-S-H) as the final product of BFS after the alkali-activation (Provis, 2018).

Interestingly, crystals like half-apricot kernels, whole and hemispherical spherulites were only observed via SEM in CC-EG specimens (**Figure 6-15**), with sizes ranging approximately from 10 to 40 μm. The main elements of the round-shaped crystals were Ca, C, and O, confirming the same microbial-induced deposit ($CaCO_3$) but with a different morphology. Previous studies reported that the morphology of crystals derived from biomineralization was highly affected by the calcium sources (Tittelboom *et al*., 2010; Muynck *et al*., 2008; Seifan *et al*., 2016).

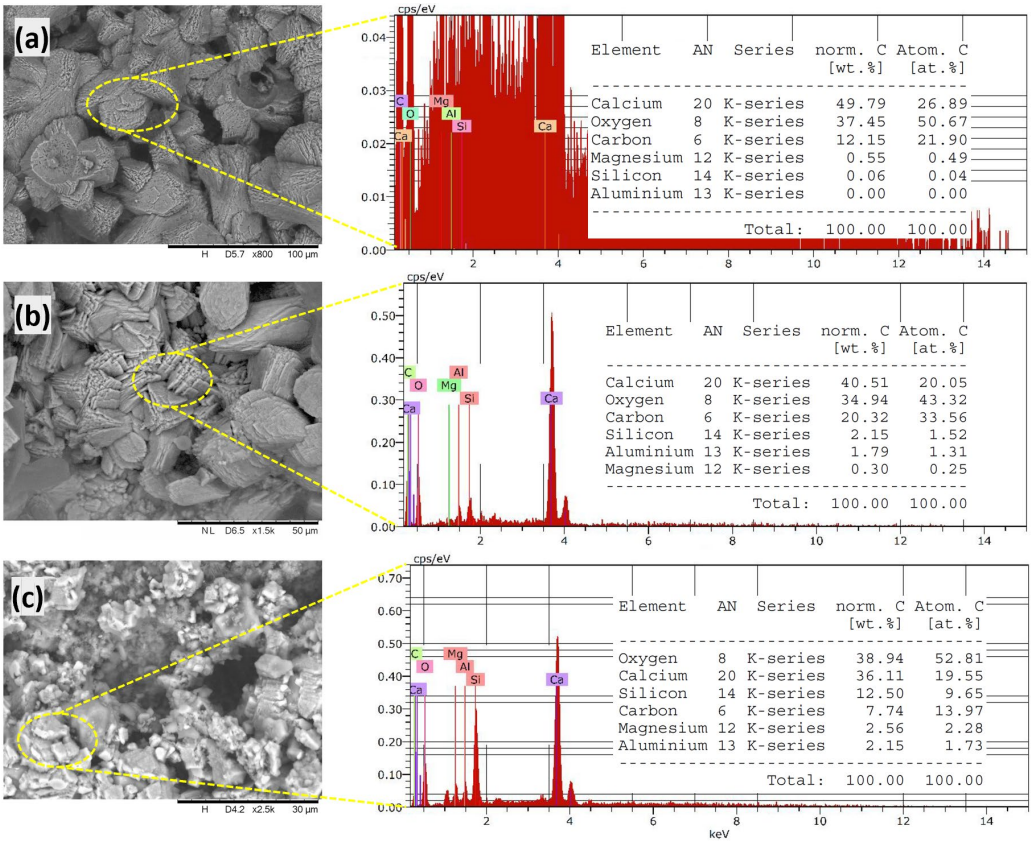

Figure 6-14: SEM images with EDX pattern of self-healing products within cracks of (a) CL-EG, (b) CC-EG, and (c) R-EG specimens.

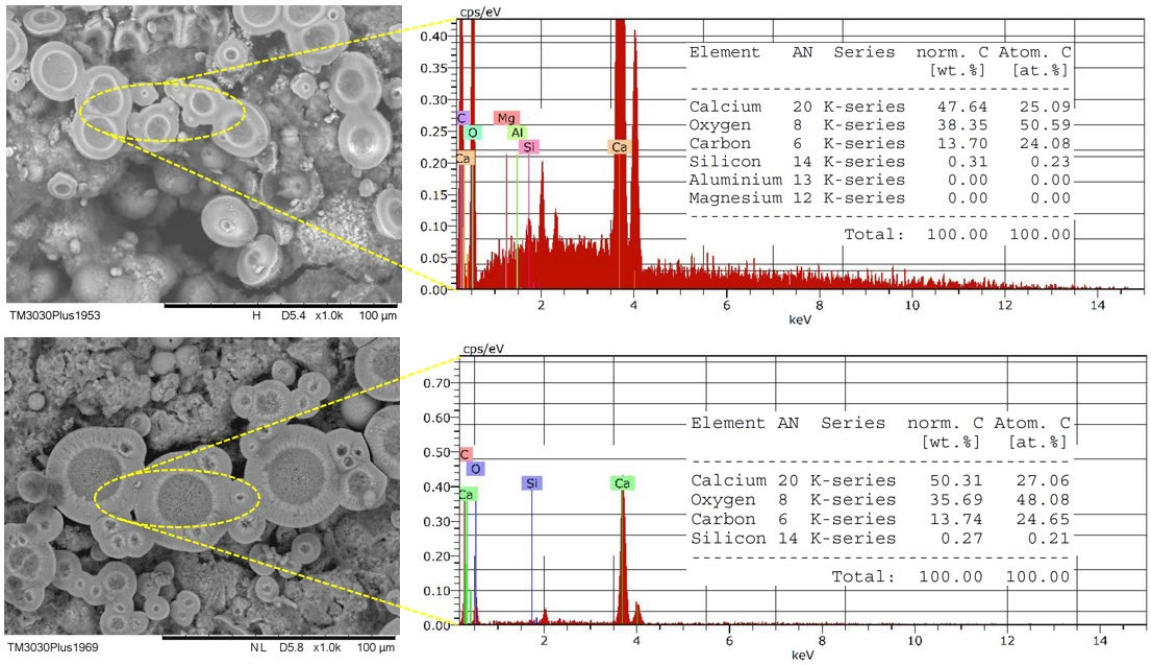

Figure 6-15: SEM images with EDX demonstrating the unique morphology of the self-healing product in CC-EG specimens.

Figure 6-16 shows many crystals covering the surface of PVA fibres. Some precipitates that look like irregular polyhedron crystals, agglomeration of rhombohedra crystals, and needle-shaped clusters were bound together. Based on the SEM images, PVA fibres may have promoted the precipitation of the self-healing products by acting as nucleation sites. A previous study (Zhang *et al*., 2020) stated that PVA fibres facilitated the precipitation of self-healing products ($CaCO_3$) via several intermolecular forces, such as Van der Waals forces, ionic bonding, and hydrogen bonding.

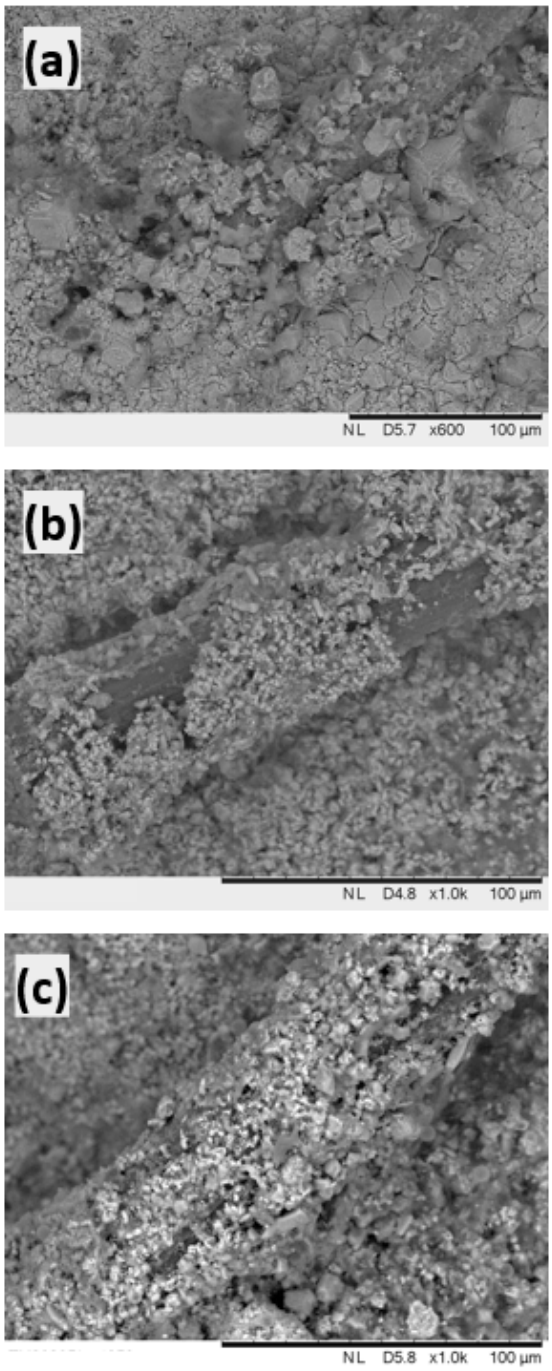

Figure 6-16: Self-healing products covering PVA fibre for (a) CL-EG, (b) CC-EG, and (c) R-EG specimens.

6.3.7 Crystal phases of self-healing products

Based on the abovementioned EDX results, the existence of calcium carbonate was confirmed. However, there are three polymorphs of anhydrous calcium carbonate: calcite, vaterite, and aragonite (Ni and Ratner, 2008). To investigate the effect of calcium sources on the crystal phase of calcium carbonate, Raman spectroscopy was used to conduct qualitative polymorphic analyses.

As shown in **Figure 6-17**, specimen groups R-EG and CL-EG had the same characteristic spectral bands, with four identical peaks of wavenumbers (also called Raman shifts). The most intense band, corresponding to the symmetric stretching mode (ν_1 vibration) of the carbonate groups, appeared at 1086 cm^{-1} (Envedi *et al*., 2020). Likewise, the other three minor bands, due to external lattice mode and in-plane bending mode (ν_4 vibration), occurred at 158 (156) cm^{-1}, 282 cm^{-1}, and 712 cm^{-1}. These four spectral bands suggest the existence of calcite, which concurs previous findings (Saracho *et al*., 2009; White, 2009; DeCarlo, 2018). Similar study by Wiktor and Jonkers (2011) revealed that calcite was the self-healing product by metabolic activities of *B. alkalinitrilicus* when calcium lactate was added as calcium source to facilitate bio-mineralization. In contrast, precipitates within the cracks of CC-EG specimens exhibited two types of spectra. One spectrum showed the evidence of calcite, the same as that of groups R-EG and CL-EG. An indicative vaterite spectrum with double peaks at 1078 and 1092 cm^{-1}, which agrees with literature bands (Zambare *et al*., 2020; Gabrielli *et al*., 2003), was also observed.

According to Ostwald's rule, less stable polymorph usually crystallizes first (Rodriguez-Navarro *et al*., 2012). It is also worth noting that a more stable polymorph has a lower solubility index (Bundur *et al*., 2017). The solubility index for the three non-hydrated crystalline $CaCO_3$ polymorphs from highest to lowest is vaterite, aragonite, and calcite, suggesting that the stability order for the $CaCO_3$ polymorphs from the most thermodynamically stable polymorph to the least stable is calcite, aragonite, and vaterite. The crystal polymorphs are affected by many factors such as temperature, ion concentration, pH, etc. (Bundur *et al*., 2017; Tai and Chen, 1998). The spherulitic morphology of vaterite interpreted by Raman spectroscopy indicates the longevity of vaterite since it remained present after several months. Compelling results demonstrated

the extraordinary longevity of vaterite (Friedman and Schultz, 1994; Giralt *et al*., 2001; Chekroun *et al*., 2004) in previous research. It appears that chloride ions might promote the formation of vaterite and contribute to its stabilization.

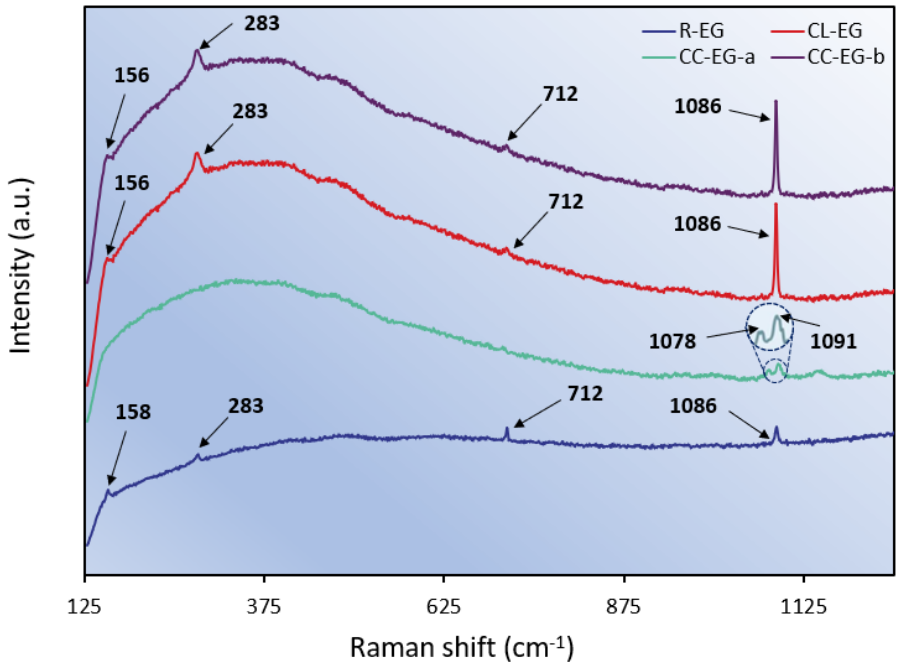

Figure 6-17: Raman spectra of polymorphic $CaCO_3$ crystals formed within cracks in the three mixtures.

6.3.8 Biomineralization with different calcium resources

S. pasteurii was involved in two main reactions in this study: urea hydrolysis and metabolic conversion of calcium lactate, which triggered calcium carbonate precipitation. In the first reaction, urea was enzymatically hydrolyzed by the bacteria with urease (**Eq. 6-2**). Carbonate ions and ammonium were derived from the decomposition of urea. Carbonate ions then simultaneously triggered the formation of calcium carbonate when soluble calcium ions (supplied by calcium chloride) were present in the surrounding environments (Castro-Alonso *et al*., 2019). In the second reaction, the metabolic conversion of calcium lactate favoured the primary precipitation of calcium carbonate, according to **Eq. 6-3** (Jonkers *et al*., 2010).

$$CO(NH_2)_2 + H_2O \xrightarrow{\text{Urease}} CO_3^{2-} + 2NH_4^+ \quad \text{Eq. 6-2}$$

$$Ca^{2+} + CO_3^{2-} \rightarrow CaCO_3 \downarrow \quad \text{Eq. 6-3}$$

In addition, CO_2 released simultaneously from the conversion of calcium lactate via bacterial metabolism can transform into carbonic acid (**Eq. 6-5**). Based on **Eq. 6-6**, hydroxyl ions leaching from the matrix react with H_2CO_3 to form carbonates (Zhang *et al*., 2017; Zhang *et al*., 2020), thereby yielding calcium carbonate precipitates.

$$CaC_6H_{10}O_6 + 6O_2 \rightarrow CaCO_3 \downarrow + CO_2 \uparrow + 5H_2O \quad \text{Eq. 6-4}$$

$$CO_2 + H_2O \rightarrow H_2CO_3 \quad \text{Eq. 6-5}$$

$$2OH^- + H_2CO_3 \leftrightarrow CO_3^{2-} + 2H_2O \quad \text{Eq. 6-6}$$

In the abovementioned two types of biomineralization mechanisms, *S. pasteurii* plays an essential role in providing continuous and stable calcium carbonate precipitation by acting as nucleation sites (Torgal *et al*., 2015; Hammes and Verstraete, 2002). Furthermore, calcium carbonate precipitation occurs at the bacterial cell surface due to the unique structure of *S. pasteurii* cell envelope as gram-positive bacteria (**Eqs. 6-7** and **6-8**).

$$Ca^{2+} + \text{Cell} \rightarrow \text{Cell} - Ca^{2+} \quad \text{Eq. 6-7}$$

$$\text{Cell} - Ca^{2+} + CO_3^{2-} \rightarrow \text{Cell} - CaCO_3 \quad \text{Eq. 6-8}$$

As shown in **Figure 6-18**, the cell walls of *S. pasteurii* are composed predominantly of peptidoglycan with multiple layers made of glycan chains that surround the cell (Pasquina-Lemonche *et al*., 2020). Interfacial effects enable the sites in the peptidoglycan to nucleate the deposition of metal ions (Sefan and Berenjian, 2018). In addition, due to the existence of functional groups in teichoic acids, like carboxyl and phosphate groups (Scott and Barnett, 2006), the negatively charged cell wall can sequester Ca^{2+} ions and bind them onto the peptidoglycan membrane (Qian *et al*., 2021). The unique cell envelope would accelerate bio-mineralization when an increase of carbonates occurs.

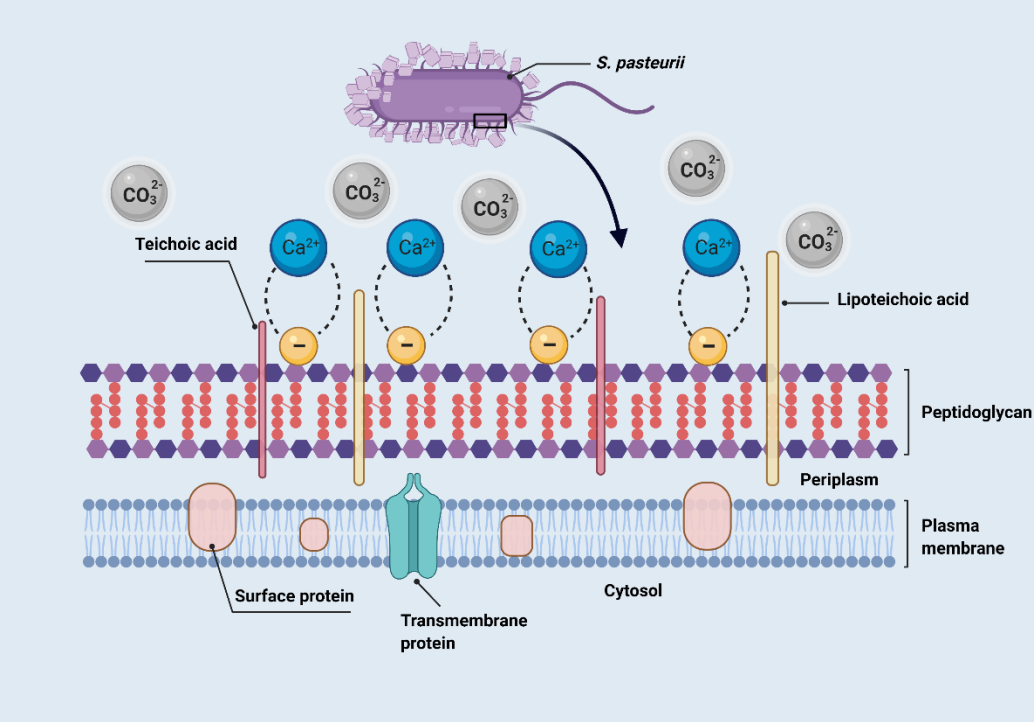

Figure 6-18: Schematic diagram of *S. pasteurii* cell wall acting as nucleation sites.

6.3.9 Comparison of two calcium sources considering economy and sustainability

In this study, calcium lactate and calcium chloride were used as calcium sources that facilitated calcium carbonate precipitation, therefore healing cracks progressively. The bacterial specimens with two calcium sources impregnated showed an equivalent crack healing ratio and a similar reduction of water absorption. Both calcium sources are good options as crack self-healing promoters. However, a better calcium source must be determined toward the future commercialization of bio-inspired AAS-based construction materials.

It is of great significance to evaluate the economic feasibility of the two calcium sources. An inexpensive additive is therefore recommended. The cost evaluation was made using 1-kg calcium carbonate yielded by the biomineralization via the two pathways mentioned in **Section 6.3.8**. The following cost calculation was made considering Canadian markets and taxes. As shown in **Figure 6-19**, an equivalent 2.18 kg calcium lactate is necessary to produce 1 kg calcium carbonate via bacterial metabolism. In contrast, the same weight of

calcium carbonate requires 1.11 kg calcium chloride and 0.6 kg urea. The lowest price for calcium lactate (food grade), calcium chloride, and urea is 1.67 CAD/kg, 1.66 CAD/kg, and 3.99 CAD/kg, respectively. It was therefore concluded that calcium lactate is more cost-effective (3.64 CAD) than calcium chloride (4.24 CAD).

Regarding sustainability, calcium chloride as a type of calcium source, can be detrimental to the durability of reinforced structures by accelerating steel rebar corrosion [123]. In addition, ammonia is generated (**Eq. 6-9**) during the ureolytic activity, which may have negative impacts on the surrounding environment [124]. None of the existing studies have evaluated the concern about this release of ammonia and ammonium into the surrounding environment. It is believed that more research should be conducted on the safe level of released ammonia and ammonium during the ureolytic process before claiming that this type of MICP is an environmentally sustainable method for crack self-healing [125].

$$CO(NH_2)_2 + H_2O \rightarrow NH_2COOH + NH_3 \uparrow \qquad \text{Eq. 6-9}$$

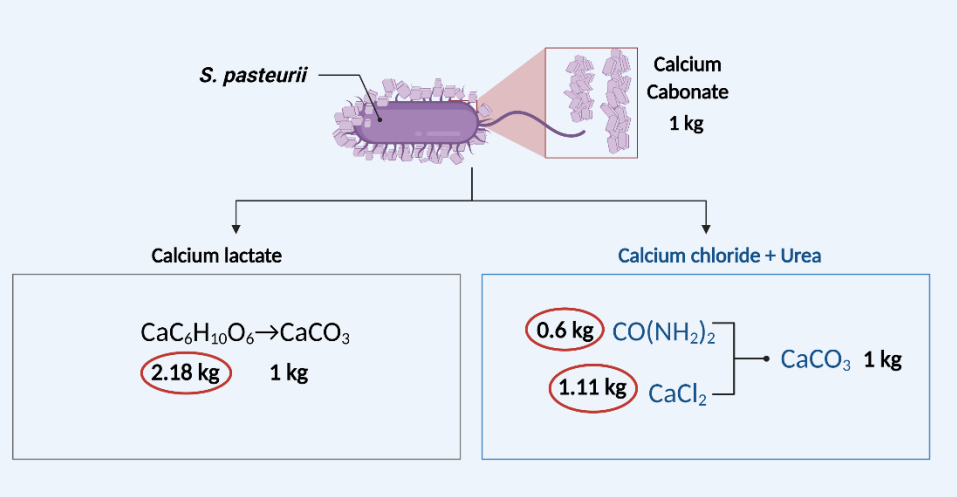

Figure 6-19: Mass calculation of two calcium sources for producing calcium carbonate in ideal conditions.

6.4 CONCLUSIONS

This chapter details a multi-technique experimental study investigating the self-healing behaviour of AAS-based composites incorporating immobilized *S. pasteurii* with two different calcium sources. Based on the experimental results, conclusions can be drawn up as follows:

- Bio-based specimens attained a remarkably enhanced surface crack healing ratio.
- The calorimetric curves for AAS paste incorporated with different calcium additives induced a retarding effect that delayed the acceleration phase compared to the reference sample
- The specimens incorporating bacteria immobilized EG compensated for the decrease in mechanical properties caused by the combination of bacterial nutrients and EG.
- Bio-specimens with calcium lactate and calcium chloride as calcium sources exhibited significant decrease in water sorptivity compared with that of abiotic control samples.
- MIP results revealed that the biomineralization via metabolic activities of *S. pasteurii* contributed to a reduction of the pore volume, which in turn confirmed the decrease in the water sorptivity coefficient.
- SEM-EDX confirmed the presence of calcium carbonate as the dominant self-healing compound. In addition, results from Raman spectroscopy indicated that the calcium carbonate in bacteria-based specimens with calcium chloride showed two polymorphs, namely, calcite and vaterite, in comparison to calcite only observed in the counterparts with calcium lactate.
- Owing to the existence of functional groups, the negatively charged cell wall of *S. pasteurii* can sequester Ca^{2+} ions and bind them onto the peptidoglycan membrane, therefore facilitating bio-mineralization when an increase of carbonates occurred. Similarly, PVA fibres acted as preferential crystal nucleation sites for calcium carbonate precipitation.
- It was suggested that calcium lactate as the calcium source was a better option considering economic feasibility and sustainability.

6.5 REFERENCES

Achal, V., and Mukherjee, A. (2015). A review of microbial precipitation for sustainable construction. *Construction and Building Materials, 93*, 1224-1235.

Achal, V., Mukherjee, A., Basu, P., and Reddy, M. S. (2009). Lactose mother liquor as an alternative nutrient source for microbial concrete production by Sporosarcina pasteurii. *Journal of industrial Microbiology and biotechnology, 36*(3), 433-438.

Aiken, T. A., Kwasny, J., Sha, W., and Soutsos, M. N. (2018). Effect of slag content and activator dosage on the resistance of fly ash geopolymer binders to sulfuric acid attack. *Cement and Concrete Research, 111*, 23-40.

Alam, M., Youssef, M., and Nehdi, M. (2007). Utilizing shape memory alloys to enhance the performance and safety of civil infrastructure: a review. *Canadian Journal of Civil Engineering, 34*(9), 1075-1086.

Alazhari, M., Sharma, T., Heath, A., Cooper, R., and Paine, K. (2018). Application of expanded perlite encapsulated bacteria and growth media for self-healing concrete. *Construction and Building Materials, 160*, 610-619.

Ali, A. M., Sanjayan, J., and Guerrieri, M. (2017). Performance of geopolymer high strength concrete wall panels and cylinders when exposed to a hydrocarbon fire. *Construction and Building Materials, 137*, 195-207.

Alyousef, R. A. M., Alabduljabbar, H. A. M., and El-Zeadani, M. (2020). Clean production and properties of geopolymer concrete; A review.

Amran, Y. M., Alyousef, R., Alabduljabbar, H., and El-Zeadani, M. (2019). Clean production and properties of geopolymer concrete; A review. *Journal of Cleaner Production*, 119679.

Atiş, C. D., Bilim, C., Çelik, Ö., and Karahan, O. (2009). Influence of activator on the strength and drying shrinkage of alkali-activated slag mortar. *Construction and Building Materials, 23*(1), 548-555.

Azarsa, P., Gupta, R., and Biparva, A. (2019). Assessment of self-healing and durability parameters of concretes incorporating crystalline admixtures and Portland Limestone Cement. *Cement and Concrete Composites, 99*, 17-31.

Bajpai, R., Choudhary, K., Srivastava, A., Sangwan, K. S., and Singh, M. (2020). Environmental Impact Assessment of Fly Ash and Silica Fume Based Geopolymer Concrete. *Journal of Cleaner Production*, 120147.

Bayati, M., and Saadabadi, L. A. (2021). Efficiency of bacteria based self-healing method in alkali-activated slag (AAS) mortars. *Journal of Building Engineering, 42*, 102492.

Bhaskar, S., Hossain, K. M. A., Lachemi, M., Wolfaardt, G., and Kroukamp, M. O. (2017). Effect of self-healing on strength and durability of zeolite-immobilized bacterial cementitious mortar composites. *Cement and Concrete Composites, 82*, 23-33.

Bonilla, L., Hassan, M. M., Noorvand, H., Rupnow, T., and Okeil, A. (2018). Dual self-healing mechanisms with microcapsules and shape memory alloys in reinforced concrete. *Journal of materials in civil engineering, 30*(2), 04017277.

Borg, R. P., Cuenca, E., Gastaldo Brac, E. M., and Ferrara, L. (2018). Crack sealing capacity in chloride-rich environments of mortars containing different cement substitutes and crystalline admixtures. *Journal of Sustainable Cement-Based Materials, 7*(3), 141-159.

Buller, A. S., Lee, K.-M., and Jang, S. Y. (2019). Using the steady-state chloride migration test to evaluate the self-healing capacity of cracked mortars containing crystalline, expansive, and swelling admixtures. *Materials, 12*(11), 1865.

Bundur, Z. B., Amiri, A., Ersan, Y. C., Boon, N., and De Belie, N. (2017). Impact of air entraining admixtures on biogenic calcium carbonate precipitation and bacterial viability. *Cement and Concrete Research, 98*, 44-49.

Bundur, Z. B., Kirisits, M. J., and Ferron, R. D. (2015). Biomineralized cement-based materials: Impact of inoculating vegetative bacterial cells on hydration and strength. *Cement and Concrete Research, 67*, 237-245.

Cai, J., Li, X., Tan, J., and Vandevyvere, B. (2020). Fly ash-based geopolymer with self-heating capacity for accelerated curing. *Journal of Cleaner Production*, 121119.

Castro-Alonso, M. J., Montañez-Hernandez, L. E., Sanchez-Muñoz, M. A., Macias Franco, M. R., Narayanasamy, R., and Balagurusamy, N. (2019). Microbially Induced Calcium Carbonate Precipitation (MICP) and Its Potential in Bioconcrete: Microbiological and Molecular Concepts. *Frontiers in Materials, 6*. doi: 10.3389/fmats.2019.00126

Celik, A., Yilmaz, K., Canpolat, O., Al-Mashhadani, M. M., Aygörmez, Y., and Uysal, M. (2018). High-temperature behavior and mechanical characteristics of boron waste additive metakaolin based geopolymer composites reinforced with synthetic fibers. *Construction and Building Materials, 187*, 1190-1203.

Chahal, N., Siddique, R., and Rajor, A. (2012). Influence of bacteria on the compressive strength, water absorption and rapid chloride permeability of fly ash concrete. *Construction and Building Materials, 28*(1), 351-356.

Chekroun, K. B., Rodríguez-Navarro, C., González-Muñoz, M. T., Arias, J. M., Cultrone, G., and Rodríguez-Gallego, M. (2004). Precipitation and growth morphology of calcium carbonate induced by Myxococcus xanthus: implications for recognition of bacterial carbonates. *Journal of Sedimentary Research, 74*(6), 868-876.

Chen, J., Dong, Q., Ma, X., Fan, T.-H., and Lei, Y. (2016). Repetitive Biomimetic Self-healing of Ca 2+-Induced Nanocomposite Protein Hydrogels. *Sci Rep, 6*, 30804.

Chindasiriphan, P., Yokota, H., and Pimpakan, P. (2020). Effect of fly ash and superabsorbent polymer on concrete self-healing ability. *Construction and Building Materials, 233*, 116975.

Chithiraputhiran, S., and Neithalath, N. (2013). Isothermal reaction kinetics and temperature dependence of alkali activation of slag, fly ash and their blends. *Construction and Building Materials, 45*, 233-242.

Choi, S.-G., Chang, I., Lee, M., Lee, J.-H., Han, J.-T., and Kwon, T.-H. (2020). Review on geotechnical engineering properties of sands treated by microbially induced calcium carbonate precipitation (MICP) and biopolymers. *Construction and Building Materials, 246*, 118415.

Dange, S., and Suryawanshi, S. (2017). Geopolymer Concrete-A Review. *Imperial J. Interdiscip. Res.*, 3.

De Muynck, W., Debrouwer, D., De Belie, N., and Verstraete, W. (2008). Bacterial carbonate precipitation improves the durability of cementitious materials. *Cement and Concrete Research, 38*(7), 1005-1014.

DeCarlo, T. M. (2018). Characterizing coral skeleton mineralogy with Raman spectroscopy. *Nature communications, 9*(1), 1-3.

Dong, B., Fang, G., Wang, Y., Liu, Y., Hong, S., Zhang, J., Lin, S., and Xing, F.. (2017). Performance recovery concerning the permeability of concrete by means of a microcapsule based self-healing system. *Cement and Concrete Composites, 78*, 84-96.

Ducasse-Lapeyrusse, J., Gagné, R., Lors, C., and Damidot, D. (2017). Effect of calcium gluconate, calcium lactate, and urea on the kinetics of self-healing in mortars. *Construction and Building Materials, 157*, 489-497.

e Portugal, C. R. M., Fonyo, C., Machado, C. C., Meganck, R., and Jarvis, T. (2020). Microbiologically Induced Calcite Precipitation biocementation, green alternative for roads–is this the breakthrough? A critical review. *Journal of Cleaner Production, 262*, 121372.

Enyedi, N. T., Makk, J., Kótai, L., Berényi, B., Klébert, S., Sebestyén, Z., Molnár, Z., Borsodi, A.K., Leél-Őssy, S., Demény, A., and Németh, P. (2020). cave bacteria-induced amorphous calcium carbonate formation. *Scietific Reports, 10*(1), 1-12.

Farle, A., Boatemaa, L., Shen, L., Gövert, S., Kok, J., Bosch, M., Yoshioka, S., Van Der Zwaag, S. and Sloof, W.G. (2016). Demonstrating the self-healing behaviour of some selected ceramics under combustion chamber conditions. *Smart Materials and Structures, 25*(8), 084019.

Feng, J., Su, Y., and Qian, C. (2019). Coupled effect of PP fiber, PVA fiber and bacteria on self-healing efficiency of early-age cracks in concrete. *Construction and Building Materials, 228*, 116810.

Ferguson, J., Schultz, B. F., and Rohatgi, P. K. (2014). Self-healing metals and metal matrix composites. *Jom, 66*(6), 866-871.

Friedman, G., and Schultz, D. (1994). Precipitation of vaterite ($CaCO_3$) during oil field drilling. *Mineralogical Magazine, 58*(392), 401-408.

Gabrielli, C., Jaouhari, R., Joiret, S., Maurin, G., and Rousseau, P. (2003). Study of the electrochemical deposition of CaCO3 by in situ Raman spectroscopy: I. Influence of the substrate. *Journal of the Electrochemical Society, 150*(7), C478.

Ghosh, P., Mandal, S., Chattopadhyay, B., and Pal, S. (2005). Use of microorganism to improve the strength of cement mortar. *Cement and Concrete Research, 35*(10), 1980-1983.

Giralt, S., Julià, R., and Klerkx, J. (2001). Microbial biscuits of vaterite in lake Issyk-Kul (Republic of Kyrgyzstan). *Journal of Sedimentary Research, 71*(3), 430-435.

Greil, P. (2019). Self-Healing Engineering Ceramics with Oxidation-Induced Crack Repair. *Advanced Engineering Materials*, 1901121.

Grillo, J., Montaño, A., González, C., and Barón, G. (2019). *Removal of cadmium in wastewater through geopolymeric materials based on pumice.* Paper presented at the Journal of Physics: Conference Series.

Gwon, S., Ahn, E., and Shin, M. (2019). Self-healing of modified sulfur composites with calcium sulfoaluminate cement and superabsorbent polymer. *Composites Part B: Engineering, 162*, 469-483.

Hager, M. D. (2017). Self-healing materials. *Handbook of Solid State Chemistry*, 201-225.

Hajimohammadi, A., Ngo, T., Provis, J. L., Kim, T., and Vongsvivut, J. (2019). High strength/density ratio in a syntactic foam made from one-part mix geopolymer and cenospheres. *Composites Part B: Engineering, 173*, 106908.

Hammes, F., and Verstraete, W. (2002). Key roles of pH and calcium metabolism in microbial carbonate precipitation. *Reviews in environmental science and biotechnology, 1*(1), 3-7.

He, Z.-h., Li, L.-y., and Du, S.-g. (2017). Creep analysis of concrete containing rice husk ash. *Cement and Concrete Composites, 80*, 190-199.

Hu, W., Nie, Q., Huang, B., Shu, X., and He, Q. (2018). Mechanical and microstructural characterization of geopolymers derived from red mud and fly ashes. *Journal of Cleaner Production, 186*, 799-806.

Imato, K., Natterodt, J. C., Sapkota, J., Goseki, R., Weder, C., Takahara, A., and Otsuka, H. (2017). Dynamic covalent diarylbibenzofuranone-modified nanocellulose: mechanochromic behaviour and application in self-healing polymer composites. *Polymer Chemistry, 8*(13), 2115-2122.

Jadhav, U. U., Lahoti, M., Chen, Z., Qiu, J., Cao, B., and Yang, E.-H. (2018). Viability of bacterial spores and crack healing in bacteria-containing geopolymer. *Construction and Building Materials, 169*, 716-723.

Janik, J. S. (2017). *Evaluation of the possibility of geopolymer concrete precast element manufacturing in a Polish production plant.* Instytut Inżynierii Budowlanej.

Jansen, D., Goetz-Neunhoeffer, F., Lothenbach, B., and Neubauer, J. (2012). The early hydration of Ordinary Portland Cement (OPC): An approach comparing measured heat flow with calculated heat flow from QXRD. *Cement and Concrete Research, 42*(1), 134-138.

Jena, S., Basa, B., Panda, K. C., and Sahoo, N. K. (2020). Impact of Bacillus subtilis bacterium on the properties of concrete. *Materials Today: Proceedings*.

Jiang, Z., Li, W., and Yuan, Z. (2015). Influence of mineral additives and environmental conditions on the self-healing capabilities of cementitious materials. *Cement and Concrete Composites, 57*, 116-127.

Jonkers, H. M., and Schlangen, E. (2008). *Development of a bacteria-based self healing concrete.* Paper presented at the Proc. int. FIB symposium.

Jonkers, H. M., Thijssen, A., Muyzer, G., Copuroglu, O., and Schlangen, E. (2010). Application of bacteria as self-healing agent for the development of sustainable concrete. *Ecological engineering, 36*(2), 230-235.

Kang, J., Tok, J. B.-H., and Bao, Z. (2019). Self-healing soft electronics. *Nature Electronics, 2*(4), 144-150.

Katpady, D. N., Takewaka, K., Yamaguchi, T., and Akira, Y. (2020). Performance of slag based Shirasu geopolymer cured under ambient condition. *Construction and Building Materials, 234*, 117210.

Khushnood, R. A., Qureshi, Z. A., Shaheen, N., and Ali, S. (2020). Bio-mineralized self-healing recycled aggregate concrete for sustainable infrastructure. *Science of The Total Environment, 703*, 135007.

Lemougna, P. N., Wang, K.-t., Tang, Q., Nzeukou, A., Billong, N., Melo, U. C., and Cui, X.-m. (2018). Review on the use of volcanic ashes for engineering applications. *Resources, Conservation and Recycling, 137*, 177-190.

Li, C., Jiang, L., and Li, S. (2020). Effect of limestone powder addition on threshold chloride concentration for steel corrosion in reinforced concrete. *Cement and Concrete Research, 131*, 106018.

Li, J., Sun, P., Li, J., Lv, Y., Ye, H., Shao, L., and Du, D. (2020). Synthesis of electrolytic manganese residue-fly ash based geopolymers with high compressive strength. *Construction and Building Materials, 248*, 118489.

Li, W., Dong, B., Yang, Z., Xu, J., Chen, Q., Li, H., Xing, F., and Jiang, Z. (2018). Recent advances in intrinsic self-healing cementitious materials. *Advanced Materials, 30*(17), 1705679.

Li, Y., Min, X., Ke, Y., Liu, D., and Tang, C. (2019). Preparation of red mud-based geopolymer materials from MSWI fly ash and red mud by mechanical activation. *Waste management, 83*, 202-208.

Ma, Y., Hu, J., and Ye, G. (2013). The pore structure and permeability of alkali activated fly ash. *Fuel, 104*, 771-780.

Markvicka, E. J., Bartlett, M. D., Huang, X., and Majidi, C. (2018). An autonomously electrically self-healing liquid metal–elastomer composite for robust soft-matter robotics and electronics. *Nature materials, 17*(7), 618-624.

Mechtcherine, V., Snoeck, D., Schröfl, C., De Belie, N., Klemm, A. J., Ichimiya, K., Moon, J., Wyrzykowski, M., Lura, P., Toropovs, N., and Assmann, A. (2018). Testing superabsorbent polymer (SAP) sorption properties prior to implementation in concrete: results of a RILEM Round-Robin Test. *Materials and Structures, 51*(1), 28.

Mehta, A., and Siddique, R. (2017). Sulfuric acid resistance of fly ash based geopolymer concrete. *Construction and Building Materials, 146*, 136-143.

Neville, A. M. (1995). *Properties of concrete* (Vol. 4): longman London.

Nguyen, T. H., Ghorbel, E., Fares, H., and Cousture, A. (2019). Bacterial self-healing of concrete and durability assessment. *Cement and Concrete Composites, 104*, 103340.

Ni, M., and Ratner, B. D. (2008). Differentiating calcium carbonate polymorphs by surface analysis techniques—an XPS and TOF-SIMS study. *Surface and Interface Analysis: An International Journal devoted to the development and application of techniques for the analysis of surfaces, interfaces and thin films, 40*(10), 1356-1361.

Noushini, A., Castel, A., Aldred, J., and Rawal, A. (2020). Chloride diffusion resistance and chloride binding capacity of fly ash-based geopolymer concrete. *Cement and Concrete Composites, 105*, 103290.

Nuaklong, P., Jongvivatsakul, P., Pothisiri, T., Sata, V., and Chindaprasirt, P. (2020). Influence of rice husk ash on mechanical properties and fire resistance of recycled aggregate high-calcium fly ash geopolymer concrete. *Journal of Cleaner Production, 252*, 119797.

Ozaki, S., Osada, T., and Nakao, W. (2016). Finite element analysis of the damage and healing behavior of self-healing ceramic materials. *International Journal of Solids and Structures, 100*, 307-318.

Pasquina-Lemonche, L., Burns, J., Turner, R., Kumar, S., Tank, R., Mullin, N., Wilson, J.S., Chakrabarti, B., Bullough, P.A., Foster, S.J., and Hobbs, J.K. (2020). The architecture of the Gram-positive bacterial cell wall. *Nature, 582*(7811), 294-297.

Pouhet, R., and Cyr, M. (2016). Formulation and performance of flash metakaolin geopolymer concretes. *Construction and Building Materials, 120*, 150-160.

Provis, J. L. (2018). Alkali-activated materials. *Cement and Concrete Research, 114*, 40-48.

Provis, J. L., and Van Deventer, J. S. J. (2009). *Geopolymers: structures, processing, properties and industrial applications*. Cambridge: Elsevier.

Provis, J. L., and Bernal, S. A. (2014). Geopolymers and related alkali-activated materials. *Annual Review of Materials Research, 44*, 299-327.

Qian, C., Rui, Y., Wang, C., Wang, X., Xue, B., and Yi, H. (2021). Bio-mineralization induced by Bacillus mucilaginosus in crack mouth and pore solution of cement-based materials. *Materials Science and Engineering: C, 126*, 112120.

Ramakrishnan, V., Bang, S., and Deo, K. (1998). *A novel technique for repairing cracks in high performance concrete using bacteria.* Paper presented at the Proc. of the Int. Conf. on HPHSC.

Ranjbar, N., and Zhang, M. (2020). Fiber-reinforced geopolymer composites: A review. *Cement and Concrete Composites, 107*, 103498.

Rodriguez-Navarro, C., Jroundi, F., Schiro, M., Ruiz-Agudo, E., and González-Muñoz, M. T. (2012). Influence of substrate mineralogy on bacterial mineralization of calcium carbonate: implications for stone conservation. *Applied and environmental microbiology, 78*(11), 4017-4029.

Roig-Flores, M., Pirritano, F., Serna, P., and Ferrara, L. (2016). Effect of crystalline admixtures on the self-healing capability of early-age concrete studied by means

of permeability and crack closing tests. *Construction and Building Materials, 114*, 447-457.

Rożek, P., Król, M., and Mozgawa, W. (2019). Geopolymer-zeolite composites: A review. *Journal of Cleaner Production*.

Saracho, A. C., Haigh, S. K., Hata, T., Soga, K., Farsang, S., Redfern, S. A., and Marek, E. (2020). Characterisation of CaCO 3 phases during strain-specific ureolytic precipitation. *Sci Rep, 10*(1), 1-12.

Scott, J. R., and Barnett, T. C. (2006). Surface proteins of gram-positive bacteria and how they get there. *Annu. Rev. Microbiol., 60*, 397-423.

Seifan, M., and Berenjian, A. (2018). Application of microbially induced calcium carbonate precipitation in designing bio self-healing concrete. *World Journal of Microbiology and Biotechnology, 34*(11), 168.

Seifan, M., Samani, A. K., and Berenjian, A. (2016). Induced calcium carbonate precipitation using Bacillus species. *Applied microbiology and biotechnology, 100*(23), 9895-9906.

Sevim, Ö., and Demir, İ. (2019). Optimization of fly ash particle size distribution for cementitious systems with high compactness. *Construction and Building Materials, 195*, 104-114.

Sha, D., Pan, B., and Sun, Y. (2020). A novel raw material for geopolymers: Coal-based synthetic natural gas slag. *Journal of Cleaner Production*, 121238.

Shi, C., Roy, D., and Krivenko, P. (2003). *Alkali-activated cements and concretes*: CRC press.

Shi, Z., Shi, C., Zhang, J., Wan, S., Zhang, Z., and Ou, Z. (2018). Alkali-silica reaction in waterglass-activated slag mortars incorporating fly ash and metakaolin. *Cement and Concrete Research, 108*, 10-19.

Shill, S. K., Al-Deen, S., Ashraf, M., and Hutchison, W. (2020). Resistance of fly ash based geopolymer mortar to both chemicals and high thermal cycles simultaneously. *Construction and Building Materials, 239*, 117886.

Singh, N., and Middendorf, B. (2020). Geopolymers as an alternative to Portland cement: An overview. *Construction and Building Materials, 237*, 117455.

Snoeck, D., Pel, L., and De Belie, N. (2020). Autogenous Healing in cementitious Materials with Superabsorbent polymers Quantified by Means of NMR. *Sci Rep, 10*(1), 1-6.

Song, C., Choi, Y. C., and Choi, S. (2016). Effect of internal curing by superabsorbent polymers–internal relative humidity and autogenous shrinkage of alkali-activated slag mortars. *Construction and Building Materials, 123*, 198-206.

Su, Y., Feng, J., Jin, P., and Qian, C. (2019). Influence of bacterial self-healing agent on early age performance of cement-based materials. *Construction and Building Materials, 218*, 224-234.

Suleiman, A., and Nehdi, M. (2018). Effect of environmental exposure on autogenous self-healing of cracked cement-based materials. *Cement and Concrete Research, 111*, 197-208.

Suleiman, A. R., Nelson, A. J., and Nehdi, M. L. (2019). Visualization and quantification of crack self-healing in cement-based materials incorporating different minerals. *Cement and Concrete Composites, 103*, 49-58.

Sun, Z., Vollpracht, A., and van der Sloot, H. A. (2019). pH dependent leaching characterization of major and trace elements from fly ash and metakaolin geopolymers. *Cement and Concrete Research, 125*, 105889.

Tai, C. Y., and Chen, F. B. (1998). Polymorphism of CaCO3, precipitated in a constant-composition environment. *AIChE Journal, 44*(8), 1790-1798.

Thakur, A. K., Pappu, A., and Thakur, V. K. (2019). Synthesis and characterization of new class of geopolymer hybrid composite materials from industrial wastes. *Journal of Cleaner Production, 230*, 11-20.

Thakur, V. K., and Kessler, M. R. (2015). Self-healing polymer nanocomposite materials: A review. *Polymer, 69*, 369-383.

Thomas, R., Lezama, D., and Peethamparan, S. (2017). On drying shrinkage in alkali-activated concrete: Improving dimensional stability by aging or heat-curing. *Cement and Concrete Research, 91*, 13-23.

Torgal, F. P., Labrincha, J. A., Diamanti, M. V., Yu, C.-P., and Lee, H.-K. (2015). *Biotechnologies and biomimetics for civil engineering*: Springer.

Van Tittelboom, K., De Belie, N., De Muynck, W., and Verstraete, W. (2010). Use of bacteria to repair cracks in concrete. *Cement and Concrete Research, 40*(1), 157-166.

Wang, X., Fang, C., Li, D., Han, N., and Xing, F. (2018). A self-healing cementitious composite with mineral admixtures and built-in carbonate. *Cement and Concrete Composites, 92*, 216-229.

Wang, X., Huang, Y., Huang, Y., Zhang, J., Fang, C., Yu, K., Chen, Q., Li, T., Han, R., Yang, Z. and Xu, P. (2019). Laboratory and field study on the performance of

microcapsule-based self-healing concrete in tunnel engineering. *Construction and Building Materials, 220*, 90-101.

Wang, X., Zhang, J., Han, R., Han, N., and Xing, F. (2019). Evaluation of damage and repair rate of self-healing microcapsule-based cementitious materials using electrochemical impedance spectroscopy. *Journal of Cleaner Production, 235*, 966-976.

White, S. N. (2009). Laser Raman spectroscopy as a technique for identification of seafloor hydrothermal and cold seep minerals. *Chemical Geology, 259*(3-4), 240-252.

White, S. R., Sottos, N. R., Geubelle, P. H., Moore, J. S., Kessler, M. R., Sriram, S., Brown, E.N. and Viswanathan, S. (2001). Autonomic healing of polymer composites. *Nature, 409*(6822), 794-797.

Wiktor, V., and Jonkers, H. M. (2011). Quantification of crack-healing in novel bacteria-based self-healing concrete. *Cement and Concrete Composites, 33*(7), 763-770.

Williams, S. L., Kirisits, M. J., and Ferron, R. D. (2017). Influence of concrete-related environmental stressors on biomineralizing bacteria used in self-healing concrete. *Construction and Building Materials, 139*, 611-618.

Xiang, J., Liu, L., He, Y., Zhang, N., and Cui, X. (2019). Early mechanical properties and microstructural evolution of slag/metakaolin-based geopolymers exposed to karst water. *Cement and Concrete Composites, 99*, 140-150.

Yao, X., Zhang, Z., Zhu, H., and Chen, Y. (2009). Geopolymerization process of alkali–metakaolinite characterized by isothermal calorimetry. *Thermochimica Acta, 493*(1-2), 49-54.

Yıldırım, G., Keskin, Ö. K., Keskin, S. B., Şahmaran, M., and Lachemi, M. (2015). A review of intrinsic self-healing capability of engineered cementitious composites: Recovery of transport and mechanical properties. *Construction and Building Materials, 101*, 10-21.

Yıldırım, G., Khiavi, A. H., Yeşilmen, S., and Şahmaran, M. (2018). Self-healing performance of aged cementitious composites. *Cement and Concrete Composites, 87*, 172-186.

Zambare, N. M., Naser, N. Y., Gerlach, R., and Chang, C. B. (2020). Mineralogy of microbially induced calcium carbonate precipitates formed using single cell drop-based microfluidics. *Sci Rep, 10*(1), 1-11.

Zhang, H. Y., Qiu, G. H., Kodur, V., and Yuan, Z. S. (2020). Spalling behavior of metakaolin-fly ash based geopolymer concrete under elevated temperature exposure. *Cement and Concrete Composites, 106*, 103483.

Zhang, J., Liu, Y., Feng, T., Zhou, M., Zhao, L., Zhou, A., and Li, Z. (2017). Immobilizing bacteria in expanded perlite for the crack self-healing in concrete. *Construction and Building Materials, 148*, 610-617.

Zhang, J., Zhou, A., Liu, Y., Zhao, B., Luan, Y., Wang, S., Yue, X. and Li, Z. (2017). Microbial network of the carbonate precipitation process induced by microbial consortia and the potential application to crack healing in concrete. *Scientific Reports, 7*(1), 1-10.

Zhang, L., Suleiman, A., and Nehdi, M. (2020). Self-healing in fiber-reinforced alkali-activated slag composites incorporating different additives. *Construction and Building Materials, 262*, 120059.

Zhang, L., Suleiman, A., and Nehdi, M. (2021). Crack Self-Healing in NaOH-Activated Slag-Based Composites Incorporating Calcium Hydroxide. *Journal of materials in civil engineering, 33*(4), 04021012.

Chapter 7

7 CHEMISTRY-INFORMED MACHINE LEARNING PREDICTION OF COMPRESSIVE STRENGTH FOR ALKALI-ACTIVATED MATERIALS[5]

The critical step towards the broader implementation of AAMs as construction materials is compressive strength. Wide-ranging research has been undertaken to explore diverse AAMs formulations. However, predicting the engineering properties of AAMs using traditional empirical and statistical methods is still hampered by inaccuracy and incertitude. This chapter proposes a chemistry-informed machine learning (ML) model to estimate the compressive strength of AAMs based on their mixture proportions and the chemical compositions of their precursors and activators. Purposefully, a comprehensive dataset encompassing 676 mixture design examples was extracted from peer-reviewed published research studies. A chemistry-based feature engineering was implemented to elevate the prediction performance of four applied ML models, including support vector machine, random forest, extra trees, and gradient boosting. Consequently, accurate predictions were achieved, having a low mean absolute error of 3.228 MPa. In addition, extensive computational experiments were performed using the best predictive model to unravel the impact of several mixture design variables on the compressive strength development of AAMs. Accordingly, the effect of the formulation of the precursor and activator on the compressive strength was broadly examined, and the results were thoroughly scrutinized.

7.1 INTRODUCTION

Ordinary Portland Cement (OPC) production emits approximately 5-8% of global anthropogenic CO_2 emissions (Castro-Alonso *et al*., 2019). It is forecasted to rise by 7% in 2050 under current scenarios (Habert *et al*., 2020), causing ever-increasing concerns about the net-zero target of the Paris Agreement. Therefore, there is an imperative need to

[5] A version of this chapter was submitted to the *Journal of Cleaner Production*.

substitute OPC with more environmentally sustainable materials, thereby curtailing CO_2 emissions from the OPC industry.

As one of the most promising construction materials with low environmental impact and energy consumption, alkali-activated materials (AAMs) have attracted tremendous attention over the past decades (Juenger *et al*., 2011). AAMs are inorganic polymers based on reactions between aluminosilicate resources (natural minerals, industrial by-products, and mining wastes) and alkaline activators (Nasr *et al*., 2018). A variety of aluminosilicates can be used as precursors for AAM production, including fly ash, blast furnace slag (Gruskovnjak *et al*., 2006), metakaolin (Davidovits, 1994), red mud, and rice husk ashes (He *et al*., 2013). Sodium-based alkalis, such as sodium hydroxide, waterglass, and sodium carbonate, have been extensively used as activators owing to their low-cost and activation effectiveness in achieving desirable engineering properties (Passuello *et al*., 2017; Provis and Van Deventer, 2014). Despite some noticeable challenges to be addressed, such as e.g. susceptibility to shrinkage-induced cracking (Kumarappa *et al*., 2018; Pacheco-Torgal *et al*., 2017), AAMs have been used in some full-scale construction projects, such as offshore structures (Criado and Provis, 2018), residential housing (Gavali and Ralegaonkar, 2020), watertight structures (Provis and Bernal, 2014), and heavy metal immobilizations (Tian *et al*., 2020), and demonstrated superior performance as substitutes to OPC concrete.

Being a primary property of AAMs', compressive strength (CS) has been extensively investigated (Okoye *et al*., 2015; Xing *et al*., 2019; Yang *et al*., 2012; Yang *et al*., 2019). Yet, there is currently no prevailing and widely accepted standard related to AAMs construction. In addition, many factors such as the water-to-binder (w/b) ratio, type of precursors and activators, curing regime, etc., can affect the compressive strength of AAMs, thereby making it complex to predict. Broader construction applications of AAMs have accordingly been impeded by the lack of fundamental knowledge of the complex effects of the multitude of parameters on compressive strength of AAMs.

To mitigate such lack of knowledge considering variations in mixture components, the current study proposes a soft computing framework for estimating the compressive

strength of AAMs based on their key mixture design variables. At the outset, a critical overview of the state-of-the-art is conducted below to identify the fundamental knowledge gaps, and thus, adopt a capable research methodology.

7.2 OVERVIEW OF STATE-OF-THE-ART

7.2.1 Knowledge background

Considerable research efforts have been devoted to investigating the effects of parameters, including the w/b ratio, type of the precursors and activators, activator dosage, and curing regime on the compressive strength of AAMs. For instance, the mechanical properties of $Ca(OH)_2$-based alkali-activated slag concrete with various w/b ratios were investigated by Yang *et al*. (2012). They reported that a lower w/b ratio resulted in higher compressive strength, showing a similar growth rate to that of OPC concrete. Currently, ground granulated blast furnace slag (GGBFS) and fly ash are the two most widely used precursors in alkali activation. Xie *et al*. (2019) examined the synergistic effect of GGBFS and fly ash on the fresh and hardened properties of alkali-activated geopolymer concrete with recycled aggregates. The results showed that a higher GGBS/fly ash ratio had a positive effect on compressive strength. This finding is in line with the work by Puertas *et al*. (2000), where the compressive strength of sodium hydroxide-activated slag/fly ash blends was improved by increasing the slag proportion.

The mechanical properties of AAMs can be tailored by modifying the activator types and their corresponding ratios. Alkali-activation of Turkish slag was explored by Aydın and Baradan (2014) via investigating the effect of sodium silicate and sodium hydroxide activators on mechanical properties. The test results demonstrated that sodium silicate-activated slag mortars exhibited higher compressive strength than that of similar specimens activated by sodium hydroxide. In addition, the SiO_2/Na_2O ratio (M_S) and Na_2O content played a vital role in compressive strength development. For example, the mortars activated by the combination of sodium silicate and sodium hydroxide with M_S=1.2 and Na_2O = 8% of slag content achieved the highest 28-d compressive strength. The curing temperature in the initial stage is essential to the geo-polymerization. Rovnaník (2010) analyzed the effects of various curing temperatures (10, 20, 40, 60, and

80 °C) on the microstructure and mechanical properties of metakaolin-based geopolymer. The results indicated that elevated temperature accelerated the strength development.

When designing AAM mixtures, the compressive strength should be considered based on the abovementioned influencing variables. Traditionally, many trial batches in the laboratory are required to obtain desirable compressive strength. However, the preparation of many AAM specimens is both labor-intensive and costly. Therefore, predictions of the compressive strength of AAMs without need for laborious batch trials is desirable since it saves time and cost and eliminates materials wastage.

7.2.2 Machine learning modelling

There has been a rapidly growing interest in soft computing techniques to model the engineering properties of different materials. Machine learning (ML) models are powerful intelligent tools to predict a target of interest based on input data. Owing to their complex design process and stochastic nature of production, the estimation of the properties of construction materials involves several intricacies. To tackle such complexities, ML techniques have been extensively adopted to estimate the engineering properties of construction materials. For instance, different properties of conventional and modern concretes, such as high and ultra-high performance concrete, recycled aggregate concrete, PCM-integrated concrete, fibre-reinforced concrete, self-compacting concrete, lightweight concrete, etc., have been investigated using various ML algorithms (Marani *et al*., 2020; Marani and Nehdi, 2020; Nunez *et al*., 2020; Zhang *et al*., 2020a; Zhang *et al*., 2020b). Accordingly, the compressive strength has been widely modelled in research studies being the most pivotal engineering characteristic of concrete.

Multifarious research studies have proven that robust ML models outperform traditional physical and empirical models in estimating various engineering properties of concrete. The complexities involved with cement hydration and microstructural development, along with the non-linear time and temperature dependent behaviour of cement paste are some of the computational obstacles in the accurate prediction of concrete properties (Naseri *et al*., 2020; Rajasekar *et al.*, 2019; Young *et al.*, 2019). On the other hand, ML models can be constructed based on input data of mixture proportions and curing

conditions to achieve precise estimation of the desired properties. Accurate and generalized predictions, less computational complexity, and convenient reproducibility are among the many advantages of ML models.

Nevertheless, AAMs entail a higher level of modelling complexity compared to conventional concrete. The reaction kinetics and microstructural development, and consequently the mechanical and durability properties of AAMs are substantially dependent on the chemistry and dosage of the precursors and activators. Furthermore, the chemical compositions of the precursors widely vary in different types of binders, such as slag or fly ash (Gomaa *et al*., 2021; Ke and Duan, 2021a). Such intricacies impose the need for establishing comprehensive models that account for the chemical compositions of the precursors and their reactions with different types of activators.

Despite extensive research on modelling different properties of conventional and modern concrete using ML approaches, few studies aimed at establishing robust data-driven models to forecast the mechanical properties of AAMs (Ali Khan *et al*., 2021; Gomaa *et al*., 2021; Ke and Duan, 2021a,b). Gomaa *et al*. (2021) deployed a random forest model to predict the slump and compressive strength of AAMs. The compressive strength dataset included 180 data examples along with 20 input attributes. Six different types of fly ash were used for preparing the mixture design data. The chemical composition of the fly ash and the curing conditions (curing time, temperature and regime) were included in the dataset. Their results indicated ability of the random forest model to unravel the underlying correlation of the chemical composition to predict the compressive strength. In another study, Ke and Duan (2021a) also concluded that ML models could be employed to recognize the mixture composition-property correlations and facilitate the design of AAM systems having various aluminosilicate resources.

A generalized ML framework to predict the mechanical properties of AAMs should be developed based on the chemical composition of the binder system and be capable of achieving the following objectives: 1) accurate and unbiased prediction of the desired characteristic(s); 2) adequately representing the chemical activity of the binder system; 3) accurately forecasting the behaviour of AAMs given its mixture design and chemical

compositions of its precursor(s); 4) capturing the mechanistic underpinnings of how chemically various precursors and activators affect the strength development of AAMs.

The overview of the state-of-the-art above suggests that well-trained ML techniques can establish a reliable computational framework to predict the compressive strength of AAM composites. Utilizing a comprehensive dataset incorporating the chemical compositions of the precursors and activators can assist the reliability and accuracy of model predictions and facilitate the design of various AAM systems. Purposefully, the present study intends to investigate the compressive strength of AAMs using several robust chemistry-informed ML models. A comprehensive dataset including 676 data examples of slag- and fly ash-based AAMs have been collected from peer-reviewed published research studies in the open literature. A chemistry-based feature engineering was implemented before model development. Support vector machine, random forest, extra trees, and gradient boosting regressors were developed to model the compressive strength of AAMs. Furthermore, extensive numerical experiments were performed to capture the effects of various mixture design variables on the compressive strength development of AAMs mixtures using the best predictive framework.

7.3 MODEL DEVELOPMENT

This section describes the data collection and the fundamentals of the applied machine learning (ML) models to predict the compressive strength of AAMs. After model development, profound numerical experiments were carried out to unravel the underlying chemistry linkages influencing the strength gain in AAMs.

7.3.1 Data collection and analysis

This study considers the mixture proportions of AAMs having slag or fly ash as precursors and sodium hydroxide and sodium silicate as activators. The mixture design variables contributing to the strength development of AAMs are accordingly selected. They include the dosages of slag (S), fly ash (F), sodium hydroxide (SH), sodium silicate (SS), water (W), fine aggregate (FA), and coarse aggregate (CA). The chemical compositions of the precursors were also involved in the data collection. Furthermore, the influential curing variables were considered through the curing temperature (T),

curing relative humidity (RH), and curing age (Age). Ultimately, a comprehensive dataset was compiled from peer-reviewed research studies published in reputed research forums. The criteria for selecting reliable references to construct the dataset are listed below:

- The data collection should come exclusively from eminent reputed and peer-reviewed journals.
- The mixture proportion of AAMs should be provided in detail.
- Only slag from the steel industries and fly ash from thermal power plants are considered in this research as precursors. Other types of by-products or wastes rich in silica and alumina have been excluded due to the lack of robust and comprehensive experimental data.
- Detailed proportions of the chemical oxides present in each precursor must be presented.
- In some references, specimens in molds covered with plastic sheets were considered cured under humid conditions since no evaporation was allowed.
- The proportions of the three chemical compositions of the activators (Na_2O, Na_2SiO_3, and H_2O) must be provided in the reference studies.
- Only natural river sand was used in this study. Other types of fine aggregates (e.g., demolished concrete and silica sand) were excluded due to the lack of consistent and comprehensive data.
- The input feature representing the water content denotes the extra water added in the mixture design. The water content in the sodium silicate was considered as a separate input feature.

In total 676 mixture design examples were retained as the un-preprocessed dataset considering the above design variables and data collection criteria. However, feature engineering is a critical step in establishing robust predictive ML models. Therefore, a chemistry-informed feature engineering was carried out in the current study to preprocess the data and subsequently develop the ML models, as explained below.

7.3.2 Chemistry-informed feature engineering and data preprocessing

Multitudinous existing studies reported that the strength development of AAMs is a kinetic-controlled process where the chemical compositions of the precursors and activators are of particularly great significance. Therefore, not only should the dosages of the binders and activators be considered in modelling, but their chemical compositions must also be considered to accurately reflect the mechanical strength gain. This contrasts with ML modelling of cement-based concretes, where the chemical compositions of the binder are typically ignored.

From a statistical point of view, feature engineering is a fundamental step of applied machine learning, which requires extensive domain knowledge. In general, it is crucial to preprocess the data so that the developed ML model can better recognize the underlying patterns in the data. Feature engineering is carried out by combining or transforming the preliminary features of the dataset into new attributes. Furthermore, reducing the number of input features by selecting the essential features results in more efficient computational models and more accurate estimations.

On the other hand, the collected dataset in this study comprises mixture designs of AAMs having slag and fly ash as precursors. Slag and fly ash have an extensively varying chemical composition due to their different types and sources (Xie *et al*., 2019; Xie *et al*., 2020). Consequently, the dataset features diverse chemical makeups data, which can further convolute the pattern recognition process. **Figure 7-1** indicates a ternary diagram of the chemical composition of the slag and fly ash in the collected dataset.

Nevertheless, considering the multitude of oxides in each type of binder generates a high-dimensional tabular dataset, which hinders establishing robust and accurate ML predictive frameworks considering the limited number of data examples. Therefore, the current study explores a feature engineering approach to incorporate the influential features that account for the chemical compositions of the binder system based on their respective reactivity. The reactivity of different binders, including OPC and supplementary cementitious materials (SCMs), can be quantified based on the major oxides in their chemical structure.

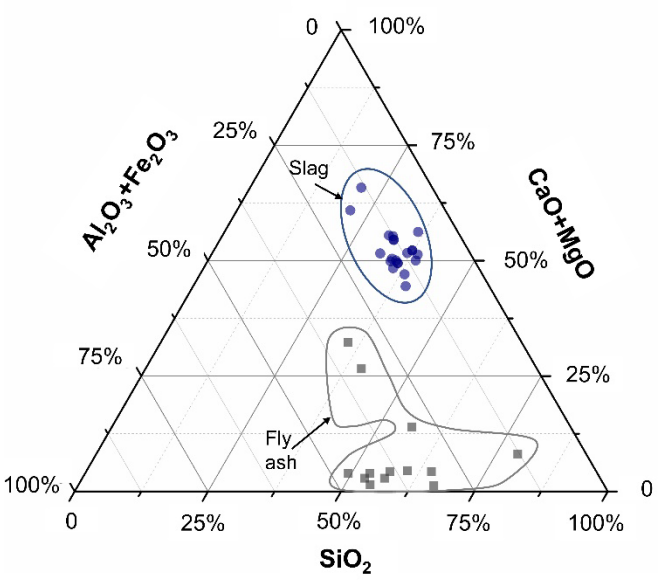

Figure 7-1: Ternary diagram of source materials of GGBFS and fly ash. Slag has a chemical composition comparable to that of OPC with high CaO, SiO_2, Al_2O_3, Fe_2O_3, and MgO as the major oxides. On the other hand, the CaO content in fly ash is typically lower, whereas the SiO_2 and Al_2O_3 contents are higher, resulting in different hydraulic or pozzolanic activities. Hence these oxides predominate the kinetic reactions of the unary or binary precursors. The activity of each binder can be quantified using reactivity indices, including the reactivity modulus (RM), silica modulus (SM), alumina modulus (AM), hydraulic modulus (HM), and lime modulus (LM). Such indices can be empirically calculated based on the weight percentage of the oxides extracted by X-ray fluorescence (XRF) in the desired precursor, regardless of being a unary or binary system, as follows (Binici *et al*., 2007; Xie and Visintin, 2018; Xie *et al*., 2020):

$$RM = \frac{\mathrm{CaO} + \mathrm{Al_2O_3} + \mathrm{MgO}}{\mathrm{SiO_2}} \quad \text{Eq. 7-1}$$

$$SM = \frac{\mathrm{SiO_2}}{\mathrm{Al_2O_3} + \mathrm{Fe_2O_3}} \quad \text{Eq. 7-2}$$

$$AM = \frac{\mathrm{Al_2O_3}}{\mathrm{Fe_2O_3}} \quad \text{Eq. 7-3}$$

$$HM = \frac{\mathrm{CaO}}{\mathrm{SiO_2} + \mathrm{Al_2O_3} + \mathrm{Fe_2O_3}} \quad \text{Eq. 7-4}$$

$$LM = \frac{100\mathrm{CaO}}{2.8\mathrm{SiO_2} + 1.1\mathrm{Al_2O_3} + 0.7\mathrm{Fe_2O_3}} \quad \text{Eq. 7-5}$$

The reactivity moduli of the blended precursor systems having n distinct binder can be calculated using the weighted average modulus of each binder as expressed below, where $wr\%$ is the weight percentage of the reactivity modulus of each single binder.

$$RM = \frac{\sum_{i=1}^{n} (RM_i \cdot wr\%)}{100\%} \quad \text{Eq. 7-6}$$

$$SM = \frac{\sum_{i=1}^{n} (SM_i \cdot wr\%)}{100\%} \quad \text{Eq. 7-7}$$

$$AM = \frac{\sum_{i=1}^{n} (AM_i \cdot wr\%)}{100\%} \quad \text{Eq. 7-8}$$

$$HM = \frac{\sum_{i=1}^{n} (HM_i \cdot wr\%)}{100\%} \quad \text{Eq. 7-9}$$

$$LM = \frac{\sum_{i=1}^{n} (LM_i \cdot wr\%)}{100\%} \quad \text{Eq. 7-10}$$

After calculating the reactivity moduli of the binder system for each mixture design example, the chemical compositions of the slag and fly ash are replaced with the reactivity moduli. **Figure 7-2** illustrates the scatter plots of the binder system and its reactivity moduli. **Table 7-1** outlines the final input features of the dataset along with their statistical description.

Table 7-1: Input features of the dataset along with their statistical description

Input feature	Symbol	Unit	Mean	STV	Min	25%	50%	75%	Max
Fly ash	F	kg/m^3	201.713	246.035	0	0	170	345	1530
Slag	S	kg/m^3	304.270	255.734	0	70.5	275	531	775
Reactivity modulus	RM	-	1.303	0.595	0.231	0.872	1.420	1.675	3.645
Hydraulic modulus	HM	-	0.547	0.387	0.001	0.177	0.569	0.834	1.818
Silica modulus	SM	-	2.648	1.284	1.058	1.733	2.342	3.521	6.180
Alumina modulus	AM	-	31.576	66.763	0.892	6.362	18.571	23.536	310
Lime modulus	LM	-	23.520	16.722	0.048	7.956	23.958	34.987	86.556
NaOH	SH	kg/m^3	29.5342	19.051	0	15	24.270	46	87.430
Sodium silicate	SS	kg/m^3	107.860	64.419	0	71	100.1	120	466.2
Na_2O in sodium silicate	SS_Na_2O	kg/m^3	15.382	10.421	0	8.277	12.281	17.279	64.802
Silica in sodium silicate	SS_SiO_2	kg/m^3	32.272	20.738	0	19.159	28.983	35.090	153.85
Water in sodium silicate	SS_W	kg/m^3	60.206	37.469	0	39.689	56.55	66.866	247.55
Water	W	kg/m^3	149.995	87.655	14.36	104	135.4	172.69	423
Fine aggregate	FA	kg/m^3	767.493	385.34	0	648	734.8	885	1500
Coarse aggregate	CA	kg/m^3	632.179	569.89	0	0	1035	1200.25	1294
Temperature	T	°C	22.827	4.805	20	20	23	23	60
Relative humidity	RH	%	71.836	20.030	33	50	65	95	100

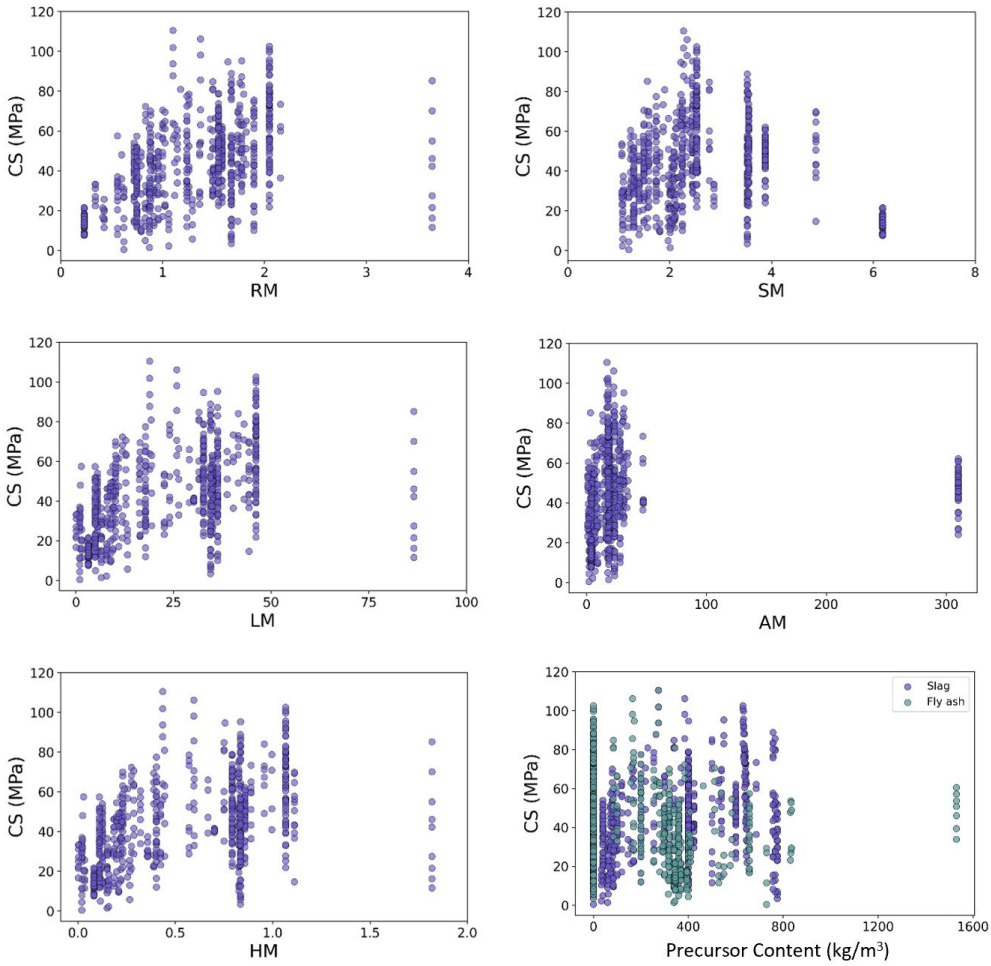

Figure 7-2: Scatter plots of binder systems and their reactivity moduli.

Machine learning (ML) models

Four different chemistry-informed ML models were created to explore the strength development of AAMs based on the binder reactivity. Support vector regressor (SVR), random forest regressor (RFR), extra trees regressor (ETR), and gradient boosting regressor (GBR) were used as elaborated on below.

7.3.3.1 Support vector regressor (SVR)

SVR is a powerful non-parametric technique that has been widely used for predicting the compressive strength of several construction materials (Naseri *et al*., 2020; Thilakarathna *et al.*, 2020). SVR has proven to enhance the generalization performance in regression problems owing to its ability to analyze non-linear problems (Farooq *et al*., 2021; Pan *et*

al., 2020; Yan and Shi, 2010). Using epsilon-intensive SVR ($\varepsilon - SVR$), non-linear patterns in the data can be better captured and thus, more accurate predictions are achieved. Accordingly, a training dataset including the input features X_n and the actual output Y_n, *i.e.* $\{(X_1, Y_1), (X_2, Y_2), (X_3, Y_3), \dots, (X_n, Y_n)\}$ was used to find the prediction function, $f(x)$. The predictions made by $f(x)$ should not deviate more than ε from the actual target value for each data observation, X_n (Farooq *et al*., 2021; Pan *et al*., 2020). Consider a regression function as follows:

$$f(x) = \omega . \varphi(x) + b \qquad \text{Eq. 7-11}$$

where b is the scalar threshold, ω is the weight vector, and $\varphi(x)$ is the high-dimensional feature space. To achieve a flat function, ω and b need to be minimized using a regularized risk function as follows (Jalal *et al*., 2020; Thilakarathna *et al.*, 2020):

$$R_{reg}(C) = C\frac{1}{n}\sum_{i=1}^{n} L_{\varepsilon}\big(y_i, f(x_i)\big) + \frac{1}{2} \parallel \omega \parallel^2 \qquad \text{Eq. 7-12}$$

$$L_{\varepsilon}(y, f(x)) = \begin{cases} |y - f(x)| - \varepsilon & \text{for } |y - f(x)| \geqslant \varepsilon \\ 0 & \text{otherwise} \end{cases} \qquad \text{Eq. 7-13}$$

Where $\frac{1}{2} \parallel \omega \parallel^2$ is the norm of weight that minimizes the flatness of the function, $C\frac{1}{n}\sum_{i=1}^{n} L_{\varepsilon}\big(y_i, f(x_i)\big)$ is the empirical error, $L_{\varepsilon}\big(y_i, f(x_i)\big)$ is the loss function, and coefficient c represents the trade-off between the empirical and flatness errors (Jalal *et al*., 2020; Thilakarathna *et al*., 2020).

Since a function that satisfies the above optimization constraints (a deviation of ε from the actual output) may not always exist, slack variables ξ_i and ξ_i^* are introduced to make the prediction errors within ξ_i and ξ_i^*. Therefore, the previous optimization problem is transformed to a dual optimization as follows (Jalal *et al*., 2020):

$$\begin{gathered} \text{Minimize: } R(\omega, b, \xi^*, \xi) = \frac{1}{2} \parallel \omega \parallel^2 + C \sum_{i=1}^{l} (\xi_i + \xi_i^*) \\ \text{Subjected to } y_i - \omega \cdot \phi(x_i) - b \leqslant \varepsilon + \xi_i \\ \omega \cdot \phi(x_i) + b \leqslant \varepsilon + \xi_i^* \\ \xi_i^*, \xi \leqslant 0 i = 1,2, \dots, l \end{gathered} \qquad \text{Eq. 7-14}$$

This optimization problem can be solved by Lagrangian multipliers including a kernel function to avoid computational complexity of nonlinearly mapping $\varphi(x)$ (Dong *et al.*, 2005; Jalal *et al.*, 2020):

$$f(x, a_i, a_i^*) = \sum_{i=1}^{nsv} (a_i - a_i^*) K(x_i, x_j) + b \quad \text{Eq. 7-15}$$

$$K(x_i, x_j) = \varphi(x_i) \cdot \phi(x_j) \quad \text{Eq. 7-16}$$

where a_i and a_i^* are Lagrangian multipliers, *nsv* is the number of support vectors, and K is the kernel function.

Polynomial, radial basis, Gaussian, and ANOVA are among the widely used kernel functions (Jalal *et al.*, 2020; Naseri *et al.*, 2020). **Figure 7-3** schematically displays an epsilon-intensive SVR model with various kernel functions. Interested readers can find more details regarding SVR in *(Boser et al.,* 1992; Smola and Schölkopf, 2004). In the present study, a scikit-learn package was employed to implement the SVR model for predicting the compressive strength (Pedregosa *et al*., 2011).

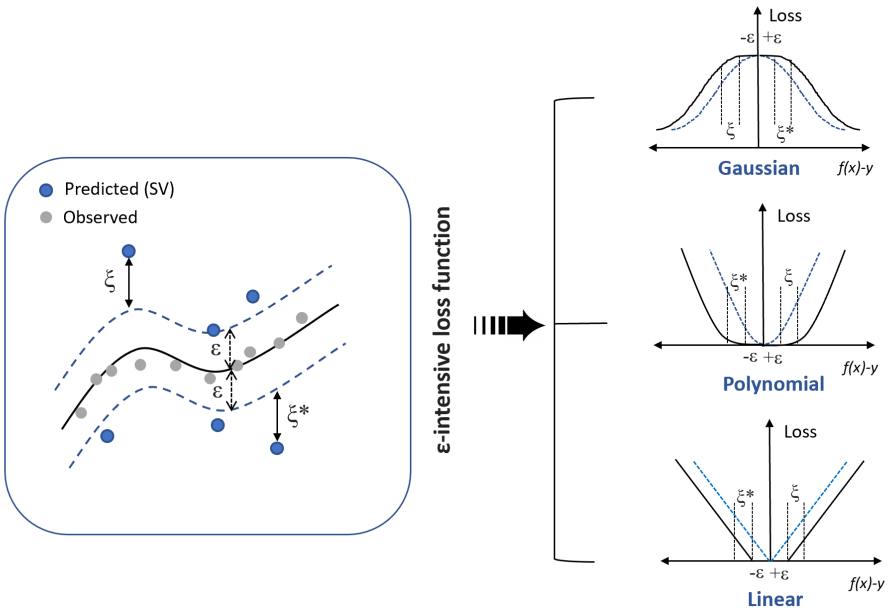

Figure 7-3: Schematics of the ε-insensitive support vector machine.

7.3.3.2 Random forest regressor (RFR)

Random forest is an extension of the classification and regression trees (CART) algorithm widely utilized for classification and regression problems. Breiman *et al.* (2017) proposed CART as a non-parametric model for developing connections from input data to estimate a target. The primary idea of the CART algorithm is dividing a complex prediction problem into several less complicated processes using decision trees. Ensembles can be constructed based on the CART algorithm to improve prediction performance and reduce over-fitting errors (Zhang *et al*., 2020b; Zhang *et al*., 2019). Bagging and boosting are predominant methodologies to develop robust tree-based ensembles, including random forest, extra trees, and gradient boosting.

RFR is an extension of the CART regression algorithm. This method has been employed to solve several problems in material science, including predicting the mechanical properties of concrete. RFR creates a certain number of decision trees and combines them using the "Bagging" algorithm to enhance the prediction accuracy and reduce the prediction variance. For this purpose, a subset of features is randomly allocated to each individual decision tree. Consider $X = \{x_1, x_2, x_3, \dots, x_m\}$ as the input vector having m attributes and Y as the single output. For a given dataset containing n observations, $S_n = \{(X_1, Y_1), (X_2, Y_2), (X_3, Y_3), \dots, (X_n, Y_n)\}$, the bagging technique applies the decision tree algorithm on several so-called "bootstrap" ($S_n^{D_i}$) data examples, ($S_n^{D_1}, S_n^{D_2}, S_n^{D_3}, \dots, S_n^{D_j}$). Those samples not incorporated in the bootstrap set are called out-of-bag (OOB) samples and can be used to determine the feature importance. In the training process, j regression trees are created for j bootstrap samples to estimate the output, Y. These estimators are defined as $\hat{Y}_1 = \hat{h}(X, S_n^{D_1})$, $\hat{Y}_2 = \hat{h}\left(X, S_n^{D_2}\right)$, $\hat{Y}_3 = \hat{h}(X, S_n^{D_3})$, …, $\hat{Y}_j = \hat{h}(X, S_n^{D_j})$. $\hat{Y}$ is the estimation by each decision tree, $\hat{h}$. Ultimately, the final prediction is aggregated by averaging the predicted outputs of all trees, *i.e.* $\hat{Y} = \frac{1}{j}\sum_{i=1}^{j} \hat{Y}_j$ (Ahmad *et al*., 2018; Han *et al*., 2019; Zhang *et al*., 2020a; Zhang *et al.*, 2019). Details on random forest algorithms can be found in (Breiman, 2001). Scikit-learn package was used to develop RFR models herein (Pedregosa *et al*., 2011).

7.3.3.3 Extra trees regressor (ETR)

Extremely randomized trees, also known as extra trees, are a recent extension of the random forest algorithm. Similar to RFR, ETR utilizes a randomly selected subset of features to train the base predictors. In contrast to RFR, which employs a bootstrap to train the model, ETR trains each prediction tree with the entire training data. Furthermore, ETR selects a split point of a decision tree randomly, unlike RFR, which deploys a greedy algorithm to find the optimum split node (Marani *et al.*, 2020). Additional information can be found in (Geurts *et al*., 2006).

7.3.3.4 Gradient boosting regressor (GBR)

Boosting is a robust learning method preliminary designed for classification tasks. Its promising performance led to being extended for complicated regression problems. Accordingly, gradient boosting regressor (GBR) integrates several weak estimators called weak learners (*e.g.* decision trees) utilizing a boosting strategy. The prediction $\widehat{y_i}$ for a given input data X_i in a GBR model is expressed in **Eq. 7-17**:

$$\widehat{y_i} = F_M(x_i) = \sum_{m=1}^{M} h_m(x_i) \qquad \text{Eq. 7-17}$$

where $\hbar_m(x)$ is the mth weak learner. In the boosting method, additive weak learners are appended in a stage-wise fashion without further alteration in model parameters. Gradient boosting searches for the function $\mathcal{F}(\mathcal{X})$ by which the loss function $\mathcal{L}(\mathcal{F}(\mathcal{X}), \mathcal{Y})$ (*e.g.* mean squared error or mean absolute error) is minimized for the given dataset, $\{(X_1, Y_1), (X_2, Y_2), (X_3, Y_3), \dots, (X_n, Y_n)\}$. GBR finds the best $\mathcal{F}(\mathcal{X})$ by weighting the weak learners, $\hbar(x_i)$. $\hbar(x_i)$ is the weak learner trained with the input data along with the negative gradient of the loss function for the last learner. GBR is initiated with a constant function $F_0(X)$ which greedily constructs the model as follows (Farooq *et al*., 2021; Kumari and Toshniwal, 2021; Zhang *et al*., 2020b):

$$F_0(X) = argmin \sum_{i=1}^{N} \mathcal{L}(y_i, \gamma) \qquad \text{Eq. 7-18}$$

$$\mathcal{F}_m(\mathcal{X}) = \mathcal{F}_{m-1}(\mathcal{X}) + \gamma_m \hbar_m(x) \qquad \text{Eq. 7-19}$$

where $\mathcal{F}_m(\mathcal{X})$ is the integration of the predictions yielded by the weak learner, $\hbar_m(x)$ is the mth weak learner, and γ_m is the weight coefficient of the mth regression estimator, also called learning rate. The learning rate is one of the hyperparameters of the GBR model which considerably affects the prediction performance. Also, the number of trees and the max-depth of the tree is amongst other hyperparameters that are of great importance. A higher number of trees, which in turn indicates more weak learners, boosts the prediction accuracy of the regressor model. Nevertheless, an excessive number of trees could lead to a model over-fitted towards the training data, thus lacking a satisfactory level of generalization for new unobserved data. The contribution of the weak learners to the target prediction can be controlled with the learning rate and max-depth hyperparameters. Imperfect values of these hyperparameters can adversely impact the model's performance, resulting in erroneous predictions (Marani and Nehdi, 2020).

7.3.4 Hyperparameter optimization

Utilizing advanced ML models requires fine-tuning of the hyperparameters to ensure an efficacious performance. The different ML models explained above have several hyperparameters that impact the output estimation, and thus need to be tuned. Various optimization or search techniques have been employed to tune those hyperparameters. In this research, a Bayesian optimization algorithm (BOA) was used to tune the applied models described earlier. BOA is a computationally effective method to solve optimization problems in which the optimal solution of a black-box function is required. BOA is developed based on the Bayes theorem in which the prior knowledge is employed to search for posterior possibility as shown below (Alam *et al*., 2021; Pelikan *et al*., 1999):

$$p(w \mid D) = \frac{p(D|w)p(w)}{p(D)} \qquad \text{Eq. 7-20}$$

Where $p(w)$ and $p(w \mid D)$ are the prior and posterior distributions, w is the unseen data and $p(D \mid w)$ is the probability. Using the Bayes rule, the value of the last iteration is used to search for the value in the next iteration. Therefore, the search for the optimum

value is more efficient than the arbitrary or random search algorithms (Frazier, 2018; Pelikan *et al*., 1999).

To further mitigate the over-fitting risk in training ML models, the BOA was coupled with the 5-fold cross-validation (CV) technique. Consequently, the training data was divided into 5 subsets, *i.e.* folds. Then, the model fits the data 5 times such that four folds are used for training, and one fold is allocated for testing the model in each training attempt (Marani and Nehdi, 2020; Nunez *et al.*, 2020). Ultimately, the values achieving the highest CV score (*i.e.* lowest error) are selected as the tuned hyperparameter values. **Table 2** presents the hyperparameters of each applied ML model along with their search space.

Table 7-2: Tuned hyperparameters with the respective search space of the four models.

Model	Hyperparameter	Search space
SVR	Kernel coefficient (gamma)	[0,1]
	Regularization (C)	[1,2000]
	Epsilon (ε)	[0.1,10]
RFR	N_estimator	[100,500]
	Max_depth	[1,30]
	Max_features	[1,18]
	Min_sample_split	[2,40]
	Min_sample_leaf	[1,40]
ETR	N_estimator	[100,500]
	Max_depth	[1,30]
	Max_features	[1,18]
	Min_sample_split	[2,40]
	Min_sample_leaf	[1,40]
GBR	N_estimator	[200,800]
	Learning_rate	[0.001,1]
	Max_depth	[1,30]
	Max_features	[1,18]
	Min_sample_split	[2,30]
	Min_sample_leaf	[1,30]

7.3.5 Model performance evaluation

The predictive performance of the applied ML models was assessed using several statistical metrics, including the mean absolute error (*MAE*), root-mean-square error

(*RMSE*), coefficient of determination (R^2), mean absolute percentage error (*MAPE*), and $a20$ index as follows:

$$MAE = \frac{1}{m}\sum_{i=1}^{m}\left|Y_i - \hat{Y}_i\right| \quad \text{Eq. 7-21}$$

$$RMSE = \sqrt{\frac{1}{m}\sum_{i=1}^{m}\left(Y_i - \hat{Y}_i\right)^2} \quad \text{Eq. 7-22}$$

$$R^2 = 1 - \frac{\sum_{i=1}^{m}(Y_i - \hat{Y}_i)^2}{\sum_{i=1}^{m}(Y_i - \bar{Y})^2} \quad \text{Eq. 7-23}$$

$$MAPE = \frac{1}{m}\sum_{i=1}^{m}\left|\frac{Y_i - \hat{Y}_i}{Y_i}\right| \times 100 \quad \text{Eq. 7-24}$$

$$a20 = \frac{m20}{m} \quad \text{Eq. 7-25}$$

where Y_i and $\hat{Y}_i$ are the observed and predicted outputs, respectively, m is the number of dataset samples, and $m20$ is the number of data observed to the predicted value within 0.8 to 1.2. *MAE* and *RMSE* are measures of the difference between the observed and predicted values, and thus lower *MAE* and *RMSE* values indicate superior performance of the model. *MAPE* is another measure of the predictive performance of the model in terms of the relative error. A *MAPE* of zero indicates a perfectly trained model. R^2 represents a measure of how accurate the observed outputs are predicted by the model based on the total variations of the outputs. An R^2 of 1 denotes that the predictions of the regression model perfectly fit the data. $a20$ is a reliability index measuring the percentage of the predictions having less than 20% deviation from the experimental observations. Therefore, higher $a20$ represents a better-trained model (Almustafa and Nehdi, 2021; Asteris *et al*., 2021; Marani and Nehdi, 2020).

7.4 RESULTS AND DISCUSSION

This section presents the results of the developed chemistry-informed machine learning methods, including the SVR, RFR, ETR, and GBR models in predicting the compressive strength of AAMs.

7.4.1 Hyperparameter tuning

Optimizing the model hyperparameters is an essential step in developing predictive ML frameworks. Tuned models typically achieve superior accuracy while minimizing over-fitting errors. In this study, a 5-fold cross-validated Bayesian optimization algorithm (BOA) was performed to obtain the optimum parameters of the SVR, RFR, ETR, and GBR models. The hyperparameters considered for tuning along with the search space are provided in **Table 7-3**.

Table 7-3: Tuned hyperparameters of the four models

Model	Hyperparameter	Tuned value
SVR	Kernel coefficient (gamma)	0.975
	Regularization (C)	1050
	Epsilon (ε)	5.2
RFR	N_estimator	100
	Max_depth	30
	Max_features	12
	Min_sample_split	2
	Min_sample_leaf	1
ETR	N_estimator	500
	Max_depth	17
	Max_features	18
	Min_sample_split	2
	Min_sample_leaf	1
GBR	N_estimator	690
	Learning_rate	0.085
	Max_depth	26
	Max_features	2
	Min_sample_split	13
	Min_sample_leaf	13

In the SVR model, a radial basis function (RBF) kernel was selected, and the kernel coefficient (gamma), regularization parameter, and epsilon were tuned accordingly. *MAE* was monitored as the cross-validation score to select the tuned hyperparameters. In tree-based models (*i.e.* RFR, ETR, and GBR), the number of weak learners (*n*_estimators) is an impactful hyperparameter. Additionally, the learning rate in GBR model, which indicates the extent to which each weak learner contributes to the output prediction, should be fine-tuned. In other words, there is a trade-off between the learning rate and the

number of weak learners, and thus optimum values for such hyperparameters should be selected to achieve a robustly trained model. Furthermore, the tuned values of other influential hyperparameters determining the criteria for splitting the data were obtained. **Table 7-3** lists the tuned hyperparameters of all models in the current study.

7.4.2 Model predictive performance

After tuning the hyperparameters, each model was trained with the training data and tested using the test data. **Figure 7-4** illustrates the regression fit of each model to the training and testing subsets. The primary observation that emerges from the fitting curves is that although all predictive models demonstrated promising performance, tree-based ensembles achieved higher prediction accuracy. For instance, the SVR model reached an R^2 of 0.847, along with an *MAE* of 6.058 MPa when evaluated using the testing dataset. Nevertheless, RFR, ETR, and GBR achieved testing R^2 of 0.911, 0.915, 0.944 and *MAE* of 4.44, 4.31, and 3.228, respectively, indicating lower prediction error. Furthermore, the scatter in the predictions performed by SVR was more significant compared to that of tree-based estimators. This can be better explored using the *M20* indicator presented in **Table 7-4**. Accordingly, the training and testing $a20$ of the SVR model was approximately 75% and 67%, respectively. This denotes that only 67% of the testing predictions of the SVR had a deviation less than $\pm$20% from the actual experimental values. In contrast, this indicator for the RFR, ETR, and GBR models was 96%, 93%, and 97%, respectively, for the training set, and 77%, 80%, and 87%, respectively for the testing set. The GBR model demonstrated superior performance among the tree-based ensembles with the highest prediction accuracy and minimum overfitting towards the training data. This could be understood by comparing the performance of each model on training and testing sets. For instance, although the ETR model achieved perfect fit to the training set, a less robust performance was evidenced on the testing set. However, the GBR model indicated comparable performance on the training and testing data, and thus attained more robust generalized forecasting capability.

Table 7-4: Performance evaluation of models using statistical error indicators

Error indicator	SVR		RFR		ETR		GBR	
	Train	Test	Train	Test	Train	Test	Train	Test
R^2	0.907	0.846	0.967	0.910	0.984	0.914	0.981	0.943
***MAE* (MPa)**	5.132	6.057	2.302	4.459	0.553	4.31	1.26	3.253
***RMSE* (MPa)**	6.598	8.053	3.927	6.165	2.72	6.00	2.919	4.894
***MAPE* (%)**	14.9	6.628	6.83	12.696	1.438	12.994	4.002	10.325
$a20$ **(%)**	75.47	66.995	92.6	80.295	97.4	77.340	95.77	88.67

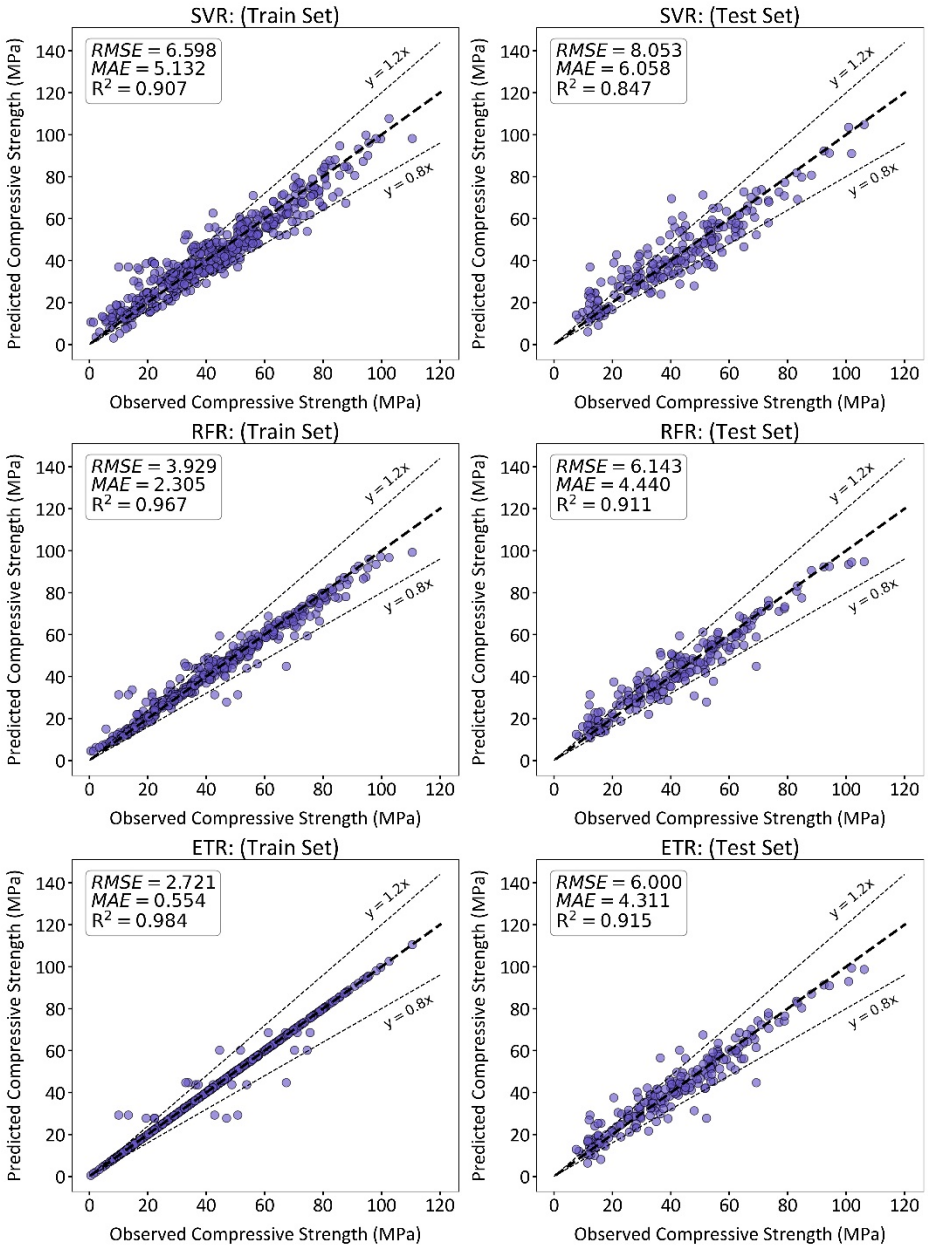

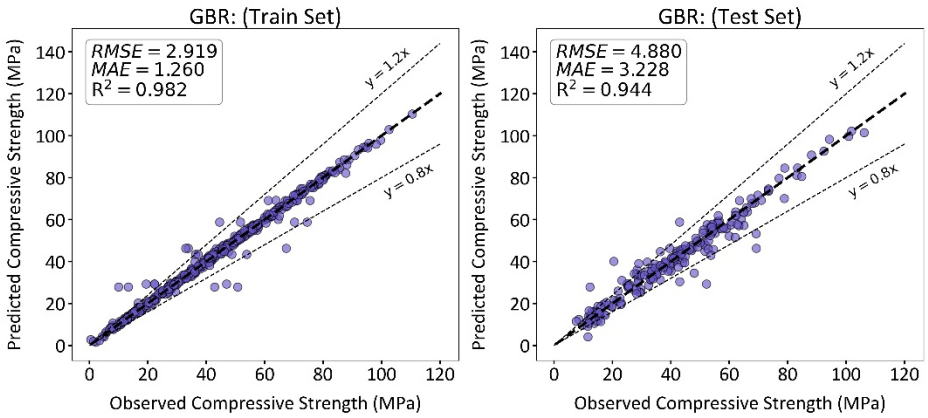

Figure 7-4: Observed versus predicted compressive strengths for training datasets.

Figure 7-5 compares the estimation performance of all models using the Taylor diagram. This graph depicts how well the performance of each model is correlated to the real observations using the Pearson correlation, *RMSE*, and standard deviation indicators. Accordingly, the model with the lowest *RMSE* value and highest correlation to the observed targets has the best prediction performance. Accordingly, the GBR model achieved the most desirable functionality, as depicted in **Figure 7-5**. The overall predictions of all developed models are illustrated in **Figure 7-6**.

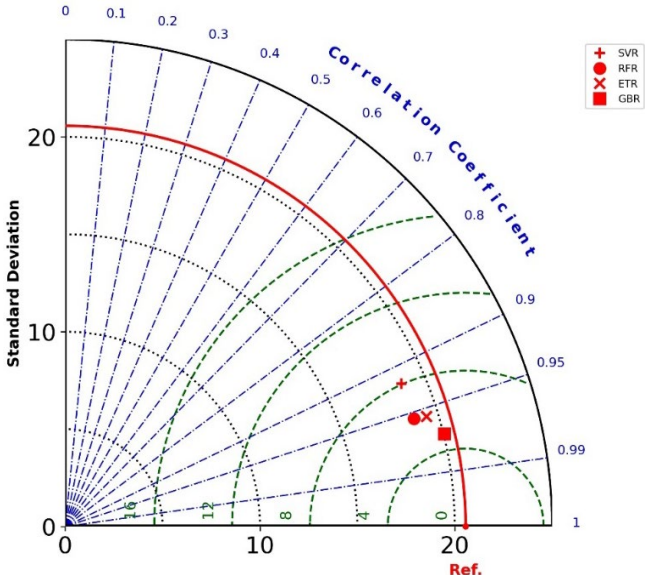

Figure 7-5: Taylor diagram for comparison of the four models. All models indicated similar performance, with SVR having slightly less error (red lines) and higher correlation (blue lines).

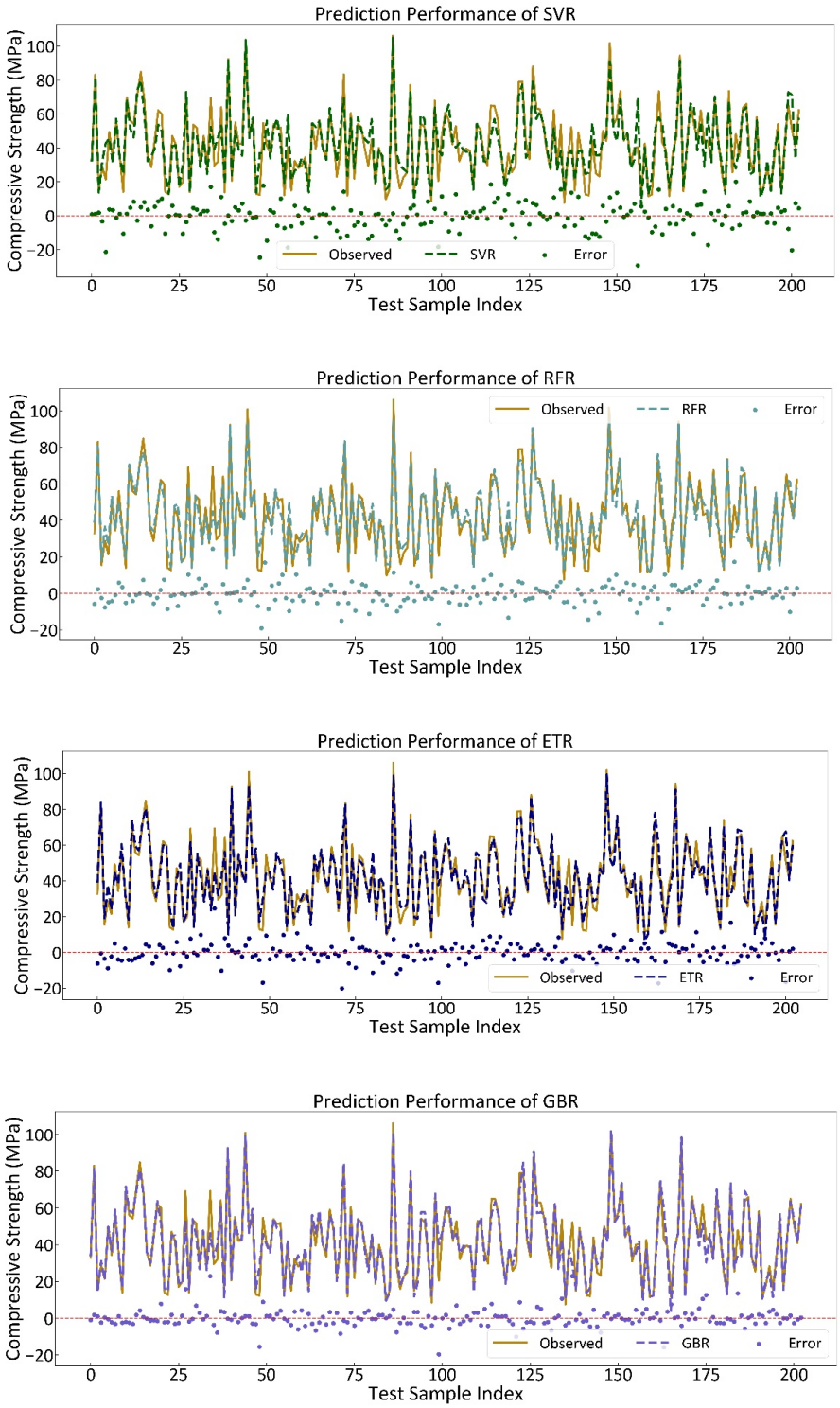

Figure 7-6: Prediction performance of SVR, RFR, TR, and GBR.

Once ML models are rigorously tuned, they can provide further insights into the input data using feature importance evaluation. Feature importance refers to assigning scores to the input attributes of a dataset used to develop predictive models. Feature importance is helpful in better understanding the data, model, and underlying patterns constructing the estimation framework. **Figure 7-7** shows the feature importance of the tree-based ensembles developed herein. It can be observed that the curing age had the highest effect on strength development, as expected. Additionally, the properties of the precursor and activator greatly affected the compressive strength prediction for all models. This includes the reactivity moduli of the binder since it has been recognized as the top input feature in all models. The formulation of the activators also had a high importance degree since sodium oxide and sodium silicate were amongst the top-ranked parameters. Such results provide new insights into the chemistry-controlled parameters affecting the strength development of AAMs and stimulate further studies to better explore the underlying mechanisms. Purposefully, several numerical experiments were designed to further analyze the effects of various mixture design parameters on the compressive strength of AAMs as scrutinized below.

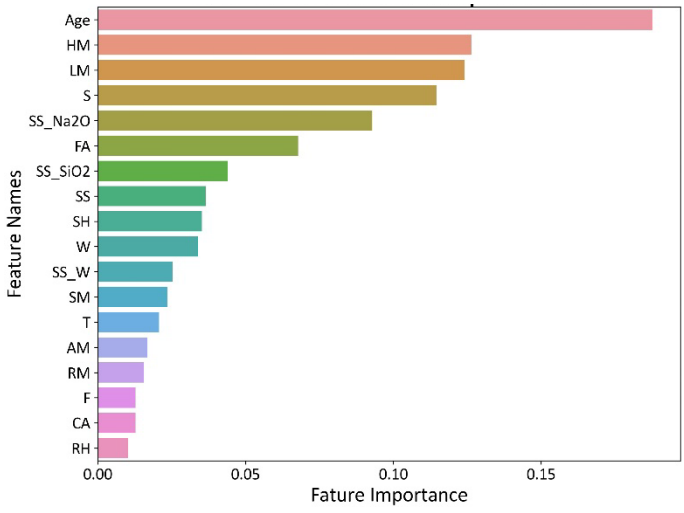

(a)

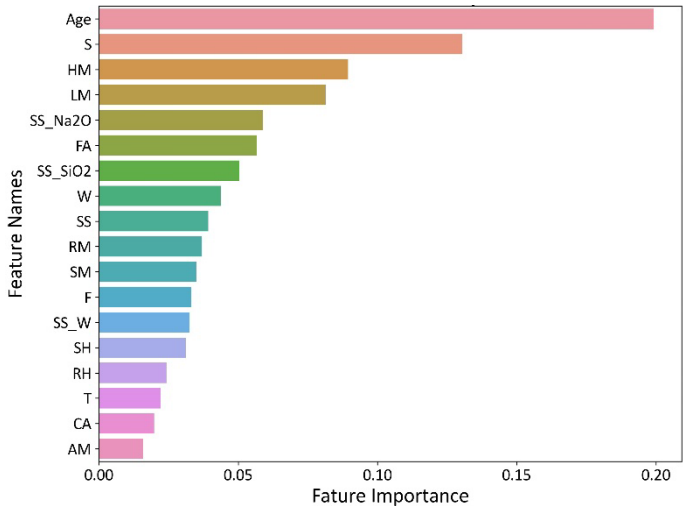

(b)

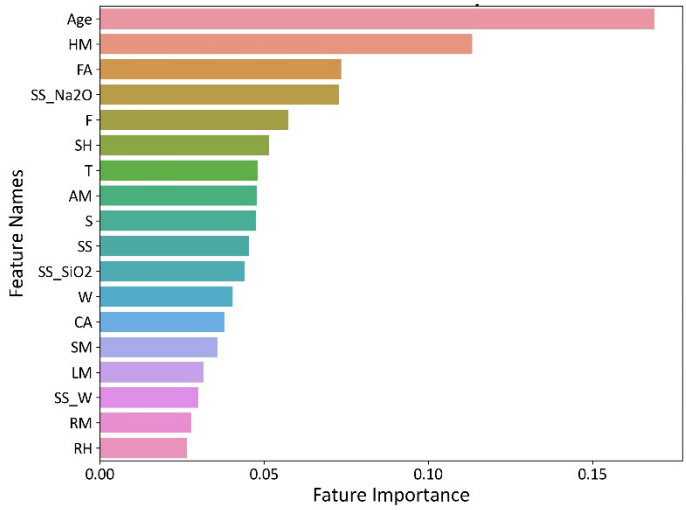

(c)

Figure 7-7: Feature importance of models: (a) RFR model; (b) ETR model; (c) GBR model.

7.5 RESULTS AND DISCUSSION

After establishing a robust predictive framework to estimate the compressive strength of AAMs based on their mixture design parameters and chemistry of key ingredients, several numerical experiments were performed to explore the influence of the predominant design variables on the compressive strength using the GBR model, which

proved to be the best performing. For this purpose, three different design experiments were considered. Experiment 1 examines the effect of the partial replacement of slag with fly ash on the 28-d compressive strength of AAMs under different design scenarios. Experiment 2 accounts for the activator formulation and its influence on the compressive strength. Ultimately, experiment 3 monitors the strength development of AAM mixtures versus the curing time. The studied parameters and design scenarios of each experiment are summarized in **Table 7-5**.

It is noteworthy that the control mixture proportions were designed for $1m^3$ of AAMs. Furthermore, some design parameters were maintained constant in all the studied mixtures in each experiment including the chemical composition of the precursors, the fine aggregate dosage (800 kg/m^3), the curing temperature (23 °C), and curing age (28 days). The considered chemical compositions of slag and fly ash are presented in **Table 7-6**.

Table 7-5: Details of the three experiments with studying parameters and design scenarios

Experiment	Objective	Studying parameter	Design scenario	
			Parameter	**Value**
1	Effect of blended precursor on the CS	Partial replacement of slag with fly ash	SS content	75, 100, 125 kg/m^3
			SH Content	0, 20, 40, 80 kg/m^3
			w/b ratio	0.35, 0.45
			RH	30, 100 %
2	Effect of SiO_2 and Na_2O content on the CS	SiO_2 and Na_2O content	SS content	75, 150 kg/m^3
			SH content	0, 20, 40 kg/m^3
			w/b ratio	0.35, 0.45
			RH	30, 100 %
3	The CS development vs. age	Age	SS content	75, 150 kg/m^3
			SH content	0, 10, 40 kg/m^3
			RH	30, 100 %

Table 7-6: Chemical compositions set for numerical experiments

Oxide	Slag	Fly ash
SiO_2	33.8	54.29
CaO	42.56	1.34
Al_2O_3	13.68	22.55
Fe_2O_3	0.4	5.53
MgO	5.34	1.08

7.5.1 Experiment 1

This experiment explores the effects of the partial replacement of slag with fly ash on the 28-day compressive strength of AAMs as described earlier**.** A control mixture design was considered to have 600 kg/m^3 slag with varying partial fly ash replacement. The fly ash-to-slag weight ratio varied from 0 to 4. **Figures 7-8 and 7-9** plot the predicted compressive strength versus the partial fly ash replacement content under various mixture design scenarios (e.g., SH content, SS content, and w/b ratio) when cured at RH = 30% and 100%, respectively. The following trends can be distinguished:

(1) Fly ash content in blended binder systems

The compressive strength rose gradually to a peak when the fly ash content increased to approximately 160 kg/m^3, followed by a consistent fall beyond this threshold level. This trend can be explained by the synergetic effects of fly ash and slag in improving the binding of the blended hydrated gel system during the geo-polymerization, therefore resulting in denser microstructure (Xie *et al*., 2019). This result is in good agreement with previous study (Chi and Huang, 2013), revealing that alkali-activated mortars made with fly ash/slag ratio of 30/70 exhibited higher compressive strength at 14 and 28 days of curing than that of specimens made with slag alone. It is noteworthy that this trend may change when the fly ash chemistry is varied. Some parameters, such as the glass phase fraction, major oxides, and particle size distribution based on different types of fly ash, could determine the final gel formation, which affects the mechanical properties. The chemical compositions in both fly ash and slag were fixed in this experiment, as outlined in **Table 7-6**. The combination of fly ash and slag for producing a blended alkali-

activated binder system has long been considered a good option since slag is more costly than fly ash in most places across the globe (Provis and Bernal, 2014).

(2) w/b ratio

The compressive strength decreased as the w/b ratio increased from 0.45 to 0.35 considering fixed RH, SS, and SH contents, which is analogous to the effect of the water-to-cement ratio on the compressive strength of OPC-based concrete. For example, when SH=40 kg/m^3, RH=30%, SS=100 kg/m^3, the compressive strength of the hardened mixture made with a fly ash content of 160 kg/m^3 increased from 50 MPa to 55 MPa when the w/b ratio dropped from 0.45 to 0.35. This trend can be explained by the increased porosity caused by water when mixing with increased w/b ratio (Zhang and Wang, 2015). In addition, higher water content can weaken the solid-to-solid phase connectivity within the AAM microstructure, therefore reducing the mechanical properties (Duxson *et al*., 2005; Gomaa *et al.*, 2021; Provis and Van Deventer, 2009; Van Jaarsveld *et al.*, 2002). Similar trends were reported in previous studies (Joseph and Mathew, 2012; Li *et al*., 2018).

(3) SH content

Given the fixed parameters such as RH, w/b ratio, and SS content, the compressive strength showed an upward trend when the SH content was within 0-20 kg/m^3. The strength stayed constant within the range of 20-40 kg/m^3. However, a slight decrease in compressive strength occurred when the SH content was 80 kg/m^3. The increase in compressive strength with increasing SH content can be explained by the geo-polymerization process whose kinetics are faster at higher pH value due to the greater SH dosage, leading to improved compressive strength (Provis, 2014). The high alkalinity dissolves more aluminosilicate sources to continue the rearrangement and exchange among dissolved species like the Si and Ai ions, followed by gel nucleation enabling the material to harden at an accelerated speed (Provis and Bernal, 2014). However, excessive SH may result in a block effect on alkali-activation, leading to reduced strength development (Fernández-Jiménez and Palomo, 2005). Similar results were observed by Cho *et al.* (2017), who found that the 28-d compressive strength drastically increased

when increasing the Na_2O content; however, the rate of the strength development fell when further increasing the Na_2O content.

(4) SS content

As can be observed in **Figures 7-8 and 7-9**, the compressive strength showed an upward trend when increasing the SS content. For instance, given SH=40 kg/m^3, RH=30%, w/b =0.35, and fly ash content =160 kg/m^3, the compressive strength increased from 50 MPa to 68 MPa when the SS content rose from 75 to 125 kg/m^3. Interestingly, the effect of the SS content on increasing the compressive strength appeared to be more pronounced when the SS content was 125 kg/m^3. The effect of the SS content on the compressive strength suggests that more silicate ions supplied by higher SS dosage facilitate alkali-activation to form solid binder products (Provis and Bernal, 2014).

(5) Relative humidity

When comparing **Figures 7-8 and Figure 7-9**, it can be determined that the specimens cured under RH=100% exhibited higher compressive strength than those cured under RH=30%. For instance, given SH=40 kg/m^3, SS=125 kg/m^3, w/b =0.35, and fly ash content = 0 kg/m^3, the compressive strength increased from 55 MPa to 68 MPa when the curing RH rose from 30% to 100%. It was hypothesized that higher RH could facilitate enhanced rearrangement and exchange among dissolved species to form gel nucleation, thereby developing mechanical strength. In addition, it is well known that AAMs have significantly higher shrinkage strains than that of OPC-based materials, causing cracking-initiated degradation, which is detrimental to their mechanical properties (Wu *et al*., 2020).

To better demonstrate how the fly ash content affects the 28-d compressive strength with varying SS content and w/b ratio when SH=20 kg/m^3 and RH=100%, the surface response plots are displayed in **Figure 7-10**. It can be observed that the compressive strength reached a peak when fly ash and slag were blended.

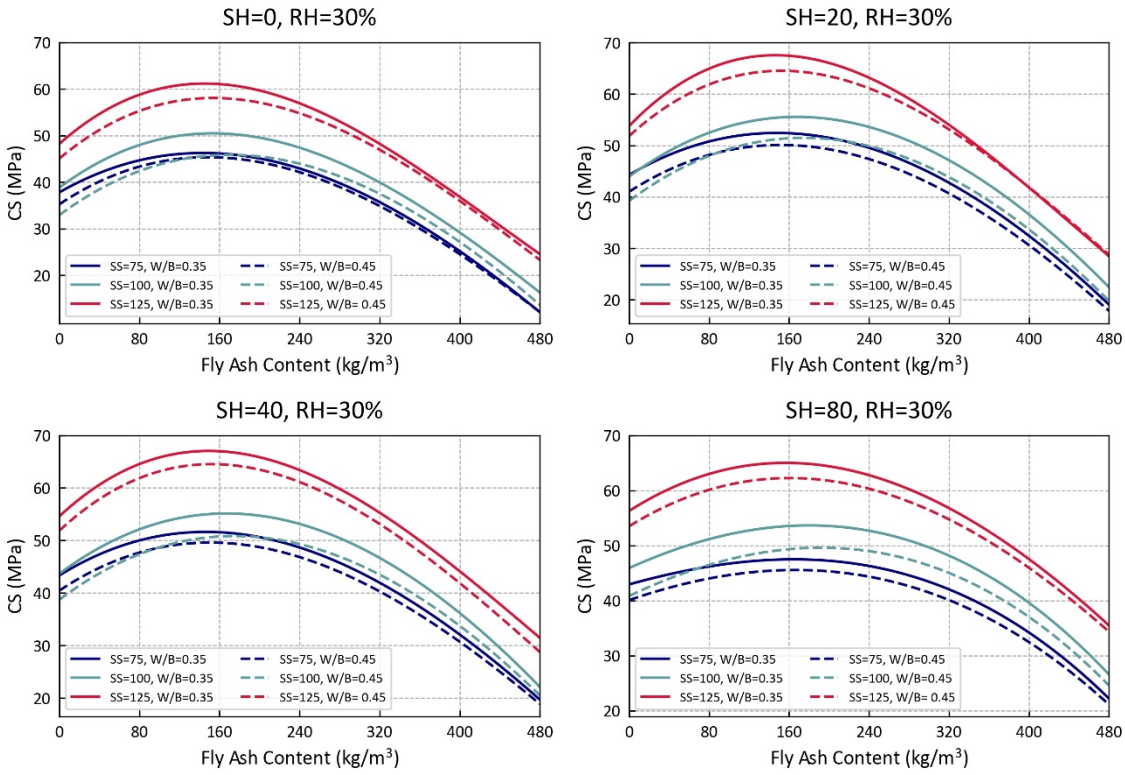

Figure 7-8: Effect of partial replacement of slag with fly ash on the compressive strength cured at RH= 30% considering various mix design parameters.

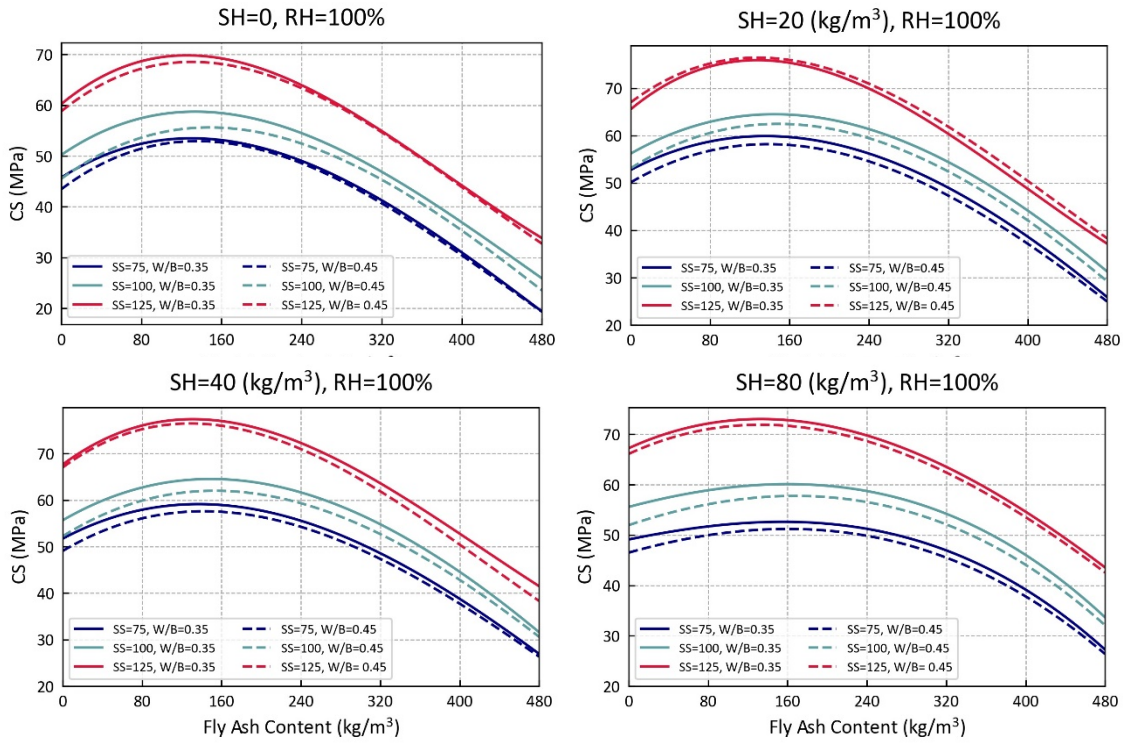

Figure 7-9: Effect of fly ash partial replacement for slag on the compressive strength of AMMs cured at RH= 100% considering various mixture design parameters.

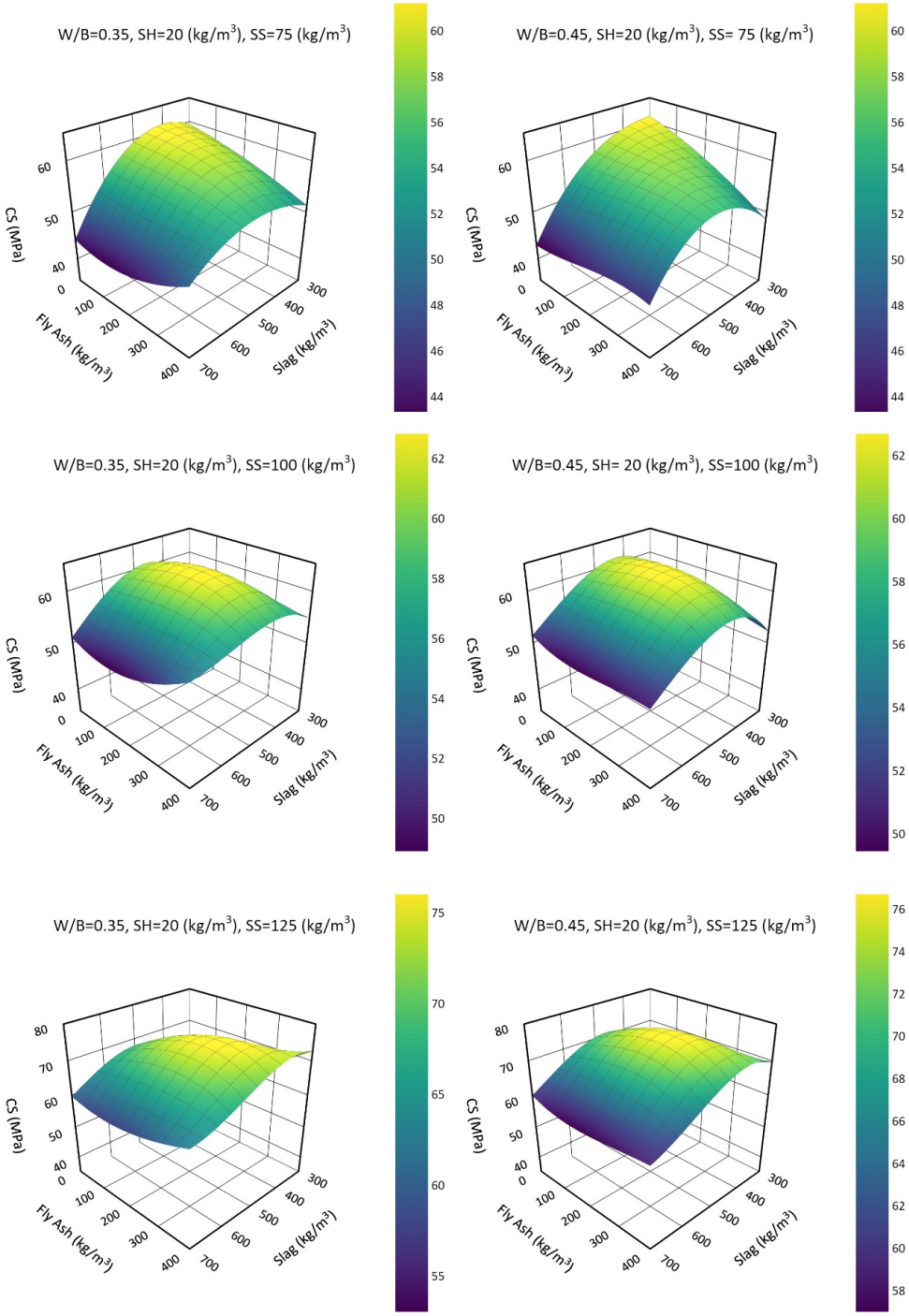

Figure 7-10: Response surface plots showing compressive strength in relation to the fly ash content considering variable SS content and w/b ratio.

7.5.2 Experiment 2

Figures 7-11 and 7-12 depict the predicted compressive strength versus the SiO_2 and Na_2O contents under various mixture design scenarios (e.g., SH content, SS content, slag content, and w/b ratio) when cured under RH = 30% and 100%, respectively. It is noted that in this experiment, the change in the SiO_2 and Na_2O contents of the sodium silicate activators was investigated considering that 60 wt.% of the sodium silicate solution is water and the remaining is SiO_2 and Na_2O. The effect of various parameters on the compressive strength is discussed below.

As shown in **Figures 7-11 and 7-12**, higher compressive strength was attained by mixture designs cured at RH=100% compared with the same mixtures cured at RH=30%. For instance, the compressive strength of the hardened mixture with slag content = 600 kg/m^3 and Na_2O content = 15 kg/m^3 increased by 14% when the curing RH was raised from 30% to 100%, as observed in **Figures 7-11(e)** and **7-12(e)**. Hence, higher RH facilitated geo-polymerization and gel nucleation, and better mitigated cracking-related shrinkage, thus improving the compressive strength.

The effect of various slag contents (300, 400, 500, and 600 kg/m^3) on the compressive strength was also investigated in Experiment 2. It was found that when SS= 150 kg/m^3, the alkali-activated slag-based concrete made with larger amounts of slag in the precursor consistently attained higher compressive strength, regardless of the SiO_2/ Na_2O ratio. As shown in **Figure 7-11(b)**, considerably higher compressive strength (54.5 MPa) was observed for the hardened mixture made with 600 kg/m^3 compared with that of its counterparts made with lower slag contents. The results obtained from the modelling predictions are in partial agreement with the findings by Bernal *et al.* (2011), who reported that higher compressive strength was consistently observed in the alkali-activated slag concretes made with higher slag content. Yet, this trend was not observed in all cases. When the RH=30%, w/b=0.35, and SS=75 kg/m^3 (**Figures 7-11(a), (c), and (e)**), the highest compressive strength was observed for the mixture made with 600 kg/m^3 of slag occurred only when the SiO_2/Na_2O ratio was less than 2. This trend suggests that slag content of 600 kg/m^3 requires enough Na_2O dosage to activate, thereby resulting in developing enhanced mechanical strength. Interestingly, when the RH=30%, w/b=0.35,

and SS=150 kg/m^3 (**Figures 7-11(b), (d), and (f)**), the compressive strength was consistently highest when the slag content was 600 kg/m^3, despite the change of the SiO_2/ Na_2O ratio.

The synergistic effect of the SH content, SS content, and SiO_2/Na_2O ratio of the SS solution on the compressive strength are demonstrated in **Figures 7-11 and 7-12**. It can be observed that when SH=0 kg/m^3 and SS=75 kg/m^3, the compressive strength rose steadily when decreasing the SiO_2/Na_2O ratio before reaching a peak, followed by a gradual drop when further reducing the SiO_2/Na_2O ratio. Noticeably, this trend changed when the S=75 kg/m^3 was increased to S=150 kg/m^3. As can be observed in **Figures 7-12(b), (d), and (f)**, the compressive strength decreased as the SiO_2/Na_2O ratio dropped from 3 to 0.5. This trend suggests that SiO_2 played an essential role in contributing to mechanical strength development. Without enough silicate supplied by SS, the final alkali-activation product (C-A-S-H) primarily responsible for strength development cannot form completely, thus resulting in a reduction of compressive strength.

To better demonstrate how the SiO_2 and Na_2O contents affect the 28-d compressive strength with varying SH content and w/b ratio when SS=50 kg/m^3 and RH=100%, surface response plots are portrayed in **Figure 7-13**. It can be observed that the w/b ratio did not change the overall trend. In addition, a peak value was observed when the SiO_2/ Na_2O ratio was within the specific ranges.

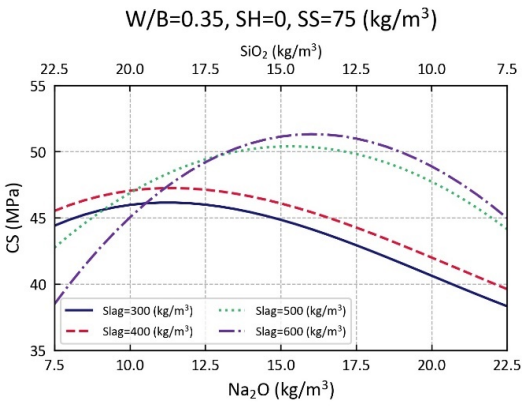
W/B=0.35, SH=0, SS=75 (kg/m3)
SiO2 (kg/m3)
22.5 20.0 17.5 15.0 12.5 10.0 7.5
CS (MPa)
55 50 45 40 35
Slag=300 (kg/m3)
Slag=400 (kg/m3)
Slag=500 (kg/m3)
Slag=600 (kg/m3)
7.5 10.0 12.5 15.0 17.5 20.0 22.5
Na2O (kg/m3)

(a)

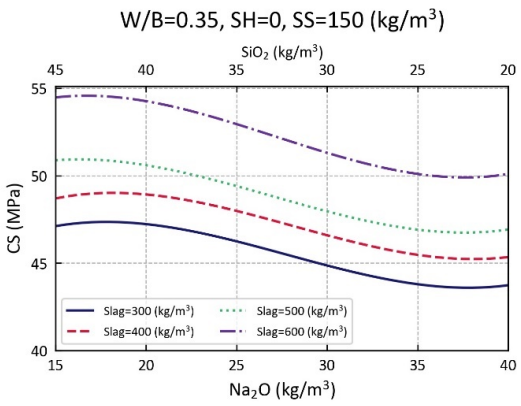
W/B=0.35, SH=0, SS=150 (kg/m3)
SiO2 (kg/m3)
45 40 35 30 25 20
CS (MPa)
55 50 45 40
Slag=300 (kg/m3)
Slag=400 (kg/m3)
Slag=500 (kg/m3)
Slag=600 (kg/m3)
15 20 25 30 35 40
Na2O (kg/m3)

(b)

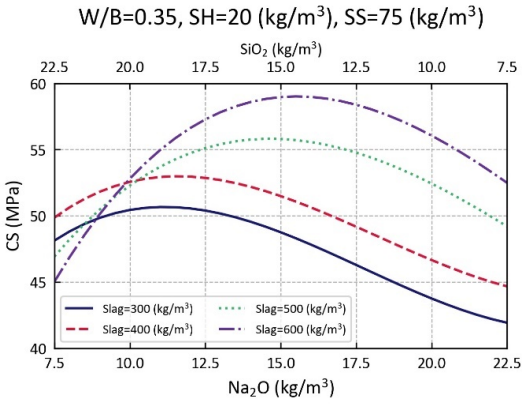
W/B=0.35, SH=20 (kg/m3), SS=75 (kg/m3)
SiO2 (kg/m3)
22.5 20.0 17.5 15.0 12.5 10.0 7.5
CS (MPa)
60 55 50 45 40
Slag=300 (kg/m3)
Slag=400 (kg/m3)
Slag=500 (kg/m3)
Slag=600 (kg/m3)
7.5 10.0 12.5 15.0 17.5 20.0 22.5
Na2O (kg/m3)

(c)

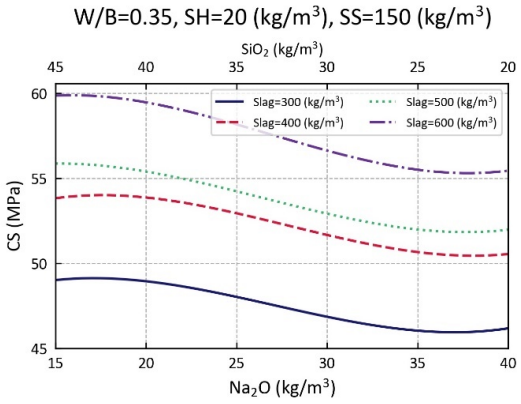
W/B=0.35, SH=20 (kg/m3), SS=150 (kg/m3)
SiO2 (kg/m3)
45 40 35 30 25 20
CS (MPa)
60 55 50 45
Slag=300 (kg/m3)
Slag=400 (kg/m3)
Slag=500 (kg/m3)
Slag=600 (kg/m3)
15 20 25 30 35 40
Na2O (kg/m3)

(d)

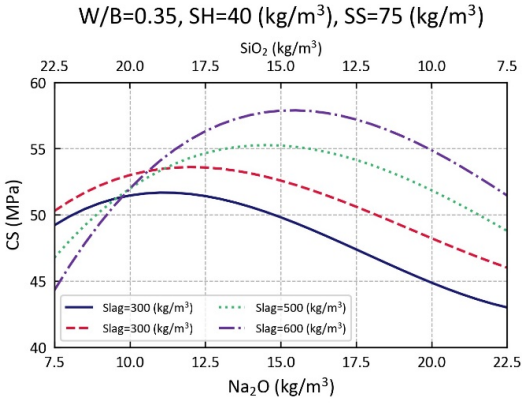
W/B=0.35, SH=40 (kg/m3), SS=75 (kg/m3)
SiO2 (kg/m3)
22.5 20.0 17.5 15.0 12.5 10.0 7.5
CS (MPa)
60 55 50 45 40
Slag=300 (kg/m3)
Slag=300 (kg/m3)
Slag=500 (kg/m3)
Slag=600 (kg/m3)
7.5 10.0 12.5 15.0 17.5 20.0 22.5
Na2O (kg/m3)

(e)

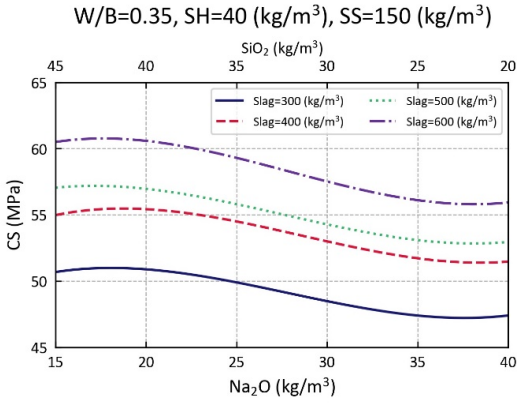
W/B=0.35, SH=40 (kg/m3), SS=150 (kg/m3)
SiO2 (kg/m3)
45 40 35 30 25 20
CS (MPa)
65 60 55 50 45
Slag=300 (kg/m3)
Slag=400 (kg/m3)
Slag=500 (kg/m3)
Slag=600 (kg/m3)
15 20 25 30 35 40
Na2O (kg/m3)

(f)

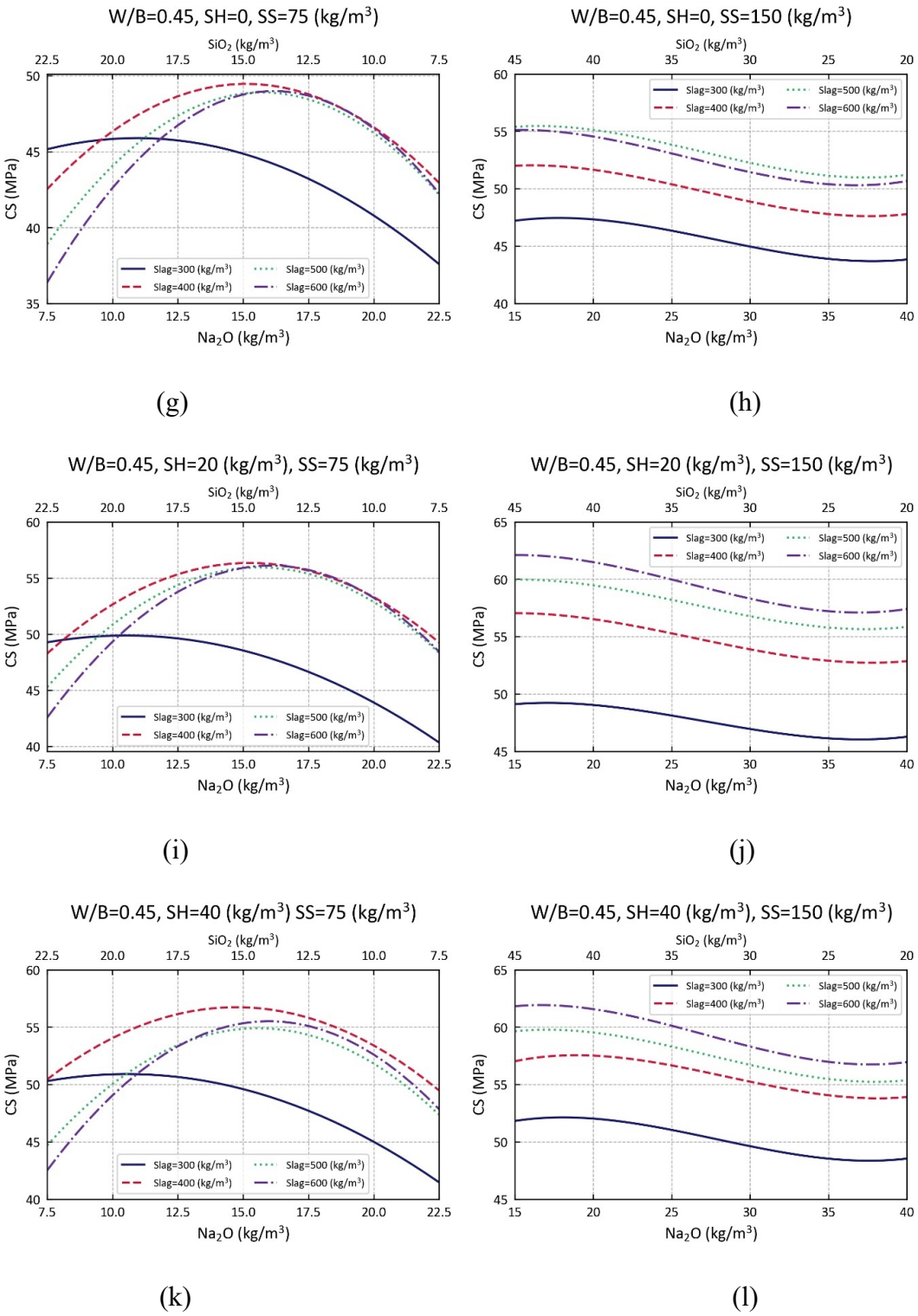

Figure 7-11: Effect of SiO_2 and Na_2O contents on the compressive strength of AMMS cured at RH= 30% considering various mixture design parameters (w/b ratio, slag content, SS content, and SH content).

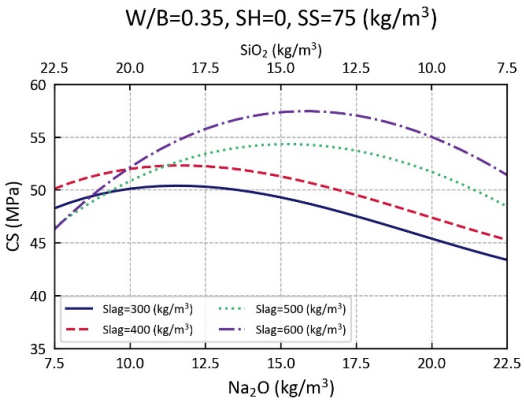
W/B=0.35, SH=0, SS=75 (kg/m³)
SiO₂ (kg/m³)
CS (MPa)
Na₂O (kg/m³)
Slag=300 (kg/m³)
Slag=400 (kg/m³)
Slag=500 (kg/m³)
Slag=600 (kg/m³)

(a)

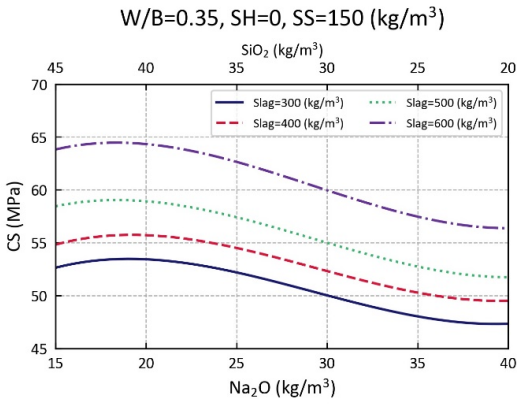
W/B=0.35, SH=0, SS=150 (kg/m³)
SiO₂ (kg/m³)
CS (MPa)
Na₂O (kg/m³)
Slag=300 (kg/m³)
Slag=400 (kg/m³)
Slag=500 (kg/m³)
Slag=600 (kg/m³)

(b)

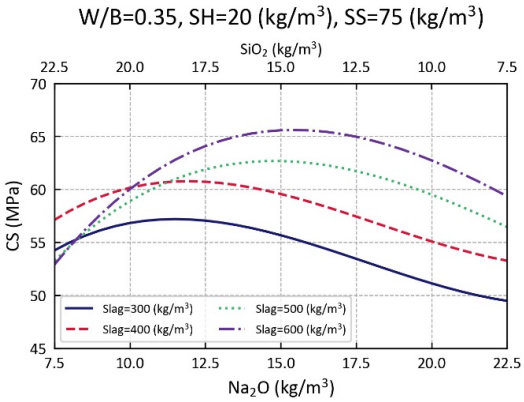
W/B=0.35, SH=20 (kg/m³), SS=75 (kg/m³)
SiO₂ (kg/m³)
CS (MPa)
Na₂O (kg/m³)
Slag=300 (kg/m³)
Slag=400 (kg/m³)
Slag=500 (kg/m³)
Slag=600 (kg/m³)

(c)

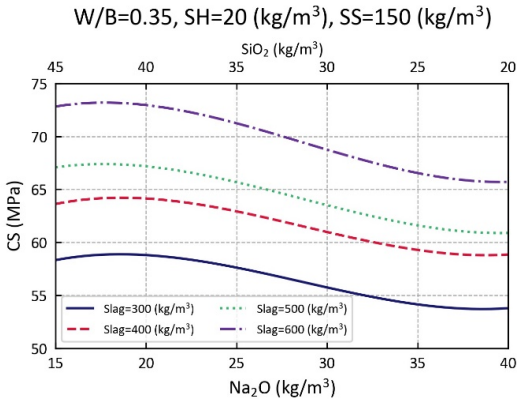
W/B=0.35, SH=20 (kg/m³), SS=150 (kg/m³)
SiO₂ (kg/m³)
CS (MPa)
Na₂O (kg/m³)
Slag=300 (kg/m³)
Slag=400 (kg/m³)
Slag=500 (kg/m³)
Slag=600 (kg/m³)

(d)

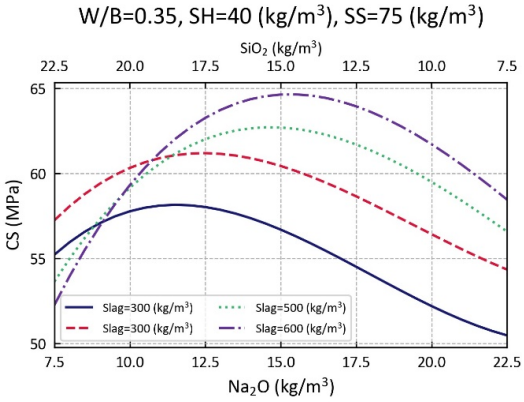
W/B=0.35, SH=40 (kg/m³), SS=75 (kg/m³)
SiO₂ (kg/m³)
CS (MPa)
Na₂O (kg/m³)
Slag=300 (kg/m³)
Slag=300 (kg/m³)
Slag=500 (kg/m³)
Slag=600 (kg/m³)

(e)

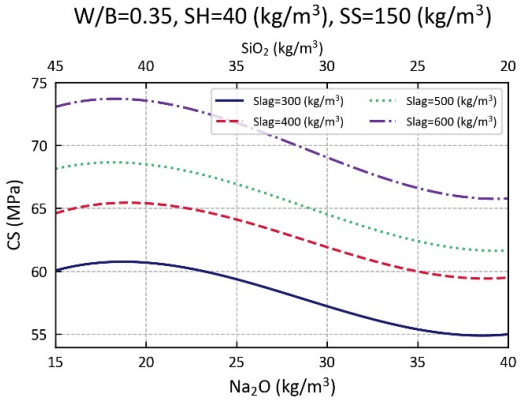
W/B=0.35, SH=40 (kg/m³), SS=150 (kg/m³)
SiO₂ (kg/m³)
CS (MPa)
Na₂O (kg/m³)
Slag=300 (kg/m³)
Slag=400 (kg/m³)
Slag=500 (kg/m³)
Slag=600 (kg/m³)

(f)

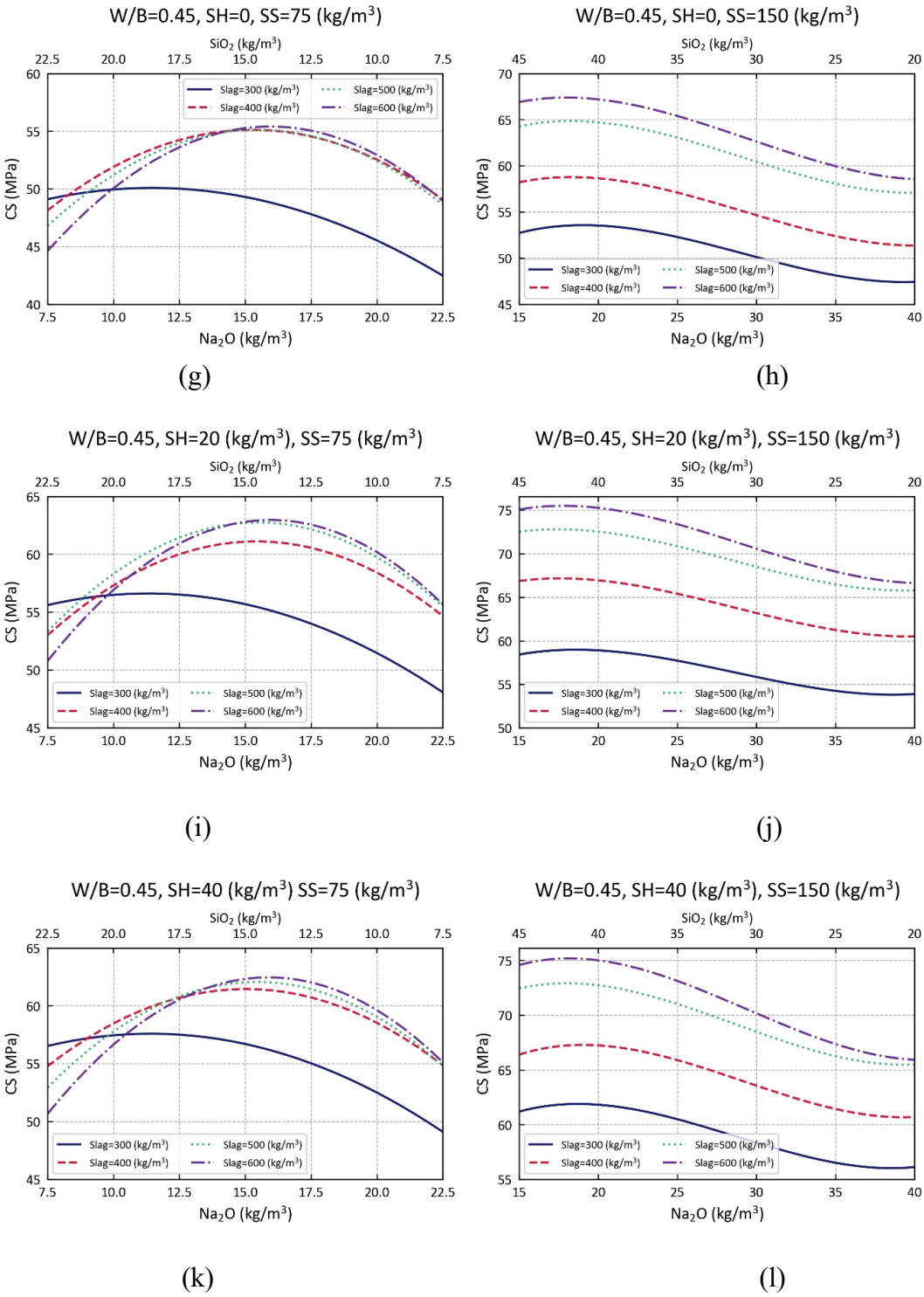

Figure 7-12: Effect of SiO_2 and Na_2O contents on the compressive strength of AAMs cured at RH= 100% considering various mixture design parameters (w/b ratio, slag content, SS content, and SH content).

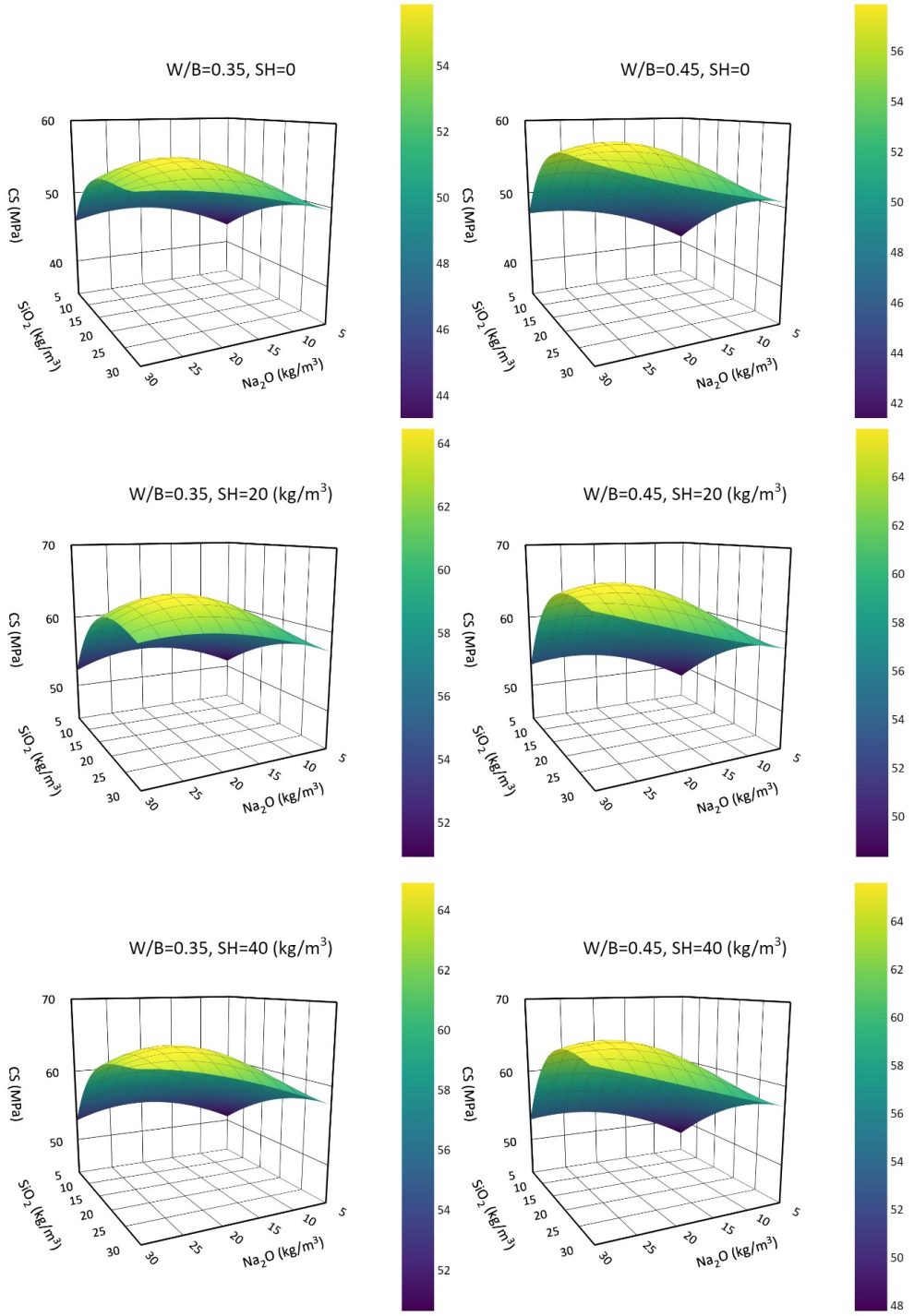

Figure 7-13: Response surface plots showing compressive strength in relation to Na_2O and SiO_2 contents considering various SS content and w/b ratio.

7.5.3 Experiment 3

Figure 7-14 explores the compressive strength development of concretes made with different SH content, SS dosage, and various at RH over 28 days. Generally, the results indicate that the ML model successfully captured the pattern in the data and could predict the compressive strength over the curing time. All curves showed the same trend, which is analogous to that of conventional concrete. For example, the compressive strength increased substantially in the first 7 days, followed by a gradual rise at a lower rate until 28 days. In this experiment, the effect of the SH content, SS content, and RH on the compressive strength development was well-captured based on the proposed ML models and abovementioned discussions in **Experiments 1 and 2**.

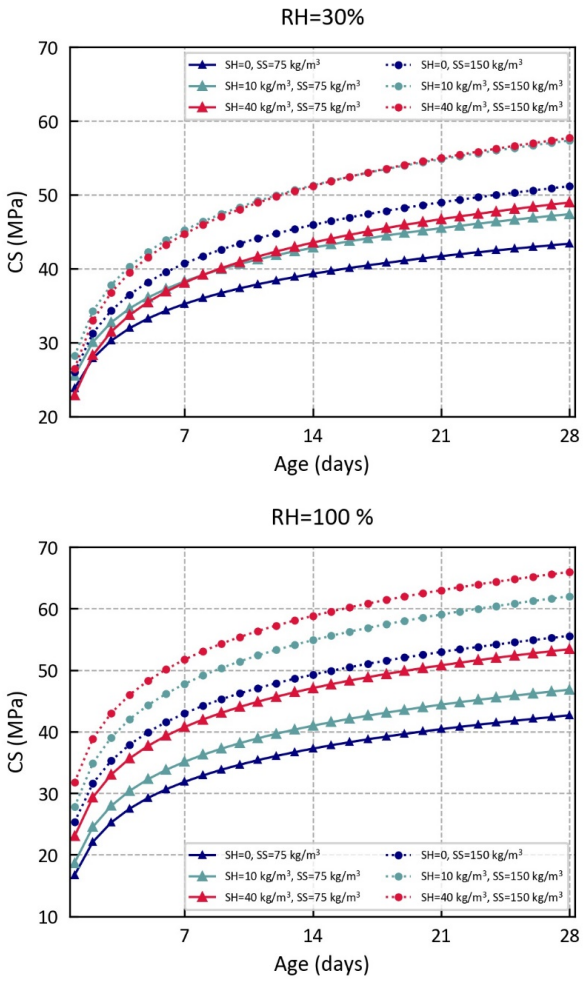

Figure 7-14: Effect of SH content, SS content, and curing RH on compressive strength development over time.

7.6 CONCLUSIONS AND REMARKS

This study aims at developing chemistry-informed machine learning (ML) models to estimate the compressive strength of alkali-activated materials (AAMs) based on their mixture proportions. For this purpose, a comprehensive dataset capturing 676 experimental mixture designs was compiled from peer-reviewed publications. A chemistry-based feature engineering approach was implemented before establishing ML frameworks to elevate the performance of models. Support vector regressor (SVR), random forest regressor (RFR), extra trees regressor (ETR), and gradient boosting regressor (GBR) were deployed for predicting the compressive strength. Accordingly, all developed models demonstrated promising capability of compressive strength prediction. The GBR model outperformed the other models achieving a testing R^2 of 0.944 and testing MAE and RMSE of 3.228 and 4.88 MPa, respectively. The feature importance analysis of tree-based ensembles revealed the design variables having high-impact. In addition to the curing age, the binder content, hydraulic and lime moduli, activator content, and fine aggregate content were identified as the input features with most significant contribution to the strength development.

Multiple numerical experiments conducted using the GBR model recognized the effects of several design parameters on AAMs' compressive strength development, including the formulation of the binder system, the formulation of the activator system, and the curing conditions. The contribution of fly ash in the blended binder system along with the SiO_2/Na_2O ratio in the activator to strength development was accurately captured by the GBR model. Furthermore, the effect of the W/B ratio and curing condition on the compressive strength was determined.

The results of the current research provide new insights into the design of AAMs using the robust predictive frameworks developed herein. The methodology applied in this study can assist researchers and engineers in rapidly evaluating, improving, and rationalizing the mixture proportioning of AAMs. In addition, the ML models aided mixture design can provide a solid foundation for the rational use of industrial and

mining byproducts, thereby promoting sustainable construction, and mitigating the environmental issues of the conventional concrete industry.

7.7 REFERENCES

Ahmad, M. W., Reynolds, J., and Rezgui, Y. (2018). Predictive modelling for solar thermal energy systems: A comparison of support vector regression, random forest, extra trees and regression trees. *Journal of Cleaner Production, 203*, 810-821.

Alam, M. S., Sultana, N., and Hossain, S. Z. (2021). Bayesian optimization algorithm based support vector regression analysis for estimation of shear capacity of FRP reinforced concrete members. *Applied Soft Computing, 105*, 107281.

Ali Khan, M., Zafar, A., Akbar, A., Javed, M. F., and Mosavi, A. (2021). Application of Gene Expression Programming (GEP) for the prediction of compressive strength of geopolymer concrete. *Materials, 14*(5), 1106.

Almustafa, M. K., and Nehdi, M. L. (2021). Machine learning prediction of structural response for FRP retrofitted RC slabs subjected to blast loading. *Engineering Structures, 244*, 112752.

Asteris, P. G., Skentou, A. D., Bardhan, A., Samui, P., and Pilakoutas, K. (2021). Predicting concrete compressive strength using hybrid ensembling of surrogate machine learning models. *Cement and Concrete Research, 145*, 106449.

Aydın, S., and Baradan, B. (2014). Effect of activator type and content on properties of alkali-activated slag mortars. *Composites Part B: Engineering, 57*, 166-172.

Bernal, S. A., de Gutiérrez, R. M., Pedraza, A. L., Provis, J. L., Rodriguez, E. D., and Delvasto, S. (2011). Effect of binder content on the performance of alkali-activated slag concretes. *Cement and Concrete Research, 41*(1), 1-8.

Binici, H., Temiz, H., and Köse, M. M. (2007). The effect of fineness on the properties of the blended cements incorporating ground granulated blast furnace slag and ground basaltic pumice. *Construction and Building Materials, 21*(5), 1122-1128.

Boser, B. E., Guyon, I. M., and Vapnik, V. N. (1992). *A training algorithm for optimal margin classifiers.* Paper presented at the Proceedings of the fifth annual workshop on Computational learning theory.

Breiman, L. (2001). Random forests. *Machine learning, 45*(1), 5-32.

Breiman, L., Friedman, J. H., Olshen, R. A., and Stone, C. J. (2017). *Classification and regression trees*: Routledge.

Castro-Alonso, M. J., Montañez-Hernandez, L. E., Sanchez-Muñoz, M. A., Macias Franco, M. R., Narayanasamy, R., and Balagurusamy, N. (2019). Microbially Induced Calcium Carbonate Precipitation (MICP) and Its Potential in Bioconcrete: Microbiological and Molecular Concepts. *Frontiers in Materials, 6*. doi: 10.3389/fmats.2019.00126

Chi, M., and Huang, R. (2013). Binding mechanism and properties of alkali-activated fly ash/slag mortars. *Construction and Building Materials, 40*, 291-298.

Cho, Y.-K., Yoo, S.-W., Jung, S.-H., Lee, K.-M., and Kwon, S.-J. (2017). Effect of Na2O content, SiO2/Na2O molar ratio, and curing conditions on the compressive strength of FA-based geopolymer. *Construction and Building Materials, 145*, 253-260.

Criado, M., and Provis, J. L. (2018). Alkali activated slag mortars provide high resistance to chloride-induced corrosion of steel. *Frontiers in Materials, 5*, 34.

Davidovits, J. (1994). High-alkali cements for 21st century concretes. *Special Publication, 144*, 383-398.

Dong, B., Cao, C., and Lee, S. E. (2005). Applying support vector machines to predict building energy consumption in tropical region. *Energy and Buildings, 37*(5), 545-553.

Duxson, P., Provis, J. L., Lukey, G. C., Mallicoat, S. W., Kriven, W. M., and Van Deventer, J. S. (2005). Understanding the relationship between geopolymer composition, microstructure and mechanical properties. *Colloids and Surfaces A: Physicochemical and Engineering Aspects, 269*(1-3), 47-58.

Farooq, F., Ahmed, W., Akbar, A., Aslam, F., and Alyousef, R. (2021). Predictive modeling for sustainable high-performance concrete from industrial wastes: A comparison and optimization of models using ensemble learners. *Journal of Cleaner Production, 292*, 126032.

Fernández-Jiménez, A., and Palomo, A. (2005). Composition and microstructure of alkali activated fly ash binder: Effect of the activator. *Cement and Concrete Research, 35*(10), 1984-1992.

Frazier, P. I. (2018). A tutorial on Bayesian optimization. *arXiv preprint arXiv:1807.02811*.

Gavali, H. R., and Ralegaonkar, R. V. (2020). Design of eco-efficient housing with sustainable alkali-activated bricks. *Journal of Cleaner Production, 254*, 120061.

Geurts, P., Ernst, D., and Wehenkel, L. (2006). Extremely randomized trees. *Machine learning, 63*(1), 3-42.

Gomaa, E., Han, T., ElGawady, M., Huang, J., and Kumar, A. (2021). Machine learning to predict properties of fresh and hardened alkali-activated concrete. *Cement and Concrete Composites, 115*, 103863.

Gruskovnjak, A., Lothenbach, B., Holzer, L., Figi, R., and Winnefeld, F. (2006). Hydration of alkali-activated slag: comparison with ordinary Portland cement. *Advances in Cement Research, 18*(3), 119-128.

Habert, G., Miller, S., John, V., Provis, J., Favier, A., Horvath, A., and Scrivener, K. (2020). Environmental impacts and decarbonization strategies in the cement and concrete industries. *Nature Reviews Earth and Environment, 1*(11), 559-573.

Han, Q., Gui, C., Xu, J., and Lacidogna, G. (2019). A generalized method to predict the compressive strength of high-performance concrete by improved random forest algorithm. *Construction and Building Materials, 226*, 734-742.

He, J., Jie, Y., Zhang, J., Yu, Y., and Zhang, G. (2013). Synthesis and characterization of red mud and rice husk ash-based geopolymer composites. *Cement and Concrete Composites, 37*, 108-118.

Jalal, M., Arabali, P., Grasley, Z., Bullard, J. W., and Jalal, H. (2020). Behavior assessment, regression analysis and support vector machine (SVM) modeling of waste tire rubberized concrete. *Journal of Cleaner Production, 273*, 122960.

Joseph, B., and Mathew, G. (2012). Influence of aggregate content on the behavior of fly ash based geopolymer concrete. *Scientia Iranica, 19*(5), 1188-1194.

Juenger, M., Winnefeld, F., Provis, J. L., and Ideker, J. (2011). Advances in alternative cementitious binders. *Cement and Concrete Research, 41*(12), 1232-1243.

Ke, X., and Duan, Y. (2021). Coupling machine learning with thermodynamic modelling to develop a composition-property model for alkali-activated materials. *Composites Part B: Engineering, 216*, 108801.

Kumarappa, D. B., Peethamparan, S., and Ngami, M. (2018). Autogenous shrinkage of alkali activated slag mortars: Basic mechanisms and mitigation methods. *Cement and Concrete Research, 109*, 1-9.

Kumari, P., and Toshniwal, D. (2021). Extreme gradient boosting and deep neural network based ensemble learning approach to forecast hourly solar irradiance. *Journal of Cleaner Production, 279*, 123285.

Li, N., Shi, C., Zhang, Z., Zhu, D., Hwang, H.-J., Zhu, Y., and Sun, T. (2018). A mixture proportioning method for the development of performance-based alkali-activated slag-based concrete. *Cement and Concrete Composites, 93*, 163-174.

Marani, A., Jamali, A., and Nehdi, M. L. (2020). Predicting Ultra-High-Performance Concrete Compressive Strength Using Tabular Generative Adversarial Networks. *Materials, 13*(21), 4757.

Marani, A., and Nehdi, M. L. (2020). Machine learning prediction of compressive strength for phase change materials integrated cementitious composites. *Construction and Building Materials, 265*, 120286.

Naseri, H., Jahanbakhsh, H., Hosseini, P., and Nejad, F. M. (2020). Designing sustainable concrete mixture by developing a new machine learning technique. *Journal of Cleaner Production, 258*, 120578.

Nasr, D., Pakshir, A. H., and Ghayour, H. (2018). The influence of curing conditions and alkaline activator concentration on elevated temperature behavior of alkali activated slag (AAS) mortars. *Construction and Building Materials, 190*, 108-119.

Nunez, I., Marani, A., and Nehdi, M. L. (2020). Mixture Optimization of Recycled Aggregate Concrete Using Hybrid Machine Learning Model. *Materials, 13*(19), 4331.

Okoye, F., Durgaprasad, J., and Singh, N. (2015). Mechanical properties of alkali activated flyash/Kaolin based geopolymer concrete. *Construction and Building Materials, 98*, 685-691.

Pacheco-Torgal, F., Abdollahnejad, Z., Miraldo, S., and Kheradmand, M. (2017). *Alkali-activated cement-based binders (AACBs) as durable and cost-competitive low-CO2 binder materials: some shortcomings that need to be addressed*: Butterworth-Heinemann, Oxford, UK.

Pan, M., Li, C., Gao, R., Huang, Y., You, H., Gu, T., and Qin, F. (2020). Photovoltaic power forecasting based on a support vector machine with improved ant colony optimization. *Journal of Cleaner Production, 277*, 123948.

Passuello, A., Rodríguez, E. D., Hirt, E., Longhi, M., Bernal, S. A., Provis, J. L., and Kirchheim, A. P. (2017). Evaluation of the potential improvement in the environmental footprint of geopolymers using waste-derived activators. *Journal of Cleaner Production, 166*, 680-689.

Pedregosa, F., Varoquaux, G., Gramfort, A., Michel, V., Thirion, B., Grisel, O., Blondel, M., Prettenhofer, P., Weiss, R., Dubourg, V. and Vanderplas, J. (2011). Scikit-learn: Machine learning in Python. *the Journal of machine Learning research, 12*, 2825-2830.

Pelikan, M., Goldberg, D. E., and Cantú-Paz, E. (1999). *BOA: The Bayesian optimization algorithm.* Paper presented at the Proceedings of the genetic and evolutionary computation conference GECCO-99.

Provis, J., and Van Deventer, J. (2014). Alkali Activated Materials: State-of-the-Art Report, RILEM TC.

Provis, J. L. (2014). Geopolymers and other alkali activated materials: why, how, and what? *Materials and Structures, 47*(1), 11-25.

Provis, J. L., and Bernal, S. A. (2014). Geopolymers and related alkali-activated materials. *Annual Review of Materials Research, 44*, 299-327.

Provis, J. L., and Van Deventer, J. S. J. (2009). *Geopolymers: structures, processing, properties and industrial applications*: Elsevier.

Puertas, F., Martínez-Ramírez, S., Alonso, S., and Vazquez, T. (2000). Alkali-activated fly ash/slag cements: strength behaviour and hydration products. *Cement and Concrete Research, 30*(10), 1625-1632.

Rajasekar, A., Arunachalam, K., and Kottaisamy, M. (2019). Assessment of strength and durability characteristics of copper slag incorporated ultra high strength concrete. *Journal of Cleaner Production, 208*, 402-414.

Rovnaník, P. (2010). Effect of curing temperature on the development of hard structure of metakaolin-based geopolymer. *Construction and Building Materials, 24*(7), 1176-1183.

Smola, A. J., and Schölkopf, B. (2004). A tutorial on support vector regression. *Statistics and computing, 14*(3), 199-222.

Thilakarathna, P., Seo, S., Baduge, K. K., Lee, H., Mendis, P., and Foliente, G. (2020). Embodied carbon analysis and benchmarking emissions of high and ultra-high strength concrete using machine learning algorithms. *Journal of Cleaner Production, 262*, 121281.

Tian, X., Rao, F., Morales-Estrella, R., and Song, S. (2020). Effects of aluminum dosage on gel formation and heavy metal immobilization in alkali-activated municipal solid waste incineration fly ash. *Energy and Fuels, 34*(4), 4727-4733.

Van Jaarsveld, J., Van Deventer, J. S., and Lukey, G. (2002). The effect of composition and temperature on the properties of fly ash-and kaolinite-based geopolymers. *Chemical Engineering Journal, 89*(1-3), 63-73.

Wu, M., Zhang, Y., Jia, Y., She, W., and Liu, G. (2020). Study on the role of activators to the autogenous and drying shrinkage of lime-based low carbon cementitious materials. *Journal of Cleaner Production, 257*, 120522.

Xie, J., Wang, J., Rao, R., Wang, C., and Fang, C. (2019). Effects of combined usage of GGBS and fly ash on workability and mechanical properties of alkali activated geopolymer concrete with recycled aggregate. *Composites Part B: Engineering, 164*, 179-190.

Xie, T., and Visintin, P. (2018). A unified approach for mix design of concrete containing supplementary cementitious materials based on reactivity moduli. *Journal of Cleaner Production, 203*, 68-82.

Xie, T., Yang, G., Zhao, X., Xu, J., and Fang, C. (2020). A unified model for predicting the compressive strength of recycled aggregate concrete containing supplementary cementitious materials. *Journal of Cleaner Production, 251*, 119752.

Xing, J., Zhao, Y., Qiu, J., and Sun, X. (2019). Microstructural and mechanical properties of alkali activated materials from two types of blast furnace slags. *Materials, 12*(13), 2089.

Yan, K., and Shi, C. (2010). Prediction of elastic modulus of normal and high strength concrete by support vector machine. *Construction and Building Materials, 24*(8), 1479-1485.

Yang, K.-H., Cho, A.-R., and Song, J.-K. (2012). Effect of water–binder ratio on the mechanical properties of calcium hydroxide-based alkali-activated slag concrete. *Construction and Building Materials, 29*, 504-511.

Yang, S., Xu, J., Zang, C., Li, R., Yang, Q., and Sun, S. (2019). Mechanical properties of alkali-activated slag concrete mixed by seawater and sea sand. *Construction and Building Materials, 196*, 395-410.

Young, B. A., Hall, A., Pilon, L., Gupta, P., and Sant, G. (2019). Can the compressive strength of concrete be estimated from knowledge of the mixture proportions?: New insights from statistical analysis and machine learning methods. *Cement and Concrete Research, 115*, 379-388.

Zhang, J., Huang, Y., Aslani, F., Ma, G., and Nener, B. (2020). A hybrid intelligent system for designing optimal proportions of recycled aggregate concrete. *Journal of Cleaner Production, 273*, 122922.

Zhang, J., Li, D., and Wang, Y. (2020). Toward intelligent construction: Prediction of mechanical properties of manufactured-sand concrete using tree-based models. *Journal of Cleaner Production, 258*, 120665.

Zhang, J., Ma, G., Huang, Y., Aslani, F., and Nener, B. (2019). Modelling uniaxial compressive strength of lightweight self-compacting concrete using random forest regression. *Construction and Building Materials, 210*, 713-719.

Zhang, Z., and Wang, H. (2015). Analysing the relation between pore structure and permeability of alkali-activated concrete binders. *Handbook of Alkali-Activated Cements, Mortars and Concretes*, 235-264.

Chapter 8

8 SUMMARY, CONCLUSIONS, AND RECOMMENDATIONS FOR FUTURE WORK

8.1 SUMMARY AND CONCLUSIONS

Despite decades of intensive research on crack self-healing in cement-based materials, very few studies have been carried out on the new binder type of green and sustainable AAMs. In addition, the feasibility of self-healing technologies for cement-based materials in AAMs is not well-understood, which needs to be explored. To help bridge this knowledge gap, this dissertation attempts to provide fundamental investigations on enhancing the self-healing efficiency in alkali-activated slag-based composites with multiple autonomic healing methods. Moreover, strategies for producing self-healing alkali-activated slag-based composites were evaluated with various assessment techniques.

At the start of this research, Chapter 2 provides a comprehensive review of the development of stimulated autogenous healing and autonomic healing methods and self-healing assessment techniques in cementitious materials. It was revealed that the maximum healed crack width does not significantly improve using stimulated autogenous healing compared to pure autogenous healing due to the lack of flowable healing agents. In contrast, autonomic healing methods, including encapsulation of self-healing agents and MICCP, can achieve significant crack self-healing in a shorter time. Furthermore, the progress, limitations, and future perspectives of different healing approaches were discussed.

In Chapter 3, the potential of using $Ca(OH)_2$ to enhance the self-healing capability of cracks in alkali-activated slag-based mortars was explored using a portfolio of testing methods. Results showed that alkali-activated slag-based composites incorporating

$Ca(OH)_2$ (7% by weight of slag) achieved a higher level of self-healing than that of control specimens without calcium hydroxide. X-ray μCT coupled with three-dimensional image analysis demonstrated that the observed self-healing was a surface mechanism, only occurring at surface cracks. SEM results revealed that calcium carbonate was found to be the main self-healing product in all test specimens. Leaching experimental results indicated that the concentration of Ca^{2+} ions in the AAM matrix played a critical role in calcium carbonate precipitation and, thus, self-healing potential.

The findings from Chapter 3 have motivated research on exploring new additives and expansive minerals that promote the self-healing potential. For this purpose, Chapter 4 employs a wide array of experimental techniques to investigate the self-healing properties of PVA fibre-reinforced alkali-activated slag-based composites incorporating CA and BN. The experimental results showed that CA specimens achieved the highest crack sealing ratio among the three mixtures investigated, and surface cracks with smaller width attained better self-healing potential. Fibre-reinforced alkali-activated slag composites incorporating CA reached higher compressive and tensile strength compared to that of control mixtures. In contrast, BN mixtures had slightly decreased mechanical properties. In addition, sorptivity decreased by 54.3% for pre-cracked CA-AAS after 15-d water curing, which was more than that of pre-cracked 0-AAS and BN-AAS specimens.

In Chapter 5, the potential of immobilized *S. pasteurii* bacteria to impart crack self-healing in fibre-reinforced alkali-activated slag-based composites subjected to different environmental exposures was investigated. Porous expanded glass granules made from recycled glass were used as bacterial and nutrient carriers. Results indicate that the crack self-healing ability of bio-green concrete incorporating *S. pasteurii* impregnated expanded glass granules was substantially enhanced. Compared to water submersion under normal temperature, the condition of higher temperature coupled with water-dry cycles could accelerate the metabolism of *S. pasteurii*, resulting in improved crack self-healing. The specimens incorporating bacteria immobilized in expanded glass compensated for the decrease in mechanical properties caused by bacterial nutrients and expanded glass granules. The specimens treated with bacteria yielded a significant decline in the water sorptivity coefficient compared with that of the reference specimens

without bacteria. SEM-EDS results showed that calcium carbonate was the dominant self-healing compound. In addition, calcite, as the polymorph of calcium carbonate, was further characterized via Raman spectroscopy. PVA fibres incorporated into the composite matrix acted as preferential crystal nucleation sites for calcium carbonate precipitation. In summary, the alkaline environment, *S. pasteurii* driven-ureolysis, and calcium ions acted synergistically in contributing to the precipitation of calcium carbonate to heal surface cracks in fibre-reinforced alkali-activated slag-based composites.

Chapter 6 expanded on the findings of Chapter 5. The effect of different calcium sources (calcium lactate and calcium chloride) on the reaction kinetics, mechanical properties, capillary water absorption, and final self-healing compounds was investigated. The calorimetric results revealed that the specimens incorporating different calcium additives induced a retarding effect that delayed the acceleration phase compared to the reference sample. Bio-specimens with calcium lactate and calcium chloride as calcium sources exhibited a significant decrease in water sorptivity compared with abiotic control samples. SEM-EDS confirmed the presence of calcium carbonate as the dominant self-healing compound. In addition, results from Raman spectroscopy indicated that the calcium carbonate in bacteria-based specimens with calcium chloride showed two polymorphs, namely, calcite and vaterite, compared to calcite only observed in the counterparts with calcium lactate. Finally, it was suggested that calcium lactate, as the calcium source, was a better option considering economic feasibility and sustainability.

Chapter 7 proposes a chemistry-informed machine learning model to estimate the compressive strength of AAMs based on their mixture proportions and the chemical compositions of their precursors and activators. A comprehensive dataset encompassing 676 mixture design examples was extracted from peer-reviewed published research studies. A chemistry-based feature engineering was implemented to elevate the prediction performance of four applied machine learning models, including SVR, RF, ETR, and GBR. It was shown that all developed models demonstrated promising capability of compressive strength prediction. In addition, the GBR model outperformed the other models achieving R^2 of 0.944 and MAE and RMSE of 3.228 and 4.88 MPa on the test

data set unknown to the model, respectively. Multiple numerical experiments conducted using the GBR model recognized the effects of several design parameters on AAMs' compressive strength development, including the formulation of the binder system, the formulation of the activator system, and the curing conditions. The contribution of fly ash in the blended binder system and the SiO_2/Na_2O ratio in the activator to the compressive strength development was accurately captured by the GBR model. Furthermore, the effect of the W/B ratio and curing condition on the compressive strength was determined.

8.2 RECOMMENDATIONS FOR FUTURE RESEARCH

The current research introduced possible autonomic healing approaches, including $Ca(OH)_2$, CAs, bentonite, and MICCP, to enhance the self-healing efficiency of fibre-reinforced alkali-activated slag-based composites. However, there are several remaining questions and challenges. The following are indications about possible future research efforts in the field of self-healing in AAMs:

(1) Based on the findings in the current dissertation, it is indicated that the efficacy of the autonomic healing methods employed in this research was limited compared to that in cement-based materials, where maximum crack withs of up to 1mm can be entirely healed. This can be explained by the harsher environment in the matrix of alkali-activated slag-based composites and less dissolved calcium ions within this matrix. Therefore, the adoption of more effective healing methods, such as encapsulation of healing agents, should be considered.

(2) Despite investigations on the surface crack change under various self-healing behaviour, the entire crack volume change as a function of the self-healing time is unclear, which requires further exploration using X-ray μCT.

(3) Further research is needed to evaluate the self-healing efficiency using non-destructive testing techniques, such as electrical resistivity and resonant frequency, which could provide detailed information reflecting the self-healing effectiveness within a shorter time than measurements of regained transport properties.

(4) A true self-healing material should possess continuous self-healing capability throughout its service life in response to multiple cracking activities. In the present study, all cracking occurred at early age (e.g., 14 or 28 days) rather than after years of field exposure. Therefore, the crack self-healing at later stages (e.g., more than one year) should be explored.

(5) The vegetative bacteria used in this study can be metabolically active for up to one year; however, this duration is still much shorter than the lifespan of structures. Therefore, a new strain of mineral-forming bacteria with a much longer life and novel encapsulation technologies of bacteria needs to be explored in future research.

(6) Water plays an essential role in the crack self-healing of AAMs. In the present thesis, only water submersion and wet and dry cycles were used, representing the environmental exposures of underwater structures and structures in tidal zones and frequent wetting. However, there is a much more difference in real-life environmental exposures. Future work is therefore needed to investigate the effect of varied curing conditions on the efficacy of self-healing outside the laboratory.

(7) A life-cycle cost assessment is essential to justify the feasibility of self-healing structures, while considering carbon-savings and embodied energy for the sustainability of future construction.

(8) The cracking of AAMs is usually attributed to shrinkage when only considering durability-induced cracking. However, the extent of shrinkage that triggers cracking remains unexplored. Therefore, the development of a machine learning model to estimate AAMs' autogenous and drying shrinkage based on their mixture proportions, chemical compositions of the precursors and activators, and curing conditions is an interesting future research endeavor.

Curriculum Vitae

Name:	Lei Zhang
Post-secondary Education and Degrees:	Inner Mongolia University of Science and Technology (IMUST) Baotou, Inner Mongolia Autonomous Zone, China 2010-2014 B.E. The University of Science and Technology Beijing (USTB) Beijing, China 2014-2017 M.E. The University of Western Ontario (UWO) London, Ontario, Canada 2017-2021 Ph.D.
Honours and Awards:	Full Ph.D. Scholarship sponsored by China Scholarship Council 2017 Outstanding Graduates in USTB 2016 Provincial Outstanding Undergraduates 2012, 2013
Related Work Experience	Teaching Assistant The University of Western Ontario 2017-2021 Research Assistant Anhui Eastern Mine Design and Research Institute (China) 2010-2014

Publications:

Articles Published in Refereed Journals:

L.V. Zhang, A.R. Suleiman, and M. L. Nehdi, "Self-healing in fiber-reinforced alkali-activated slag composites incorporating different additives," *Construction and Building Materials*, 262 (2020): 120059.

Lei V. Zhang, Ahmed R. Suleiman, and Moncef L. Nehdi, "Crack self-Healing in NaOH-activated slag-based composites incorporating calcium hydroxide," *Journal of Materials in Civil Engineering*,33(4):04021012.

Murat Tuyan, **Lei V. Zhang**, and Moncef L. Nehdi, "Development of sustainable alkali-activated slag grout for preplaced aggregate concrete," *Journal of Cleaner Production*, 277 (2020): 123488.

Murat Tuyan, **Lei V. Zhang**, and Moncef L. Nehdi, "Development of sustainable preplaced aggregate concrete with alkali-activated slag grout," *Construction and Building Materials*, 263 (2020): 120227.

Y. Zhang, M. Elsayed, **L.V. Zhang**, and M.L. Nehdi, "Flexural behavior of reinforced concrete T-section beams strengthened by NSM-FRP bars," *Engineering Structures*, 233 (2021): 111922.

Yannian Zhang, Moncef L. Nehdi, Xiaohan Gao, and **Lei V. Zhang**, "Flexural Performance of Novel Nail-Cross-Laminated Timber Composite Panels," *Applied Sciences*, 10 (2020): 5983.

C. Xu, M.L. Nehdi, M. Youssef, T Wang, and **L.V. Zhang**, "Seismic performance of RC beam-column edge joints reinforced with austenite stainless steel," *Engineering Structures*, 232 (2021): 111824.

Articles Submitted to Refereed Journals:

Lei V. Zhang, Moncef L. Nehdi, Ahmed R. Suleiman, Malihe M. Allaf, Afshin Marani, and Murat Tuyan, "Crack Self-healing in Bio-Green Concrete," *Composites Part B: Engineering*.

Lei V. Zhang, Ahmed R. Suleiman, Malihe M. Allaf, Afshin Marani, and Moncef L. Nehdi, "Crack self-healing in alkali-activated slag composites incorporating immobilized bacteria," *Construction and Building Materials*.

Lei V. Zhang, Afshin Marani, and Moncef L. Nehdi, "Chemistry-informedMachine Learning Prediction of Compressive Strength for Alkali-Activated Materials," *Journal of Cleaner Production.*

Afshin Marani, **Lei V. Zhang**, and Moncef L. Nehdi, "Mixture Optimization of Concrete Incorporating Micro-encapsulated Phase Change Materials Using a Ternary Machine Learning Model," *Cement and Concrete Composites*.

Y. Zhang, U.A. Ebead, **L.V. Zhang**, and M.L. Nehdi, "Shear behavior of reinforced concrete T-beams strengthened with near-surface mounted FRP bars," *Engineering Structures*.

Y. Zhang, M.L. Nehdi, X. Gao, **L.V. Zhang**, and A.R. Suleiman, "Experimental Investigation on Axial Compression of Resilient Nail-Cross-Laminated Timber Panels," *Sustainability*.

C. Xu, M.L. Nehdi, Y. Xu, and **L.V. Zhang**, "Effect of glass-fiber geogrid configuration on seismic behavior of masonry walls," *Engineering Structures*.

Papers Accepted by Peer-Reviewed Conference Proceedings:

L.V. Zhang, A.R. Suleiman, A. Marani, and M.L. Nehdi, "Effect of various temperatures and relative humidities on crack self-healing in fiber-reinforced mortars incorporating crystalline additives," *In Proceedings, Annual Conference of the Canadian Society of Civil Engineering (CSCE)*, Niagara Falls, Ontario, Canada, May 26-29.

L.V. Zhang, A. R. Suleiman, A. Marani, and M.L. Nehdi, "Comparative study on self-healing behavior of alkali-activated composites and cement-based materials," *In Proceedings, Annual Conference of the Canadian Society of Civil Engineering (CSCE)*, Niagara Falls, Ontario, Canada, May 26-29.

A. Marani, **L.V. Zhang**, and M.L. Nehdi, "Experimental study on the effect of microencapsulated PCM addition cement hydration," *In Proceedings, Annual Conference of the Canadian Society of Civil Engineering (CSCE)*, Niagara Falls, Ontario, Canada, May 26-29.

Patents:

Yannian Zhang and **Lei V. Zhang**. "An assembled explosion-proof column structure," *China Patent CN111749525A*, filed on July 31, 2020, and issued on October 9, 2020.

Yannian Zhang and **Lei V. Zhang**. "Bilateral assembling anti-blast wall panels," *China Patent CN111794401A*, filed on August 14, 2020, and issued on October 20, 2020.

Yannian Zhang and **Lei V. Zhang**. "A blast-proof wall with built-in multi-spindle shaped pressure relief cavity" *China Patent CN111734194A*, filed on August 4, 2020, and issued on October 2, 2020.